MAX–PLANCK–INSTITUT FÜR RADIOASTRONOMIE
BONN

Searching for the Ashes of Dead Stars

Dissertation

zur

Erlangung des Doktorgrades (*Dr. rer. nat.*)

der

Mathematisch–Naturwissenschaftlichen Fakultät

der

Rheinischen Friedrich–Wilhelms–Universität Bonn

vorgelegt von

Rohit Dokara
aus
Visakhapatnam, India

Bonn 2023

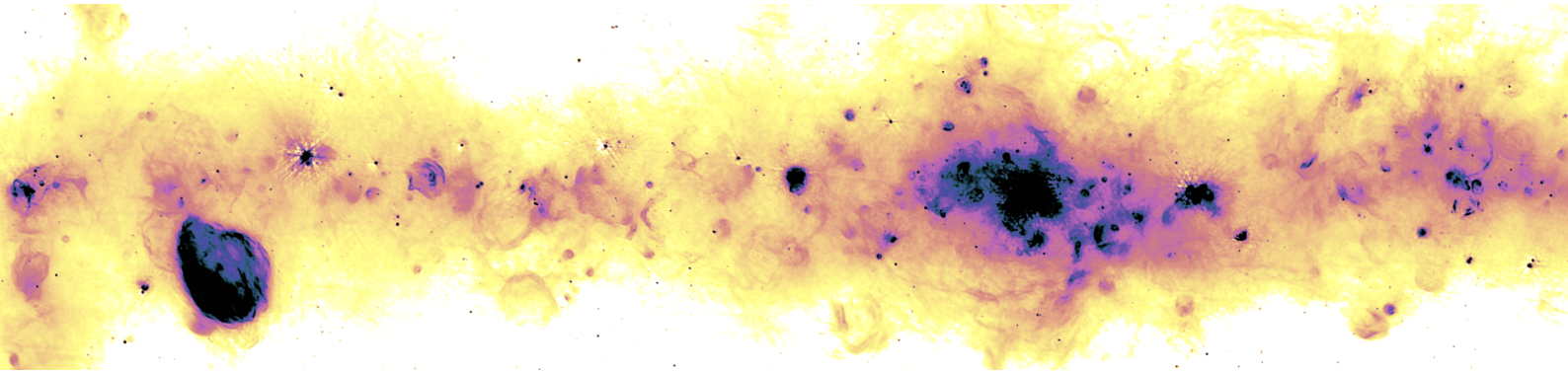

Angefertigt mit Genehmigung der Mathematisch-Naturwissenschaftlichen Fakultät der Rheinischen Friedrich–Wilhelms–Universität Bonn

Prepared with permission from the Faculty of Mathematics and Natural Sciences of the Rheinische Friedrich Wilhelm University of Bonn

1. Referent / *1st referee*: Prof. Dr. Karl M. Menten
2. Referent / *2nd referee*: Prof. Dr. Pavel Kroupa

Tag der Promotion / *Conferral Date*: 2023 July 03
Erscheinungsjahr / *Year of Publication*: 2023

Diese Dissertation ist elektronisch verfügbar auf dem Repositorium der Uni Bonn:
This thesis is available electronically at the repository of the University of Bonn:
https://nbn-resolving.org/urn:nbn:de:hbz:5-71220

RHEINISCHE FRIEDRICH–WILHELMS–UNIVERSITÄT BONN

Abstract

by Rohit Dokara

for the degree of

Doctor rerum naturalium

Hydrogen, helium, and trace amounts of lithium were formed during the Big Bang, but most other elements originally formed deep inside stars by the process of nuclear fusion. They were later scattered across the cosmos, chiefly by supernova remnants (SNRs)—*the ashes of dead stars*. SNRs are formed when the material expelled in a supernova explosion interacts with its surrounding interstellar medium. The material recycled and distributed by SNRs subsequently formed most of the material we see in the present day, including in us humans. By injecting energy, momentum, and turbulence, SNRs provide 'feedback' to the process of star formation and affect the interstellar medium and the dynamics of the Galaxy in a manner that is not yet well comprehended. In order to gain a complete understanding of the nature around us, studies on a large and representative sample of SNRs are necessary. In the Milky Way, however, such a sample does not yet exist. Currently, the two catalogs of Galactic SNRs contain less than 300 confirmed SNRs, whereas statistical studies show that there should be at least 1000 SNRs. The work done for this thesis deals with attempting to correct this apparent deficiency.

SNRs are brighter and hence more easily observed at radio frequencies below 1 GHz. A large-scale, low-frequency survey of the Milky Way is well suited to study and also discover SNRs. In order to understand the feasibility of conducting such a survey with the upgraded Giant Meterwave Radio Telescope (uGMRT), we carried out a 'pilot' study observing a small portion of the Galactic plane of the Milky Way. In the resulting images, we are able to recover diffuse emissions reasonably well. However, we found that a denser grid of pointings and better antenna performance, among other conditions, are necessary to achieve the target resolution and sensitivity. The recommendations from this study are being implemented for a full survey planned to be conducted in the near future.

It is known that SNRs are relatively brighter in the radio regime but fainter in the mid-infrared wavelengths. Using this anti-correlation property, we searched for objects that could potentially be SNRs, which we call 'SNR candidates', in the Very Large Array images of the 4–8 GHz GLObal view on STAR formation (GLOSTAR) survey. We identified 157 candidates, of which 77 were previously detected in other studies and 80 are new detections. In addition, we found spurious entries in the catalog of Galactic SNRs; four H II regions were erroneously classified as SNRs.

Confirmation of SNR candidates must be done by establishing the nonthermal nature of their radio emission, through measurements of linear polarization and spectral index. Using these properties, we showed that at least seven candidates are indeed SNRs. We justify our strategy of searching for small angular-size SNRs by conducting a Monte-Carlo simulation of the evolution of SNRs in the Milky Way, and advise future studies to continue with this strategy.

To my family

You solve one problem, and you solve the next one, and then the next.
And if you solve enough problems, you get to come home.

– *Mark Whatney, The Martian*

Publications related to this thesis

The research work made for this thesis culminated in two peer-reviewed first-author publications, and one more is under preparation. They are listed below.

- Galactic plane survey with the uGMRT: lessons from the pilot study
  Dokara et al. in prep.
  Contributions: Performed the data reduction and the scientific analysis, interpreted the results, and wrote the manuscript. Coauthors had supervised the project.
- GLOSTAR VII. Supernova remnants in the Galactic longitude range $28^\circ < l < 36^\circ$
  Dokara et al. 2023, A&A, 671, A145 arXiv:2211.13811
  Contributions: Made the combination images, performed the scientific analysis, interpreted the results, and wrote the manuscript. Coauthors had supervised the project and supplied to me the individual images, while also helping with the manuscript.
- GLOSTAR II. Supernova remnants in the first quadrant of the Milky Way
  Dokara et al. 2021, A&A, 651, A86 arXiv:2103.06267
  Contributions: Performed the visual search, the scientific analysis, interpreted the results, and wrote the manuscript. Coauthors had supervised the project and supplied to me the images, while also helping with the manuscript.

Other publications

Below is a list of papers, which I had contributed to, published during the period of this thesis work.

- GLOSTAR VI. Radio source catalog II: $28^\circ < l < 36^\circ$ and $|b| < 1^\circ$, VLA B configuration
  Dzib et al. 2023, A&A, 670, A9 arXiv:2210.00560
- GLOSTAR V. 6.7 GHz methanol maser catalogue
  Nguyen et al. 2022, A&A, 666, A59 arXiv:2207.10548
- GLOSTAR IV. Radio continuum detections of young stellar objects in the Galactic Centre region
  Nguyen et al. 2021, A&A, 651, A88 arXiv:2105.03212
- GLOSTAR III. 6.7 GHz methanol maser survey in Cygnus X
  Ortiz-Leon et al. 2021, A&A, 651, A87 arXiv:2105.07471
- GLOSTAR I. Overview and first results for the Galactic longitude range $28^\circ < l < 36^\circ$
  Brunthaler et al. 2021, A&A, 651, A85 arXiv:2106.00377

Contents

Nomenclature

Frequently used constants and symbols

pc	parsec	3.086×10^{16} m
yr	year	3.15576×10^{7} sec
$M_\odot$	solar mass	1.989×10^{30} kg
c	speed of light	2.9979×10^{8} m sec^{-1}
h	Planck's constant	6.626×10^{-34} J Hz^{-1}
m_e	mass of electron	9.110×10^{-31} kg
m_p	mass of proton	1.673×10^{-27} kg
G	Gravitational constant	6.670×10^{-11} N m^2 kg^{-1}
K	Coulomb's constant	8.989×10^{9} N m^2 C^{-2}
k or k_B	Boltzmann's constant	1.381×10^{-23} J K^{-1}
σ	Stefan–Boltzmann constant	5.67×10^{-8} W m^{-2} K^{-4}
(l, b)	Galactic longitude and latitude	
α	spectral index	
a or $\dot{V}$	acceleration	
B	magnetic flux density	
E	energy or electric field	
L	luminosity	
μ	mean molecular weight	
m or M	mass	
ν	frequency	
n	number or number density	
p	momentum	
P	pressure or power	
ρ	mass density	
r or R	distance or radius	
S_ν	flux density	
θ	angle	
τ	optical depth	
t	time	
T	time or temperature	
T_B	brightness temperature	
V	velocity or volume or voltage	
Ω	solid angle	
ω	angular frequency	
Z	atomic number	

General overview

The broad aim of this thesis is to find new supernova remnants (SNRs) in our home galaxy, the Milky Way, in order to make the current catalog of Galactic SNRs more complete. It is believed that there must be at least a thousand of them, but only about 300 have been detected as of this writing, making it a rather large inconsistency.

Why do we believe that there must be more than a thousand SNRs in the Milky Way? How do we detect the remaining ones? Why exactly do we need a catalog of Galactic SNRs in the first place? Chapter 1 deals with these questions, in addition to various astrophysical concepts that are necessary to understand SNRs. I will provide a historical perspective of how the current catalogs of Galactic SNRs came to be, and their deficiencies. The technical aspects of modern radio astronomical telescopes used in this thesis and their limitations are also discussed, including the methods to produce images from such instruments.

Chapter 2 describes the pilot study that was undertaken for a future Galactic plane survey with the Giant Meterwave Radio Telescope. I will motivate the need for such a survey in the context of SNRs and report on the data reduction techniques we used, the results we obtained, and the lessons we learnt.

The recently conducted GLOSTAR Galactic plane survey, which focuses on acquiring a comprehensive view of high-mass star formation in the Milky Way, is outlined in chapter 3. I will describe, in detail, the data products and the images from this survey. Besides detecting characteristic signs of high-mass star formation at an unprecedented sensitivity over a large portion of the first quadrant of our Galaxy, the GLOSTAR images made it possible to identify 80 new SNR candidates. We have also shown that four objects that were thought to be SNRs—out of 92 in the survey region—are not really SNRs, and provide clear evidence that seven previously identified candidates are SNRs indeed. The results from the studies and their implications are discussed in chapters 4 and 5. They are published in Dokara et al. (2021) and Dokara et al. (2023), respectively.

Finally, I provide an outlook of future work and conclude the thesis in chapter 6.

Chapter 1

Introduction

1.1 Milky Way's interstellar medium

The vast space between the stars, known as the interstellar medium (ISM), is filled with cosmic rays, magnetic fields, dust, and gas that evaded detection at least until the late 1800s. The very first scientific studies of diffuse objects in the ISM focused on planetary nebulae around stars (e.g., Huggins & Miller 1864). After the identification of several 'dark clouds' by Edward Barnard in the late 1800s and the discovery of ionized calcium in δ Orionis by Johannes Hartmann (1904) using absorption spectroscopy, it became clear that the interstellar space is in fact not empty at all. Since then astronomers discovered dust grains, and hundreds of gaseous species in the ISM that are in either ionized, atomic, or molecular forms. We now know that the ISM in the Milky Way and other galaxies is not homogeneous; it has several components in distinct phases permeating throughout the galactic volume. It is sparsely populated, with small particle number densities (typically $n < 100$ cm^{-3}), and most of its volume emits little or no radiation at optical wavelengths. An all-sky radio map is shown in Fig. 1.1, where the Galactic plane is clearly visible as a wide feature stretching from left to right across the image. The diffuse emission from the Galactic plane is mostly from the Milky Way's ISM.

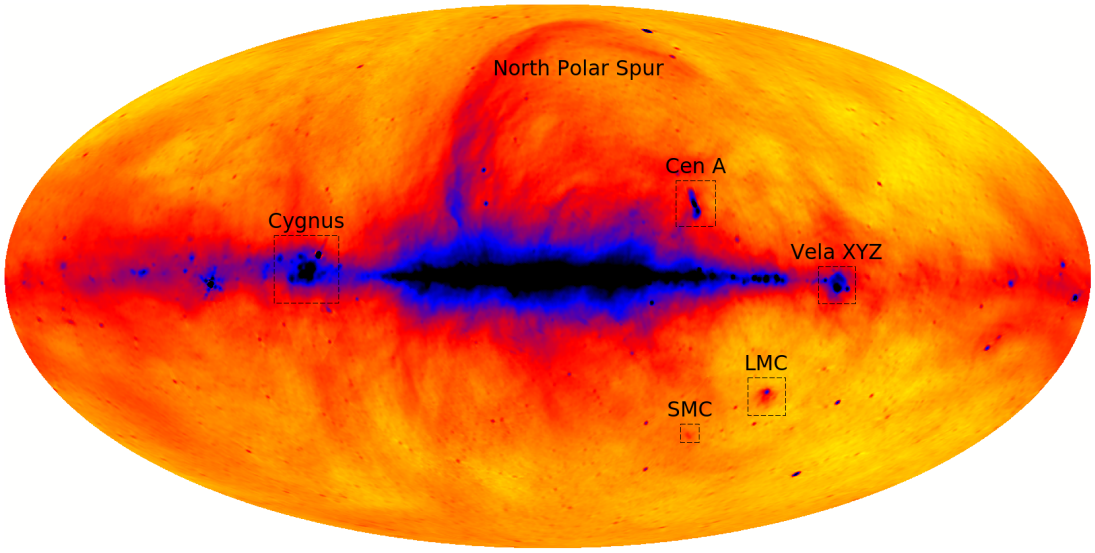

Figure 1.1: 408-MHz radio continuum all-sky map of Haslam et al. (1982). Shown in this figure is the improved, de-striped version from Remazeilles et al. (2015). Some important features are marked.

The ISM, although currently accounting for only about 10% of the mass of the ordinary 'baryonic' matter in the Milky Way (excluding dark matter), plays a key role in the evolution of the Galaxy. It acts as a gas reservoir from which new stars are formed by condensation of cold gas. Eventually the stellar interiors are once again dispersed back into the ISM through feedback processes such as supernovae and stellar winds, completing the circle of life of interstellar material.

The ISM is traditionally described in terms of 'phases', which are characterized by temperature and pressure. Field et al. (1969) introduced a two-phase model of the ISM consisting of two components in pressure equilibrium: a warm neutral medium and a cold atomic/molecular dense medium. McKee & Ostriker (1977) extended that theory by incorporating a third medium: the coronal gas that is hot, ionized and tenuous. This hot medium is theorized to be formed by heating due to shocks from supernova events, with some contributions from stellar winds too. The current widely accepted model of the ISM consists of five major components, as described in Table 1.1.

Table 1.1: Components of the gaseous ISM, adapted from Ferrière (2001).

	Temperature (K)	number density (cm^{-3})
Molecular gas	10–20	10^2–10^6
Cold atomic gas	50–100	20–50
Warm atomic gas	$(6\text{–}10) \times 10^3$	0.2–0.5
Warm ionized gas	$\sim 8 \times 10^3$	0.2–0.5
Hot ionized gas	$\sim 10^6$	$\lesssim 0.01$

While visible light is obscured by dust, the long wavelength radio waves can penetrate dust with negligible absorption, making them an excellent tool to study the ISM. In the Milky Way, and probably in most other regular star-forming galaxies as well, H II regions are the most numerous discrete radio sources in the ISM that are extended. H II regions are mostly composed of ionized hydrogen, formed around a central high-mass star or a group of stars if the flux of the ultraviolet radiation from the central source is energetic enough to ionize the surrounding ISM, known as the circumstellar medium (CSM). Supernova remnants—the focus of this thesis—are the second most numerous group of extended radio sources, which I will discuss in §1.3.

1.2 The life and times of stars

Molecular clouds, which are sometimes called stellar nurseries, are the regions in the ISM where stars are born. They primarily contain molecular hydrogen (H_2) and helium, with trace amounts of dust and other molecules. They have low temperatures (< 20K) and each molecular cloud is typically a gravitationally bound object, by its own mass. If the mass of a molecular cloud is above the critical 'Jeans mass' (Jeans 1902), the gravitational attraction among the contents of the cloud pulls together the mass into concentrated cores, while releasing gravitational potential energy as heat. When the temperature of a core reaches 10^7 K, the hydrogen starts to fuse and the star is now considered to be 'born'. The phase of the evolution before hydrogen nuclear fusion

begins is known as the protostellar stage and the object is known as a protostar. During this stage, the inflow of material to the protostar can drive powerful jets along the axis perpendicular to the plane of the infalling material.

After the fusion of hydrogen begins, a hydrostatic equilibrium between the gas pressure and the gravitational attraction is attained due to the energy released from the hydrogen fusion. This stellar phase is called the 'main-sequence'. For stars with masses less 1.3 times the mass of the sun ($M < 1.3M_\odot$), the proton-proton chain (hydrogen fusion resulting in helium via ^{3}He) is the main reaction releasing nuclear energy. On the other hand, the more massive stars ($M > 1.3M_\odot$) have much higher temperatures in their cores and generate energy predominantly via the catalytic CNO-cycle, also called the Bethe-Weizsäcker cycle. In this pathway, hydrogen produces helium by fusing with carbon, nitrogen and oxygen as catalysts.

A summary of the stellar life-cycle is shown in Fig. 1.2. The state of a star after the end of its main-sequence phase strongly depends on its mass, and the heavier the star, the shorter its lifespan is. Stars are regularly categorized into three distinct groups based on their mass. Their evolution is briefly described below:

- **Mid-sized, Sun-like stars** ($\sim$0.6–10$M_\odot$) first run out of hydrogen and become red giants. When they run out of helium as well, they release their outer layers to form planetary nebulae while the inner core eventually cools and becomes becomes a white dwarf (e.g., Frew & Parker 2010). Our Sun will exist in the main-sequence stage for about 10^{10} years.

- **Low-mass stars** ($\lesssim 0.2M_\odot$) generate less energy per time and their nuclear fuel can last trillions of years, after which they probably become an inert white dwarf with a helium core (Laughlin et al. 1997).

- **High-mass stars** ($\gtrsim 8M_\odot$) are at the other end of the spectrum. They rapidly use up all the material available for nuclear fusion, while discharging significant amounts of mass through powerful stellar winds. When the radiation pressure cannot counterbalance the gravitational pull of its own mass, which happens when the mass of the core reaches the Chandrasekhar limit of $1.44M_\odot$ (Chandrasekhar 1931), it becomes a neutron star or a black hole in a matter of a few seconds, usually by undergoing a supernova explosion which expels the outer layers of the star at high speeds. The timescale of these events for a star of mass $\sim 10M_\odot$ is about 30 million years from its birth, indicating how rapidly high-mass stars evolve compared to their less massive counterparts.

As mentioned above, what remains of a star is either a white dwarf, a neutron star, or a black hole, depending on the mass of the star and the environment. These end products are theorized to remain in their state for trillions of years if they do not interact with their surroundings.

- **White dwarfs** are inert leftover stellar cores that cannot fuse anymore. These objects are supported by electron-degeneracy pressure, which prohibits multiple electrons occupying the same quantum state. This forbiddance is colloquially known as the Pauli exclusion principle. A white dwarf can gather more material from a companion and if the temperature goes high enough, hydrogen fusion might begin and result in a 'nova'. If the Chandrasekhar limit is reached by either mass accretion or merging with another white

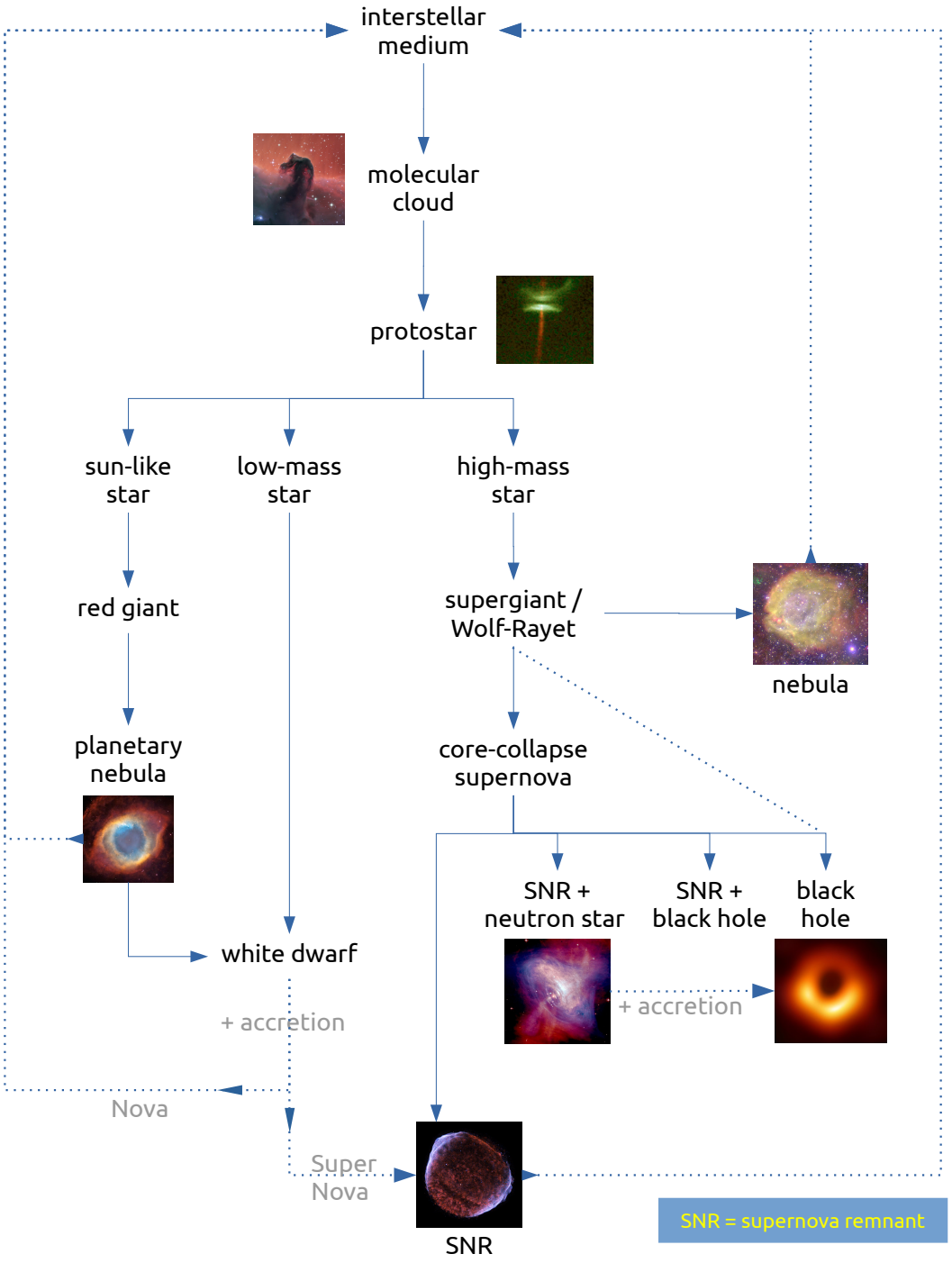

Figure 1.2: Summary of stellar evolution.

dwarf, a supernova explosion happens. Both these cases result in expulsion of material into the surroundings.

- **Neutron stars** contain almost exclusively neutrons. They are created when the electron-degeneracy pressure is insufficient to halt the collapse of a massive star and it is energetically more favorable for electrons to combine with protons and become neutrons, rather than occupying separate quantum states. Neutron stars are supported against further gravitational collapse by repulsive nuclear forces. A relatively smaller role is played by the neutron-degeneracy pressure, which, like the electron-degeneracy pressure, prohibits multiple neutrons attaining the same quantum state. If a neutron star gains enough mass so that further gravitational collapse cannot be stopped, it becomes a black hole.

- **Black holes** are objects within which the gravitational pull is so strong that not even light can escape the pull within a certain distance. They are formed when the mass in a volume is too large for any force to support against a collapse to form a singularity. This may happen during the collapse of a high-mass star either with or without a supernova, or when a neutron star accretes a large amount of matter. Merger of neutron stars is another route for the formation of black holes.

1.3 Supernovae and supernova remnants

Stars in the final stages of their evolution may blow up in a catastrophic explosion that expels the stellar interiors into the surroundings. Such an event is called a supernova (SN), which usually marks the death of the progenitor star. Supernovae (SNe) are amongst the most powerful class of explosions known in the universe, and each individual SN can even outshine its host galaxy for several days or weeks. The ejecta from such an event expand into the surrounding ISM at speeds that may exceed 5% of the speed of light. The structure formed from the ejecta is known as a supernova remnant (SNR). For several hundreds of years, SNRs can emit across the electromagnetic spectrum; but after a few thousand years they typically emit only in the radio regime. An example SN and SNR are shown in Fig. 1.3.

1.3.1 Supernova explosion mechanisms

SNe occur via one of two routes. The most frequent one is the 'core-collapse' (CC) of a high-mass star, which happens when the radiation pressure from the nuclear fusion and electron-degeneracy pressure in the stellar core cannot provide support against the gravitational infall due to its own mass. These types account for about 80% of SNe in the Milky Way (Tammann et al. 1994). As such, they can be considered as tracers of recent high-mass star formation. There are four known mechanisms of core-collapse SN (CCSN) events, summarized in Table 1.2 and also below:

- **Electron capture**: If the mass of a star is in the transitional range between the formation of a white dwarf ($M \lesssim 8M_{\odot}$) and the typical iron core collapse SN ($M \gtrsim 10M_{\odot}$), and if it has an oxygen-neon-magnesium core, the electrons can fuse with the Ne/Mg nuclei via

(a) The galaxy NGC 4526 (center) and the supernova SN1994D in its outskirts (bright spot on the bottom left). Image credit: NASA/ESA/Hubble.

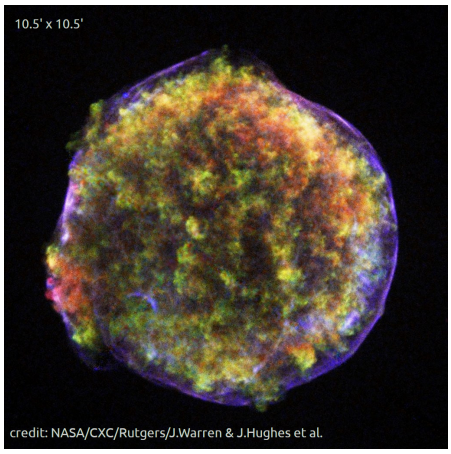

(b) Tycho's SNR as seen in X-rays. Color coding: red 0.95–1.26 keV, green 1.63–2.26 keV, and blue 4.1–6.1 keV. Image credit: NASA/CXC/Rutgers.

Figure 1.3: Examples of a supernova (a) and a supernova remnant (b).

electron capture reactions, which reduces the electron degeneracy pressure and leads to a core collapse and the formation of a neutron star.

- **Iron core gravitational collapse**: As soon as the innermost iron core of a massive star reaches the Chandrasekhar mass limit, the electron-degeneracy pressure becomes insufficient to oppose the gravitational infall. A neutron star or a black hole is then produced after the collapse of the core. This is the most common type of CCSN event, and it happens for stars with masses in the range $10M_{\odot} \lesssim M \lesssim 140M_{\odot}$.

- **Pair instability**: Very massive stars (M~140–250$M_{\odot}$), when they produce high-energy gamma rays that can turn into electron-positron pairs, may collapse when the radiation pressure drops due to the pair production process removing the gamma rays supporting against the collapse. This can happen only in low-metallicity stars, and no compact remnant is expected to remain after the event.

- **Photodisintegration**: This occurs in stars with the highest range of masses ($M \gtrsim 250M_{\odot}$), when the gamma rays in the core are so energetic that they knock off nucleons in an atomic nucleus. Since this is an endothermic reaction that also removes gamma rays from the stellar core, the pressure and the temperature are reduced, causing immediate collapse of the core.

The other, less frequent scenario of an SN event is known as 'Type Ia': thermal runaway nuclear fusion on a degenerate star, usually a white dwarf. Such an event takes place when the degenerate star accretes matter from a companion star and its mass reaches the Chandrasekhar limit. The companion may be a main-sequence star ('single-degenerate' scenario) or another

Table 1.2: Core collapse mechanisms, adapted from Heger et al. (2003)

CC-type	Stellar mass	Compact remnant
Electron capture	$8M_\odot \lesssim M \lesssim 10M_\odot$	neutron star
Iron core gravitational collapse	$10M_\odot \lesssim M \lesssim 140M_\odot$	neutron star or black hole
Pair instability	$140M_\odot \lesssim M \lesssim 250M_\odot$	none
Photodisintegration	$M \gtrsim 250M_\odot$	massive black hole

white dwarf ('double-degenerate' merger scenario). Its name comes from the original classification of SNe, which is based on absorption lines and light curves of the SN (e.g., Turatto 2003). If hydrogen lines are absent, it is called a Type I SN, otherwise it is a Type II.

1.3.2 Morphology

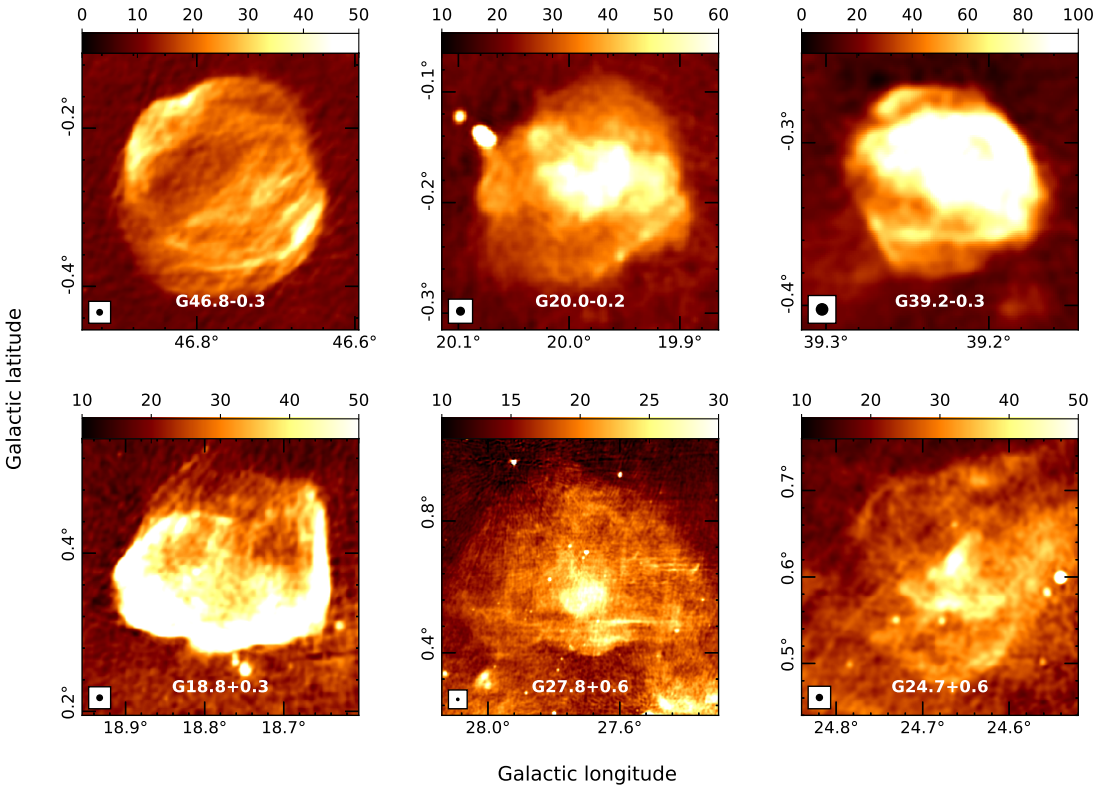

Figure 1.4: Examples of SNRs exhibiting different morphologies. The images, which are shown in mJy beam^{-1}, are from the 1.4 GHz THOR+VGPS data: the H I, OH, Recombination line survey of the Milky Way (THOR; Beuther et al. 2016) combined with the VLA Galactic Plane Survey (VGPS; Stil et al. 2006). The beam size is shown in the bottom-left corner.

As the supernova ejecta expand, they encounter resistance from the ISM. The ejecta form a circularly symmetric shell if the surroundings are homogeneous and no inhomogeneities exist

in the explosion itself. Otherwise, they trace out the inhomogeneities. In particular, if one side of the SNR confronts a very low density ISM compared to the other side, it can expand much faster in that direction and may even appear 'opened up' or blown out (see the bottom left panel of Fig. 1.4 for example).

A central remnant also affects the apparent morphology. While a core-collapse SN may leave a compact remnant such as a black hole or a neutron star, a thermal runaway SN completely obliterates the accreting degenerate star and the fate of the companion is not yet well understood. The neutron star can later accumulate the material onto its surface and give rise to a pulsar wind nebula (PWN) inside the shell of the SNR. The presence of a PWN thus rules out the possibility of a Type Ia SN being the progenitor explosion. Despite this substantial difference, both CC and Type Ia SNe may give rise to ejecta and SNRs that eventually look quite similar, and it is usually quite difficult to predict the type of the SN after a few thousand years if there exists no PWN. This is because SNe, regardless of the type, typically release 10^{51} erg of energy, making them interact with the ISM in a similar manner (e.g., Chevalier 1977).

Consider the SNRs in Fig. 1.4. While the shell-shaped structure is obvious to classify (left panels), SNRs can also have complex shapes that appear filled. They are typically called filled-center SNRs, or, in the case that both shell and filled center are visible, they are called 'composite' or 'mixed morphology' type SNRs. According to the catalog of Galactic SNRs by Green (2019), the SNRs shown in the middle panels are of the filled-center type, whereas those in the right panels are composite SNRs. As is evident from this figure, the distinction between 'filled-center' and 'composite' is a little subjective. The distinction is made by looking for the presence of a clear shell-like or limb-brightened structure.

1.3.3 Time evolution

SNRs grow and expand with time, with a rate of expansion that depends on the parameters of the progenitor star, the SN explosion, and the local ISM and the CSM. Initially, the SN ejecta speeds are much larger than the sound speeds in a typical ISM, which results in a blast-wave shock that propagates into the ISM. A reverse-shock forms later due to the expansion of the ejecta: the density of the ejecta falls below the density of the shocked medium, generating a shock that moves inward, and heats up and compresses the ejecta. The forward blast-wave shock radius is often taken to be the radius of the SNR.

Since the explosion energy ($E_{\rm SN}$) is usually $\sim 10^{51}$ erg for different kinds of SNe, a broadly consistent characterization of time evolution can be made for all SNRs, regardless of the type of the progenitor or the SN. Four stages of SNR evolution were proposed by Woltjer (1972): ejecta-dominated, Sedov-Taylor, snowplow, and dispersion. Each stage is briefly outlined below following the discussion from Draine (2011), assuming a uniform ISM around the SNR:

1. The earliest part of the evolution is known as the ejecta-dominated or the free-expansion phase, which lasts for a few hundred years, until the mass of the swept up ISM ($m_{\rm sw}$) is comparable to that of the SN ejecta ($m_{\rm ej}$). The SN ejecta are much denser than the ISM. The root-mean-square (rms) velocity of the ejecta is assumed to be constant throughout this phase. It is estimated by the expression for kinetic energy, and hence it depends on the explosion energy and the mass of the ejecta: $\langle V_{\rm ej}^2 \rangle = 2E_{\rm SN}/m_{\rm ej}$.

2. The Sedov-Taylor phase, or just the Sedov phase, begins when the shocked and swept up mass is comparable to the ejecta mass $m_{\rm sw} \sim m_{\rm ej}$, which happens after the time since the explosion crosses $R_1/\langle V_{\rm ej}^2\rangle^{1/2}$, where $R_1 = 3M_{\rm ej}/(4\pi\rho_{\rm ISM})^{1/3}$. During this stage the explosion can be approximated as a point source injecting only energy, and the solutions are calculated by imposing self-similarity. The radius of the SNR scales as $R \sim t^{2/5}$. The expressions for this stage were independently arrived at by Sedov (1946) and Taylor (1950), while working on the problem of estimating the explosion energy of a nuclear bomb. This phase lasts for a few tens of thousands of years.

3. The next phase begins when the radiative cooling losses become important and the matter behind the SNR shock cools rapidly to form a cold and dense shell. Generally, momentum conservation is assumed and this is called the snowplow phase. The conservation of momentum may not hold in this case, however. In the hot and tenuous medium that is well interior to the shock, the energy losses do not yet play a role, and the pressure from the hot central volume drives the momentum of the dense outer shell. If this effect is taken into account, the solution is referred to as the pressure-modified snowplow phase. The radius of the SNR increases with time at a rate of $R \sim t^{2/7}$.

4. The final phase is known as the 'dispersion' phase as the blast-wave shock completely stalls by turning into a sound wave. The SNR merges into the surrounding ISM and becomes indistinguishable in a timescale of the order of 10^5 years.

The above description is only valid for an ideal situation where inhomogeneities exist neither in the SN explosion nor in the nearby medium. In a more realistic scenario, such inhomogeneities not only exist, but also play a major role in the evolution of SNRs. Since the progenitors of CCSNe are high-mass stars that also blow powerful stellar winds and have episodes of significant mass-loss, the CSM is likely much less dense than the ISM that is further away. This can affect the time evolution in a profound manner. Recent studies suggest that due to cavities created during previous mass-loss events, the radio emission from even young SNRs may be so weak that our instruments may not be able to detect them (Yasuda et al. 2021). All these facts blur the lines of distinction between two stages of evolution, and, in fact, a remnant may even be in different phases at the same point of time along different directions. It is generally quite difficult to ascertain the current stage of evolution of an SNR.

1.3.4 Effects on the galaxy

As important distributors of stellar interiors, and as the most energetic events that arise from a non-degenerate star, SNe and SNRs are a crucial source of stellar feedback irreversibly affecting the star formation dynamics, the chemical complexity, and the evolution of the ISM of a galaxy. Some of their significant effects are pointed out below:

- Many metals (elements with atomic numbers ≥ 3) arise from SN nucleosynthesis. Hydrogen, helium and sparse amounts of lithium in the universe were created during the Big Bang, but all other elements, including those responsible for life, had formed much later. SNe and neutron stars are prominent sources of most of the metals (see Fig. 1.5).

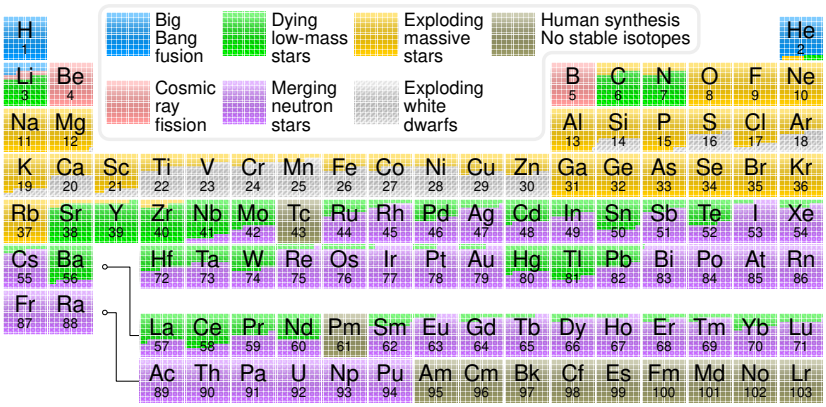

Figure 1.5: Origin of elements on the periodic table. SNe include the categories of exploding high-mass stars and exploding white dwarfs. Image credit: Jennifer Johnson / Cmglee / Wikimedia commons.

- SNRs are thought to be responsible for the production of Galactic cosmic rays through the process of diffusive shock acceleration (e.g., Berezhko & Völk 2007).
- By blowing gas out of the galactic disc, SNe and SNRs can regulate the star formation rate and control the galactic fountains, super-shells and super-bubbles (e.g., Jaskot et al. 2011; El-Badry et al. 2019).
- By compressing interstellar gas, they may trigger or accelerate star formation (e.g., Zucker et al. 2022).
- They may either create or destroy dust, which is necessary for effective condensation of interstellar gas to form the next generation of stars (e.g., Slavin et al. 2020).
- They create and maintain turbulent pressure at scales ranging from molecular clouds to the whole galaxy, which can suppress the star formation rate (e.g., Ostriker & Shetty 2011).

A vast amount of research has focused on the effects of SNe and SNRs on the surrounding ISM and the galaxy in general. However, most of the observational studies so far have focused on a single SNR or a small sample, where observational biases play a critical role in interpreting the conclusions of such studies. As a result, many open questions still exist in this sub-field of astrophysics:

- Are SNe and SNRs net destroyers or creators of dust? Can they produce enough dust to explain the extensive amounts of dust in some early galaxies (e.g., Slavin et al. 2015; Tamura et al. 2019)?
- Can they accelerate Galactic cosmic rays to PeV energies (e.g., Blasi 2013)?
- Can they consistently trigger star formation, and high-mass star formation in particular (e.g., Desai et al. 2010)?

- Why is the number of SNRs observed so far much smaller than the expected number (e.g., Anderson et al. 2017)?

1.3.5 Finding supernova remnants: A brief historical perspective

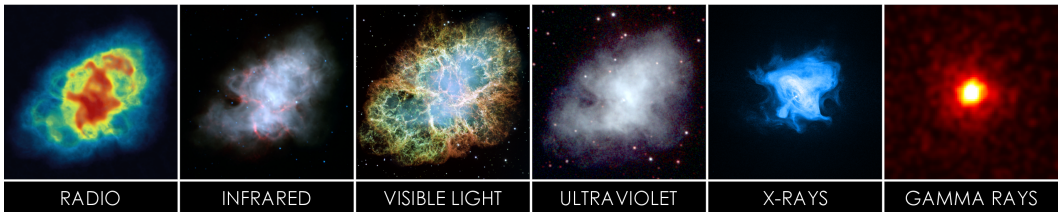

Figure 1.6: Multi-wavelength view of the SNR Crab nebula. Each panel is about 5 arcmin across. Image credits: Wikimedia commons, NRAO, NASA.

Several nebular objects, which are now known to be SNRs, H II regions, galaxies etc., had been discovered in the night sky after the invention of the optical telescope in the 17th century. The Messier catalog is a well-known example of a collection of such nebulae. However, it was not until the early- and mid-1900s that the nebulae were classified into distinct groups of objects. The Crab nebula was the first to be associated with a supernova explosion (see Mayall 1962), initially by Hubble (1928), and later confirmed beyond doubt by Mayall & Oort (1942). With the advent of radio astronomy and the theory of synchrotron emission, several new identifications of SNRs were quickly made. And by the early 1970s, the SNR catalogs already had about one hundred objects (Milne 1970; Downes 1971). Most of these identifications came from large-scale surveys of the Milky Way that were taken using single-dish radio telescopes (e.g., Altenhoff et al. 1970), and this trend of identifying new SNRs in single-dish radio surveys continued for several years (e.g., Fürst et al. 1987).

SNRs may be visible at shorter wavelengths too (see Fig. 1.6 for example), but the obscuring dust in the ISM makes it difficult or even impossible to identify distant SNRs in the infrared, optical or ultraviolet regimes. Radio waves, on the other hand, can pass through dust without much extinction. In addition, as we shall see later in §1.4.3, SNRs are brighter at longer wavelengths due to their dominant emission mechanism, the nonthermal synchrotron. These facts made radio the favored regime for astronomers attempting to discover new SNRs. From the catalog of Galactic SNRs by Green (2019), we find that nearly 90% of the SNRs in the Milky Way have detectable radio emission. Despite the advantage offered by radio astronomy, finding new SNRs is still difficult in the Milky Way due to confusion from other Galactic sources. The solar system is located quite close to the Galactic mid-plane (at a height of about 25 pc, e.g., Jurić et al. 2008), and we are looking into the Milky Way edge-on, implying that many sources other than SNRs are in our line of sight. The contrast in the number of Galactic and extragalactic SNRs detected provides an idea of the severity of this problem: over 1200 SNRs are identified in external galaxies, while, in the Milky Way, only about 300 are confirmed so far (Long 2017).

The insufficient resolution of the single-dish radio telescopes limited the studies on small-diameter objects. That limitation was circumvented by radio-synthesis arrays called 'interferometers'. These arrays provide resolving powers that now exceed even those of optical telescopes,

but the poor processing speeds and inadequate storage capacities of early computers were not conducive for large scale surveys with interferometers. In the past few decades that also has changed, and this led to a boom in SNR identifications: several dozens of SNRs have been proposed en masse by groups across the world (Whiteoak & Green 1996; Brogan et al. 2006; Helfand et al. 2006; Anderson et al. 2017; Hurley-Walker et al. 2019a; Dokara et al. 2021). Despite these significant advances with interferometry, single-dish radio telescopes remain invaluable for SNR science, mainly because of the fundamental limitation of interferometers: large scale structure is filtered out, leading to apparently low flux densities. These topics are discussed in detail in §1.5.

1.3.6 The current catalogs of Galactic supernova remnants

Considering the role that SNRs play in the evolution of a galaxy (see §1.3.4), it is clear that building a catalog of SNRs is necessary to quantify their effects and constrain various parameters using observations. As of this writing, two catalogs of Galactic SNRs are considered to be authoritative.

- One is maintained by D. A. Green, who has been collecting the works on Galactic SNRs and updating his catalog continually every few years, from the early 1980s to as recently as 2019[1] (Green 1984, 2019). Hereafter, we refer to the latest version of this catalog, which contains 294 objects, as 'the G19 catalog'.
- The other is the catalog of high-energy observations of Galactic SNRs[2] (Ferrand & Safi-Harb 2012). The original aim of this catalog was to build a consensus between the high-energy and radio observations of SNRs, but now it also serves as a useful catalog that includes all of the objects in the G19 catalog along with several other candidates that are likely to be SNRs. The total number of objects currently in this catalog is 383.

These catalogs, however, are known to be incomplete. One of the first analyses of the number of SNRs in the Milky Way was presented by Helfand et al. (1989), who estimated that there must be about 600 Galactic SNRs. A few years later, Li et al. (1991) revised the estimate to over 1000. Now it is understood that there may be as many as 3000, although a more precise prediction is yet to be calculated (Ranasinghe & Leahy 2022). All these studies use statistical arguments based on our current understanding (such as SN rate, number of nearby SNRs, and SNR lifetimes) to arrive at their estimates. We are more sensitive to the nearby, the large, and the bright SNRs, whereas we are likely to miss the farther, the small, and the faint SNRs. By using the known distances to SNRs, they had assessed the level of incompleteness in several regions of the Milky Way to approximate the total number of SNRs. As mentioned earlier, all studies conclude that the catalogs are incomplete by a significant fraction.

There is another problem in addition to the incompleteness of the SNR catalogs. Recent works have shown that there are several H II regions that are erroneously present in the SNR catalogs (Anderson et al. 2017; Dokara et al. 2021). This is unfortunately quite common due to the similar radio appearances of H II regions and SNRs: both in general have a shell-like

[1] www.mrao.cam.ac.uk/surveys/snrs/snrs.data.html
[2] http://snrcat.physics.umanitoba.ca/SNRtable.php

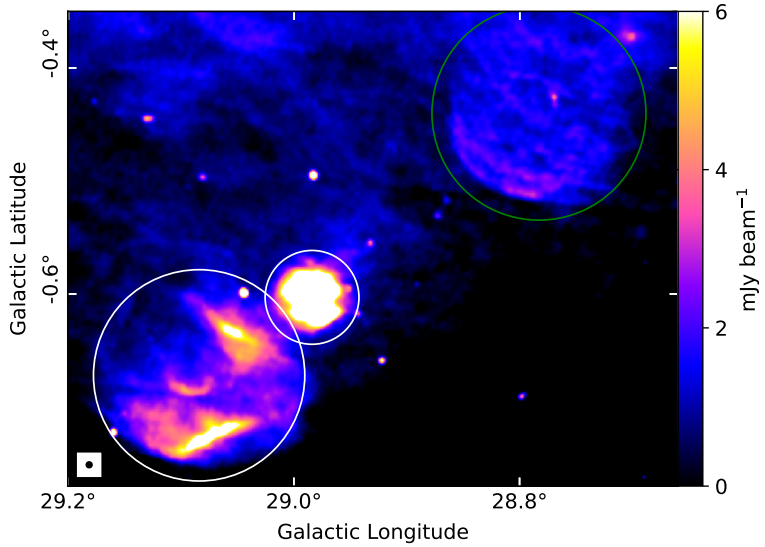

Figure 1.7: A region containing multiple H II regions and one recently discovered SNR, as visible in the continuum images of the global view of star formation (GLOSTAR) survey (Brunthaler et al. 2021). Two H II regions with the largest angular size in this region are marked with white circles, while the sole SNR is marked with a green circle.

morphology (see Fig. 1.7 for instance). D. A. Green also regularly removes the objects that were mistakenly noted as SNRs in earlier catalogs (see Green 2019, and references therein). Hence, the false identifications of H II regions as SNRs are also a shortcoming of the current catalogs.

The broad aim of the works done for this thesis is to identify new SNRs and to discard the spurious identifications to make the catalogs more complete and more accurate.

1.4 Theory of radio emission

The two emission mechanisms relevant for this thesis are the 'thermal bremsstrahlung' radiation and the 'nonthermal synchrotron' radiation, which are the dominant modes of radio emission from H II regions and SNRs, respectively.

- In H II regions, the ionized plasma is in rough thermodynamic equilibrium: the velocities of the particles of a system follow a Maxwell-Boltzmann distribution, which implies that the whole system can be described using a single temperature (T). The radio emission from such a system arises when the electrons are accelerated or decelerated during collisions with the protons. This process is called the thermal bremsstrahlung radiation. It is sometimes also referred to as 'free-free' radiation to reflect the fact that the electrons are free before and after the collision, and are not bound to any atom at any point.

- On the other hand, the radio emission from SNRs typically cannot be described by a single temperature due to the presence of magnetic fields. The system has not 'thermalized', i.e.,

the velocities of the particles do not follow a Maxwell-Boltzmann distribution. The emission, known as the nonthermal synchrotron radiation, arises from the electrons gyrating around the magnetic field lines that are compressed by the expanding SNR shock.

The mathematical descriptions of these emission mechanisms are given in the following sections and also my own master's thesis (Dokara 2018), which are a result of study of the books 'Tools of Radio Astronomy' (Wilson et al. 2013) and 'Essential Radio Astronomy' (Condon & Ransom 2016).

1.4.1 Definitions for describing radiation

Before I jump into deriving the emission properties of SNRs and H II regions, I will give a brief overview of the definitions used in describing and measuring astronomical radiation.

- Specific intensity, I_ν, is defined as the power dP from a source of angular size $d\Omega$ intercepted by a detector of area $d\sigma$ over a bandwidth $d\nu$ at an angle θ to the source:

$$I_\nu = \frac{dP}{d\Omega\, d\sigma\, d\nu\, \cos\theta} \tag{1.1}$$

- Flux density of a source, S_ν, is the specific intensity integrated over the solid angle subtended by the source:

$$S_\nu = \int_{\Omega_S} I_\nu \cos\theta\, d\Omega \tag{1.2}$$

- Radiative transfer equation along the line of sight of radiation (ds) with specific intensity I_ν, absorption coefficient κ_ν, and emissivity ε_ν:

$$\frac{dI_\nu}{ds} = \varepsilon_\nu - \kappa_\nu I_\nu \tag{1.3}$$

- Planck's law gives the expression for the spectral distribution of a black body at a temperature T in thermodynamic equilibrium (i.e., no macroscopic net flow of energy):

$$I_\nu = B_\nu(T) = \frac{2h\nu^3}{c^2}\left[\exp\{\frac{h\nu}{kT}\} - 1\right]^{-1} \tag{1.4}$$

- Planck's law (eqn. 1.4) approaches the Rayleigh-Jeans limit at low frequencies:

$$B_\nu(T) = \frac{2kT\nu^2}{c^2} \quad \text{if } h\nu \ll kT \tag{1.5}$$

- Kirchhoff's law is applicable in local thermodynamic equilibrium:

$$B_\nu(T) = \frac{\varepsilon_\nu}{\kappa_\nu} \tag{1.6}$$

- Optical depth of a medium, τ_ν, is defined using the absorption coefficient:

$$d\tau_\nu = -\kappa_\nu\, ds \tag{1.7}$$

- A medium is considered to be optically thick for a frequency if the optical depth is large ($\tau_\nu \gg 1$), and optically thin otherwise ($\tau_\nu \ll 1$).

- Radiative transfer equation (eqn. 1.3) in terms of the optical depth in an isothermal medium:

$$\frac{dI_\nu}{d\tau_\nu} = I_\nu - B_\nu(T) \implies I_\nu(\tau_\nu) = I_\nu(0)e^{-\tau_\nu} + B_\nu(T)(1 - e^{-\tau_\nu}) \tag{1.8}$$

- For an optically thick medium, the specific intensity approaches the black body limit:

$$I_\nu \longrightarrow B_\nu(T) \quad \text{if } \tau_\nu \longrightarrow \infty \tag{1.9}$$

- Brightness temperature, T_B, is defined as the equivalent thermodynamic temperature of a body that emits radiation of specific intensity in the Rayleigh-Jeans limit (eqn. 1.5) equal to that of a black body:

$$T_B = \frac{c^2 I_\nu}{2k\nu^2} \tag{1.10}$$

1.4.2 Thermal bremsstrahlung

The total power radiated by an electric charge accelerating at $\dot{V}$ is known as the Larmor power:

$$P = \frac{1}{6\pi\varepsilon_0}\frac{e^2\dot{V}^2}{c^3} \tag{1.11}$$

H II regions, as mentioned earlier, are regions of ionized hydrogen. For the following derivation, we assume that only electrons and ions are present in H II regions. In such regions, the temperatures are of the order of 10^4 K, implying that the electrons typically have energies of the order of 1 eV. Radio waves that are emitted from an electron decelerated due to a collision with an ion, however, have energies only about 10 μeV; this means that the energy lost—and by extension the change in velocity—during a collision is negligible. So we assume that the electron travels in a straight line throughout the collision, as shown in Fig. 1.8.

Taking $K = 1/4\pi\varepsilon_0$, the parallel and the perpendicular components of the electrostatic force, following the illustration in Fig. 1.8, are given by:

$$F_\parallel = m_e a_\parallel = \frac{KZe^2 \sin\psi \cos^2\psi}{b^2} \tag{1.12}$$

$$F_\perp = m_e a_\perp = \frac{KZe^2 \cos^3\psi}{b^2} \tag{1.13}$$

where we used $b = r\cos\psi$ and Z is the atomic number of the ion. The acceleration due to the parallel component results in a sine-wave-like pulse with a duration of $\tau{\sim}b/V$, which implies that the frequency of the emission due to this component ($\omega{\sim}V/b$) is in the infrared regime for all applicable impact parameters. On the other hand, the perpendicular component of the acceleration has a Gaussian profile with significant energy radiated at low frequencies. So we

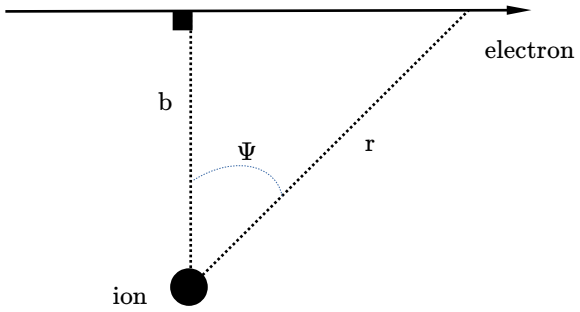

Figure 1.8: Electron-ion interaction in an H II region. The minimum distance achieved, known as the impact parameter, is b, and the electron is at a distance r from the ion at an angle ψ.

consider only the perpendicular component of the force to be contributing to the radio emission from H II regions. The Larmor power (eqn. 1.11) is now:

$$P = \frac{2Ke^2a_\perp^2}{3c^3} = \frac{2K^3e^6Z^2\cos^6\psi}{3c^3b^4m_e^2} \tag{1.14}$$

The total energy emitted is obtained by integrating the power P over time:

$$W = \int_{-\infty}^{+\infty} P\,dt = \frac{2K^3e^6Z^2}{3c^3b^4m_e^2}\int_{-\infty}^{+\infty}\cos^6\psi\,dt \tag{1.15}$$

Rewriting dt in terms of $d\psi$ by taking $\tan\psi = x/b$ and approximating the velocity V to be constant, we get:

$$W = \frac{\pi}{8}\frac{K^3e^6Z^2}{Vc^3b^3m_e^2} \tag{1.16}$$

Since most power is emitted at the frequency $\omega_{\max}{\sim}V/b$, we assume that the top of the Gaussian profile of the energy radiated is flat, and the energy density per unit frequency is thus approximated by:

$$W_\nu = \frac{\pi^2K^3e^6Z^2}{2c^3m_e^2b^2V^2} \tag{1.17}$$

In order to estimate the total energy emitted at radio frequencies for the whole H II region, we need to calculate the number of collisions per unit time, N_c. Consider the rate of electrons passing an ion with impact parameters ranging from b to $b + db$ and speeds from V to $V + dV$:

$$N_c(V,b)\,dV\,db = N_iN_e\;2\pi b\,db\;Vf(V)\,dV \tag{1.18}$$

where N_i is the number density of ions, N_e is the number density of electrons, and $f(V)$ is the probability distribution of the velocities of electrons, which is given by the Maxwell-Boltzmann distribution:

$$f(V) = \frac{4V^2}{\sqrt{\pi}}\left(\frac{m}{2kT}\right)^{3/2}\exp\{-\frac{mv^2}{2kT}\} \tag{1.19}$$

Now, the emissivity at a frequency ν can be calculated by integrating over the velocities and the impact parameters:

$$\varepsilon_\nu = \frac{1}{4\pi} \int_b \int_V W_\nu \, N_c \, dV \, db \tag{1.20}$$

$$= \frac{2K^3 Z^2 e^6 N_i N_e}{3c^3 m_e^2} \sqrt{\frac{2m_e}{\pi kT}} \ln \frac{b_{\max}}{b_{\min}} \tag{1.21}$$

Using Kirchhoff's law (eqn. 1.6) and the Rayleigh-Jeans limit (eqn. 1.5), we can write the absorption coefficient as:

$$\kappa_\nu = \frac{Z^2 K^2 e^6 N_i N_e}{c\nu^2 T^{1.5}} \frac{\pi^2/4}{\sqrt{2\pi k^3 m_e^3}} \ln\{\frac{b_{\max}}{b_{\min}}\} \tag{1.22}$$

The next step is to estimate the minimum and maximum impact parameters, $b_{\min}$ and $b_{\max}$. Clearly, they cannot be zero and infinity, but because they are within the logarithm, we can make approximations. We use the definition of impulse (ΔP) to estimate $b_{\min}$:

$$\Delta P = \int_{-\infty}^{+\infty} F \, dt = \int_{-\infty}^{+\infty} eE \, dt \tag{1.23}$$

Only $E_\perp$ contributes to the impulse because of the symmetrical action by $E_\parallel$. Further simplifying, we get:

$$\Delta P = \frac{2KZe^2}{bv} \tag{1.24}$$

The above equation implies that the impact parameter is minimum when the impulse is maximum, and this happens when there is a head-on collision. The expression for the minimum possible value of the impact parameter is thus estimated to be:

$$b_{\min} = \frac{KZe^2}{m_e v^2} \tag{1.25}$$

The maximum impact parameter can be taken to be the value at which significant radio power is emitted. Since the pulse power is negligible above the frequency $\omega \sim V/b$, we can take:

$$b_{\max} = V/2\pi\nu \tag{1.26}$$

Substituting equations 1.25 and 1.26 in 1.22, and using the definition of optical depth (eqn. 1.7), the radiative transfer equation in terms of optical depth (eqn. 1.8), and the Rayleigh-Jeans approximation (eqn. 1.5), we find that, approximately, if we neglect the background emission, in high frequencies when the region becomes optically thin:

$$S_\nu \propto \nu^2 \tau_\nu \propto \nu^{-0.1} \tag{1.27}$$

At low frequencies when the medium is considered to be optically thick, the region is basically opaque and behaves as a black body with:

$$S_\nu \propto \nu^2 \tag{1.28}$$

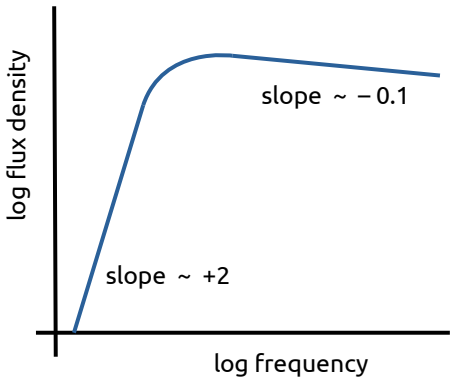

Figure 1.9: Graphic illustrating the spectrum of a typical H II region.

As is evident, the above calculations are quite simplistic because of the several approximations used. However, more detailed treatments also arrive at very similar results. The spectrum of a typical H II region is shown in Fig. 1.9.

The slope of the spectrum in logarithm scale is typically known as the spectral index, α:

$$\alpha = \frac{d \log S_\nu}{d \log \nu} \tag{1.29}$$

The spectral index at radio frequencies is a very useful quantity, and will be used throughout this thesis. This is because, as we shall see in the next section, it distinguishes nonthermal emissions from thermal bremsstrahlung radiation.

1.4.3 Nonthermal synchrotron

As a supernova remnant shock expands, it compresses the ambient magnetic fields in the ISM. The shocked and ionized plasma produces synchrotron radiation due to electrons gyrating around the magnetic field lines. Since a detailed treatment of this emission mechanism is beyond the scope of this thesis, a brief overview is given below.

Consider a moving electron in the presence of a magnetic field. It experiences an acceleration due to the relativistic Lorentz force:

$$\vec{a} = \frac{e}{m_e \gamma}(\vec{V} \times \vec{B}) \tag{1.30}$$

where γ is the Lorentz factor and $\vec{B}$ is the magnetic field vector. We define the relativistic (ω_B) and non-relativistic (ω_G) frequencies of gyration as follows:

$$\omega_B = \frac{eB}{m\gamma} \tag{1.31}$$

$$\omega_G = \frac{eB}{m} \tag{1.32}$$

Taking only the perpendicular component of the velocity, we get:

$$a = \omega_B v_\perp \tag{1.33}$$

In a frame (K') that moves along with the charge such that the charge is momentarily at rest, the power radiated is given by the Larmor formula (eqn. 1.11):

$$P' = \frac{e^2 a'^2}{6\pi\varepsilon_0 c^3} \tag{1.34}$$

Transforming the above equation to the laboratory frame, K, using $a' = \gamma^2 a$:

$$P = \frac{\gamma^4 e^2 a^2}{6\pi\varepsilon_0 c^3} \tag{1.35}$$

The time period of one gyration in the frame K' is:

$$\Delta T' = 2\pi/\omega_G \tag{1.36}$$

To calculate the pulse width in the frame K, we must account for the 'pitch angle' (ϕ, the angle between the magnetic field and the electron velocity), the relativistic 'beaming' effect (the confinement of radiation from accelerated charges to a small cone) and the relativistic Doppler effect. We find that the observed pulse width can be approximately given by:

$$\Delta T^A = \frac{1}{\gamma^3 \omega_B \sin\phi} \tag{1.37}$$

The total flux density of a system of electrons can be then calculated using:

$$S_\nu = \int_{\Omega,E} P(\nu, E)\, N(E, \phi)\, dE\, d\phi \tag{1.38}$$

where $P(\nu, E)$ is the power distribution which can be derived from eqn. 1.35, and $N(E, \phi)$ is the number distribution of energies of the electrons. $N(E)$ has a power-law dependence ($N(E) \propto E^{-\delta}$); this was observed in cosmic rays.

Finally, the dependence of the synchrotron flux density on the frequency for the optically thin case is given by:

$$S_\nu \propto \nu^{\frac{1-\delta}{2}} \tag{1.39}$$

For the optically thick case, the synchrotron flux density as a function of frequency does not depend on the distribution of the energies of the electrons:

$$S_\nu \propto \nu^{2.5} \tag{1.40}$$

Thus, for synchrotron emission, the spectral index (defined using eqn. 1.29) depends on the optical thickness:

$$\alpha = \frac{1-\delta}{2} \quad \text{for the optically thin case} \tag{1.41}$$

$$\alpha = 2.5 \quad \text{for the optically thick case} \tag{1.42}$$

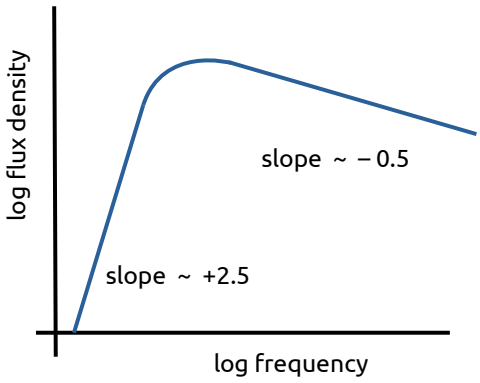

Figure 1.10: Graphic illustrating the spectrum of a typical shell-type SNR.

The spectrum of a typical shell-type SNR, with $\delta = 2$, is shown in Fig. 1.10.

The radiation from synchrotron emission is linearly polarized due to the directional preference in beaming, if the magnetic field is homogeneous. The degree of linear polarization, Π, is related to the power-law index of the energy spectrum of the electrons:

$$\Pi = \frac{\delta + 1}{\delta + 7/3} \tag{1.43}$$

meaning that the degree of polarization can be as high as 70% (with $\delta = 2$).

1.4.4 Separating thermal and nonthermal emissions

The spectral index is the most important marker of synchrotron radiation that distinguishes the thermal and the nonthermal emissions. As discussed in the previous two sections, the spectral index for H II regions and SNRs in their optically thin regimes are ~ -0.1 and ~ -0.5, respectively. While this is a good discriminator, in reality the uncertainties may be too large to clearly discriminate between the two emission mechanisms. In addition, it is known that PWNe can have spectral indices close to zero as well, especially at low frequencies. For this reason, measuring accurate flux densities across a wide range of frequencies is necessary to confidently state that the object emits nonthermally.

The degree of linear polarization, Π, can also be useful in this regard. As mentioned earlier, synchrotron radiation can have Π as high as 70%. Thermal bremsstrahlung, on the other hand, is not polarized since emission in all directions is equally likely. SNRs also, however, do not exhibit values so large as the theoretical upper limit of synchrotron. Due to non-uniform magnetic fields and Faraday depolarization effects (via insufficient resolution, wide bandwidths, or line-of-sight elements), SNRs are either unpolarized or weakly polarized with an integrated degree of polarization typically less than 10% (e.g., Sun et al. 2011; Dokara et al. 2021). Furthermore, H II regions can appear to be polarized though they are not inherently polarized, which may happen when there exists a Faraday screen along the line of sight of the H II region. With care, however, one can still manage to distinguish between thermal and nonthermal emissions using the degree of linear polarization as a tool (e.g., Sun et al. 2007; Dokara et al. 2021).

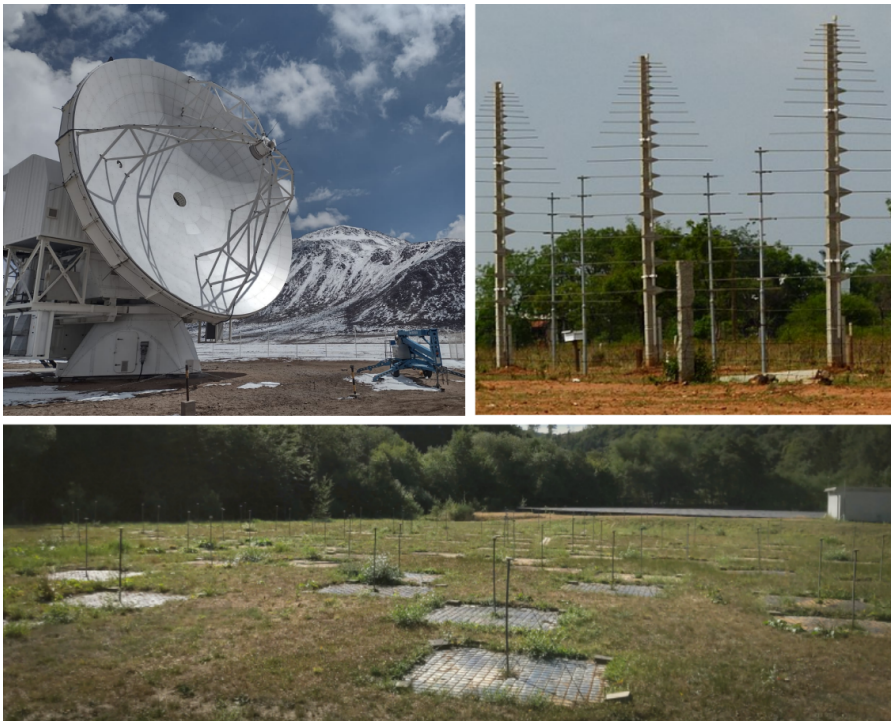

Figure 1.11: Examples of radio telescopes. *Top left*: the 12 m single-dish Atacama Pathfinder Experiment (APEX) telescope (image credit: Kartik Neralwar), *top right*: part of the dipole array of the Gauribidanur telescope (image credit: Shyamal), *bottom*: part of the tile array of the Low frequency Array (LOFAR) station at Effelsberg (image credit: own work).

1.5 Fundamentals of radio astronomy

In order to detect radio emission from celestial sources, radio telescopes are necessary. These are typically in a parabolic shape like a television dish, but dipole and 'tile' shapes and arrays of telescopes are also common at low frequencies. Fig. 1.11 shows some examples of radio telescopes. Dish antennas collect radio power from the direction in which they are pointed at. On the other hand, the pointing direction for dipole and tile arrays is managed electronically by controlling the voltage spread; this process is known as 'beam-forming'. Interferometric arrays are even different from typical tile arrays: they are several individual telescopes collecting power independently from the same direction, the radio signals from which are later combined using correlators. Radio interferometry will be discussed in detail in §1.5.2. In this thesis, we primarily use single-dish data from the 100 m diameter parabolic dish Effelsberg telescope, in addition to interferometric arrays.

Almost all radio telescopes are ground-based, because the atmosphere of the Earth is practically transparent to radio waves (see Fig. 1.12). Radio waves from ~20 MHz to ~10 GHz can even penetrate clouds and light rain with negligible absorption. The low frequency limit (~20 MHz) is set by the plasma frequency in the ionosphere of the Earth, and the high frequency limit depends on the atmospheric absorption.

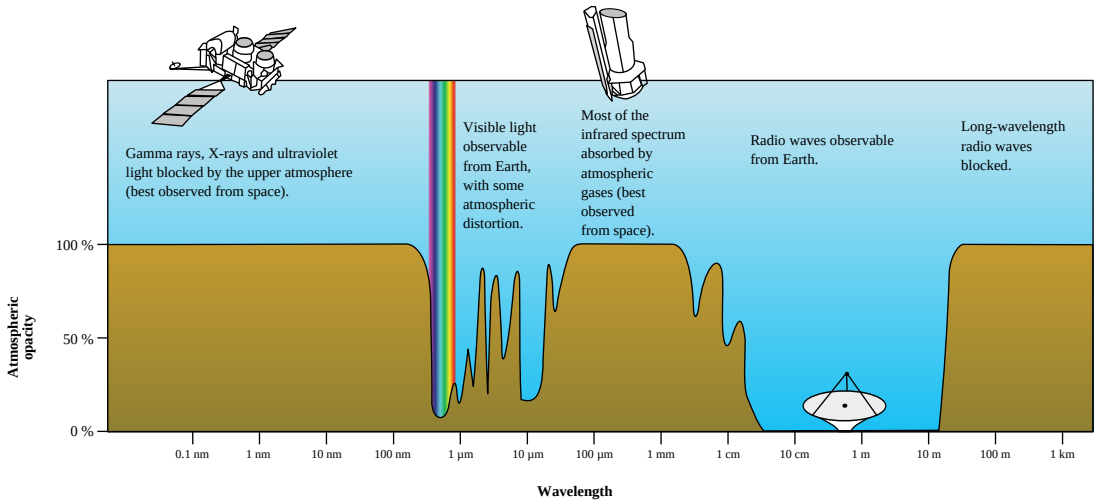

Figure 1.12: Atmospheric opacity of the Earth as a function of the wavelength of the electromagnetic wave. Image credit: NASA / Mysid / Wikimedia Commons.

1.5.1 Single-dish telescopes

The reciprocity theorem states that the properties of an antenna remain the same, whether it is transmitting or receiving. Hence, in further discussion, we will describe the properties generally in the transmission mode, although for all the work in this thesis we only use radio telescopes in the receiving mode.

A dipole antenna (two collinear conductors with a small gap between them) is the most basic form of a radio telescope. Parabolic and other shapes of antennae exist, but they all share the same nomenclature regarding their properties, which I will describe below.

- Power pattern, $P(\theta, \phi)$, is the power radiated by an antenna as a function of the angular coordinates:

$$P(\theta, \phi) = \int |\langle \vec{S} \rangle| \, dA \tag{1.44}$$

- Normalized power pattern, $P_n(\theta, \phi)$, is the power pattern divided by the maximum emitted power ($P_{\max}$):

$$P_n(\theta, \phi) = \frac{P(\theta, \phi)}{P_{\max}} \tag{1.45}$$

- Gain, or directivity, $G(\theta, \phi)$, is similar to the normalized power pattern, but with a normalization factor equal to the total power emitted, so that the 'gain' represents the fractional power emitted in a solid angle:

$$G(\theta, \phi) = \frac{4\pi P(\theta, \phi)}{\int \int P(\theta', \phi') \, d\Omega} \tag{1.46}$$

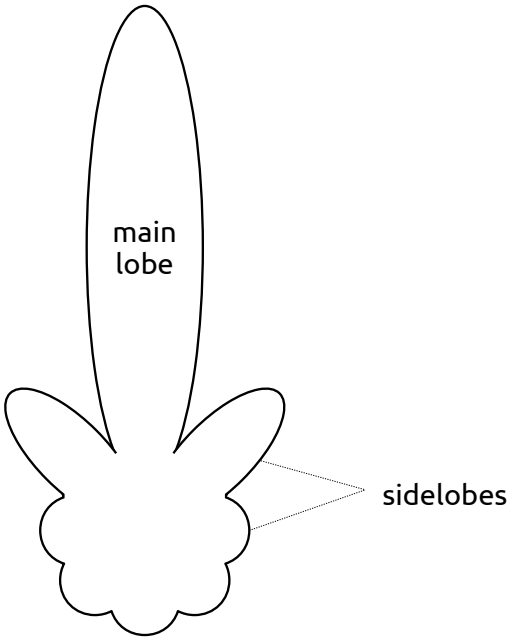

Figure 1.13: Power pattern of a typical parabolic antenna.

- Beam solid angle of an antenna, Ω_A, is defined as the solid angle within which $P_n = 1$ and $P_n = 0$ elsewhere outside the beam solid angle, if it were an ideal antenna:

$$\Omega_A = \int_0^{2\pi} \int_0^{\pi} P_n \sin\theta \, d\theta \, d\phi \tag{1.47}$$

- Main lobe solid angle, Ω_M, is defined analogous to the beam solid angle, but integrated only over the main lobe instead of the whole sphere. The main lobe is the range in which most power from an antenna is concentrated (see Fig. 1.13). The main lobe solid angle is calculated by:

$$\Omega_M = \int \int_{\text{mainlobe}} P_n \, d\Omega \tag{1.48}$$

- Main beam efficiency, η, is a measure of how much power is located in the main lobe as a fraction of the total power:

$$\eta = \frac{\Omega_M}{\Omega_A} \tag{1.49}$$

- Effective area, A_e, is the ratio of the power extracted by the antenna to the power density intercepted:

$$A_e = \frac{P_e}{|\langle \vec{S} \rangle|} \tag{1.50}$$

- Aperture efficiency, η_A, is defined as the ratio of the effective area to the geometric area:

$$\eta_A = \frac{A_e}{A_g} \tag{1.51}$$

- Power per unit bandwidth received by an antenna of with a power pattern P_n when it observes a source with sky distribution B_ν:

$$P_\nu = 0.5\, A_e \int\int B_\nu(\theta,\phi) P_n(\theta,\phi)\, d\Omega \tag{1.52}$$

- Antenna temperature, T_A, is defined as the equivalent temperature at which the power received matches the Nyquist approximation:

$$T_A = \frac{P_\nu}{k} \tag{1.53}$$

- Noise temperature, T_N, is the Nyquist-equivalent temperature of any noise with a power P_N:

$$T_N = \frac{P_{\nu,N}}{k} \tag{1.54}$$

- System noise temperature, T_S, is the temperature equivalent to the total power received by the telescope from all possible sources:

$$T_S = T_{\text{source}} + T_{\text{background}} + T_{\text{receiver}} + T_N + ... \tag{1.55}$$

- Theoretical sensitivity of the telescope, σ_T, depends on the time spent on source (t), the bandwidth ($\delta\nu$), and the system temperature:

$$\sigma_T = \frac{T_S}{\sqrt{t\delta\nu}} \tag{1.56}$$

- Theoretical diffraction-limited resolution, θ_d, depends on the wavelength (λ) of the electromagnetic radiation and the dish diameter (D):

$$\theta_d \approx \frac{\lambda}{D} \tag{1.57}$$

1.5.2 Radio interferometry

As mentioned earlier, an interferometer array is a collection of individual single-dish telescopes whose signals are combined. Such arrays offer high resolution (due to arbitrarily large dish spacing) and higher sensitivities (due to larger collecting area) compared to their single-dish counterparts. An example interferometer array is shown in Fig. 1.14.

An interferometer array is most easily understood in terms of its most basic element – a single baseline (or a two-element interferometer). A baseline is defined as the combination of two telescopes. Consider a baseline with identical dishes A and B, with the same electronics setup. Let their diameters be D, and note the displacement vector between the two dishes by $\vec{b}$, as shown in Fig. 1.15. Assume, for the sake of simplicity, that monochromatic radio frequency radiation is emitted by a point source which is observed by the baseline, and let the direction towards the source be denoted by the unit vector $\hat{s}$. Due to the geometry of the configuration, there exists a time delay (T_g) between the arrival of the signal to each dish:

$$cT_g = \vec{b} \cdot \hat{s} = |b| \cos\theta \tag{1.58}$$

Figure 1.14: Some antennas of the Atacama Large Millimeter Array (ALMA) radio telescope in its compact configuration. Image credit: Manali Jeste.

If the amplitude of the voltage induced by the monochromatic radio waves from the source is V (which is proportional to the electric field of the wave), then the voltages on the telescopes as a function of time can be written as:

$$V_A = V\cos\omega(t - T_g) \quad \text{and} \quad V_B = V\cos\omega t \tag{1.59}$$

These two signals are sent to the correlator, in which a multiplication is done:

$$V_A V_B = V\cos\omega(t - T_g)\ \ V\cos\omega t = \frac{V^2}{2}\left[\cos\omega T_g + \cos\omega(2t - T_g)\right] \tag{1.60}$$

Further, this is averaged over a time period much larger than the frequency of the radio wave ($\Delta T \gg 1/2\omega$) to yield the correlated signal:

$$R_c = \langle V_A V_B\rangle = \frac{V^2}{2}\cos\omega T_g \tag{1.61}$$

Note that since the voltage induced is proportional to the electric field of the radio wave intercepted, the output of the correlation operation (R) is proportional to the flux density of the source. It is apparent that the output signal varies sinusoidally with the phase ϕ, which depends on the observing wavelength λ:

$$\phi = \omega T_g = \frac{\omega|b|\cos\theta}{c} = \frac{2\pi|b|\cos\theta}{\lambda} \tag{1.62}$$

The direction dependence of the phase is calculated by differentiation:

$$\frac{d\phi}{d\theta} = -2\pi\frac{|b|\sin\theta}{\lambda} \tag{1.63}$$

What the above implies is that the phase is a sensitive measurement of the position on the sky. This is what allows an interferometer array to map a large area by pointing only at a

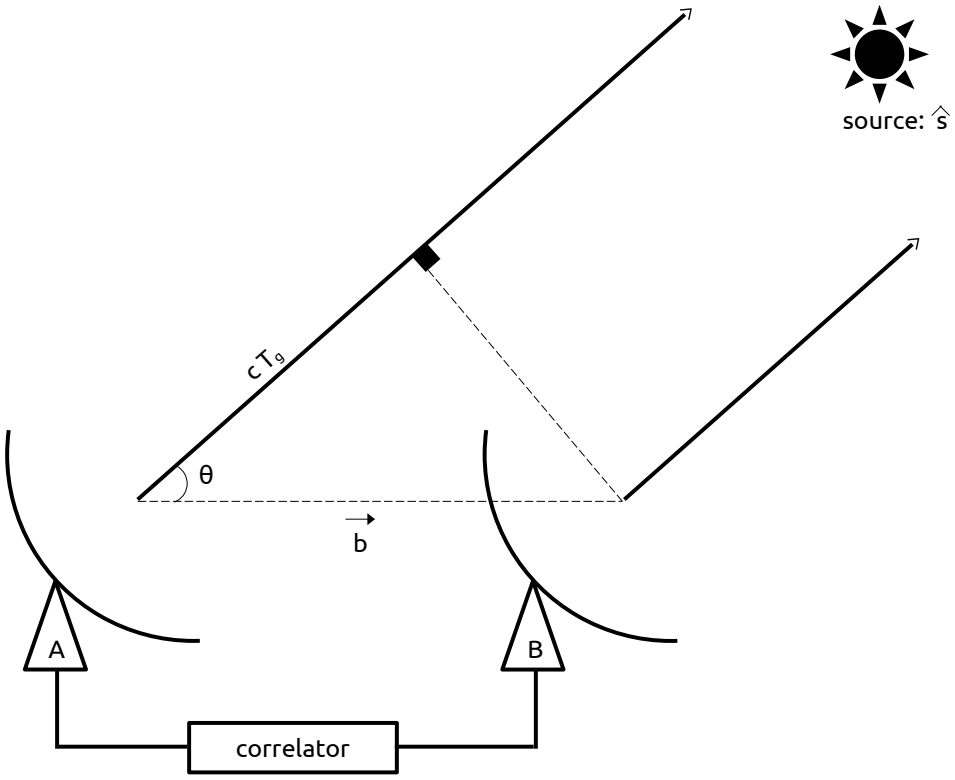

Figure 1.15: Schematic of a basic single-baseline two-element interferometer.

single direction—the position dependence is recorded in the phase of the correlator output[3]. The resolution, i.e., the smallest angular scales that can be identified distinctly, depends on the projected baseline distance and the wavelength of the radio wave. This naturally occurs from the eqn. 1.63:

$$\theta_{\rm res} \approx \frac{\lambda}{|b|} \tag{1.64}$$

If the source is slightly extended, the response of the two-element interferometer (eqn. 1.61) can be found by treating the source as a sum of multiple point sources:

$$R_c = \int I(\hat{s}) \cos(\omega T_g)\, d\Omega \tag{1.65}$$

R_c is sensitive only to the symmetric part of $I(\hat{s})$ due to the presence of the cosine term. To also obtain the anti-symmetric part of $I(\hat{s})$, we add a sine term, which can be measured by introducing a phase delay of $\pi/2$ in another correlator. We denote this response by R_s:

$$R_s = \int I(\hat{s}) \sin(\omega T_g)\, d\Omega \tag{1.66}$$

[3]The area on the sky that can be mapped in this manner is controlled by the primary beam angular dependence of each single telescope dish (see eqns. 1.47 and 1.48).

The sine and cosine terms together form the complex visibility:

$$\mathscr{V} = R_c - iR_s = Ae^{-i\phi} \tag{1.67}$$

where the visibility amplitude, A, and the visibility phase, ϕ, are defined using the Euler representation of complex numbers. Thus, the complex visibility can be written as:

$$\mathscr{V} = \int I(\hat{s})\ \exp\left(\frac{-i2\pi\vec{b}\cdot\hat{s}}{\lambda}\right) d\Omega \tag{1.68}$$

An interferometer array with a large number of telescopes is an extension of the concept of the two-element interferometer. For an array of N telescopes, there exist ${}^{N}C_2 = N(N-1)/2$ combinations of two-element interferometers, i.e., the number of baselines in an array of N telescopes is $N(N-1)/2$. Each baseline samples an angular scale given by λ/b. Thus, the minimum and maximum baseline distances determine the angular scales which the interferometer is sensitive to.

The above formulation of interferometry is perhaps best interpreted in the Fourier domain due to the form of the complex visibility function (eqn. 1.68). We start by representing the baseline vector $\vec{b}$ in a (u, v, w) coordinate system with units of the wavelength of the observation λ. The w-axis is chosen to point to the source, and the u- and v-axes point to the east and the north directions in the uv-plane, respectively. The direction cosines of any arbitrary unit vector are represented by (l, m, n). The infinitesimal area element in eqn. 1.68 can now be written as:

$$d\Omega = \frac{dl\,dm}{n} = \frac{dl\,dm}{\sqrt{1-l^2-m^2}} \tag{1.69}$$

The visibility function in the new coordinate system is:

$$\mathscr{V}(u,v,w) = \int\int \frac{I(l,m)}{\sqrt{1-l^2-m^2}} \exp\left(-i2\pi(ul+vm+wn)\right)\, dl\,dm \tag{1.70}$$

For small angles around the source, the w-term is ignored so that $I(l, m)$ and $\mathscr{V}(u, v, 0)$ are two-dimensional Fourier transforms of each other. Thus, by measuring the visibility, we can recover the source brightness distribution:

$$I(l,m) = \sqrt{1-l^2-m^2} \int\int \mathscr{V}(u,v,0) \exp\left(i2\pi(ul+vm)\right)\, du\,dv \tag{1.71}$$

The above computation can be made only if we measure the visibility function at all possible values of u and v. However, this is not possible in practice. Consider an array of telescopes scattered across a two-dimensional plane, observing a source for a short period of time, i.e., for a 'snapshot observation'. Representing each projected baseline vector on a map with a grid with the units of number of wavelengths ($u = x/\lambda$ and $v = y/\lambda$) instead of the physical distance, we get what is colloquially known as the sampling function on the uv-plane. The sampling functions for a different number of antennas observing a source at a particular direction are

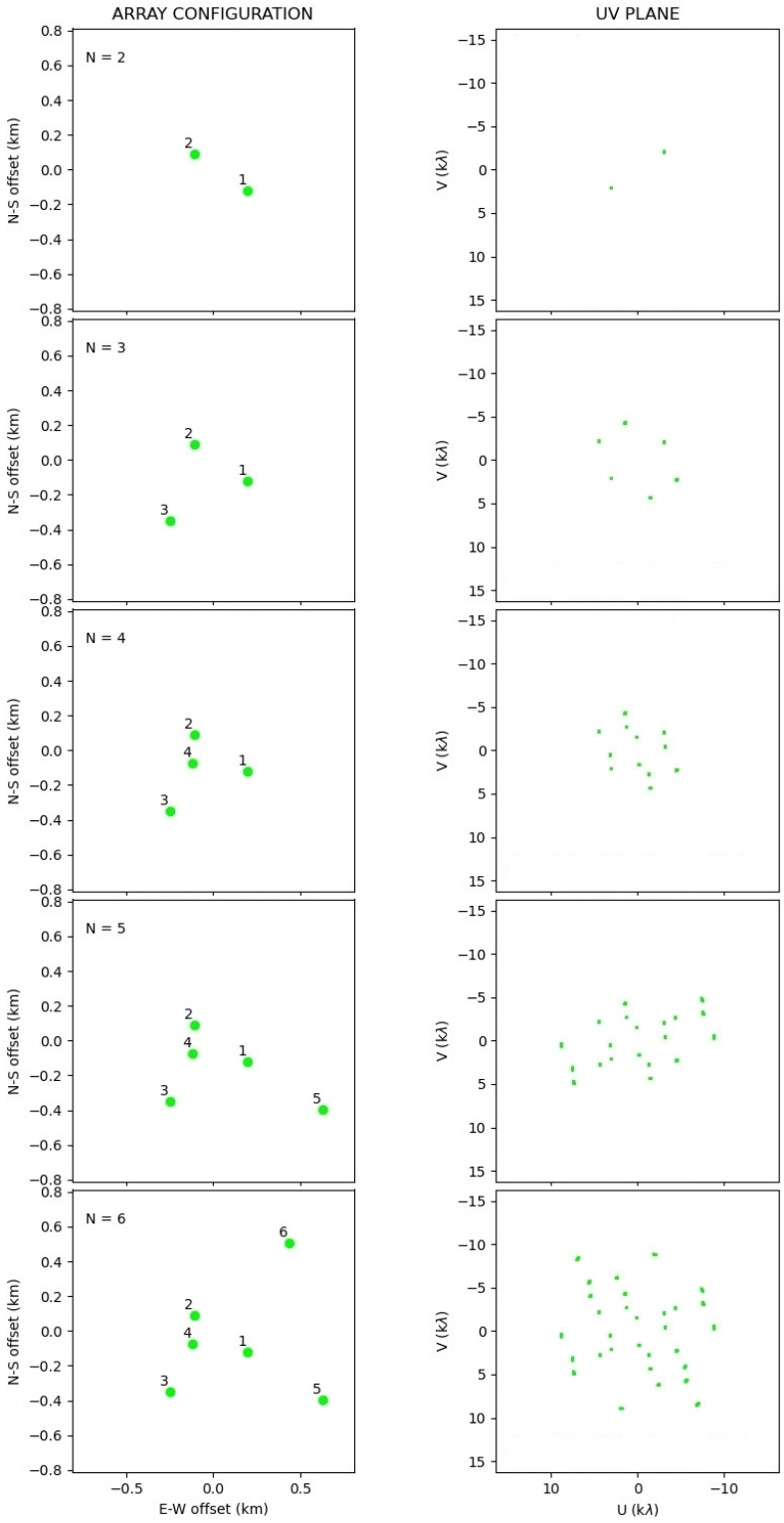

Figure 1.16: Examples of sampling functions for varying number of antennas. The array configurations are shown in the left panels, while the sampling functions are shown in the right panels.

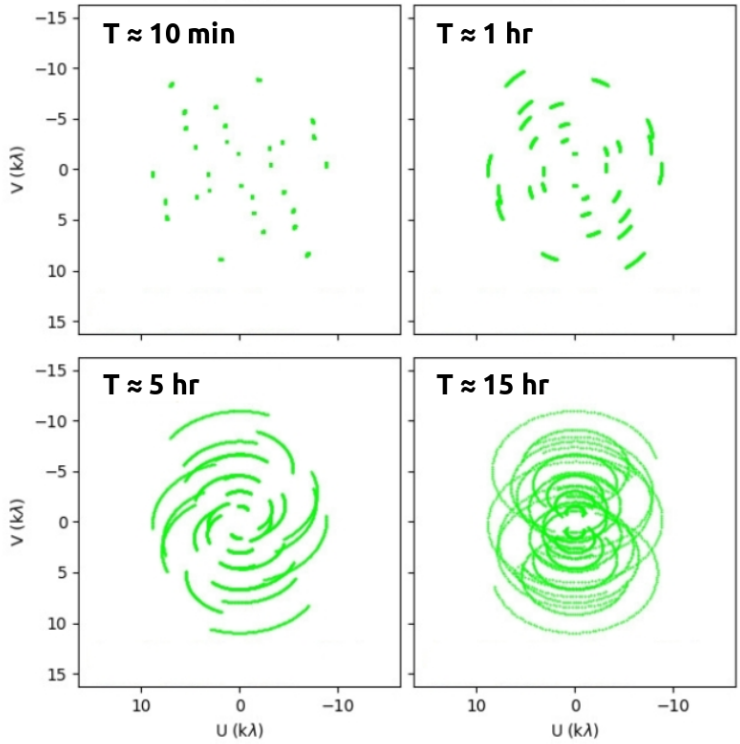

Figure 1.17: For an interferometer array of six antennas, the *uv*-tracks are shown for observations of durations of approximately 10 minutes (*top left*), 1 hour (*top right*), 5 hours (*bottom left*, and 15 hours (*bottom right*). Figure adapted from the output of the `APSYNSIM` software (Marti-Vidal 2017).

shown in Fig. 1.16. The term 'sampling function' arises from the fact that these points on the *uv*-plane sample the Fourier transform of the sky distribution $I(l, m)$.

As the Earth rotates, the projected baseline varies, and hence the sampling function also varies. This manner of observation leads to the sampling of various parts on the *uv*-plane, and this procedure is called 'Earth-rotation aperture synthesis'. The line followed by each point in the sampling function is known as a '*uv*-track', and the '*uv*-coverage' of the observation formally refers to the area sampled on the *uv*-plane. Naturally, a longer observation gives longer *uv*-tracks and hence a better *uv*-coverage. An example of Earth-rotation aperture synthesis is shown in Fig. 1.17.

As mentioned earlier, the Fourier inversion from $\mathscr{V}(u, v)$ to $I(l, m)$ is only possible in the ideal scenario where the whole *uv*-space is sampled. In practice, the sampling function determines how much of the *uv*-plane is observed. If the sampling function is denoted by $\mathscr{S}(u, v)$, the observed visibility function is:

$$\mathscr{V}_{\rm obs}(u, v) = \mathscr{S}(u, v) \cdot \mathscr{V}(u, v) \tag{1.72}$$

In turn, the sky brightness distribution recovered from the observed visibility function is not fully true. It only contains information from the angular scales that are sampled by the

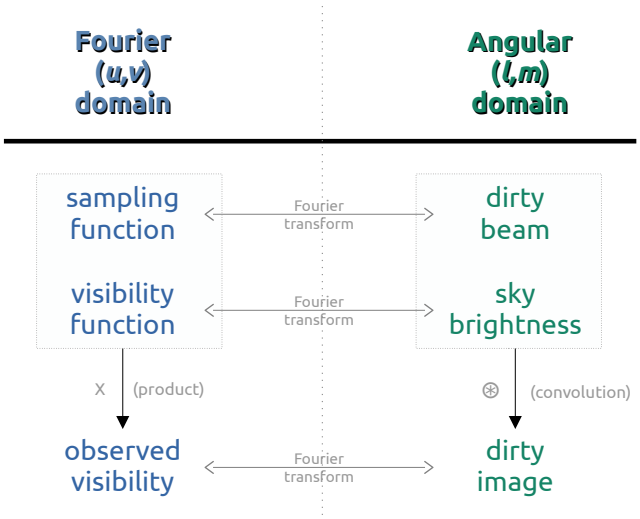

Figure 1.18: Chart describing the relationships between some essential terms in practical radio interferometry. Interferometric arrays measure the 'observed visibility', using which the sky brightness distribution is derived.

interferometer, in addition to the contribution from the sampling function which is unwanted. Note that the recovered sky brightness distribution is just the Fourier transform of the observed visibility function:

$$I_{\rm rec}(l,m) = \sqrt{1-l^2-m^2}\int\int \mathscr{V}_{\rm obs}(u,v)\exp\left(i2\pi(ul+vm)\right)\,du\,dv \tag{1.73}$$

Comparing eqns. 1.71, 1.72, and 1.73, in conjunction with the convolution theorem, we realize that the recovered sky brightness distribution is the convolution of the true sky brightness distribution with the Fourier inverse of the sampling function:

$$I_{\rm rec}(l,m) = I(l,m) \circledast \mathscr{F}^{-1}(\mathscr{S}(u,v)) \tag{1.74}$$

The Fourier inverse of the sampling function is known as the point spread function (PSF) or the 'dirty beam' of the observation, and the recovered sky brightness is known as the 'dirty image'. A summary of the important terms for radio interferometry and their relationship to each other is presented in Fig. 1.18.

In order to estimate the true sky brightness distribution, we must remove the contribution of the dirty beam in the dirty image. This is usually done by a 'deconvolution' process such as the CLEAN algorithm (Högbom 1974; Cornwell 2009). While some other techniques such as the Maximum Entropy Method exist, the CLEAN algorithm is the most widely used till date. The 'deconvolved' image resulting from the deconvolution process is, at the end, convolved with a Gaussian that is fit to the main lobe of the dirty beam of the observation; that Gaussian is known as the 'CLEAN beam' or the 'synthesized beam'. Angular resolution and synthesized beam are interchangeably used in this scenario. A few essential considerations must be taken into account during the process of imaging:

- *Weighting*: The sampling function can be modified by controlling the weights of the visibilities in the *uv*-plane. This results in the modifications of the synthesized beam, the sensitivity, and the final image quality.
- *w-term*: The transformation from the Fourier plane visibilities to the real plane sky brightness is only accurate near the pointing center. For non-coplanar baselines and at angles far away from the pointing center, this issue must be taken into account during imaging.
- *Wide bandwidth*: We assumed that a monochromatic radiation is being detected by the interferometer. This is clearly not true for observations. Especially with modern wideband receivers, this makes a major difference in the final image produced, since the properties of the source and the beam may strongly vary with frequency.
- *Multiple scales*: The original CLEAN algorithm assumes that an extended source can be modeled as several point sources (i.e., Dirac-delta functions). This results in poor image quality for complicated sources, but it can be improved by using a multi-scale algorithm that accounts for sources of various angular sizes (Rau & Cornwell 2011).
- *Thresholds*: Deconvolution must be done in a controlled manner, so that only real sources, and not artefacts, are put through the CLEAN algorithm. This is controlled by limiting the maximum number of cycles and by setting a threshold noise to be reached.
- *Outliers*: The dish may be sensitive to sources that are far from the pointing direction as well (see Fig. 1.13). The dirty beam from such sources must be deconvolved, either by imaging a very large area, or by using 'outlier' fields.
- *Primary beam*: The amplitude response across the field of view of a pointing varies with the angular distance from the pointing center due to the primary beam attenuation. This is usually only a simple multiplication for each pixel, and can be easily accounted for.

The discussion so far mostly pertains to the imaging part of the reduction of radio interferometric data. Removing the effects of the instruments and the atmosphere typically come under the process of 'calibration'. The instrumental effects arise from the frequency response, delay of signal arrival, etc. The atmospheric effects are due to the ionosphere and the Earth's atmosphere in general, which modify both the amplitude and the phase of the visibility function. Specialized tools such as CASA (McMullin et al. 2007) exist for both calibration and imaging.

A typical radio interferometric dataset contains observations of not just the targets, but also multiple 'calibrator' sources for which some properties are accurately known beforehand:

- **Flux density calibrator** to scale the amplitudes (flux densities) from the voltage induced.
- **Delay calibrator** to measure the instrumental delays.
- **Bandpass calibrator** to scale the frequency response.
- **Unpolarized calibrator** to measure the instrumental leakage (called the 'D-terms') across the cross-polarization data.

- **Polarization angle calibrator** to fix the polarization degree and angle.
- **Secondary/phase/gain calibrator** near the targets to transfer the solutions from the primary calibrators to the target, and to measure the temporal variations (colloquially called 'gains') of the visibility phase and amplitude.

The scan sequence of a typical radio interferometry session consists of multiple observations of the target interspersed among observations of the secondary calibrator, while the other calibrators are usually observed at the beginning and/or the end of the session (see Fig. 1.19). Depending on the requirements, some calibrators such as the unpolarized calibrator may be ignored altogether. In addition, a bright source such as 3C 286 is typically useful as a calibrator not just for flux density, but also to solve for the delays, the bandpass response, and the polarization angle. Finally, after the routine calibration, some rounds of 'self-calibration' may be performed to improve the image quality. Self-calibration is an iterative process where a model of the produced image is used to measure a more accurate set of temporal gains, which are then applied to produce another new image. This process is iterated over multiple times until no further improvements can be made, at which point the image is considered ready for science.

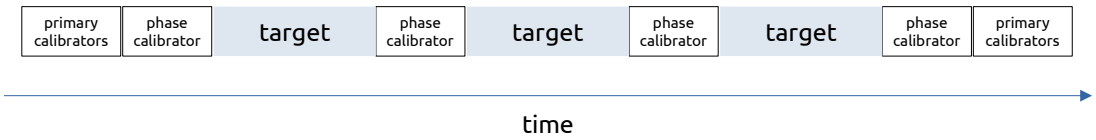

Figure 1.19: A typical observation session with a radio interferometer array.

One important caveat of radio interferometry is that the measured flux density is always underestimated if the source is more extended than the largest angular scale recoverable (LAS)[4]. The central 'hole' visible in each of the *uv*-coverage plots (see Fig. 1.17) illustrates this issue clearly. The Fourier transform of an extended source has components close to the origin, which cannot be sampled by an interferometer. This is known as the 'missing flux density' or the 'short/zero-spacing' problem. The solution is to observe the target with a single-dish telescope that is at least as large as the shortest baseline distance, and combining the single-dish data with the interferometric images in Fourier domain will yield the correct flux densities. This method is known as *feathering*. I will discuss it in further detail in §3.4.

[4] LAS $\approx \frac{\lambda}{b_{\rm min}}$, where $b_{\rm min}$ is the length of the shortest baseline

Chapter 2

Pilot study for a Galactic plane survey with the uGMRT

This chapter deals with a pilot survey that was conducted in 2019 with the upgraded Giant Meterwave Radio Telescope (uGMRT) to investigate the feasibility of performing a large scale Galactic plane survey at low frequencies. My contributions to this survey are the calibration and the imaging of the continuum data, and the preliminary verification of the final images.

2.1 Introduction

Galactic radio emission at frequencies below 1 GHz is dominated by nonthermal synchrotron radiation, which originates in the diffuse ISM and SNRs (e.g., Wilson et al. 2013). The Galactic plane in these frequencies, however, is relatively unexplored at arc second angular resolution. The GaLactic and Extragalactic All-sky Murchison Widefield Array survey (GLEAM; Hurley-Walker et al. 2019c) at 70–230 MHz covers a large portion of the Galactic plane at $2' - 4'$ resolution and a sensitivity $\sim 10 - 20$ mJy. The 150 MHz TIFR-GMRT Sky Survey (TGSS; Intema et al. 2017) is an all-sky survey that also covers the Galactic plane at a resolution of $25''$, but it does not recover extended emission. The 843 MHz Molongolo Galactic plane survey (MGPS; Murphy et al. 2007), which has a resolution of about $45''$, is sensitive to extended structures, but it covers only the southern Galactic plane, which does not include the first quadrant of the Milky Way.

Two recent high-resolution centimeter wavelength surveys of the first quadrant of the Milky Way are the 4–8 GHz GLOSTAR (a GLObal view on STAR formation survey; Brunthaler et al. 2021) and the 1–2 GHz THOR (The HI/OH/Recombination line survey; Beuther et al. 2016). Motivated by the science being extracted from these surveys and the lack of a low frequency counterpart survey at a comparable sensitivity and resolution, we observed a $\sim 5^\circ \times 2^\circ$ strip of the Galactic plane covering the Galactic longitudes $l = 30^\circ - 35^\circ$ and latitudes $|b| < 1^\circ$ in two frequency bands (300−500 MHz and 550−750 MHz) with the Giant Meterwave Radio Telescope (GMRT, Fig. 2.1). Due to its unique hybrid configuration (see Fig. 2.2), one can ideally recover extended emission (up to scales of $\sim 25'$ at 400 MHz) in addition to achieving a high resolution ($\sim 4''$ at 650 MHz). Its recent upgrade to wideband receivers afford a wide bandwidth of 200 MHz at central frequencies of 400 MHz and 650 MHz, resulting in high sensitivity in a relatively short amount of time. Inferring the dominant emission mechanism of an object is possible by comparing the data from the two frequency bands, and one will be also able to draw broadband SEDs for objects with counterparts in the THOR and GLOSTAR surveys. The frequency coverage of our observations contains hydrogen and carbon radio recombination

Figure 2.1: Three central square antennas of the Giant Meterwave Radio Telescope array at night. Image credit: GMRT.

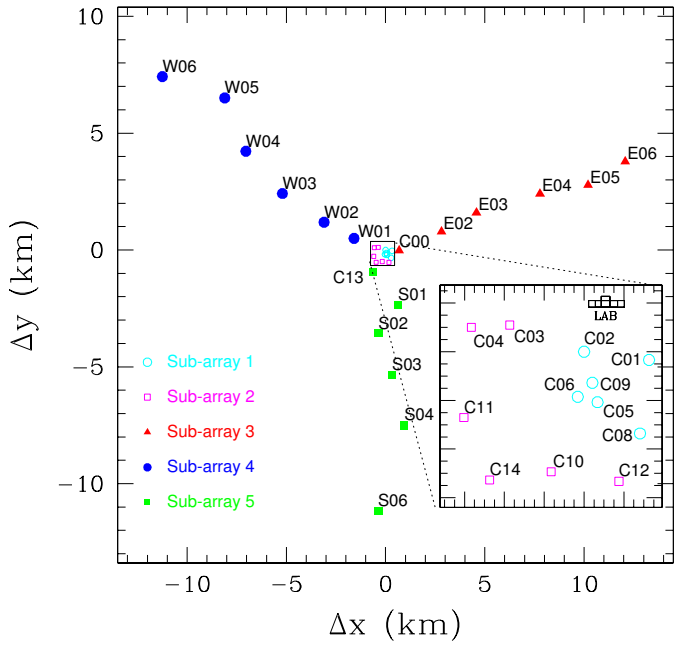

Figure 2.2: Antenna configuration of the GMRT array. Taken from Bhat et al. (2013).

lines, which help in constraining physical conditions and kinematics of star-forming regions and tracing feedback. In addition, SNRs are brighter at low frequencies, making this pilot survey potentially useful to identify new SNRs and to better characterize known ones.

The number of SNRs identified in the Milky Way so far is less than 400 (Ferrand & Safi-Harb 2012; Green 2019), which is substantially lower than the predicted value of ~1000 (Li et al. 1991). Recently, a number of objects have been identified as SNR candidates using data from the THOR and GLOSTAR surveys (Anderson et al. 2017; Dokara et al. 2021, and §4). Given that most of these candidates are of small angular size, the next natural step is to search for such objects in the images of high resolution large scale Galactic plane surveys at low frequencies, since SNRs are typically brighter at longer wavelengths. However, imaging structures larger than a few arc minutes with interferometers, at arc second resolution and poor *uv*-coverage (due to snapshot observations), is quite challenging. This problem is only worse at frequencies below 1 GHz, where the variable ionospheric conditions greatly affect the phase stability due to which achieving good positional accuracy is difficult.

The chosen region of the Galactic plane covers a region where the Scutum-Centaurus Arm meets the bar of the Milky Way. It is home to several bright extended Galactic sources such as the W44 SNR and the W43 star-forming complex in addition to numerous unresolved extra-galactic sources (Chakraborty et al. 2020), and hence it is an excellent test-bed for our purpose. This region covering the Galactic longitudes $l = 30^\circ - 35^\circ$ and latitudes $|b| < 1^\circ$ overlaps with the 'pilot' regions of the THOR and GLOSTAR surveys, too (Beuther et al. 2016; Brunthaler et al. 2021). The primary goal of this study is to understand the feasibility of performing a large scale low frequency snapshot survey with the GMRT that maps the Galactic plane at an angular resolution of a few arc second and a point source sensitivity of a few hundred μJy, simultaneously observing both compact and extended sources. The rest of the chapter is organized as follows. In §2.2, we describe the observations and the data reduction steps. In §2.3, we present the continuum and spectral index mosaics, along with the results of the analyses of positions and flux densities. Finally, the conclusions from this study and its implications for future low frequency Galactic plane surveys are discussed in §2.4.

2.2 Data

2.2.1 Observations

Located near Pune, India, the Giant Meterwave Radio Telescope (GMRT) is an array of 30 dishes, each with a 45 m diameter. A sample of the central square antennas and the antenna configuration are shown in Figs. 2.1 and 2.2. The over-density of antennas in the central square is useful to recover extended emission, while the moderately long baselines (~25 km) formed by the outer antennas provide high angular resolution.

The data presented in this chapter were obtained from observations with the GMRT that were carried out in 2019 under the proposal code 36_061 (PI: Nirupam Roy). We observed in two frequency ranges: band-4 (550−750 MHz) in May 2019 with the full 200 MHz bandwidth, band-3 (300−500 MHz) in June 2019 with 100 MHz bandwidth, and band-3 again in August 2019 with the full 200 MHz bandwidth. The total time allotted to the project initially was 26

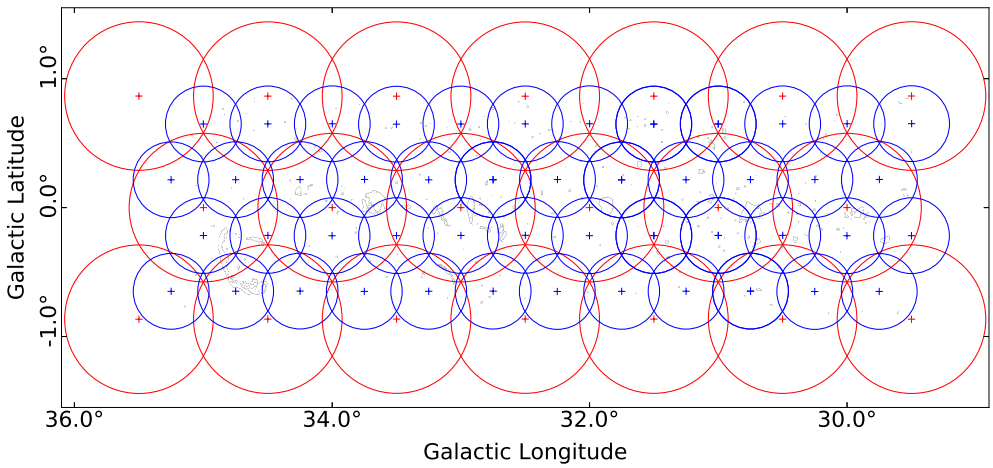

Figure 2.3: Pointing configuration map of our pilot survey. The large red circles mark the field of view used for imaging each pointing of band-3 data, with their centers marked with red crosses. Similarly, the band-4 fields of view and pointing centers are marked in blue.

hours. We were unable to recover any useful data from the June (band-3) observation due to strong broadband radio frequency interference (RFI) from artificial satellites near the target sky positions. This prompted us to re-observe with a larger bandwidth of 200 MHz to account for the sensitivity loss due to channels corrupted by RFI, which was done in August 2019. The band-3 data used in this work are from the August observations only.

The region observed covers the Galactic longitude range $l = 30^\circ - 35^\circ$, from the Galactic latitude $b = -1^\circ$ to $b = +1^\circ$. We followed a hexagonal mapping pattern to observe the target region in several individual pointings. The pointing centers are shown in Fig. 2.3, along with the fields of view used for imaging. Each target field was observed for ~14 minutes in total, done in two separate scans of seven minutes each that were spaced across the observation time in order to achieve slightly better *uv*-coverage. The standard primary calibrator 3C 286 was observed at least once during an observation night, and the gain calibrator J1851+005 was observed about once every hour. The best continuum point source sensitivity theoretically achievable is about 100 μJy beam^{-1} and 50 μJy beam^{-1} in band-3 and band-4, respectively. The expected resolutions of the data are about 8″ and 5″ in band-3 and band-4, respectively. These observations, like all other GMRT projects, are recorded in spectral line mode, which helps in isolating the RFI to a relatively small number of channels of the observed bandwidth. The steps to reduce the continuum data and produce mosaics are detailed below.

2.2.2 Data reduction

The raw visibility data from an interferometer are corrupted due to the atmosphere and the receiving instruments. The process of calibration estimates the actual visibilities from the observed visibilities, which are related to each other by a measurement equation as described by Hamaker et al. (1996). Imaging the calibrated data constitutes removing the point spread function (PSF) of the interferometer, and this is done by deconvolution. These two steps (calibration

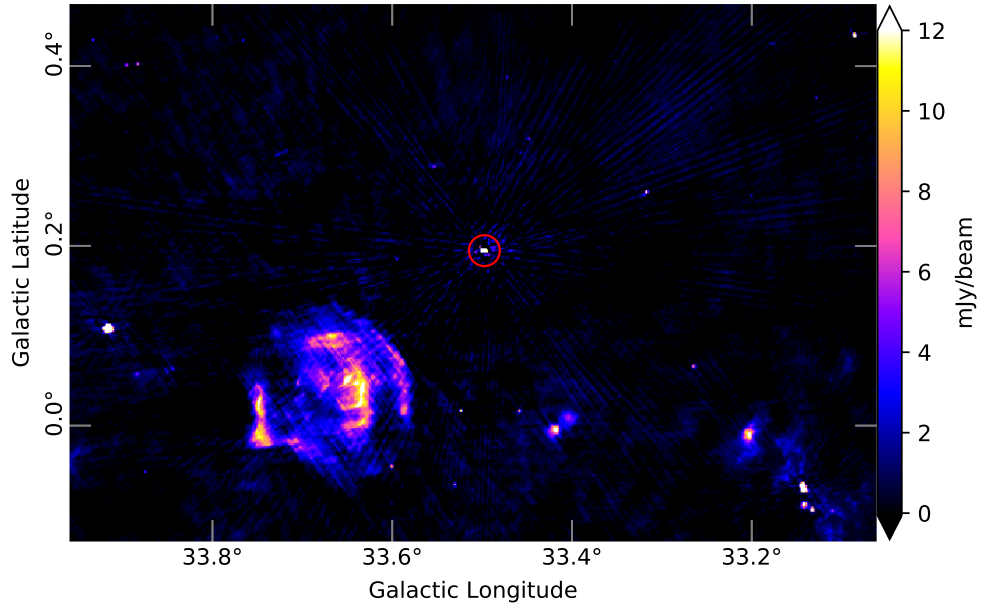

Figure 2.4: A preliminary 650 MHz image of the phase calibrator field of our observations. Circled in red at the center is the phase calibrator (J1851+005; Galactic coordinates l = 33.5°, b = 0.2°). The large and extended structure to its southeast is the SNR G33.6+0.1. The beam size is about 10″.

and imaging) are explained in detail in the following sections.

2.2.2.1 Calibration

The data were calibrated in the CASA software suite (McMullin et al. 2007)[1]. The compact quasar 3C 286 served as the primary flux calibrator with its flux density scale given by Perley & Butler (2017), and J1851+005 was used as the gain calibrator. A routine direction-independent calibration strategy was followed except for the phase calibrator field. As J1851+005 lies in the Galactic plane with bright and extended sources in its vicinity (see Fig. 2.4), we first generated a model of this region by self-calibrating this field and then obtained new gain calibration solutions, which were later applied to the visibilities of the target fields. The data corrupted due to RFI were "flagged" using automated techniques and not used further. We used some strategies and modules of the VLA scripted pipeline[2] to make our calibration scripts fast and reliable. Due to the bright extended structures in the Galactic plane which we intend to detect and study, direction-dependent calibration is extremely complicated in this case (e.g., Albert et al. 2020). Even with full synthesis observations, imaging extended structures with the GMRT using direction-dependent gains is challenging (Wykes et al. 2014), and we do not find any previous studies that had successfully imaged extended sources with direction-dependent calibration. Hence we decided to proceed with the standard direction-independent calibration only.

[1] casa.nrao.edu
[2] science.nrao.edu/facilities/vla/data-processing/pipeline/scripted-pipeline

The flowchart of this whole process is shown in Fig. 2.5, and a full description is given in Appendix A.

Preliminary images of the calibrators were produced with the task `tclean` in order to confirm that the calibration procedure was successful. The task `statwt` was applied on the target data to weigh down outliers based on local variances. It is helpful to reduce the imaging artefacts caused by residual RFI which may not have been flagged during the previous steps. The corrected data of targets are now considered ready for further processing.

At the end of this calibration procedure, about 50% of the data in band-3 were flagged, which is typical of GMRT observations at these frequencies due to strong RFI. In band-4, ∼15−45% of the data were flagged, depending on the night of the observation. RFI at these frequencies is relatively less of an issue, and most of the flagging occurs due to non-working antennas. The data from May 27 were the most affected with ∼45% data loss; five antennas were dead during this observation (see Fig. 2.6). We also find that several fields had a number of central square antennas flagged during the calibration due to RFI, especially in band-4. This means that the large scale structure will not be well reconstructed for these fields, and the largest angular scale to which the data are sensitive will be significantly smaller than the theoretical values of ∼25′ and ∼15′ in band-3 and band-4 respectively.

2.2.2.2 Polarization

The band-4 observations (550−750 MHz) were done in full-polarization mode, meaning we can make images of the Stokes Q and U parameter data in addition to Stokes I. Linearly polarized emission is expected from synchrotron emitters such as SNRs, whereas emissions due to thermal bremsstrahlung is unpolarized. Hence polarization plays a key role in separating thermal and nonthermal emissions, and thus in identifying new SNRs (e.g., Dokara et al. 2021). The polarization calibration involves obtaining cross-hand delays, characterizing instrumental polarization by determining the leakage terms, and calibrating the absolute polarization position angle. 3C 48 served as the unpolarized calibrator (Perley & Butler 2013; Farnes et al. 2014) using which we were able to determine the leakage terms. For calibrating the position angle, we used 3C 286 following Mohan et al. (2019). However, we obtain a polarization fraction of ∼3.5% for 3C 286 at 650 MHz, which agrees with the value of 2.7% at 610 MHz by Farnes (2012) but not with the value of 7.6% at 607 MHz given by Mohan et al. (2019). We note that the polarization properties of 3C 286 are not well known below 1 GHz, and the source is known to strongly depolarize (well below 1%) at frequencies below 500 MHz (Perley & Greisen 2019). We imaged Stokes Q and U for a field containing the W44 supernova remnant, for which we expected a polarization signal of at least a few percent, but we were unable to recover any.

Sources with Faraday rotation measure[3] more than ∼7 rad m^{-2} will appear de-polarized in our images, since their polarization angle rotates multiple times over the 200 MHz bandwidth. To account for this problem, we decided to split the data into several frequency bins and image each bin separately. The images are later combined by averaging to form a single output image.

[3]Faraday rotation measure is defined as the slope of the plot of polarization angle versus wavelength squared. It is a measure of the product of the average electron density and the average axial magnetic field from the source to the observer (e.g., Mancuso & Spangler 2000; Brentjens & de Bruyn 2005).

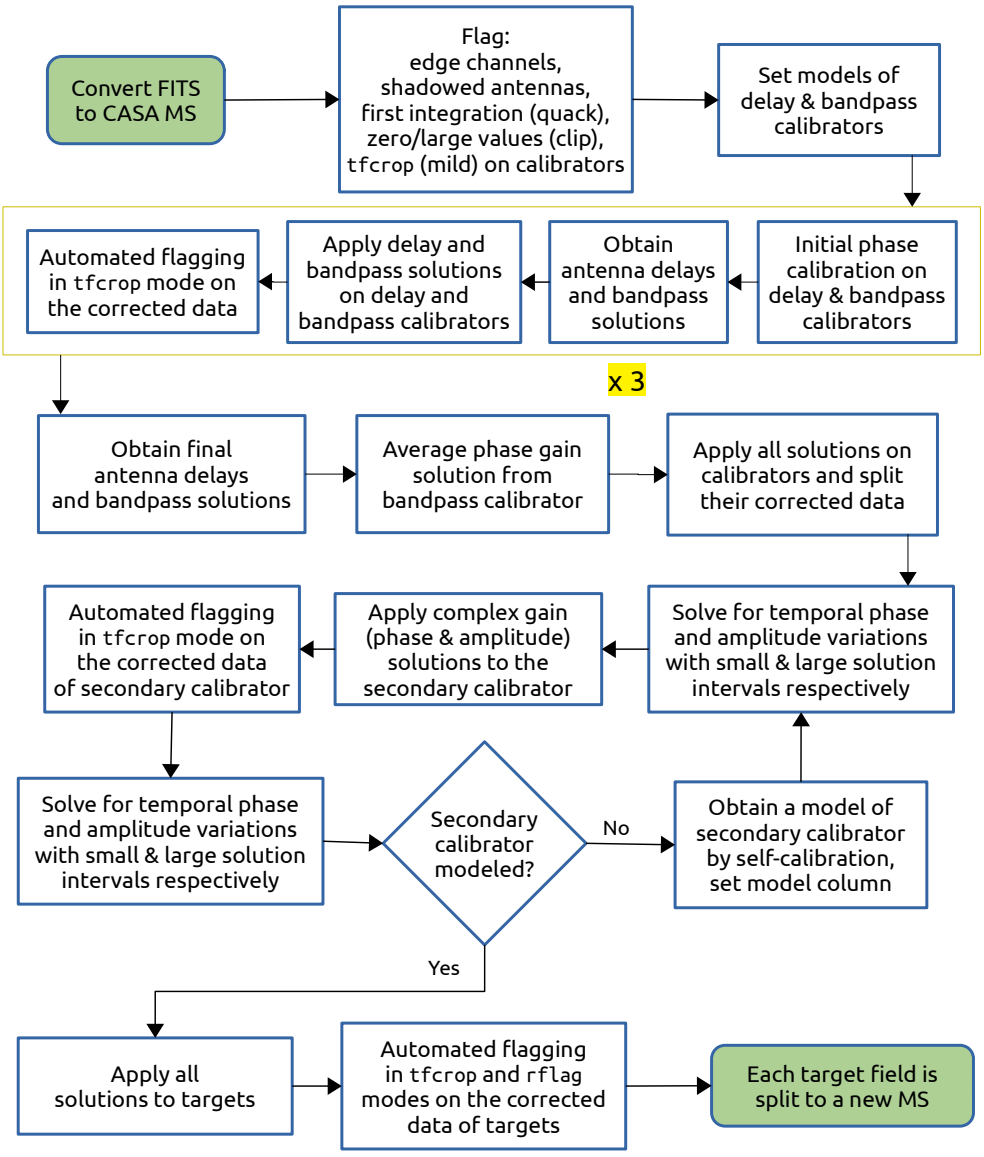

Figure 2.5: Calibration scheme that we followed to reduce the uGMRT data.

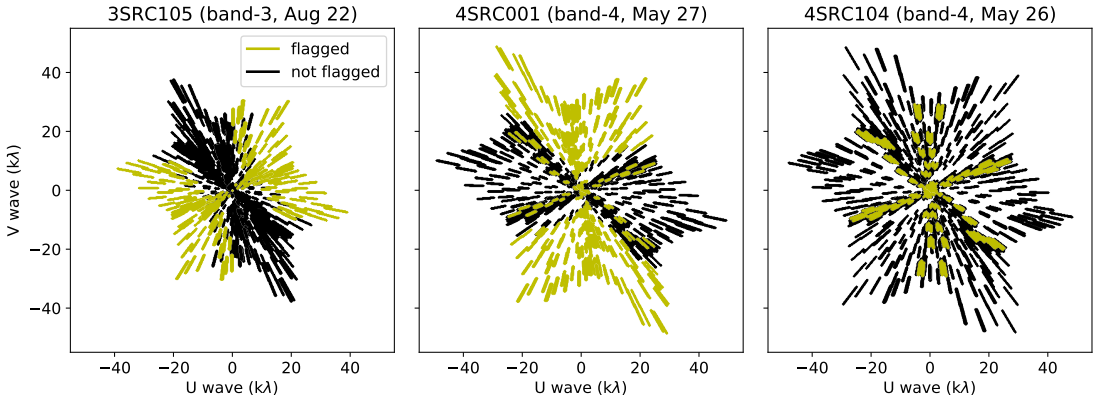

Figure 2.6: *uv*-coverage plots of typical fields observed on August 22 (*left*, 3SRC105), May 27 (*middle*, 4SRC001), and May 26 (*right*, 4SRC104). The asymmetry caused by dead antennas (marked in yellow) is clearly visible in the fields observed on August 22 and May 27, which leads to the synthesized beam being elongated on one side.

Despite this process, we were unable to obtain any useful Stokes Q and U images, which is due to poor signal-to-noise ratio in each frequency bin. Since the total time spent on each pointing is less than 15 minutes, the image reconstruction is quite poor, especially in Stokes Q and U. Hence, we imaged only Stokes I data for the survey.

2.2.2.3 Imaging

Generally, imaging is the most intensive part of the reduction of radio interferometric data, both in terms of CPU time and manual effort. The task `tclean`[4] of CASA was employed for imaging. Several deconvolution algorithms based on Cotton-Schwab CLEAN (Schwab & Cotton 1983) are available in this task. It was used in parallel mode on four cores in order to speed up the imaging process. The wide field of view and the 200 MHz wide bandwidth receivers of the GMRT observing the emission from complex structures across the Galactic plane pose significant challenges in imaging. We briefly explain our imaging strategies below:

- *w-projection:* To account for the non-coplanar baseline effect, we use w-projection (Cornwell et al. 2008). The number of planes was set to be automatically calculated using the parameter `wprojplanes=-1`.

- *Outliers:* We image a region that covers at least until the first null of the primary beam (~2.3° and ~1.4° at 400 MHz and 650 MHz respectively), and in some cases we use outlier fields as well. This is done in order to image very bright sources that are well outside the primary beam. Such sources, if not CLEANed, produce noticeable features and significantly increase the root mean square (rms) background noise.

[4] https://casadocs.readthedocs.io/en/stable/api/tt/casatasks.imaging.tclean.html

- *Wide bandwidth:* In order to account for the spectral structure across the 200 MHz bandwidth, we use multi-frequency synthesis (`specmode='mfs'`; Rau et al. 2009) with two Taylor coefficients in the spectral model (`nterms=2`).

- *Multiple scales:* To model emissions of various sizes, we use the Multi-Term Multi-Frequency-Synthesis algorithm (`deconvolver='mtmfs'`; Rau & Cornwell 2011). The scales are decided such that they roughly correspond to the sizes of the structures expected in the given region.

- *Thresholds:* The MT-MFS algorithm in the task `tclean` is prone to divergence if the stopping criteria are not carefully set, especially if the noise threshold to be reached is set to a value that is too low. Hence, we use a dynamic threshold based on the local image statistics, fixed the maximum number of minor cycle iterations with the parameter `cycleniter=2000`, and lowered the loop gain from the default of 0.1 to 0.06. This comes at the cost of a larger computational footprint and more processing time due to major CLEAN cycles being visited more often. However, we never found the algorithm to diverge with these parameters, and the images are also more accurate due to better residual image construction.

- *Weighting:* The Briggs weighting scheme (Briggs 1995) with a robust parameter of 0.5 is used, which is a compromise between the best resolution and large scale structure sensitivity.

- *Pixel size:* The pixel size is chosen such that there are at least three pixels across the minor axis of the expected synthesized beam. This is necessary to ensure a good Gaussian fit to the point spread function.

- *Masking:* It is impractical to manually identify real emission for CLEAN masks since we covered a large region. So we make use of the auto-masking feature of `tclean` (`usemask='auto-multithresh'`; Kepley et al. 2020). This also helps to keep the imaging process reproducible.

- *Self-calibration:* By modeling the phases from an initial shallow CLEAN, we self-calibrated the targets, and repeated this process once more to generate a better model and a better final image. Although the improvement in dynamic range is quite low (~15%)—which is expected due to poor *uv*-coverage—we find that the image fidelity was improved by reducing the sidelobe artefacts caused by imperfect deconvolution.

- *Uniform resolution:* To compare the images of both bands, a uniform beam size is necessary. Hence we restricted the *uv*-range during imaging and all the fields are eventually restored to a common circular beam with the size of the largest synthesized beam.

- *Wide-band primary beam correction:* The attenuation caused due to the primary beam response is corrected for using the contributed CASA task `wbpbgmrt`[5].

[5] `github.com/ruta-k/uGMRTprimarybeam`

- *Mosaics:* We image each field individually first and then combine later to form a mosaic using the tool `linearmosaic` of CASA, in which the data are weighted by the primary beam response.

- *Coordinate transformation:* Finally, the mosaic is processed from the CASA default equatorial (right ascension and declination) to Galactic coordinates (latitude and longitude).

We find that the synthesized beams obtained after imaging depended strongly on the night of the observation (caused by the different amount of usable data) and the software being used. AIPS, and the versions of CASA prior to v5.8, have a PSF-fitting algorithm that works best only if the range of over-sampling factor (number of pixels across an axis of the expected synthesized beam) is about 3−5. Because of the dead outer antennas during the nights of May 27 and August 22 (see Fig. 2.6), satisfying the condition of over-sampling by a factor of 3 – 5 was not possible on both the major and the minor axes of the synthesized beam when we imaged using all possible baselines. This led to an incorrect beam size estimation if AIPS or an older version of CASA was used for imaging (see Appendix B for more details). Hence, we used a newer version of CASA, v5.8, in which the PSF fitting algorithm was updated[6]. This is able to deliver correct results even in extreme cases such as ours. Unfortunately, the dead antennas meant that the final common beam size is 25″ for both bands, which is much larger than the best possible resolution of about 8″.

The background noise maps corresponding to each band are created using the software `SExtractor` (Bertin & Arnouts 1996). A spectral index map is created using the images from the two bands, after reprojecting them onto the same grid. This map is obtained on a pixel-by-pixel basis, and the calculation is done only if the signal-to-noise ratio of a pixel is larger than three. We note that although the multi-frequency synthesis algorithm in CASA (Rau et al. 2009) is capable of producing spectral index maps, we find that it delivers unphysical spectral indices for our data (typical values of the order of tens), even after accounting for primary beam attenuation. This was true not just for extended emissions, but also some point-like sources. While the sparse *uv*-coverage and low signal-to-noise ratio play an important role, we do not fully understand the reason behind this. A recent study by Rashid et al. (in prep.) confirms our results using simulated GMRT observations. Hence, for this work, we use only the spectral index map derived using the band-3 and band-4 images.

2.3 Results

The mosaics of band-3 and band-4, along with the spectral index map, are shown in Fig. 2.7. All the pointings are dynamic range limited, with rms noise about ∼5 mJy beam^{-1} in band-3 and ∼2 mJy beam^{-1} in band-4. The distributions of the values of the pixels on the combined mosaics, and the cumulative distributions of the values of pixels on their respective background noise maps are shown in Fig. 2.8. We notice sidelobe artefacts near a few bright point sources in both bands, which likely result from the lack of direction-dependent calibration and imperfect deconvolution in conjunction with the sparse *uv*-coverage. Bright sources that are not close to

[6] `casadocs.readthedocs.io/en/v6.2.0/notebooks/introduction.html`

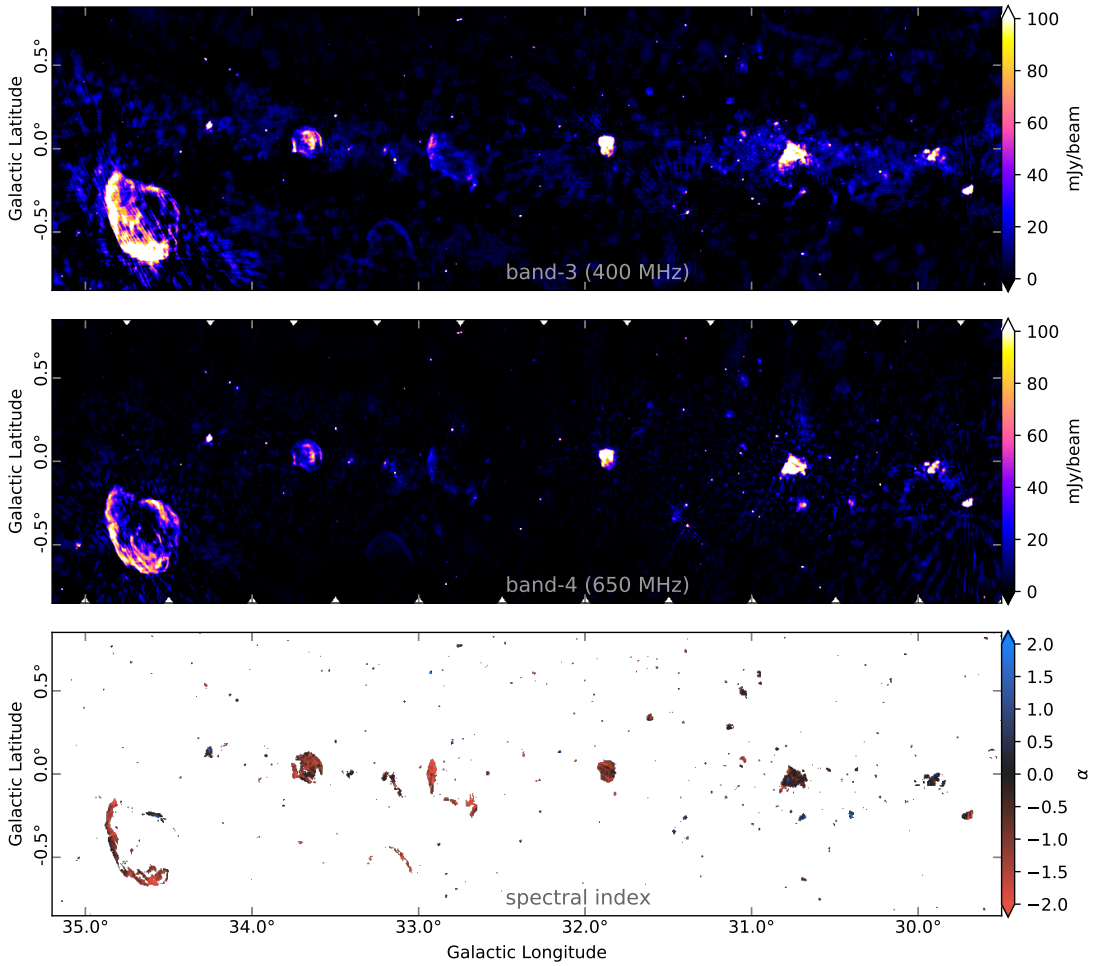

Figure 2.7: Mosaics of band-3 (*top*), band-4 (*middle*) and the resulting spectral index (*bottom*) images. The beam size is 25″.

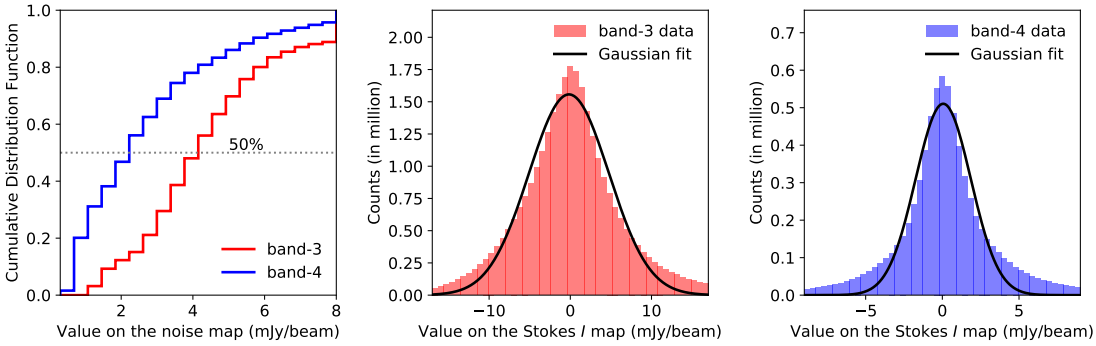

Figure 2.8: Cumulative distribution functions of the noise maps (*left*), and the histograms of values of the pixels on the continuum mosaics of band-3 (*middle*) and band-4 (*right*). Gaussian least-squares fits are performed on the histograms, which gave the standard deviations as ∼4.9 mJy beam^{-1} for band-3 and ∼1.8 mJy beam^{-1} for band-4.

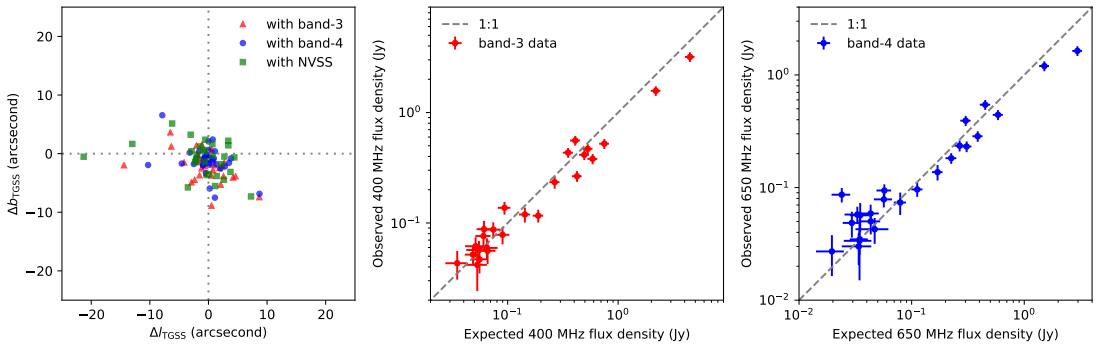

Figure 2.9: *Left*: Position offsets of the TGSS sources seen in our survey and the NVSS, with obvious extended sources excluded. Observed and expected flux density comparison for sources in band-3 (*middle*) and band-4 (*right*), where the expected flux density is obtained using spectral indices from de Gasperin et al. (2018).

the center of the pointing corrupt the image, since the gains are truly applicable only at the phase center of the field. In addition, the regions close to the SNR W44 (G34.7−0.4) have a larger rms noise because the SNR is quite bright and extended with a complex structure.

2.3.1 Comparison with other surveys

At these frequencies (300–750 MHz), no other high resolution surveys cover the part of the sky imaged by us. Hence we use data from surveys at other frequencies to compare the positions and flux densities. The TGSS covers the region we observed at the same resolution (25″) and a comparable sensitivity (∼10 mJy beam^{-1} in the Galactic plane). Since the inner baselines were severely down-weighted during the reduction, only the brightest edges of extended sources were detected in their images. The catalog of this survey lists 50 sources in the region we observed. We detect all the sources except one, named J185141.6+003739 in the TGSS catalog. Its signal-to-noise ratio is about nine, but this source is not detected in any radio survey other than the TGSS, according to the SIMBAD database. There are two bright sources very close to this object: J185146.7+003531, which is in fact our phase calibrator, and the SNR G33.6+0.1, which is an extended source (Fig. 2.4) and thus not well sampled in the TGSS images. Hence, the sole TGSS source that we do not detect in our data is likely to be a 'ghost' (Grobler et al. 2014). Of the remaining 49 TGSS sources, 17 are clearly either a part of a supernova remnant or are double-lobed sources, and the other 32 are compact sources.

The NRAO-VLA sky survey (NVSS; Condon et al. 1998) is a 1.4 GHz survey of the whole sky north of $\delta = -40°$, at a resolution of 45″. While the NVSS catalog contains over 1300 sources in the area we covered, a visual inspection reveals that most of these sources have a low signal-to-noise ratio and are clearly not real. This was noted by earlier studies as well (e.g., Bihr et al. 2016), and is not unexpected. The techniques used for the imaging and cataloging of the NVSS data are best suited for detecting compact extragalactic objects, and do not perform well in very crowded and complicated fields such as ours. However, of the 32 compact sources detected in the TGSS, 28 were detected in the NVSS as well, using which we made position and

flux density comparisons to validate our mosaics. For these sources, we evaluated the peak and integrated flux densities, along with their positions, by performing two-dimensional Gaussian fits on our images. We compared these values to the values from the TGSS and the NVSS source catalogs, and the results are shown in Fig. 2.9.

While the position accuracy of both TGSS and NVSS are reported to be better than 2″ (Condon et al. 1998; Intema et al. 2017), we find that there are significant offsets between the peak positions of a few sources in this field (Fig. 2.9; left panel). The complex background in this region moves the peak of a source along the local noise gradient, which makes the positions of these source catalogs less reliable compared to the regions outside the Galactic plane. In addition to the background contamination, the emission at different frequencies may be dominated by different mechanisms, which do not necessarily have the same peak positions. Since we have not performed direction-dependent calibration, that may also play a role in offsetting the peak position. However, we note that most of the offsets are within 1-2 pixels, and all are smaller than the beam size.

Assuming a power-law index holds between 150 MHz and 1.4 GHz and that the sources are not variable, a spectral index catalog was prepared by de Gasperin et al. (2018) using the data from the TGSS and the NVSS surveys. It was already shown to be useful to discriminate between the thermal and nonthermal emissions from SNRs and H II regions (Dokara et al. 2018), and not just to identify extragalactic sources. Here we use this spectral index catalog to derive an 'expected' flux density of the sources at 400 MHz (band-3) and 650 MHz (band-4). We compare these values with the integrated flux densities from the Gaussian fits to band-3 and band-4 sources, and the results are shown in the middle and right panels of Fig. 2.9.

Although there appears to be a general agreement of our measurements with the derived estimations, the number of bright sources with observed flux densities lower than the expected flux density is visibly greater than vice versa. While this may have physical reasons such as the incorrect assumptions of single power-law spectral index and non-variability, it may also point to a systematic error within one of the TGSS, NVSS, and our band-3/4 images. The NVSS flux densities are based on the scale of Baars et al. (1977), and we used the more recent Perley & Butler (2017) scale. On the other hand, the TGSS is scaled using the low frequency scale of Scaife & Heald (2012), which is based not on an absolute and independent standard, but still consistent to within 2% of the other two scales. Hurley-Walker (2017) finds systematic position-dependent amplitude offsets on the angular scale of degrees, which can reach 40% in some regions (see their Fig. 3). We note that the higher system temperature, $T_{\rm sys}$, is not a cause for concern for our observations, since they were performed with the upgraded receivers which guarantee a linear regime of operation even up to a factor of 5 change in $T_{\rm sys}$ [7].

2.3.2 Nonthermal emissions

H II regions are routinely mis-identified as SNRs in the Galactic plane due to their similar radio morphology (see §4 and Dokara et al. 2021); however, spectral index is an excellent discriminant between the two. H II regions typically have a 'flat' or 'rising' spectrum at radio

[7] www.ncra.tifr.res.in/ncra/gmrt/gmrt-users/galactic-plane

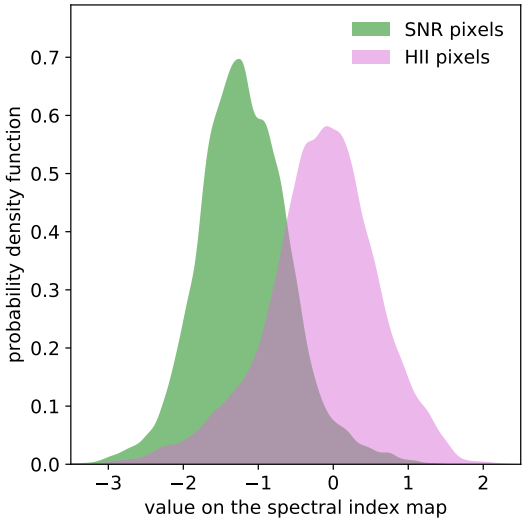

Figure 2.10: Probability density functions, obtained using kernel density estimations, of the values of spectral index pixels belonging to SNRs and H II regions.

Table 2.1: Supernova remnant flux densities (lower limits)

name	$S_{400\mathrm{MHz}}$ (Jy)	$S_{650\mathrm{MHz}}$ (Jy)
G29.6+0.1	1.6	0.5
G29.7−0.3	17.3	10.9
G31.9+0.0	39.6	24.3
G32.8−0.1	16.7	5.0
G33.2−0.6	2.4	2.3
G33.6+0.1	22.0	13.6
G34.7−0.4	217	118

frequencies ($-0.1 < \alpha \leq 2$), depending on their optical thickness (Wilson et al. 2013), while shell-type SNRs have $\alpha \lesssim 0.5$ and Crab-like (pulsar wind nebula, PWN) or composite SNRs have $\alpha \sim -0.2$ (Dubner & Giacani 2015). In Fig. 2.10, we show the probability distribution functions of the pixels on the spectral index map belonging to SNRs and H II regions. The list of H II regions is taken from the WISE catalog of H II regions (Anderson et al. 2014), and the that of the SNRs from Green's catalog (Green 2019). Despite the central frequencies of the two bands being close (400 MHz and 650 MHz) and the non-trivially overlapping *uv*-coverage of the two bands, we see the spectral index values of SNRs to be significantly lower than those of H II regions, which is what we expect to find.

Measuring the flux densities of SNRs, we find them to be consistent with the spectral index and 1 GHz flux density given in the Green's catalog. Our measurements are presented in Table 2.1. We note that these values must be treated only as lower limits, since part of the flux density is filtered out due to the lack of short-spacing data. This is especially apparent in the band-4 (650 MHz) values as a number of inner baselines were flagged due to RFI.

We searched for recently proposed SNR candidates from the THOR and GLOSTAR surveys (Anderson et al. 2017; Dokara et al. 2021) in our images, but at a 3σ-level, we cannot positively identify any of the 15 candidates that exist in this region. For the PWN-like GLOSTAR SNR candidate G031.256-0.041 and THOR SNR candidate G32.22-0.21, we are able to derive a lower limit for the spectral index using the average surface brightness: ~ -0.1 and ~ -0.5 respectively. We also searched for shell-shaped objects that may have been undetected in THOR and GLOSTAR surveys because of synchrotron ageing at higher frequencies, but we do not find any such objects. If the images were deeper, we would be able to constrain the spectral index for more candidates and possibly identify new SNR candidates as well.

2.4 Future work

We performed this pilot study as a precursor to a larger low frequency survey of the Milky Way, which we wish to undertake in the coming years. We developed automated calibration and imaging pipelines to reduce the large amount of data in an efficient manner. The primary goal was to study the feasibility of imaging extended structures with the wide-band uGMRT at a high resolution, using only snapshot observations. As is evident from Fig. 2.7, we recover extended emissions reasonably well, although the situation would be much better if the degradation in the sensitivity and the resolution due to dead antennas did not occur.

Based on the experiences from this study, for the upcoming larger survey, we make the following recommendations:

- We suggest multiple scans of each field instead of only two scans as was done for this work. The *uv*-coverage can be improved if we use four scans of 4–5 minutes spread over the observing session. This also helps in minimizing the *uv*-coverage loss in case antennas are not working during the observation.

- Since the sensitivity across the primary beam is not uniform, we recommend using a denser grid of pointings to survey the Galactic plane, as it was done in the GLOSTAR survey (Brunthaler et al. 2021). While this may increase the observation time, it will be worth to get better sensitivity.

- In targeted observations, one can afford to observe the phase calibrator only once in an hour or so, since self-calibration is almost always guaranteed to enhance the dynamic range. However, in our snapshot survey mode, self-calibration results in only a marginal improvement. Hence, it is better to observe the phase calibrator more frequently.

- In addition, if possible, having the phase calibrator outside of the complex emission from the Galactic plane may be a good choice in order to avoid problems arising due to poor gain calibration.

- While polarization data are incredibly useful to study nonthermal emissions, we realized that it is quite difficult to obtain any meaningful Stokes Q and U images from broadband snapshot observations below 1 GHz, due to de-polarization that occurs across the wide bandwidth. Also, given that a large number of sources are not situated at the center of the

pointing, it is necessary to know the angular dependence of the instrumental polarization, which is not available for uGMRT yet. However, cross polarization data are still valuable due to their role in RFI identification, and it is recommended to be recorded during the observations.

Based on these lessons, we plan to propose for a larger Galactic plane survey with the uGMRT in the near future.

Chapter 3

A global view on star formation: The GLOSTAR Galactic plane survey

I will provide an overview of the GLOSTAR survey in this chapter. The complete details of this survey can be found in Medina et al. (2019) and Brunthaler et al. (2021). The observations and the data products are discussed in §3.2 and §3.3 respectively. My contributions for this survey include producing the combination images from the interferometer and the single-dish telescopes, which is described in §3.4 and also in Dokara et al. (2023).

3.1 Introduction

While high-mass stars ($M \gtrsim 8 M_{\odot}$) are relatively rare, their effects are far-reaching in the context of the evolution of a galaxy. They ionize their surroundings to form H II regions, use up their nuclear fuel quickly, and dominate the luminosity output from the ensemble of stars in a galaxy. Through protostellar accretion and outflows before their birth, powerful stellar winds and ionizing flux during their lives, and the catastrophic supernova events in their eventual deaths, high-mass stars inject energy and momentum into their surroundings, and provide feedback to the formation of new stars. Negative feedback arises from either generating or driving turbulence which acts against the condensation of gas and thus against the formation of new stars. Positive feedback comes from the compression of surroundings which accelerates or even triggers next generation star formation. In addition, high-mass stars are formed in clusters, making their effects even more pronounced due to the presence of multiple such objects confined in a volume. H II regions and SNRs are key players in these feedback mechanisms. Due to these processes, high-mass star formation is intricately connected to the properties of a galaxy. Despite the importance, the conditions for high-mass star formation such as the necessary initial physical and chemical properties, and the accretion mechanisms, are not well constrained.

In view of this challenge, several sensitive and high-resolution Galactic plane surveys were performed to help paint an unbiased picture of high-mass star formation in the Milky Way. Two prominent surveys in the mid-infrared (MIR) wavelengths are GLIMPSE (Galactic Legacy Infrared Mid-Plane Survey Extraordinaire; Churchwell et al. 2009) and MIPSGAL (Multiband Infrared Photometer for Spitzer Galactic plane survey; Carey et al. 2009) undertaken by the *Spitzer* space telescope. Hi-GAL (*Herschel* Infrared Galactic Plane Survey; Molinari et al. 2010) and ATLASGAL (APEX Telescope Large Area Survey of the Galaxy; Schuller et al. 2009) are two such Galactic plane surveys in the far-infrared and sub-mm regimes. Emissions at all these wavelengths trace dust (either diffuse emission or high-mass clumps) and polycyclic aromatic hydrocarbons which are associated with infrared dark clouds, massive protostars, and young

Figure 3.1: An areal view of the *Jansky* Very Large Array (VLA) in its most compact D-configuration. Image credit: NRAO/AUI/NSF.

stellar objects. Similarly, in the radio regime, the 1–2 GHz H I, OH, and radio recombination line survey[1] (THOR; Beuther et al. 2016) and the 4–8 GHz global view on star formation survey[2] (GLOSTAR; Brunthaler et al. 2021) were conducted to study the Milky Way at an unprecedented detail over large areas. These wavelengths are suitable to study not just the atomic H I gas and the continuum emission, but also spectral lines such as the 6.7 GHz methanol maser and radio recombination lines, which trace high-mass star formation and thermal emission from ionized gas, respectively. The wide frequency range covered across all these surveys also helps us to construct spectral energy distributions and identify thermal and nonthermal emissions from the Galaxy. These surveys together help us understand better the various stages of high-mass star formation.

In this chapter I briefly describe the GLOSTAR survey, the observations, and the resultant data products. The data from this survey have already been used to make catalogs of radio continuum and maser sources (Medina et al. 2019; Ortiz-León et al. 2021; Nguyen et al. 2021, 2022; Dzib et al. 2023) mainly in the context of high-mass star formation. SNRs, which are the result of the deaths of high-mass stars and are connected to star formation via feedback, can also be studied. The results from these SNR studies, presented in Dokara et al. (2021) and Dokara et al. (2023), are summarized in Chapters 4 and 5, respectively.

3.2 Observations

The goal of the GLOSTAR survey is to study star formation in an unbiased manner across a large portion of the Milky Way with an excellent sensitivity, detecting radiation over a wide range of angular scales in the target frequency range of 4–8 GHz (C-band). In order to do this in a reasonable amount of time, efficient and reliable telescopes equipped with wideband

[1] https://www2.mpia-hd.mpg.de/thor/Overview.html
[2] https://glostar.mpifr-bonn.mpg.de/glostar/

Figure 3.2: The 100 m Effelsberg telescope. Image credit: Norbert Tacken.

receivers are necessary. The GLOSTAR survey uses two telescopes that are well suited for this purpose: the *Jansky* Very Large Array (VLA) interferometer (Fig. 3.1) and the 100 m Effelsberg single-dish telescope (Fig. 3.2).

3.2.1 Jansky VLA observations

The VLA is a radio interferometer array of 27 identical dishes, each with a diameter of 25 m. It is located atop an ancient lake-bed in New Mexico, United States. The upgrade from the VLA to the *Jansky* VLA started in the early 2000s in order to tackle the growing technological needs of radio astronomy. New high sensitivity receiver systems, together with the Wideband Interferometric Digital ARchitecture (WIDAR) correlator have led to a drastic performance improvement during this period. The instantaneous frequency coverage has widened, which provides excellent sensitivity in a short time. This makes the VLA an excellent telescope suited for large scale surveys.

The antennas of the VLA are arranged in a Y-shape next to rails so that the spacing between them can be modified (see Fig. 3.1). Its most compact arrangement, the D-configuration, makes it possible to observe angular scales as large as two arc minutes in the C-band. On the other hand, the more extended configurations (A, B, and C) provide much higher resolution. For the GLOSTAR survey, the VLA was employed in its B- and D-configurations, observing all the Stokes parameters in several spectral windows detecting both spectral line and continuum emission. The approximate values of the largest recoverable angular scales and the synthesized beams for these two datasets in the GLOSTAR observations are given in Table 3.1. A small

Table 3.1: GLOSTAR VLA configurations and relevant approximate angular scales

	$b_{\rm min}$ (km)	$\theta_{\rm LAS}$ (arcsec)	$b_{\rm max}$ (km)	$\theta_{\rm res}$ (arcsec)
B	0.21	15	11.1	1.5
D	0.035	120	1.03	18

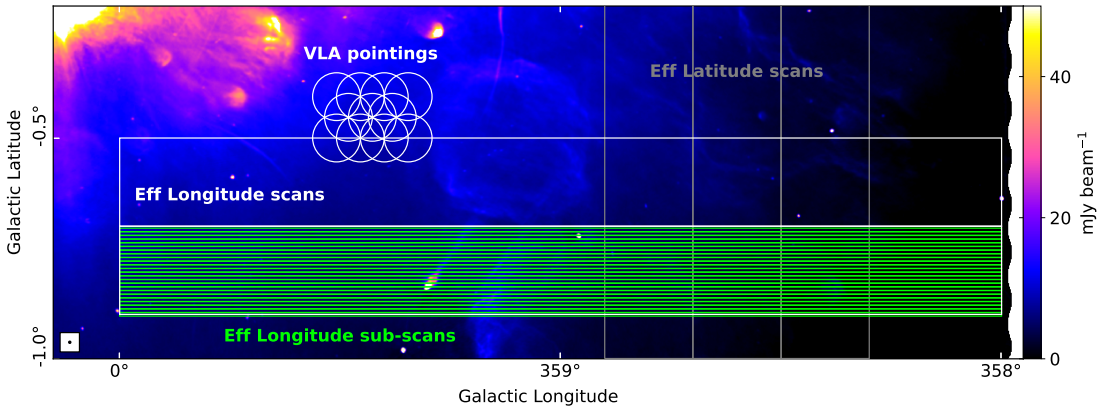

Figure 3.3: Some examples of VLA pointings with their fields of view marked by circles, and the Effelsberg scans and sub-scans marked by rectangles (longitude scans in white, latitude scans in grey, and longitude sub-scans in green). In the background is a part of the GLOSTAR VLA D-configuration + Effelsberg combination image of the Galactic center.

portion near the Galactic center region was observed with BnA and DnC configurations instead of B and D in order to have a roughly similar *uv*-coverage and thus a similar circular beam across the whole survey region.

A traditional hexagonal pointing grid was used for mosaicing. Generally, the primary beam overlap is determined by Nyquist sampling: the distance between pointing centers is fixed at $\theta_B/\sqrt{2}$, where θ_B is the size of the primary beam where its attenuation drops to half the maximum. However, the grid spacing in the GLOSTAR survey is set to $\theta_B/2$ in the high-frequency band for a larger area of overlap (see Fig. 3.3). In addition, each pointing was observed twice in order to improve the *uv*-coverage (see Fig. 3.4). Finally, the total time spent on each pointing was roughly 15 seconds. Due to the pointings being densely packed and each of them being observed twice, an excellent point source sensitivity of about 60 μJy is achieved in only a small amount of observing time.

3.2.2 Effelsberg observations

The single-dish 100 m Effelsberg telescope is used to account for the missing zero-spacings in the VLA images. The large dish size allows us to obtain good sensitivity to large scale structures in a relatively short amount of time. Two back-end systems were simultaneously employed for the GLOSTAR observations: the Spectro-polarimeter (SPECPOL) and the Fast Fourier Transform Spectrometer (FFTS). SPECPOL observes all four Stokes parameters in two

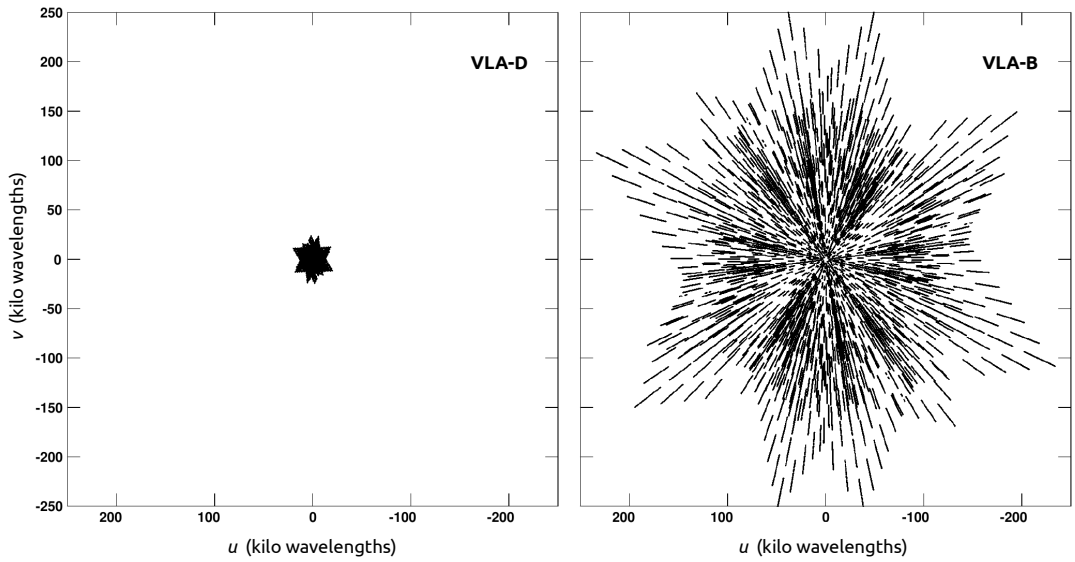

Figure 3.4: The *uv*-coverage of the GLOSTAR observations of an example field showing the contrast between the VLA in its D (*left*) and B (*right*) configurations. Image adapted from Brunthaler et al. (2021).

bands covering the frequencies 4–6 GHz and 6–8 GHz while the FFTS back-end observes in two low and two high spectral resolution bands. The regions observed were divided into cells of size $2^\circ \times 0.2^\circ$ that were observed as scans, aligning with either the Galactic longitude or latitude. The cells were further divided into smaller sub-scans of step size $30''$ for the minimum Nyquist sampling, with a scanning speed of $90''$ per second. A schematic of the observing pattern is shown in Fig. 3.3. The beam sizes of the continuum bands centered at 4.88 GHz and 6.89 GHz are $145''$ and $106''$, respectively.

3.2.3 Survey coverage

The GLOSTAR observations cover the first quadrant of the Milky Way in the Galactic longitude range $-2^\circ < l < +60^\circ$, with a two degree latitude coverage ($|b| < 1^\circ$). The Galactic center (l~0°) and the near end of the Galactic bar (l~30°) are included in this region. In addition, the Cygnus X star forming complex ($78^\circ < l < 83^\circ$ and $-1^\circ < b < +2^\circ$) is also observed. The total area covered is about 145 square degrees and a schematic is shown in Fig. 3.5.

This region is also covered by the *Spitzer* GLIMPSE and MIPSGAL surveys in addition to the ATLASGAL and the THOR surveys mentioned earlier. Overlapping coverage from multiple complementary surveys provides an invaluable tool for astronomers. Surveys detecting different parts of the electromagnetic spectrum at comparable resolutions and sensitivities can be used to infer the dominant emission mechanisms and constrain the physical and chemical conditions of a large sample of objects in the Galaxy.

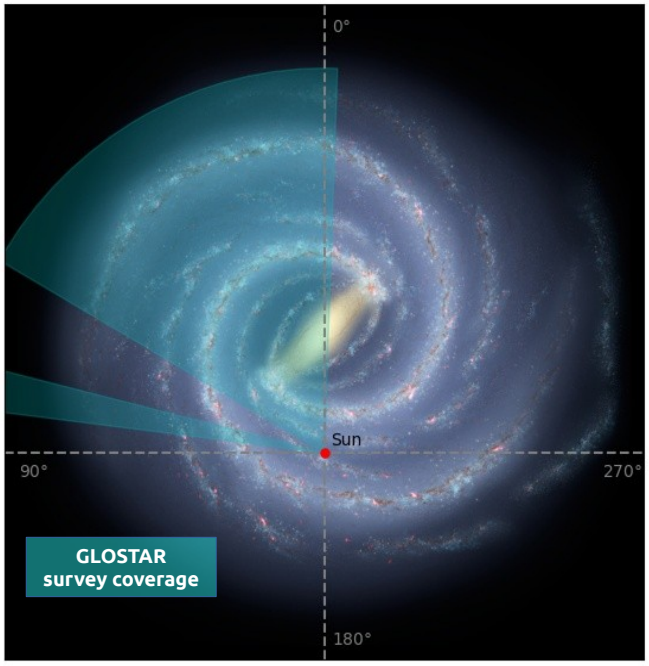

Figure 3.5: Image showing the GLOSTAR survey longitude coverage in cyan, over-plotted on an artist's conception of the top-view of the Milky Way (credit: R. Hunt).

3.3 Data products

The GLOSTAR data products relevant to this thesis are the continuum images from the 100 m Effelsberg telescope and the VLA D-configuration, which I will describe in the following sections.

3.3.1 VLA D-configuration continuum images

Calibration and imaging are carried out using the *Obit* software (Cotton 2008). A standard data reduction scheme was used similar to the procedure described in §2.2.2, with special considerations during imaging. The spectral window setup for the GLOSTAR observations is such that the 4–8 GHz band is divided into nine different sub-bands for the continuum images. Each pointing and each sub-band was imaged separately. Outlier fields, up to 0.4° angular distance from the phase center, are imaged using either the NVSS catalog or a previous imaging run. Multi-scale CLEAN was used to image angular sizes up to 100″. Self-calibration cycles were triggered for sufficiently bright fields so that the gains are better estimated. Finally, all the pointings were smoothed to a common circular beam of 18″ FWHM and a weighted average was used to produce the final mosaic.

Both circular polarizations and the cross correlations (RR, LL, RL, LR) are recorded in the GLOSTAR VLA observations so that all four Stokes parameters (I, Q, U, V) can be imaged. The typical rms noise in the final averaged image is 60–150 μJy in Stokes I (i.e., total intensity), and 50–100 μJy in the other Stokes parameters. We note that the last sub-band was

RFI-contaminated during the observations. For some operations such as feathering, it is better to drop the last sub-band instead of using it. This will be further discussed in §3.4.

3.3.2 Effelsberg continuum images

The SPECPOL backend in C-band records data in two bands. After RFI excision, the central frequencies of the two continuum bands are 4.88 GHz and 6.89 GHz. The GLOSTAR-Effelsberg continuum images are produced by the basket-weaving technique using both the latitude and the longitude scans. The NOD3 software is used for data reduction (Müller et al. 2017). A first order baseline is subtracted to remove the gain shifts along each sub-scan. Since the latitude coverage of the GLOSTAR survey is limited to $-1^\circ < b < +1^\circ$, the baseline subtraction results in a shift of the background level. This shift is corrected using data from the Urumqi 6 cm survey (Sun et al. 2007) for the 4.88 GHz band, by applying in reverse the background filtering method (also known as unsharp masking; Sofue & Reich 1979).

As the name suggests, the background filtering method was originally developed to remove the contribution from the large scale background emission. I will briefly explain the algorithm behind this method below:

1. The original image (I_0) is convolved with a Gaussian kernel (K) to get the first estimate of the background ($B_0 = I_0 \circledast K$).

2. The background B_0 is subtracted from the original image, resulting in the first estimate of the residuals ($R_0 = I_0 - B_0$).

3. The compact objects show up as the regions where the residuals are positive ($R_0 > 0$), and the background emission is at the pixels with residual values negative ($R_0 < 0$).

4. The compact objects in the original image are replaced by the values of the background to get a new image, i.e., $I_1 = I_0$ if $R_0 < 0$ and $I_1 = B_0$ if $R_0 > 0$.

5. The new image is convolved with the Gaussian kernel to get the final background estimate ($B_1 = I_1 \circledast K$).

6. Final residuals are obtained by subtracting the final background from the original image, i.e., $R_1 = I_1 - B_1$.

The above process is repeated several times by using the final residuals in step 6 as the original image for next iteration, until the background is completely removed. The zero-level restoration using the Urumqi data we intend to do on the GLOSTAR-Effelsberg data is similar to this process because the zero-level shift in the GLOSTAR-Effelsberg data is effectively a loss in the very large scale structure. The algorithm to do this is described below:

1. Apply a 'high-cut' to saturate the bright compact sources; this is done in order to reduce the contaminating effect of the bright compact sources in further convolution.

2. Convolve both Urumqi and Effelsberg images to a common resolution of 15′.

3. Perform background filtering on the difference map to estimate the missing extended emission (i.e., the large scale background) in the Effelsberg images.

4. Add the extended component to the Effelsberg images to restore the large scale structure.

While the Urumqi 6 cm survey is used for the 4.88 GHz band due to the central frequencies being close, there exists no such counterpart for the 6.89 GHz band. For this reason, the background is obtained by extrapolating the data from two different surveys: the Effelsberg 11 cm (Reich et al. 1990) and the Urumqi 6 cm surveys. Naturally, this process leads to an uncertainty in the 6.89 GHz band that is not really quantifiable. However, in order to measure the flux density of any source, the large scale background must be subtracted anyway. For this reason, in this thesis, only the 'non-restored' Effelsberg images are used for doing science.

3.4 Combining the VLA-D and the Effelsberg images

As mentioned in §1.5.2, the flux densities measured using the images made by an interferometer are only considered to be lower limits of the true emission distributions since the large scale structure is filtered out. In order to correct for this issue, the images from a single dish telescope may be added to the images from the interferometer. This can be done either by 'feathering', 'joint deconvolution', or by using the single-dish image as the starting model during the traditional deconvolution. The joint deconvolution method also performs a deconvolution like the interferometer-only imaging, but the constraints are provided by both the single-dish data and the interferometer data (e.g., Rau et al. 2019). Since these require the CLEAN algorithm, they are computationally expensive methods.

Feathering, on the other hand, is much simpler and faster, and hence more widely used. The single-dish image and the interferometer image are transformed into the Fourier domain, added according to appropriate weights such that the flux density scale is preserved on all scales (e.g., Koda et al. 2011). Since feathering works well with our images, we used this method to combine the GLOSTAR VLA D-configuration and the Effelsberg images. The algorithm we followed is explained in the next paragraph, and also in our recent paper Dokara et al. (2023).

Despite the simplicity of the feathering method, the combination is not straightforward due to the non-trivially overlapping frequency coverages of the VLA and the Effelsberg data. The VLA continuum data are in nine frequency sub-bands from 4.2 GHz to 7.5 GHz, whereas the Effelsberg continuum data are in two sub-bands centered at $f_{\rm E,lo}$ =4.88 GHz and $f_{\rm E,hi}$ =6.89 GHz. The images must be at the same frequency for the feathering process to work. With this in mind, we present the full algorithm for the Stokes I combination below:

1. The ninth sub-band of the VLA images is discarded since it is contaminated by RFI.

2. The first five and the next three sub-bands of the VLA images are separately averaged to form the 'VLA-low' and 'VLA-high' images, which we denote by $I_{\rm V,f_{V,lo}}$ and $I_{\rm V,f_{V,hi}}$ respectively. The central frequencies of these two images turn out to be $f_{\rm V,lo}$~4.7 GHz and $f_{\rm V,lo}$~6.9 GHz respectively.

3. A pixel-by-pixel spectral index ($\alpha_{\rm pix}$) is measured from the VLA images if the signal-to-noise ratio (s2n) is above three, and it is taken to be zero otherwise:

$$\alpha_{\rm pix} = \frac{\ln\left(I^{\rm pix}_{\rm V,f_{V,lo}} / I^{\rm pix}_{\rm V,f_{V,hi}}\right)}{\ln\left(f_{\rm V,hi}/f_{\rm V,lo}\right)} \quad \text{if s2n} > 3 \quad \text{and} \quad \alpha_{\rm pix} = 0 \ \text{ if s2n} < 3 \tag{3.1}$$

4. In order to bring the two VLA images to the exact frequencies of the Effelsberg images, we scale them using $\alpha_{\rm pix}$. The new VLA images at the Effelsberg frequencies are represented by $I^{\rm pix}_{\rm V,f_{E,lo}}$ and $I^{\rm pix}_{\rm V,f_{E,hi}}$:

$$I^{\rm pix}_{\rm V,f_{E,lo}} = I^{\rm pix}_{\rm V,f_{V,lo}} \left(\frac{f_{\rm E,lo}}{f_{\rm V,lo}}\right)^{\alpha_{\rm pix}} \quad \text{and} \quad I^{\rm pix}_{\rm V,f_{E,hi}} = I^{\rm pix}_{\rm V,f_{V,hi}} \left(\frac{f_{\rm E,hi}}{f_{\rm V,hi}}\right)^{\alpha_{\rm pix}} \tag{3.2}$$

5. Then, we feather the VLA and the Effelsberg maps $I_{\rm V,f_{E,lo}} + I_{\rm E,f_{E,lo}}$ to produce the low frequency combination image, and $I_{\rm V,f_{E,hi}} + I_{\rm E,f_{E,hi}}$ to produce the high frequency combination image.

6. Finally, the low and high frequency images are averaged to form the 5.85 GHz GLOSTAR combination image.

For the Stokes Q and U images, a similar procedure is followed, except that we skip the steps 3 and 4. What this means is that we do not scale the VLA images to the Effelsberg frequencies, and we feather them as is. A direct spectral index calculation is not possible since both the Stokes Q and U images have positive and negative features. We note that this method may introduce a bias in the measured polarized intensities and the polarization vectors due to the different central frequencies. However, we find that this bias is negligible, since the frequencies are quite close ($f_{\rm V,lo} \approx f_{\rm E,lo}$ and $f_{\rm V,hi} \approx f_{\rm E,hi}$). Assuming a spectral index of -0.7 for synchrotron emission, the different central frequencies of the feathered VLA and Effelsberg images of linearly polarized emission introduce an error of approximately 4%, which is close to the calibration uncertainty. For the polarization vector to change by just five degrees from $f_{\rm V,lo}$ to $f_{\rm E,lo}$, the rotation measure must be greater than about 2500 rad m^{-2}, which is unlikely to be seen in any typical Galactic source. Nonetheless, to introduce this bias in the uncertainty measurement of flux densities and also the instrumental polarization ($\lesssim$2% in both VLA and Effelsberg data), we adopt a conservative 10% error that will be added in quadrature to the usual uncertainty we obtain from the measurement of flux density of a source. In addition, we observe that the linearly polarized flux density measured in the combination images may be lower than the values measured in the VLA D-configuration only images. This can happen due to the depolarization that occurs when the polarization vectors in the small scale structure detected by the VLA are misaligned with the polarization vectors measured from the Effelsberg data. It is worth noting that, in this thesis, the exact degree of polarization is not exceptionally important except to the degree it establishes whether the source is or is not polarized, i.e., we only use it as a tool to identify nonthermal emission.

The images of the 'pilot region' ($28^\circ < l < 36^\circ$ and $|b| < 1^\circ$) of the GLOSTAR survey are shown in Fig. 3.6 as an example of the result of the combination exercise described above. The combination image shows clear improvement; it has excellent angular resolution from the VLA-D data as well as incredible sensitivity to large scale structure from the Effelsberg data.

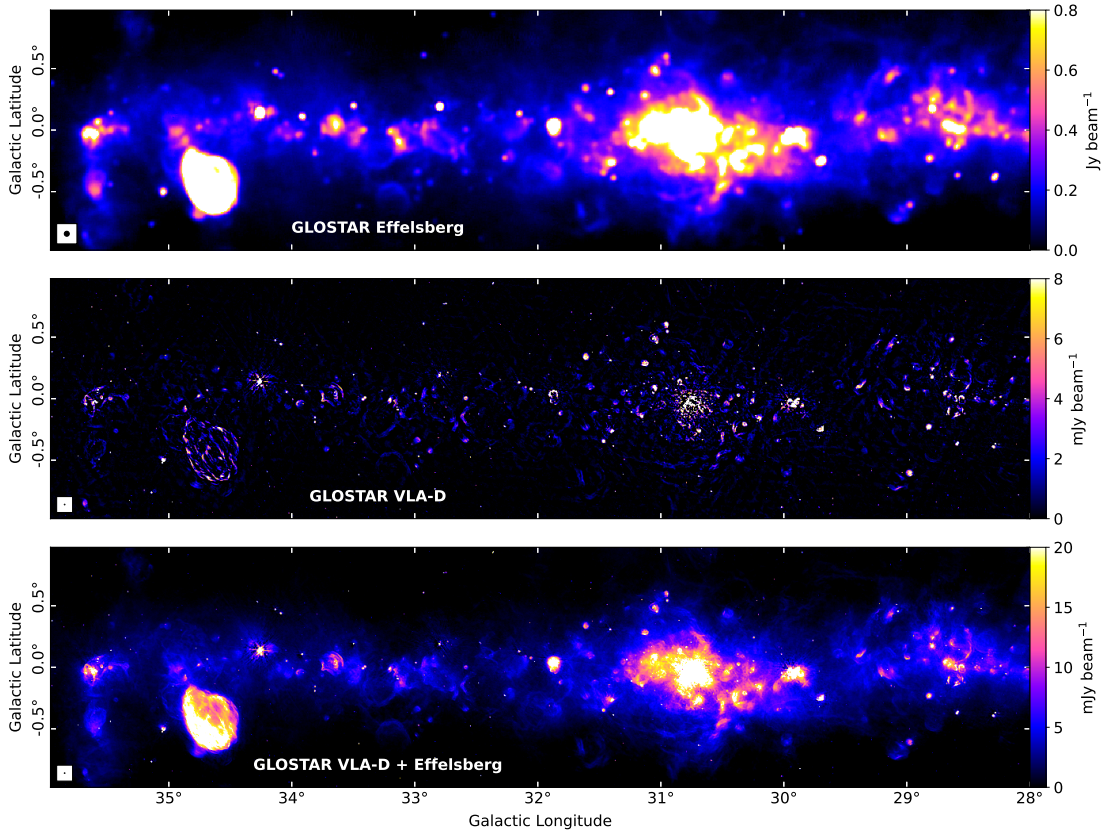

Figure 3.6: The total power images of the GLOSTAR pilot region as seen in the Effelsberg data (*top panel*), the VLA-D data (*middle panel*), and the combination (*bottom panel*). The beams are shown in the lower left corner.

Chapter 4

Identifying SNRs using the GLOSTAR VLA D-configuration images

In the context of investigating the apparent deficiency of SNRs in the Milky Way (see §1.3.6), we identified 80 new candidates from the VLA D-configuration images of the GLOSTAR survey. We also detected 77 previously identified candidates. Linear polarization is identified from nine of these candidates, confirming the presence of nonthermal emission. In addition, four objects that are thought to be SNRs are now classified as H II regions, following their detection in mid-infrared wavelengths. This work, published in the article listed below, is reproduced as Appendix C and summarized here.

Dokara et al. (2021): "**A global view on star formation: The GLOSTAR Galactic plane survey. II. Supernova remnants in the first quadrant of the Milky Way**" in Astronomy & Astrophysics, vol. 651, A86; by R. Dokara, A. Brunthaler, K. M. Menten, S. A. Dzib, W. Reich, W. Cotton, L. D. Anderson, C. -H. R. Chen, Y. Gong, S. -N. X. Medina, G. Ortiz-León, M. Rugel, J. S. Urquhart, F. Wyrowski, A. Y. Yang, H. Beuther, S. J. Billington, T. Csengeri, C. Carrasco-González, and N. Roy.

4.1 Introduction

Objects are labelled as SNR candidates when they show an indication of nonthermal emission from only one or two previous studies, and they may be "confirmed" when more concrete evidence is demonstrated. Of the numerous SNR candidates identified, only a fraction have been confirmed as SNRs so far (see Green 2019, for instance). Recent studies using radio Galactic plane surveys with interferometers have identified more than 170 candidates (Brogan et al. 2006; Helfand et al. 2006; Green et al. 2014; Anderson et al. 2017; Hurley-Walker et al. 2019a).

H II regions show strong mid-infrared (MIR) radiation emitted by warm dust grains and polycyclic aromatic hydrocarbons (Cox et al. 1986; Churchwell et al. 2009), while SNRs emit little or no radiation at MIR wavelengths. Whiteoak & Green (1996) measured the ratio of 60 μm MIR to 36 cm radio flux densities of SNRs and H II regions to be $\leq$ 50 and $\gtrsim$ 500, respectively. This distinction has been widely used as a criterion by many of the aforementioned surveys to detect new SNR candidates. In this work, we identify SNR candidates using VLA radio continuum data from the D-configuration data of the GLOSTAR survey (Brunthaler et al. 2021), and MIR images from the *Spitzer* 3.6–8 μm Galactic Legacy Infrared Mid-Plane Survey Extraordinaire (GLIMPSE; Churchwell et al. 2009) and the 24 μm & 70 μm MIPS Galactic plane survey (MIPSGAL; Carey et al. 2009). Anderson et al. (2014) report that the sensitivity of these MIR surveys is good enough to detect all the H II regions present in the Milky Way.

Two reference catalogs of SNRs and H II regions in the Galactic plane by Green (2019, hereafter G19 catalog) and Anderson et al. (2014, hereafter A14 catalog), respectively, are used in this study. The old SNR candidates are taken from the aforementioned radio surveys, and also from the internet-accessible version of the G19 SNR catalog[1]. For the new candidates, along with the already confirmed SNRs and the previously identified candidates, we have examined MIR surveys and the polarization data of the GLOSTAR-VLA data, to classify their emission as thermal or nonthermal. Although not inherently polarized, H II regions may show an apparent polarization primarily due to the prominent diffuse nonthermal background emission from the Galactic plane. We take a degree of linear polarization of 8% as the threshold to distinguish between SNRs and H II regions.

4.2 Identification of new SNR candidates

In order to identify new SNR candidates, we follow an approach that is not biased towards any particular morphology, similar to the process followed by Anderson et al. (2017). First, we searched the GLOSTAR-VLA Stokes I 5.8 GHz integrated mosaics by eye for extended emission regions that are not already identified as SNRs. We have ignored regions where the negative sidelobes are as strong as the emission. These radio emission regions are then examined in the images of the GLIMPSE 8 μm and the MIPSGAL 24 μm MIR surveys, again visually. The objects that are associated with strong MIR emission in either of the GLIMPSE 8 μm and MIPSGAL 24 μm images are removed from our list. What remains is a group of previously unclassified extended objects, which emit at radio wavelengths and have no associated MIR emission. These are the new SNR candidates. A circular region is defined for each object such that it encompasses its radio emission, and if only an arc or a partial shell is observed, then the curvature is followed. As an example, Fig. 4.1 shows the GLOSTAR-VLA and MIR images of the GLOSTAR SNR candidate G005.161−0.321. Although there is MIR emission from this region, it is confined to the H II regions G005.189−0.285 (large solid magenta circle) and G005.189−0.354 (dashed magenta circle), but absent on the shell of the SNR candidate G005.161−0.321 (encircled in white). The data on the right panel are from MIPSGAL 24 μm (red) and GLIMPSE 8 μm (cyan). The GLOSTAR-VLA image is presented in the left panel with the synthesized beam shown in black at the bottom left corner.

4.3 Results

4.3.1 G19 catalog

In the GLOSTAR survey region, we identify 91 out of 94 objects in the G19 catalog. Studying the GLOSTAR-VLA images, we find that four G19 SNRs are actually H II regions: G8.3−0.0, G10.5−0.0, G11.1−1.0, and G14.3+0.1. They have coincident MIR emission (Fig. 4.2) and are present in the A14 catalog. They were also noted as H II regions by earlier studies (Lockman 1989; Lockman et al. 1996; Gao et al. 2019). We detect no significant polarization from these objects, which agrees with their identifications as H II regions.

[1] http://www.mrao.cam.ac.uk/surveys/snrs/snrs.info.html

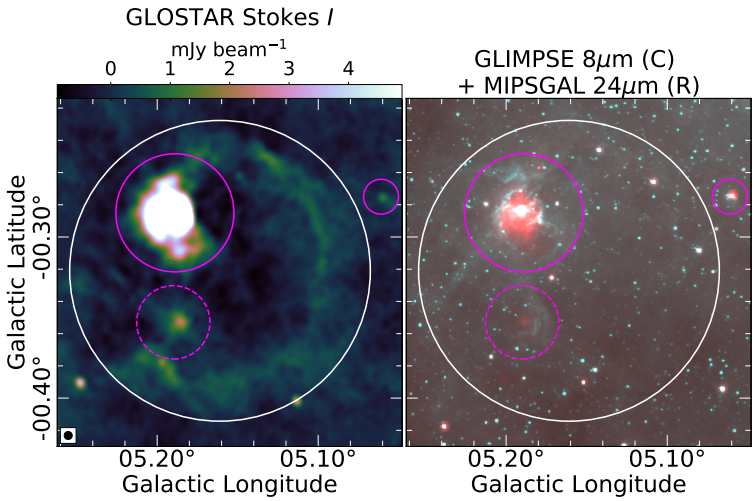

Figure 4.1: An example illustrating the criteria used to identify SNR candidates. The colors are described in the text. The SNR candidate, marked by a white circle, does not have any coincident MIR emission from its shell.

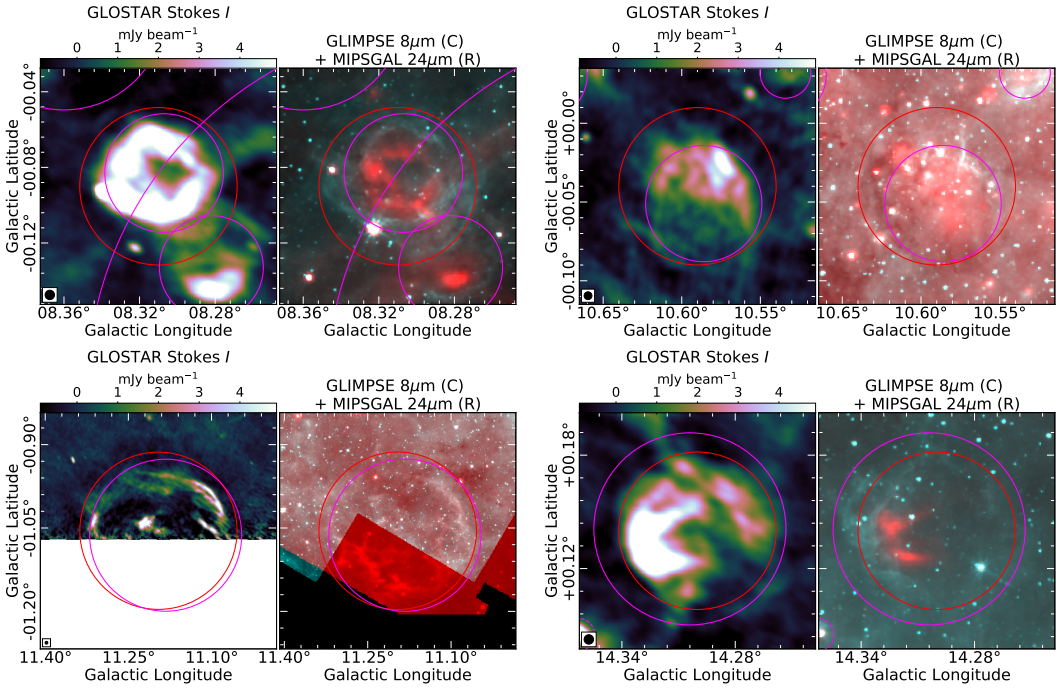

Figure 4.2: Objects in both G19 SNR and A14 H II region catalogs: G8.3−0.0 (top left), G10.5−0.0 (top right), G11.1−1.0 (bottom left, partially covered) and G14.3+0.1 (bottom right). The left panels are the GLOSTAR-VLA images and the right panels are MIR data: MIPSGAL 24 μm (red) and GLIMPSE 8 μm (cyan). The red and magenta circles are the objects present in the G19 and the A14 catalogs, respectively.

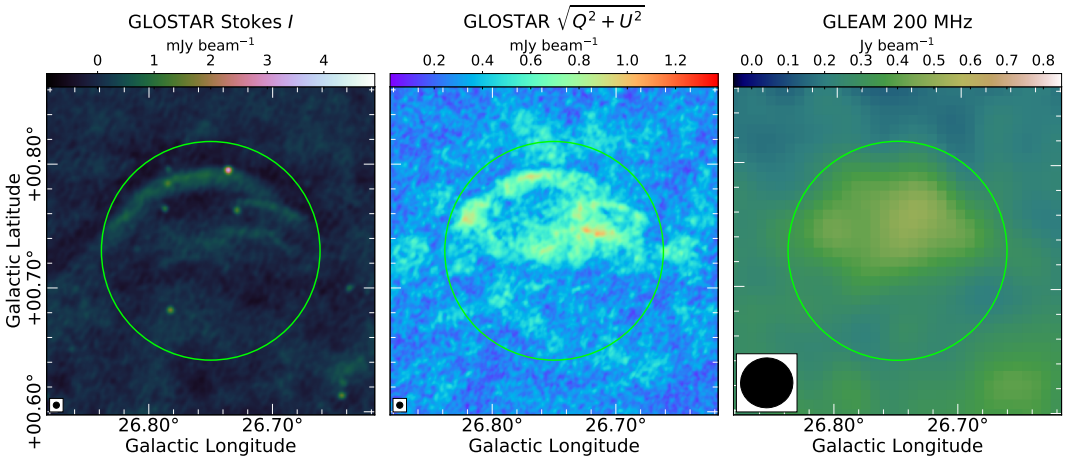

Figure 4.3: G26.75+0.73, encircled in green, as seen in the GLOSTAR-VLA data (left and middle panels) and the GLEAM 200 MHz data (right panel).

4.3.2 New SNR candidates

We identify 80 new candidate SNRs. Counterparts of 50 of these objects are visually identified in either of the 20 cm (1400 MHz) THOR+VGPS, the 20/90 cm (1400/325 MHz) MAGPIS, or the 150 cm (200 MHz) GLEAM data. As SNRs are brighter at lower frequencies, the detection of the SNR candidates in these lower frequency surveys can be used as an assessment of our confidence level in these new candidates. In addition, we also identify 77 SNR candidates in the GLOSTAR-VLA data that were discovered in earlier studies. The positions and images of these candidates, their sizes, and their flux densities can be found in Dokara et al. (2021). Three new candidates (G005.989+0.019, G034.524−0.761, and G039.539+0.366) and six old candidates (G26.75+0.73, G27.06+0.04, G28.78−0.44, G29.38+0.10, G51.04+0.07, and G51.26+0.11) also have been detected in linear polarization, providing further evidence of nonthermal emission. An example detection of linear polarization is shown in Fig. 4.3.

In Fig. 4.4, we present the cumulative distribution functions (CDFs) of the 5.8 GHz surface brightness (defined as the ratio of flux density to the area subtended), the GLOSTAR-VLA flux densities, and the radii of the three samples of G19 SNRs, the previously identified SNR candidates detected in the GLOSTAR-VLA data, and the newly discovered GLOSTAR-VLA SNR candidates. The CDFs show that the new SNR candidates discovered in the GLOSTAR-VLA data are in general smaller and fainter than in the other two samples; this is expected because of the survey's better surface brightness sensitivity and better resolution than many previous large-scale studies.

4.4 Conclusions

The GLOSTAR-VLA data highlight the importance of resolution and sensitivity in large-scale surveys: we were able to detect almost all radio SNRs in the survey due to the remarkable sensitivity, and the higher resolution made it possible to identify new ones and also reclassify

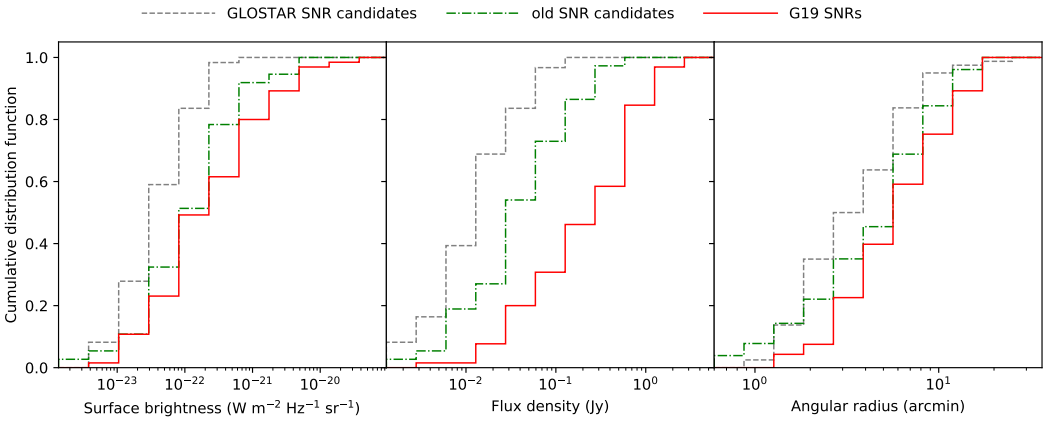

Figure 4.4: Cumulative distribution functions of average 5.8 GHz surface brightness (left), flux density (middle), and angular radius (right) of G19 SNRs (red), the SNR candidates discovered in earlier studies (green), and the new SNR candidates identified in the GLOSTAR-VLA survey (gray). The average surface brightness is obtained by dividing the flux density by the angular area subtended by the object. All the properties presented here have been measured in the GLOSTAR-VLA data.

several objects. Four objects in the G19 catalog are shown to be not SNRs. A total of 157 SNR candidates are identified, with 80 of them being new. Six candidates have strong evidence of nonthermal emission due to their clearly polarized emission and detection in multiple surveys. Comparing our results with the predictions by Li et al. (1991), we find that over 50% of SNRs in our survey region are yet to be discovered.

The addition of single-dish data to the GLOSTAR-VLA images, which I will discuss in the next chapter of my thesis, will make reliable spectral index measurements possible for extended objects. This will prove useful in confirming the SNR candidates. If all the detected candidates were confirmed as SNRs, it would nearly triple the number of SNRs in the first quadrant of the Galaxy, bringing us closer to the predicted number of SNRs in the Milky Way (~1000; Li et al. 1991). Further deeper large-scale surveys covering the entire Galactic plane should be able to rectify the apparent deficiency of SNRs in the Galaxy.

Chapter 5

Studies on SNRs using the GLOSTAR combination images

Following the identification of over 150 candidates in the VLA D-configuration images of the GLOSTAR survey (see Chapter 4), we turn our attention to the GLOSTAR combination data, using which the measurement of spectral indices of SNR candidates must be possible. This work, published in the accepted article listed below, is reproduced as Appendix D and summarized here.

Dokara et al. (2023): "**A global view on star formation: The GLOSTAR Galactic plane survey. VII. Supernova remnants in the Galactic longitude range $28° < l < 36°$**" in Astronomy & Astrophysics, vol. 671, A145; by R. Dokara, Y. Gong, W. Reich, M. R. Rugel, A. Brunthaler, K. M. Menten, W. D. Cotton, S. A. Dzib, S. Khan, S. -N. X. Medina, H. Nguyen, G. N. Ortiz-León, J. Urquhart, F. Wyrowski, A. Y. Yang, L. D. Anderson, H. Beuther, T. Csengeri, P. Müller, J. Ott, J. D. Pandian, and N. Roy.

5.1 Introduction

The presence of nonthermal synchrotron radio emission is vital to determine whether an object is truly an SNR. Most of the SNR candidates discovered recently (e.g. Anderson et al. 2017; Dokara et al. 2021) are yet to be confirmed. In addition, some objects in the Galactic SNR catalogs either do not have good radio measurements (such as G32.1−0.9 and G32.4+0.1), or, worse, the evidence that they emit synchrotron radiation is rather weak (e.g., G31.5−0.6; Mavromatakis et al. 2001). Here, we focus on confirming the status of SNR candidates and the sample of objects that were catalogued as SNRs in the region of the Galactic longitude range $28° < l < 36°$ and $|b| < 1°$ (hereafter called 'the pilot region') by measuring linearly polarized flux densities (LPFD) and spectral indices.

The pilot region contains numerous extended and compact sources overlapping with a strong Galactic background (see Fig. 5.1). The W43 "mini-starburst" complex located at l∼30° (where the bar of the Milky Way touches the Scutum-Centaurus spiral arm, e.g., Zhang et al. 2014) and the W44 supernova remnant at l∼35° are among the brightest objects observed in this region. In our previous work (Chapter 4), we detected over 150 SNR candidates in the D-configuration VLA images of the full survey, with the pilot region containing 35 of them. We use only the D-configuration VLA and the Effelsberg continuum images in this work. The Effelsberg images are used without zero-level restoration (see §3.3.2) since we need to subtract the large scale background anyway.

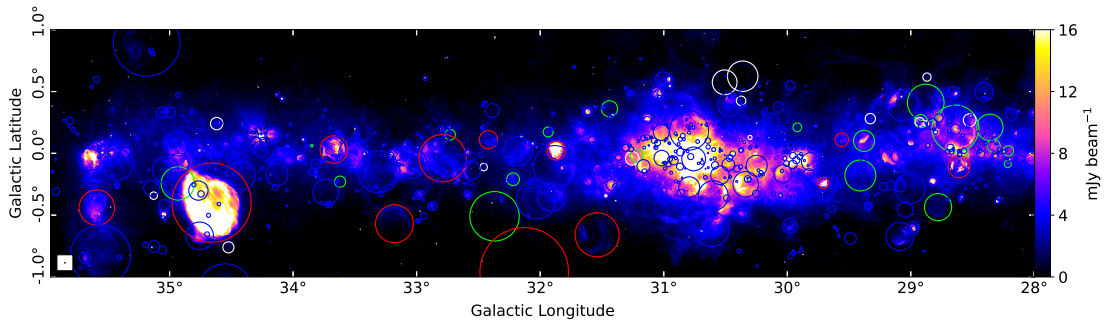

Figure 5.1: GLOSTAR combination (VLA-D+Effelsberg; Brunthaler et al. 2021) image of the region of interest of this study. The red, green, and white circles mark the G19 SNRs (Ferrand & Safi-Harb 2012; Green 2019), the THOR SNR candidates (from Anderson et al. 2017), and the GLOSTAR SNR candidates (from Dokara et al. 2021), respectively. The much more numerous H II regions, from the WISE catalog (Anderson et al. 2014) and the GLOSTAR (Medina et al. 2019), are marked using blue circles.

5.2 Methods

In order to estimate the spectral index, we do not measure the flux densities from the individual GLOSTAR images made from the covered sub-bands to derive an 'in-band' spectral index, since each of those images depends upon—though only partly—the pixel-by-pixel spectral index from the VLA data, which suffer from the problem of the undetected large scale flux density (see §3.4). Instead, we measure the flux densities using data at other frequencies to derive a broadband spectral index. The following data are used in addition to the GLOSTAR combination images at 5.85 GHz:

- The 1.4 GHz THOR survey (Beuther et al. 2016) combined with the VLA Galactic Plane Survey (VGPS; Stil et al. 2006), which is called the THOR+VGPS[1].
- The 200 MHz images from the GaLactic and Extragalactic All-sky Murchison Widefield Array survey (GLEAM; Hurley-Walker et al. 2019c)[2].
- The Effelsberg 11 cm (~2.7 GHz) survey of the Galactic plane by Reich et al. (1984)[3].
- The 3 cm (10 GHz) survey of the Galactic plane with the Nobeyama telescope by Handa et al. (1987)[4].

5.2.1 Background subtraction

The presence of background emission may bias the value of the measured spectral index. This is particularly true for extended objects in the Galactic plane since the nonthermal Galactic background emission is strong and ubiquitous at low radio frequencies. In addition, the intensity of

[1] https://www2.mpia-hd.mpg.de/thor/Data_%26_Publications.html
[2] http://gleam-vo.icrar.org/gleam_postage/q/form
[3] https://www3.mpifr-bonn.mpg.de/survey.html
[4] http://milkyway.sci.kagoshima-u.ac.jp/~handa/

this background is dependent on frequency and position (e.g., Paladini et al. 2005). The method of 'unsharp masking' (Sofue & Reich 1979) is generally used to filter out the large scale Galactic emission, but it is not appropriate for smaller scale background emission across an object with the size of a few arc minutes. In this work, we fit a 'twisted plane' that removes the background contribution up to a first order variation. Points are chosen around an object such that they represent the background emission in that area, and a two-dimensional least-squares linear fit is performed to the pixel intensities to measure the background variation. The uncertainty from this background subtraction operation is determined by choosing multiple sets of vertices. We subtract the local background in both the total intensity and the polarized intensity images, and we mask pixels typically below a 3σ-level, where the noise is determined locally by a sigma-clipping algorithm. These tasks, in addition to the TT-plots described below, are available as python functions in the openly available `astromulti` package[5].

5.2.2 TT-plots

The spectral indices determined using flux densities are sensitive to the presence of background emission. Turtle et al. (1962) introduced the concept of temperature-temperature (TT) plots, in which a spectral index is extracted from the slope of a straight line fit to the pixel intensities at one frequency against the pixel intensities at another frequency. In essence, we integrate over the whole area to measure the flux density spectral index ($\alpha_{\rm FD}$), whereas the TT-plot spectral index ($\alpha_{\rm TT}$) is calculated by measuring the variation of each pixel at different frequencies.

The intensities on TT-plots can be represented by brightness temperatures in Kelvin, or pixel intensities in Jy beam^{-1}. In this work, we exclusively use pixel intensities, and the spectral index is calculated using:

$$\alpha_{\rm TT} = \frac{\log(m_{\rm S})}{\log(\nu_1/\nu_2)} \tag{5.1}$$

where $m_{\rm S}$ is the slope of the line that is fit to pixel intensities. This is a more reliable measurement of spectral index of an extended object because the flux density bias introduced by a constant large scale background emission moves all the points equally, and hence does not affect the slope of the fit. Since the combination images are produced using the spectral index derived from the D-configuration GLOSTAR-VLA images, they are not suitable to measure the TT-plot spectral index ($\alpha_{\rm TT}$). We only use the GLOSTAR-Effelsberg images for this purpose. We also measure the flux density spectral index ($\alpha_{\rm FD}$); this serves as a useful consistency check since we subtract the background regardless, as described in §5.2.1.

5.3 Results

5.3.1 G19 SNR G31.5-0.6

In Fig. 5.2, we show the GLOSTAR combination Stokes I image of the G19 SNR G31.5−0.6 along with its flux density spectrum. We find no significant linear polarization in agreement with the observations of Fürst et al. (1987), who suggest that this is an SNR–H II region complex. The

[5] https://pypi.org/project/astromulti/

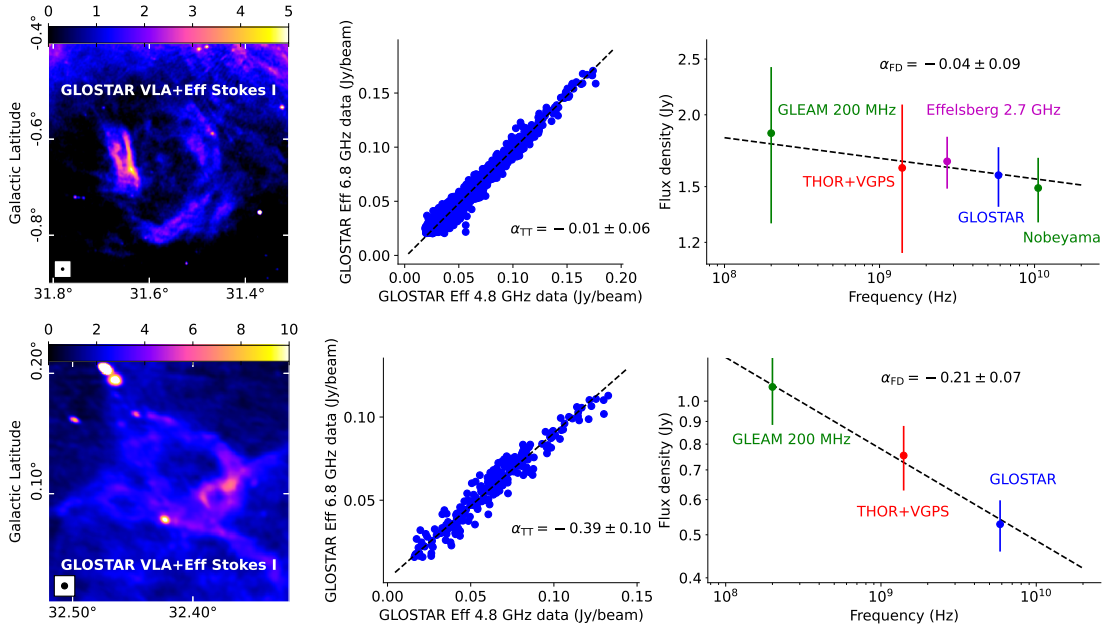

Figure 5.2: G31.5-0.6 (*top*) and G32.4+0.1 (*bottom*). Left panels show the GLOSTAR combination images. The TT-plot from GLOSTAR-Effelsberg images, and the flux density spectrum using the GLOSTAR combination images and ancillary data are presented in the middle and right panels respectively.

Stokes *I* flux densities we measure are consistent with those given by Fürst et al. (1987) within uncertainties, and we also find a morphology similar to their image. However, the spectral index we derive from 200 MHz to 10 GHz is essentially zero, which is consistent with our TT-plot result (Fig. 5.2), but in slight tension with the value of ~ -0.2 given by Fürst et al. (1987). Even after separating the region containing the thermal emission that they reported, we find no evidence for synchrotron emission. In the 24 μm images of MIPSGAL (Carey et al. 2009), we find weak emission following the radio morphology, hinting that the emission may be thermal. Based on sulfur and Hα optical lines, Mavromatakis et al. (2001) also suggest that this may be an H II region instead of an SNR. High resolution deeper observations at lower frequencies will shed more light on the nature of the emission from this object, but the evidence so far suggests that G31.5−0.6 is not an SNR.

5.3.2 G19 SNR G32.4+0.1

G32.4+0.1 was discovered in the X-ray regime by Yamaguchi et al. (2004), who also noted a possible counterpart in the images of the 1.4 GHz NRAO VLA Sky Survey (Condon et al. 1998). The radio emission from this SNR is faint, but clearly visible in the GLEAM, the THOR+VGPS and the GLOSTAR combination images, allowing us to measure, for the first time for this SNR, a spectral index of -0.21 ± 0.07 (from flux densities) to -0.39 ± 0.10 (from a TT-plot). The GLOSTAR combination image and the plots for spectral index determination are shown in Fig. 5.2. The low frequency emission detected in GLEAM may be self-absorbed,

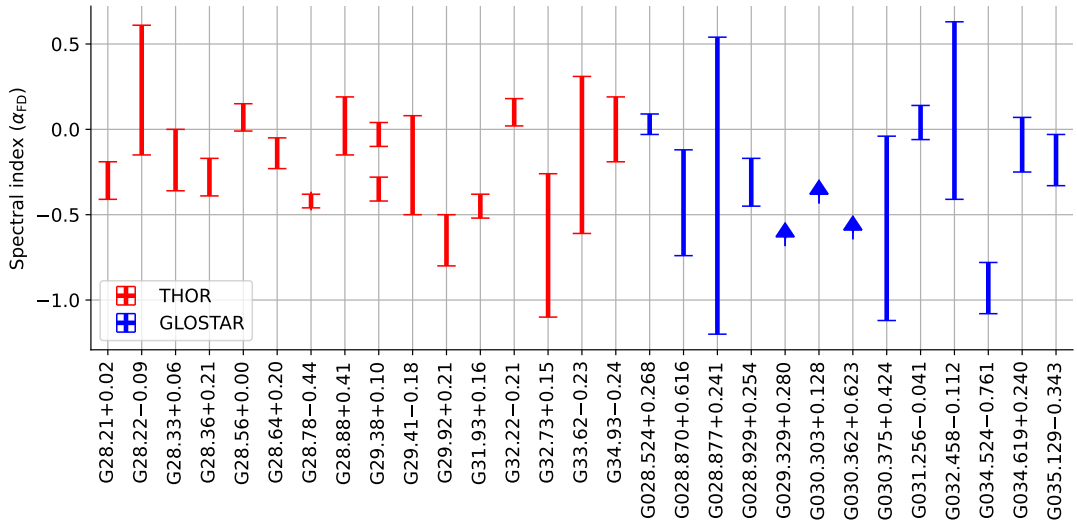

Figure 5.3: Flux density spectral indices (α_{FD}) of the candidate SNRs being studied in this work. Candidates with lower limits are represented by upward arrows. Since G29.38+0.10 has a spectral break, both the spectral indices are shown.

which brings the spectral index close to zero; hence we favor the TT-plot spectral index (~ -0.4) for higher frequencies where the effects of synchrotron self-absorption are not important. Linear polarization is undetected, with an upper limit on the linearly polarized flux density of ~0.3 Jy.

5.3.3 Candidate SNRs

In previous work, we discovered 14 new candidate SNRs in the pilot region of the GLOSTAR survey (Dokara et al. 2021), in addition to the 21 candidates discovered by Anderson et al. (2017) using THOR+VGPS images. We derived flux density spectral indices whenever possible, and these are plotted in Fig. 5.3. Five objects have good evidence of nonthermal emission from spectral index and polarization measurements (e.g., G28.78−0.44; see Fig. 5.4) and 14 other candidates possibly have a negative spectral index.

5.4 Discussion

While the combination data are very useful to study the SNRs that are already confirmed, it is however evident from Fig. 5.3 that the spectral indices of several SNR candidates are not well constrained yet. Most of them have a small angular size and a low surface brightness, and they lie in crowded regions with a strong background; these conditions result in large uncertainties in the measurement of their spectral indices. The current results on SNR candidates do not look very promising since the rate of confirmation appears to be quite low, and we are forced to ponder the strategy to identify new SNRs.

Recent SNR studies have focused on identifying small angular sized candidates; Anderson et al. (2017) suggest that this should be the strategy because most of the large and bright SNRs

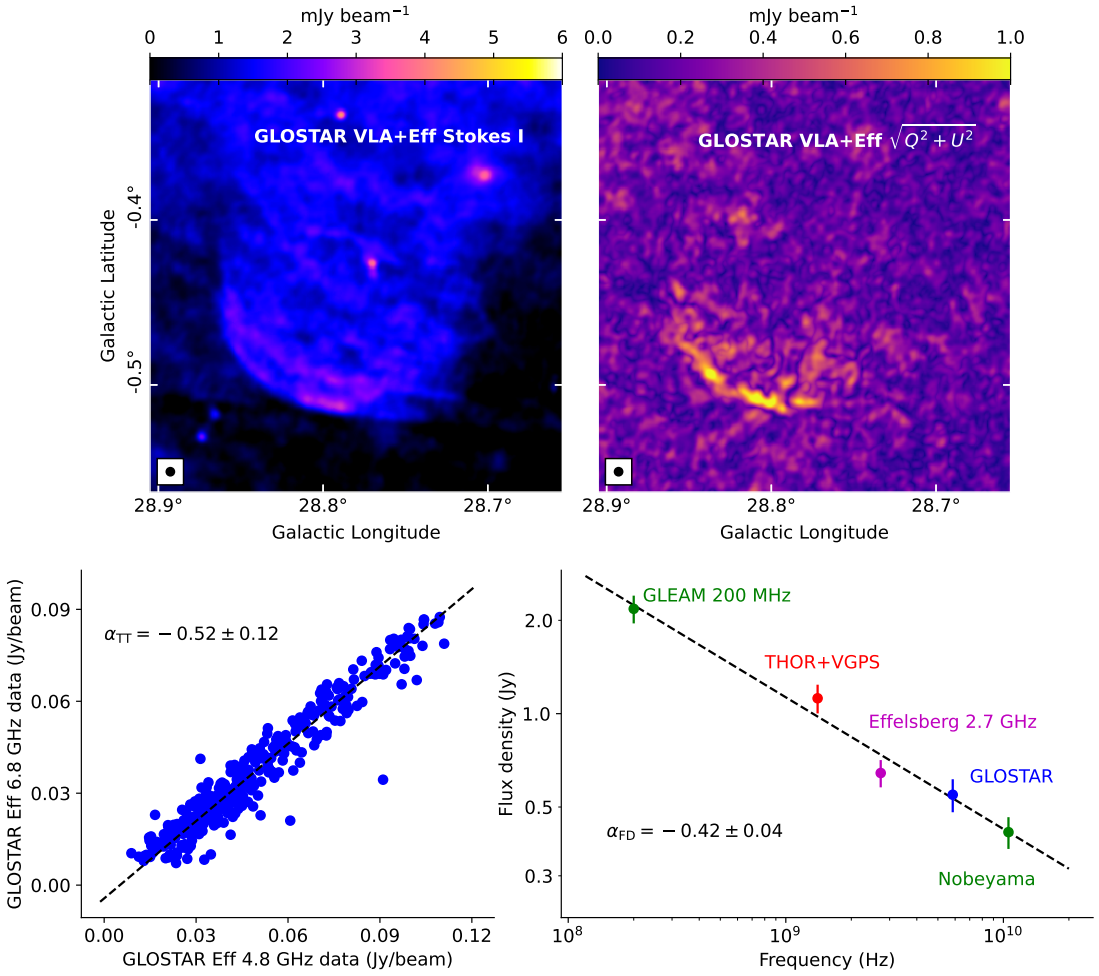

Figure 5.4: Candidate SNR G28.78-0.44: the top left and right panels show the GLOSTAR combination images of total and linearly polarized intensity. The TT-plot from GLOSTAR-Effelsberg images and the flux density spectrum are presented in the bottom left and right panels respectively.

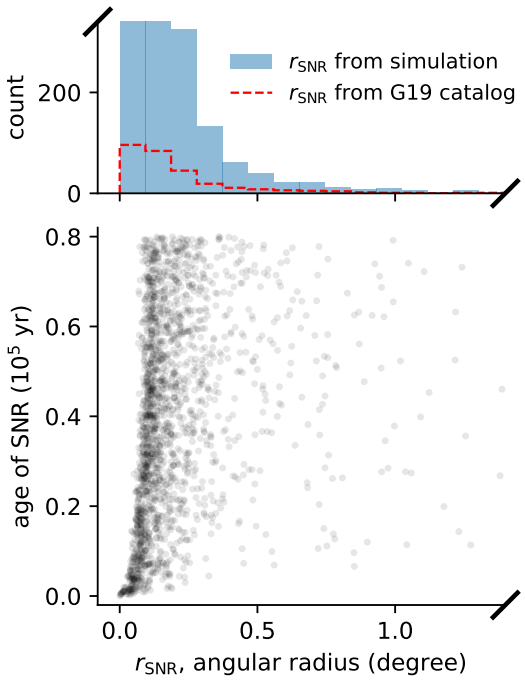

Figure 5.5: Snapshot of the age and the angular radius distribution of SNRs (as seen from the Sun) from the simulation, at a time of 1.8 million years, is shown in the bottom panel. The angular radius distribution is shown on the top panel in blue, along with the distribution of the SNRs in the catalog of Green (2019) in red dashed lines. The axes are clipped to show the distributions better.

are already discovered. To support that this is indeed the case, we made a simple Monte-Carlo simulation of SNRs in the Milky Way. SNRs are evolved in a locally uniform ISM using the expressions for radius of SNRs from Draine (2011), which are based on the four classical stages as proposed by Woltjer (1972). We used a three dimensional gas density model of the Milky Way from Misiriotis et al. (2006) and several other parameters from recent studies such as Scalzo et al. (2014) and Martinez et al. (2022).

We ran the simulation for two million years, which is several generations of SNRs. A snapshot at a time of 1.8 million years is presented in Fig. 5.5, and a movie of the whole two million years is available online[6]. It is clear that most of the SNRs are quite small with angular radii of only a few arc minutes, similar to the THOR and the GLOSTAR SNR candidates. While this simulation only serves as a first approximation since we do not consider effects such as clustering, it is nevertheless useful to give us an idea of what to expect. And the result reiterates the views of Anderson et al. (2017) that SNR searches must focus on small angular sized objects to make the most gains.

[6] https://cloud.mpifr-bonn.mpg.de/index.php/s/m3TxJESGs7tNQxo

Chapter 6

Conclusions and Outlook

SNRs, which are responsible for the creation of elements that make life possible, are in an apparent deficiency in the Milky Way. Studies have shown that at least 1000 SNRs should exist, but with only about 300 being confirmed so far, over 700 SNRs remain to be detected. H II regions are a major obstacle for confirming new SNRs because they have similar radio morphologies. Both H II regions and SNRs are consequences of high-mass star formation, and, together, they are spread over much of the volume of the Galactic plane. Their formation is controlled by the physical and chemical conditions in the nearby ISM, which are in turn affected by these objects themselves, creating a complex feedback loop.

The problem of Milky Way's missing SNRs is thought to be due to only selection effects and observational bias—the faint, the far, and the small SNRs are unlikely to be detected very easily (Brogan et al. 2006; Anderson et al. 2017). However, in conjunction with the lack of clarity on their net effects on star formation (e.g., feedback, dust creation/destruction by SNRs, cosmic ray production), this issue of missing SNRs presents itself as a glaring inconsistency between observations and the theory, and it exposes an important shortcoming in our understanding of the nearby universe.

Currently, astronomers are searching for new SNRs in several surveys and targeted observation campaigns. The world's largest filled-aperture single-dish telescope, the Five-hundred-meter Aperture Spherical Telescope (FAST) in China (e.g., Gao et al. 2022), the 100 m Effelsberg telescope (e.g., Reich et al. 2021), the VLA (e.g., Brogan et al. 2006), the low-frequency array (LOFAR; e.g., Driessen et al. 2018), and the Murchison Widefield Array (e.g., Hurley-Walker et al. 2019b) have been put to use for this purpose, among others. The focus of the work performed for this thesis is the same as the focus of the other works mentioned above—to make some progress in filling the apparent gaps in our knowledge by attempting to make the catalogs of Galactic SNRs more complete and reliable.

The long wavelength radio regime ($\lambda \gtrsim 30$ cm, $\nu \lesssim 1$ GHz), offers a unique opportunity in the study of SNRs, since SNRs are typically brighter at these wavelengths. However, the effects of ionospheric variability and RFI are also more severe, and the instantaneous bandwidth is also limited at low frequencies, making it difficult to achieve both high resolution and high sensitivity to extended emissions. In order to understand the feasibility of a large scale 300–750 MHz survey of the Milky Way with the uGMRT, a pilot study was conducted, the results of which are described in this thesis in Chapter 2. To summarize:

- Two images covering 300–500 MHz and 550–750 MHz in frequency at 25″ resolution were produced, with sensitivity about 2–5 mJy beam^{-1}.

- The target resolution (∼8″) and the target sensitivity (∼0.1 mJy beam^{-1}) could not be reached due to poor *uv*-coverage which was in turn caused by dead antennas and strong RFI.

- The *uv*-coverage, and hence the sensitivity, will be improved if multiple scans, and overall a longer integration time per pointing, are used.

- A denser grid of pointings will also be helpful to gain better sensitivity.

- Polarization properties of the uGMRT antennas are not yet well characterized, and snapshot observations are not suitable to recover any useful polarization images below 1 GHz anyway, so the personnel must focus on the total power images.

The lessons learnt during this study are being used to propose a full survey in the near future. This survey will be useful not just for SNRs, but also to study star-forming regions by detecting radio recombination lines. One can also develop a catalog of compact continuum sources, most of which are background external galaxies (Chakraborty et al. 2020), which can then be used to constrain the spectral energy distributions of a large sample of galaxies while also providing clues about the intervening ISM (e.g., Shanahan et al. 2019).

The GLOSTAR project was started to obtain a global view on star formation in the Milky Way. The VLA in its B- and D-configurations, along with the 100 m Effelsberg telescope, were employed to survey Galactic plane from 4–8 GHz, covering the regions in between the Galactic longitudes $-2^\circ < l < +60^\circ$ with a two degree latitude coverage ($|b| < 1^\circ$), and the Cygnus X star forming complex ($78^\circ < l < 83^\circ$ and $-1^\circ < b < +2^\circ$). An excellent continuum sensitivity better than 100 μJy beam^{-1} was achieved. Radio catalogs were produced for continuum sources and maser sources as well (Medina et al. 2019; Ortiz-León et al. 2021; Nguyen et al. 2021, 2022; Dzib et al. 2023), and more studies in the context of high-mass star formation are about to be published in the near future (Gong et al., in prep.). Brunthaler et al. (2021) provide an overview of the GLOSTAR survey and the initial results. I used the images from this survey to study SNRs in the Milky Way. The results, which are presented in Dokara et al. (2021) and Dokara et al. (2023), are summarized below.

- 157 SNR candidates were found in the VLA D-configuration images. 80 of these SNR candidates are new, indicating the advantages of high sensitivity and high resolution large scale surveys for detecting SNRs en masse.

- We showed that, despite the diffuse synchrotron polarized background that permeates the ISM, the polarization signal can reliably distinguish between SNRs and H II regions.

- If all of these candidates were confirmed, this would potentially increase the number of known Galactic SNRs by about 50%.

- The SNR G6.1+0.5 consists of two distinct objects, both of which appear to be SNRs.

- The candidates G27.39+0.24 and G27.47+0.25 are more likely to be filaments than SNRs.

- The addition of the single-dish 100 m Effelsberg telescope images in the "pilot region" ($28^\circ < l < 36^\circ$ and $|b| < 1^\circ$), made accurate measurements of the spectral index possible for several SNRs, though not all.
- The first radio spectral index determinations for SNRs G32.1−0.9 and G32.4+0.1 are reported now. In addition, we show that that G35.6−0.4 has a spectral break.
- We find strong evidence that the candidates G26.75+0.73, G27.06+0.04, G28.36+0.21, G28.78−0.44, G29.38+0.10, G51.04+0.07, and G51.26+0.11 are true SNRs. The SNR G29.38+0.10 is a PWN+shell complex, G51.04+0.07 shows a filled center morphology, and the rest are typical SNR shells.
- There are also several other candidates that show some evidence of synchrotron emission, such as G005.989+0.019, G18.76−0.07, G034.524−0.761, and G039.539+0.366, but their morphology is not shell-like, and hence we reserve judgment on them.
- Four H II regions are incorrectly classified as SNRs in the Galactic SNR catalogs by Green (2019) and Ferrand & Safi-Harb (2012). We found them by cross-matching with MIR surveys and the WISE catalog of H II regions (Anderson et al. 2014). They are G8.3−0.0, G10.5−0.0, G11.1−1.0, and G14.3+0.1. Spectral index measurements show that G31.5−0.6 is also likely to be an H II region.
- The rate of confirmation of SNR candidates appears to be quite low. While this is slow progress, we justify our methods and targets by performing a Monte-Carlo simulation, which shows that most of the SNRs that are yet to be detected must have angular sizes smaller than half a degree. Also considering the fact that most of the bright and large SNRs are already probably detected, the slow progress is quite expected.

The Effelsberg images for the rest of the GLOSTAR survey coverage ($-2^\circ < l < 28^\circ$ and $36^\circ < l < 60^\circ$) will also be available in the coming months, which will undoubtedly help us study many more SNRs in detail, in both total power and linear polarization.

Recently, we had proposed VLA targeted observations of about nine hours from 4–8 GHz, targeting a sample of 70 SNR candidates detected in the VLA D-configuration images by (from Dokara et al. 2021). The sample was selected based on surface brightness and a lack of previous detection of polarization signal. The integration time for each pointing in these targeted observations is about two minutes, which is an order of magnitude larger than the time spent per pointing in the GLOSTAR survey. We expect this to yield not just better images of the candidates, but also the faint polarization signal that may have been under the detection limit in the GLOSTAR survey. We chose to have the same frequency setup as the GLOSTAR survey not just because of the wide usable bandwidth, but also because of the issues we would be facing at other frequencies. For instance, the polarization at lower frequencies is dominated by the diffuse nonthermal background emission, which makes even the thermal emission of H II regions appear polarized. Beam de-polarization, which occurs when the polarization vector rotates within a resolution element of the telescope, is also more severe at lower frequencies. And SNRs are not as bright at higher frequencies, so we believe that the chosen frequency range of 4–8 GHz is ideal for quick and effective detection of polarization from SNRs.

The observations have been already carried out in 2022 July, and I expect to start analysing the data and produce the images in the near future. If the polarization signal is indeed detected, this will boost our confidence levels on the studied candidates and may eventually increase the number of SNRs. Otherwise, we must ponder whether the SNRs yet to be detected may have different physical conditions, or if the current strategy of using the radio-MIR anti-correlation property to detect small angular size SNRs is really working.

It is not just the number of SNRs that is in tension with theory. The question of the origin of the magnetic fields is still very much debated. While early predictions implied that amplification of the ambient magnetic fields in the ISM can happen when the SNR shock compresses the ISM, recent evidence suggests that this alone is unlikely to sustain the observed magnetic field strengths (e.g., Ballet 2006; Patnaude & Fesen 2007; Dubner & Giacani 2015). The physical distances to SNRs, knowledge of which is fundamentally necessary to determine various other parameters of SNRs, are notoriously difficult to measure accurately and reliably. In the early studies, the Σ–D (surface brightness to diameter) relation had been widely used, but its applicability is now dismissed by most astronomers working on SNRs (see Green 1991, for instance), since there appears to exist no real reason why such a relationship should hold. Recently, kinematic distances to several SNRs have been determined based on H I absorption spectra (e.g., Ranasinghe & Leahy 2018), which are generally reliable but come with their own caveats (Dubner & Giacani 2015). To conclude, solving the conundrum of the missing SNRs is only a first step towards achieving a complete understanding of the effects of SNRs in the local universe. Upcoming radio telescopes such as the MeerKAT and the next generation VLA (ngVLA) appear very promising in the context of not only SNRs but high-mass star formation in general.

This page is intentionally left empty.

APPENDIX A

uGMRT survey: Calibration scheme

1. *FITS to CASA Measurement Set (MS) conversion:* The data for each observing session are provided on the NAPS website[1] in a standard FITS format, which is converted to an MS using the CASA task `importgmrt`.

2. *Hanning smoothing:* In order to prevent Gibbs ringing, the task `hanningsmooth` is used to smooth the data with a Hanning window.

3. *Initial flagging:* 'Flagging' is the process of masking flawed data that cannot be recovered (generally due to poor instrument performance or RFI). The task `flagdata` is used for this purpose. We flag dead antennas, shadowed antennas, and edge channels with low amplitude gains. Then, using the `tfcrop` mode of the task `flagdata`, we perform a round of automated RFI excision. The `tfcrop` mode uses an algorithm that identifies and flags outliers in the 2D time-frequency plane based on local statistics. It can operate on uncalibrated data as it can account for the bandpass shape, and it is especially helpful in flagging short duration RFI and time-persistent narrow-band RFI.

4. *Set models:* The task `setjy` is used to set the model of the primary flux calibrator, 3C 286, based on the flux density scale of Perley & Butler (2017). The secondary calibrator, J1851+005, is initially assumed to be a point source with an amplitude 1 Jy before a CLEAN component model of the field is produced.

5. *Delay and bandpass solutions:* Phase-corrected data of the primary flux calibrator are used to derive the corrections due to instrumental delays and the bandpass shape.

6. *Apply, flag, and repeat twice:* The delay and bandpass solutions are applied to the calibrator fields and the corrected data are flagged with `tfcrop`. New solutions are then derived keeping these flags. This was done twice in order to ensure that the calibration tables are obtained only from reliable data.

7. *Prepare for gain calibration:* The final tables for delay and bandpass calibration are applied to the primary and secondary gain calibrator data. These corrected data are split to a new MS with appropriate channel-averaging. This step significantly speeds up[2] the upcoming temporal gain calibration steps.

[1] naps.ncra.tifr.res.in

[2] All GMRT data are taken in spectral line mode (typically 8192 or 16384 channels) in order to isolate the narrow-band RFI which is ubiquitous below 1 GHz at the observatory. Because of the large number of channels, applying delay and bandpass tables 'on the fly' (see https://casadocs.readthedocs.io/en/stable/notebooks/synthesis_calibration.html?highlight=fly#Solve-for-Calibration) in order to obtain temporal gain solutions takes a much longer time compared to the method we used.

8. *Gain calibration:* Using the data of the primary (3C 286) and secondary (J1851+005) calibrator fields, time-dependent solutions are derived for gain amplitude and phase variations caused by instrumental response and ionospheric effects. The gain calibration tables are applied to the secondary calibrator field, and outliers in the corrected data column are flagged using the `tfcrop` mode of the task `flagdata`. New gain solutions are obtained keeping the latest flags. The amplitude corrections to the secondary calibrator are then scaled using the gains from the primary calibrator, with the task `fluxscale`.

9. *A better gain calibration by modeling the secondary calibrator:* If the secondary calibrator has been modeled as a point source, then a correct model needs to be made by self-calibration[3]. The CLEAN components of the final self-calibrated image are used as the model of J1851+005. This step is done in order to account for the nearby extended sources in the model of the phase calibrator field. New gain solutions are obtained using this model of the phase calibrator field.

10. *Apply calibration tables:* The latest set of tables are then applied to the target fields. The time-dependent gain solutions are linearly interpolated between adjacent scans, and the data that could not be calibrated and those with low signal-to-noise ratio are flagged.

11. *Flag RFI on targets:* We perform a step of automated flagging on the target fields with the task `flagdata` in the modes `tfcrop` and `rflag`.

12. *Split target fields:* The calibrated data of target fields are split into separate MSs with the task `split` and averaged in bandwidth in order to make the imaging process faster and convenient. The data are averaged only to some extent such that no bandwidth smearing occurs (channel width must be $\lesssim$0.7 MHz in the observed frequency regime).

[3]The CLEAN parameters used for the self-calibration of the phase calibrator field are the same as those for target fields, and are discussed in the imaging section (§2.2.2.3).

Appendix B

uGMRT survey: Beam size estimation

The point spread function (PSF, dirty beam, or $B_{\rm dirty}$) of an observation depends on the interferometer array configuration and the sky position of the target being observed. The raw image (dirty image, or $I_{\rm dirty}$) made by an interferometer before the CLEAN process is the sky brightness distribution ($I_{\rm sky}$) convolved with the PSF. The final reconstructed image ($I_{\rm reconstr}$) is made by adding the residuals ($I_{\rm res}$) to the convolution of a Gaussian CLEAN beam ($B_{\rm clean}$) with the model of the sky image obtained by deconvolving the PSF from the dirty image, where the Gaussian CLEAN beam is estimated by fitting a Gaussian to the central lobe of the dirty beam. In effect, the dirty beam is replaced by the CLEAN beam.

$$\begin{aligned} I_{\rm dirty} &= I_{\rm sky} \circledast B_{\rm dirty} \\ &= I_{\rm model} \circledast B_{\rm dirty} + I_{\rm res} \\ I_{\rm reconstr} &= I_{\rm model} \circledast B_{\rm clean} + I_{\rm res} \end{aligned} \tag{B.1}$$

In CASA, all of the above is taken care of by a single task `tclean`. In the version 5.8/6.2, a major upgrade was made to the PSF fitting algorithm[1], which changes the results of the Gaussian CLEAN beam fitting. The images from the observations of May 27 during which one arm of antennas was completely flagged are drastically affected by this change. The older CASA versions before 5.8 (i.e., ≤5.7) gave the beam size for the May 27 observations as $\sim 9'' \times 8''$, whereas we obtain a size of $\sim 20'' \times 5''$ when using v5.8. The result from v5.7 is incorrect because the southern arm was completely flagged during that observation and the PSF must be highly asymmetric for snapshot observations such as ours.

To make sure that this discrepancy was not a result of improper calibration, we imaged a simulated GMRT dataset made with CASA simulations without any corrupting gains. We flagged the antennas on one arm and imaged the data with the same parameters in AIPS, CASA v5.7 and CASA v5.8. The retrieved beam sizes were similar to those obtained for the real data, and hence we confirm that the PSF fitting algorithm used in AIPS and older versions of CASA delivers incorrect results when applied to our data. All imaging of the uGMRT data used in this thesis took place in CASA v5.8 in order to ensure that the beam sizes are correctly estimated. Incorrect beam size estimation leads to unnatural flux densities of imperfectly deconvolved sources.

[1] see https://casadocs.readthedocs.io/en/v6.2.0/notebooks/introduction.html

Appendix C

Paper I: SNRs in GLOSTAR VLA D-configuration images

The pdf of Dokara et al. (2021), which is summarized in Chapter 4, is reproduced in its original form below.

A&A 651, A86 (2021)
https://doi.org/10.1051/0004-6361/202039873

Astronomy & Astrophysics

A global view on star formation: The GLOSTAR Galactic plane survey

II. Supernova remnants in the first quadrant of the Milky Way*

R. Dokara[1,**], A. Brunthaler[1], K. M. Menten[1], S. A. Dzib[1], W. Reich[1], W. D. Cotton[2,3], L. D. Anderson[4], C.-H. R. Chen[1], Y. Gong[1], S.-N. X. Medina[1], G. N. Ortiz-León[1], M. Rugel[1], J. S. Urquhart[5], F. Wyrowski[1], A. Y. Yang[1], H. Beuther[6], S. J. Billington[5], T. Csengeri[7], C. Carrasco-González[8], and N. Roy[9]

[1] Max-Planck-Institut für Radioastronomie (MPIfR), Auf dem Hügel 69, 53121 Bonn, Germany
e-mail: rdokara@mpifr-bonn.mpg.de
[2] National Radio Astronomy Observatory, 520 Edgemont Road, Charlottesville, VA 22903, USA
[3] South African Radio Astronomy Observatory, 2 Fir St, Black River Park, Observatory 7925, South Africa
[4] Department of Physics and Astronomy, West Virginia University, Morgantown, WV 26506, USA
[5] Centre for Astrophysics and Planetary Science, University of Kent, Canterbury CT2 7NH, UK
[6] Max Planck Institute for Astronomy, Königstuhl 17, 69117 Heidelberg, Germany
[7] Laboratoire d'astrophysique de Bordeaux, Univ. Bordeaux, CNRS, B18N, allée Geoffroy Saint-Hilaire, 33615 Pessac, France
[8] Instituto de Radioastronomía y Astrofísica (IRyA), Universidad Nacional Autónoma de México Morelia, 58089, Mexico
[9] Department of Physics, Indian Institute of Science, Bengaluru 560012, India

Received 6 November 2020 / Accepted 9 March 2021

ABSTRACT

Context. The properties of the population of Galactic supernova remnants (SNRs) are essential to our understanding of the dynamics of the interstellar medium (ISM) in the Milky Way. However, the completeness of the catalog of Galactic SNRs is expected to be only ∼30%, with on order 700 SNRs yet to be detected. Deep interferometric radio continuum surveys of the Galactic plane help in rectifying this apparent deficiency by identifying low surface brightness SNRs and compact SNRs that have not been detected in previous surveys. However, SNRs are routinely confused with H II regions, which can have similar radio morphologies. Radio spectral index, polarization, and emission at mid-infrared (MIR) wavelengths can help distinguish between SNRs and H II regions.
Aims. We aim to identify SNR candidates using continuum images from the *Karl G. Jansky* Very Large Array GLObal view of the STAR formation in the Milky Way (GLOSTAR) survey.
Methods. GLOSTAR is a C-band (4–8 GHz) radio wavelength survey of the Galactic plane covering $358° \leq l \leq 60°, |b| \leq 1°$. The continuum images from this survey, which resulted from observations with the most compact configuration of the array, have an angular resolution of 18″. We searched for SNRs in these images to identify known SNRs, previously identified SNR candidates, and new SNR candidates. We study these objects in MIR surveys and the GLOSTAR polarization data to classify their emission as thermal or nonthermal.
Results. We identify 157 SNR candidates, of which 80 are new. Polarization measurements provide evidence of nonthermal emission from nine of these candidates. We find that two previously identified candidates are filaments. We also detect emission from 91 of the 94 known SNRs in the survey region. Four of these are reclassified as H II regions following detection in MIR surveys.
Conclusions. The better sensitivity and resolution of the GLOSTAR data have led to the identification of 157 SNR candidates, along with the reclassification of several misidentified objects. We show that the polarization measurements can identify nonthermal emission, despite the diffuse Galactic synchrotron emission. These results underscore the importance of higher resolution and higher sensitivity radio continuum data in identifying and confirming SNRs.

Key words. ISM: supernova remnants – radio continuum: ISM – polarization – HII regions – surveys

1. Introduction

Supernova remnants (SNRs) inject energy and material into the interstellar medium (ISM) of the Galaxy; they produce and accelerate cosmic rays, drive turbulence within molecular clouds, and impact the dynamics of the ISM (Iffrig & Hennebelle 2017; Brose et al. 2020). Based on the statistics of massive stars, pulsars, supernova rates, and iron abundances, it was estimated that the Milky Way should contain ≳1000 SNRs (Li et al. 1991; Tammann et al. 1994). However, the most recent version of the catalog of Galactic SNRs (Green 2019) contains fewer than 300 objects, pointing to a large inconsistency. This is thought to be the result of observational bias that hinders the detection of low surface brightness SNRs in the one extreme, and

* Tables 2–4 are only available in electronic form at the CDS via anonymous ftp to cdsarc.u-strasbg.fr (130.79.128.5) or via http://cdsarc.u-strasbg.fr/viz-bin/cat/J/A+A/651/A86
** Member of the International Max Planck Research School (IMPRS) for Astronomy and Astrophysics at the Universities of Bonn and Cologne.

the small angular size of many SNRs in the other (Brogan et al. 2006; Anderson et al. 2017).

Radio surveys covering the Galactic plane have proved to be highly effective in the identification of SNR candidates en masse (see Dubner & Giacani 2015, for a review including a historical perspective). While single-dish telescopes have repeatedly been used to study Galactic SNRs (see Clark & Caswell 1976; Sun et al. 2011, for instance), more recent efforts using interferometer arrays have identified more than 170 candidates in data from the following projects: a 330 MHz survey conducted with the Very Large Array (VLA) by Brogan et al. (2006), the 1.4 GHz Multi-Array Galactic Plane Imaging Survey (MAGPIS; Helfand et al. 2006), the 843 MHz Molonglo Galactic Plane Survey (MGPS; Green et al. 2014), the 1–2 GHz H I, OH, Recombination line survey of the Milky Way (THOR; Anderson et al. 2017), and the 80–300 MHz GaLactic and Extragalactic All-sky Murchison Widefield Array survey (GLEAM; Hurley-Walker et al. 2019a).

Generally, objects are labeled as SNR candidates when there is an indication of nonthermal emission from only one or two studies, and they may be "confirmed" when more evidence is demonstrated. Of the SNR candidates identified so far, only a fraction have been confirmed as SNRs (see Hurley-Walker et al. 2019b).

H II regions, like SNRs, are routinely observed at radio wavelengths, and also have a morphology similar to that of SNRs in the radio continuum. This represents a major obstacle in the confirmation of more candidates as SNRs. In the earlier versions of the catalog of Galactic SNRs by Green (2019), several objects that were thought to be SNRs were subsequently reclassified as H II regions (Anderson et al. 2017; Hurley-Walker et al. 2019b; Gao et al. 2019). In addition, pulsar wind nebulae (PWNe), also referred to as plerion or Crab-like remnants, are another source of confusion. Their emission is driven by the winds from the central pulsar and they may have a spectral index[1] similar to that of H II regions (Gaensler & Slane 2006), although some exceptions are known (see Kothes et al. 2008). An extended radio object in the Galaxy may be classified as a SNR or an H II region based on whether its emission is thermal or nonthermal. H II regions emit thermal Bremsstrahlung radiation, which is unpolarized and has a spectral index of $-0.1 \lesssim \alpha \lesssim 2$ depending on the optical thickness (Wilson et al. 2013). These regions also show strong mid-infrared (MIR) radiation emitted by warm dust and polycyclic aromatic hydrocarbons (Cox et al. 1986; Churchwell et al. 2009). On the other hand, the emission from SNRs is primarily nonthermal synchrotron radiation emitted by relativistic electrons gyrating around magnetic field lines in a magneto-ionic medium. Synchrotron emission has a characteristic falling spectral index ($\alpha \lesssim -0.5$), and is generally linearly polarized (Wilson et al. 2013). PWNe may have a thermal-like spectral index ($\alpha \sim -0.1$), but their emission is nevertheless linearly polarized. SNRs are also generally quite faint or even not detected at MIR wavelengths (Fürst et al. 1987). Whiteoak & Green (1996) measured the ratio of 60 μm MIR to 36 cm radio flux densities of SNRs and H II regions to be typically $\lesssim$50 and $\gtrsim$500 respectively.

The above characteristics help to distinguish SNRs from H II regions. In particular, the presence or absence of MIR wavelength emission has been widely used as a criterion by many of the aforementioned surveys. In this paper, we identify SNR candidates using radio continuum data from the D-array data of the GLObal view of STAR formation in the Milky Way survey that we conducted with the *Karl G. Jansky* VLA (GLOSTAR-VLA, Brunthaler et al. 2021; Medina et al. 2019). For these objects, along with already confirmed SNRs and previously identified candidates, we have examined MIR surveys and the polarization data of GLOSTAR-VLA in order to classify their emission as thermal or nonthermal.

This paper has the following structure: in Sect. 2, we discuss the GLOSTAR-VLA radio and the GLIMPSE and MIPSGAL MIR surveys, as well as the catalogs of H II regions and known and candidate SNRs. In Sect. 3, we describe the method we use to identify new SNR candidates and the process of measuring the linearly polarized and total flux densities of extended objects. In Sect. 4, we present the results, consider their implications, and discuss several individual objects. Section 5 summarizes our work and concludes with remarks on future efforts.

2. Data

2.1. GLOSTAR survey

The GLOSTAR survey, with a 4–8 GHz frequency band, covers the Galactic center region and the first quadrant of the Galactic plane up to a Galactic longitude of $l = 60°$ in a $\pm 1°$ wide band in latitude, b. In addition, the Cygnus X region was covered, but is not considered in the present study. It was performed with the Jansky VLA in the compact D-configuration, and in the more extended B-configuration with the wideband receivers observing in full polarization in a mixed setup of continuum and spectral lines. For this paper, we used only the D-array continuum data covering the region $358° \leq l \leq 60°, |b| \leq 1°$. Calibration and imaging of the continuum data are done using standard VLA procedures and calibrators. Details of the data reduction of a part of the survey ($28° \leq l \leq 36°, |b| \leq 1°$) are described by Medina et al. (2019) and a full presentation will be given by Brunthaler et al. (2021) and Medina et al. (in prep.).

The products of the continuum data-reduction process are mosaic FITS cubes of Stokes I, Q, and U, with each mosaic covering about 16 square degrees. Each cube has 11 planes containing the images for nine frequency intervals across the 4–8 GHz band with sections affected by man-made radio frequency interference (RFI) discarded, an averaged image, and the in-band spectral index map computed from the nine frequency planes. The averaged image is obtained by taking a mean of each pixel across the nine planes weighted by the inverse of the square of the RMS noise. This averaged image has an effective frequency of 5.8 GHz. The images were smoothed to a common resolution of 18″ after the CLEAN process. The RMS noise of the averaged Stokes I images typically ranges from 60 to 150 μJy (Medina et al. 2019).

Although the largest scale that can be observed ($\sim\lambda/B_{\rm min}$) is about 2′, mosaicking the pointings helped recover several larger angular scale structures (see Medina et al. 2019). However, there still exists a significant fraction of undetected flux density in objects larger than 1′, especially in the higher frequency images. This "missing" flux density causes a systematic reduction of spectral index. Measuring the spectral index of an extended structure is only logical if the angular scales being probed are roughly the same at all of the frequencies employed for its determination. Within the 4–8 GHz band of GLOSTAR, the highest frequency images are only sensitive to structures smaller than ∼1.5′, and the lowest frequency images to ∼3′. There is also no added single-dish data, making the interpretation of spectral index of an extended object quite uncertain. Almost all the objects that we discuss in this paper have sizes

[1] The spectral index, α, is defined as the slope of the linear fit to the log-log plot of flux density, S_ν, versus frequency, ν: $S_\nu \propto \nu^\alpha$.

larger than 1′, and we typically recover only a fraction of the flux density of extended objects (further discussed in Sect. 4.2.1). Therefore, the GLOSTAR-VLA flux densities we report are only used as lower limits, and we measure spectral index only in two cases: (i) if the size of the object is comparable to the beam, in which case the spectral index derived would be reliable, and (ii) for deriving a lower limit of the spectral index by comparing the GLOSTAR-VLA flux density with lower frequency data that have comparatively reliable flux density estimates, such as the 1.4 GHz THOR+VGPS. In the second case, a lower limit on the spectral index close to zero is useful in identifying thermal emission and PWNe, because SNRs (other than PWNe) do not have a spectral index $\gtrsim$0.

2.2. Other surveys covering the Galactic plane

The Galactic Legacy Infrared Mid-Plane Survey Extraordinaire (GLIMPSE) is a four-band (3.6–8 μm) survey of the Galactic plane by the *Spitzer* Space Telescope covering $|l| < 65°$ and $|b| < 1°$ to 2°, with a resolution <2″ (Churchwell et al. 2009). The MIPS Galactic plane survey (MIPSGAL) is a complementary 24 μm and 70 μm survey by *Spitzer* with coverage overlapping with that of the GLIMPSE survey (Carey et al. 2009). The resolutions of the 24 μm and 70 μm bands are 6″ and 24″, respectively. Anderson et al. (2014) report that the sensitivity of these MIR surveys is good enough to detect all the H II regions present in the Milky Way.

We also studied the mosaics of recent radio surveys such as the NRAO VLA Sky Survey (NVSS; Condon et al. 1998)[2] and the TIFR GMRT Sky Survey (TGSS; Intema et al. 2017)[3]. The Galactic plane surveys MAGPIS (Helfand et al. 2006)[4] and THOR+VGPS (Beuther et al. 2016)[5] are particularly useful because they are at lower frequencies, but with surface brightness sensitivity comparable to that of the GLOSTAR-VLA data. As the 1.4 GHz MAGPIS has a resolution of ∼6″, we convolved these data to the beam size of GLOSTAR-VLA (18″) for our analysis.

2.3. Lists of objects

We search the literature for previously identified SNRs and H II regions. We find the catalogs by Green (2019) and Anderson et al. (2014) to be the most authoritative compilations of SNRs and H II regions respectively. A brief description of these catalogs, along with some recent SNR candidate lists, is given below.

2.3.1. The catalog of Galactic SNRs

The D. Green catalog of Galactic SNRs is updated every few years with additions of new SNRs and removals of misidentified objects (see Green 2019, and references therein). The most recent version contains 295 SNRs, with 94 of these being found in the region covered by the GLOSTAR survey. Hereafter, we refer to these objects as G19 SNRs.

2.3.2. WISE catalog of H II regions

Anderson et al. (2014) produced the most complete catalog of H II regions in the Milky Way using data from the Wide-Field Infrared Survey Explorer (WISE) satellite. It contains about 6000 candidate H II regions (identified using their characteristic MIR morphology) and about 2000 confirmed H II regions (with radio recombination line or Hα emission) spanning the entire Galaxy. The GLOSTAR survey region contains the positions of approximately 1000 confirmed H II regions in this catalog. We hereafter refer to these objects as A14 H II regions.

2.3.3. Previously discovered SNR candidates

We compiled a list of SNR candidates from the literature, especially focusing on large-area surveys that have a significant overlap with the GLOSTAR survey region. These are summarized below:

– Using data from the THOR survey with the VGPS data added, Anderson et al. (2017) identified 76 SNR candidates. The GLOSTAR survey region covers 74 of these candidates;

– Helfand et al. (2006) discovered 49 "high-probability" SNR candidates in the MAGPIS data, all of which are located in the GLOSTAR survey region;

– The inner Galactic plane was observed at 330 MHz using the VLA by Brogan et al. (2006) and 35 SNR candidates were discovered, all of which are covered in the GLOSTAR survey region;

– Hurley-Walker et al. (2019a) identified 27 SNR candidates using data from the GLEAM survey. The GLOSTAR survey region covers 10 of these candidates;

– An internet-accessible version[6] of the catalog of Galactic SNRs by Green (2019) discusses several candidates identified across the electromagnetic spectrum. A machine-readable list of 70 SNR candidates in the GLOSTAR survey region was provided by D. Green in a private communication.

From these previously reported SNR candidates, we removed the objects that have already been included in either the G19 SNR or the A14 H II region catalogs, and those that were noted as misidentifications, such as the candidates discussed by Anderson et al. (2017, Sect. 4.3). The GLOSTAR-VLA data were then searched by eye at the positions of the remaining objects. From this search, we identify 77 previously reported SNR candidates (presented in Table 4). The process that was followed to discover new SNR candidates is explained below in Sect. 3.1.

3. Methods

3.1. Identification of new candidate SNRs

In order to identify new SNR candidates, we follow an approach that is not biased toward any particular morphology and is similar to the process followed by Anderson et al. (2017). First, we searched the GLOSTAR-VLA Stokes *I* 5.8 GHz integrated mosaics by eye for extended emission regions that are absent from the list of previously identified objects (including previously discovered SNR candidates; see Sect. 2.3). We ignored regions where the negative side lobes are as strong as the emission. These radio emissions are then searched for in the images of GLIMPSE 8 μm and MIPSGAL 24 μm MIR surveys, again visually. At MIR wavelengths, SNRs usually emit little or no radiation. In some cases, such as SNR W49B, they may have significant MIR emission, but the MIR-to-radio flux density ratio is still low (Whiteoak & Green 1996; Pinheiro Gonçalves et al. 2011). Conversely, H II regions have strong MIR emission and

[2] https://www.cv.nrao.edu/nvss/postage.shtml
[3] https://vo.astron.nl/tgssadr/q_fits/cutout/form
[4] https://third.ucllnl.org/cgi-bin/gpscutout
[5] https://www2.mpia-hd.mpg.de/thor/Overview.html
[6] http://www.mrao.cam.ac.uk/surveys/snrs/snrs.info.html

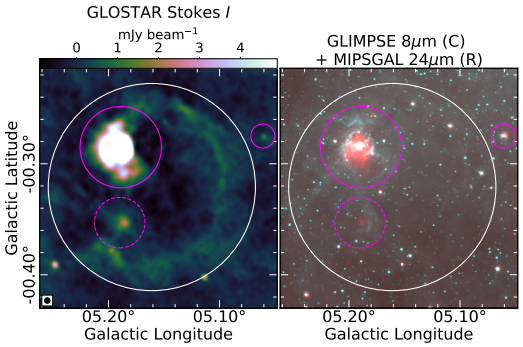

Fig. 1. Example illustrating the criteria used to identify SNR candidates. The SNR candidate G005.161−0.321 (encircled in white) has a bright confirmed H II region G005.189−0.285 (large solid magenta circle) and a faint candidate H II region G005.189−0.354 (dashed magenta circle) within its angular extent. The data in the right panel are from MIPSGAL 24 μm (red) and GLIMPSE 8 μm (cyan). The GLOSTAR-VLA image is presented in the left panel with the synthesized beam shown in black in the bottom left corner. This beam convention is followed throughout the paper. The object-marking scheme for all the figures in this paper is as follows: white circles mark newly identified SNR candidates, solid magenta circles mark confirmed H II regions, dashed magenta circles mark candidate H II regions, red circles mark G19 SNRs, and green circles mark previously identified SNR candidates described in Sect. 2.3.3.

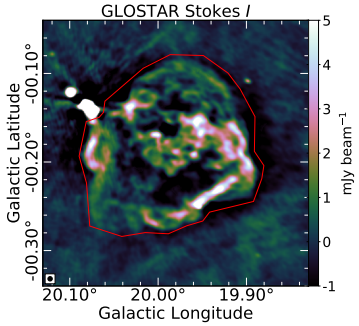

Fig. 2. Measuring the integrated flux density of SNR G20.0−0.2. The polygon used to select the region of the SNR is shown in red. As we mask values below the $3\sigma_I$ level, choosing the negative bowls around real emission does not affect our measurement. The regions with compact emission to the northeast of the SNR (near $l = 20.09$, $b = -0.13$) are A14 H II regions, and hence excluded.

generally have a characteristic radio-MIR morphology: coincident radio and 24 μm emissions, which are surrounded by 8 μm emission (see Churchwell et al. 2009, for instance). Therefore, the objects that are associated with strong MIR emission in either of the GLIMPSE 8 μm or MIPSGAL 24 μm images are removed from our list. What remains is a group of previously unclassified extended objects that emit at radio wavelengths and have no associated MIR emission. A circular region is defined for each object such that it encompasses its radio emission, and if only an arc or a partial shell is observed, then the curvature is followed. Figure 1 shows the GLOSTAR-VLA and MIR images of an example GLOSTAR SNR candidate G005.161−0.321. Although there is MIR emission from this region, it is confined to the H II regions G005.189−0.285 and G005.189−0.354, but absent from the shell of the SNR candidate G005.161−0.321.

We do not make use of the GLOSTAR-VLA source catalogs by Medina et al. (in prep.) and Medina et al. (2019) because their method is optimized to identify compact sources with high reliability. These latter authors use `SExtractor` (Bertin & Arnouts 1996) to create the background noise map, and then `BLOBCAT` (Hales et al. 2012) to perform the automated source extraction. A mesh size of 80×80 pixels^2 and a detection threshold of 5σ were used. In addition, during the visual inspection stage, these latter authors exclude the sources with low signal-to-noise ratio if no counterparts are found in MIR surveys (see Medina et al. 2019, for details). This process imparts a two-fold systematic bias against identifying SNR candidates. Firstly, the constant mesh size is not suitable for identifying extended emission as noise levels are overestimated[7], and as we aim to identify candidates that have not been detected before, we expect these objects to be quite faint and possibly be judged by the software as background noise. Secondly, as the counterparts for these sources are searched only in MIR surveys during the visual inspection, SNRs are again excluded because they typically have no MIR emission. For these reasons, we search the images visually. An assessment of our confidence level that an object is not an interferometric artefact can be made by comparing the flux density with its uncertainty, whose measurements are explained in the following section.

3.2. Measuring flux densities

Because of confusion in the crowded Galactic plane, measuring the integrated flux densities of extended objects is not straightforward. The lack of short-spacing data and the poor *uv*-coverage of snapshot observations cause strong negative side lobes near bright sources, further complicating the issue. For these reasons, we decided to manually measure the flux densities by drawing a polygon aperture around the emission that is clearly associated with the object being analyzed. An example illustrating this procedure is shown in Fig. 2.

The total flux density is measured using the integrated mosaic at an effective frequency of 5.8 GHz. In order to solve the negative side lobe problem, we masked all pixels below $3\sigma_I$, where σ_I is the background RMS in the surrounding regions determined using an iterative sigma-clipping algorithm. The integrated flux density, S, of an object and the error in this measurement, ΔS, are given by

$$S = \frac{\sum_i I_i}{A_{\rm beam}} \text{ and } \Delta S = \sigma_I \sqrt{\frac{N_{\rm src}}{A_{\rm beam}}}, \quad (1)$$

where I_i is the value of the pixel, $A_{\rm beam}$ is the area of the beam in number of pixels, $N_{\rm src}$ is the number of pixels in the aperture defined for the source, and i is the summation index that runs over the pixels with values greater than the threshold ($I > 3\sigma_I$).

We do not attempt to measure the flux densities of partially observed or severely confused objects, and of those that overlap with clear artefacts that arise from imperfect CLEANing. We note that the Stokes I flux densities are generally only lower limits due to missing short spacing data. Nevertheless, we report

[7] A mesh size of 80×80 pixels^2 ($\sim 10 \times 10$ beam^2) is too small for `SExtractor`'s sigma-clipping algorithm to converge on a robust background in a region with extended emission.

these values because they can be used to derive useful information such as the degree of polarization and spectral index limits.

We measure linearly polarized flux densities, $L = \sqrt{Q^2 + U^2}$, in each frequency plane first and then use the weighted mean and variance of these values to obtain the source integrated linearly polarized flux density and its uncertainty. This is done in order to take care of any bandwidth de-polarization effects, which may cause significant de-polarization in the ~4 GHz wide bandwidth of our survey. To include only the statistically significant pixels, we applied two masks to each plane of the Stokes Q and U mosaics: one based on the Stokes I ($> 3\sigma_I$) and the other on the Stokes Q or U ($> 3\sigma_{Q,U}$, where $\sigma_{Q,U}$ is the local RMS noise[8]). This masking also somewhat helps in the removal of low-level noise, and spurious polarization from artefacts.

Apart from artefacts due to bright, compact sources, we also observe spurious polarization in regions without Stokes I counterparts (see e.g., Sect. 4.6.3), and also from a few H II regions. This may be caused by diffuse Galactic synchrotron emission, or a foreground intervening ionized medium with a strong magnetic field generally known as a Faraday screen (see Sun et al. 2007, for instance). Unlike Stokes I, which has mostly smooth structure, Stokes Q and U have fine-scale structure that is not filtered out by the interferometer. As we limit the polarization measurement to only the pixels above a $3\sigma_I$ level in the Stokes I, the effects of differential filtering and diffuse emissions are minimized. However, we note that the degree of polarization, $p = L/S$, is an overestimate because the filtering in Stokes I is much more severe compared to Stokes Q and U due to the small-scale structure mentioned above (also see Sect. 4.1 of Gaensler et al. 2001).

There exists a bias in the measured polarization because the uncertainties in Stokes Q and U are added, which results in a positive polarization measurement even if the true polarization is null. We corrected for this polarization bias in each pixel using

$$L = \sqrt{Q^2 + U^2 - (1.2\sigma_{Q,U})^2}, \quad (2)$$

where $\sigma_{Q,U}$ is the noise in Stokes Q and U maps (Wardle & Kronberg 1974). Above $3\sigma_{Q,U}$, all bias estimators converge (see Fig. 2 of Simmons & Stewart 1985), and we masked all pixels below $3\sigma_{Q,U}$. Hence, we do not expect the choice of method of bias estimation to influence the measurement significantly.

3.3. Rotation measures and electric field vectors

When electromagnetic radiation passes through a plasma with a nonzero magnetic field along the direction of propagation, the birefringence property of the medium causes the polarization vector to rotate. This is known as the Faraday effect. The rotation of the electric vector position angle (EVPA; $\chi = 0.5 \arctan(U/Q)$) can be measured using the relation

$$\Delta\chi = \mathrm{RM} \cdot \lambda^2, \quad (3)$$

where λ is the wavelength and RM is the rotation measure. The RM is the strength of the magnetic field component parallel to the line of sight (l.o.s.), $B_\parallel$, weighted by the electron density, n_e, in the foreground medium integrated along the l.o.s.:

$$\frac{\mathrm{RM}}{\mathrm{rad\ m^{-2}}} = 0.81 \int \frac{n_e(L)}{\mathrm{cm^{-3}}} \frac{B_\parallel(L)}{\mu\mathrm{G}} \frac{\mathrm{d}L}{\mathrm{pc}}. \quad (4)$$

[8] $\sigma_{Q,U}$ generally varies from 40 to 100 μJy.

Although Faraday rotation measure synthesis is necessary to fully disentangle the contribution of different ionized sources along the l.o.s. to the RM (Brentjens & de Bruyn 2005), the reduced GLOSTAR-VLA data are not suited for such an analysis because of the large width (~1000 rad m^{-2}) of the RM transfer function (see Eq. (61) of Brentjens & de Bruyn 2005). Therefore, we estimate the RM from the slope of a simple linear fit of EVPA versus wavelength-squared, where such a fit is possible. The EVPA at $\lambda = 0$ is then estimated by extrapolating the linear fit, which is plotted on the polarization maps such as Fig. 13. This fitting and estimation of EVPAs at $\lambda = 0$ are handled by the function `RMFit.Cube` of the software *Obit* (Cotton 2008). Given an input of Stokes Q and U cubes, `RMFit.Cube` produces maps of the RM and the EVPAs at $\lambda = 0$.

4. Results

4.1. Degree of linear polarization as a measure of nonthermal emission

Synchrotron radiation, which is emitted by SNRs, is linearly polarized with a degree of linear polarization ($p = L/S$) that can be as high as 0.7 (Wilson et al. 2013), although only a few SNRs have been reported to have a degree polarization larger than 0.5 (Kothes et al. 2017). Thermal emission from H II regions on the other hand is inherently unpolarized. However, because of the diffuse Galactic synchrotron emission, H II regions may also show an apparent polarized emission. To confirm that the SNRs have higher degrees of polarization than the H II regions, we plotted the degree of linear polarization against the source integrated total flux density for the three samples of A14 H II regions, G19 SNRs, and SNR candidates (Fig. 3). The method used to measure the flux densities is discussed in Sect. 3.2.

We measure significant polarized emission from most SNRs, and also some H II regions. The polarized emission from H II regions is probably from the diffuse Galactic synchrotron emission. Some SNRs have a low degree of polarization, which is not uncommon (see Sun et al. 2011). However, the majority of SNRs have a higher degree of polarization than H II regions. As no H II region brighter than 9 mJy has $p > 0.08$, we use this as the threshold to separate SNRs from H II regions and the diffuse Galactic synchrotron emission. Confirming the candidates with a lower degree of polarization will require further observations at different wavelengths.

4.2. G19 SNRs

We identify 91 out of 94 objects in the catalog of Galactic SNRs (G19 SNRs, Green 2019) covered in the GLOSTAR survey region. The SNRs G0.0+0.0 and G0.3+0.0 near the Galactic center are in a heavily confused region, and the radio emission from the SNR G32.1−0.9 still remains undetected. The positions of these objects along with their measured flux densities are given in Table 2. Studying the GLOSTAR-VLA images, we find that four G19 SNRs are actually H II regions, and four have ambiguous radio emission. We briefly discuss these objects in Sects. 4.2.2 and 4.2.3. Below, we discuss the flux densities of G19 SNRs as measured in the GLOSTAR-VLA data.

4.2.1. Flux densities of G19 SNRs

Because of the missing short-spacing information, there is a significant amount of undetected flux density in the GLOSTAR-VLA data. The amount of flux density recovered depends on

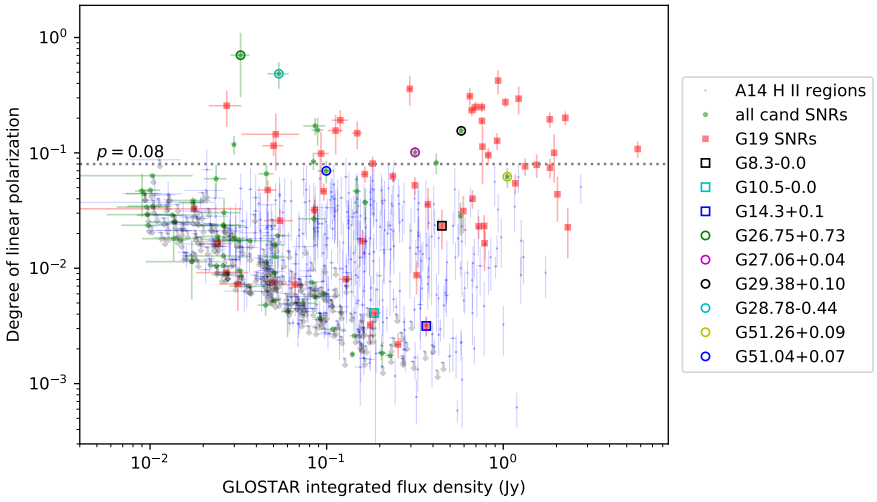

Fig. 3. Degree of linear polarization p plotted against flux density for A14 H II regions, G19 SNRs, and SNR candidates brighter than 9 mJy. Objects with upper limits on the degree of polarization are marked with gray arrows. Some SNR candidates and G19 SNRs discussed in the later sections have been marked for the sake of comparison: open squares represent the misidentified G19 SNRs (see Sect. 4.2.2), and the open circles represent SNR candidates that we confirm as true SNRs (see Sect. 4.5). The lower end of the group of points follows an approximate linear relation due to the nearly constant detection threshold of linearly polarized flux density (~300 μJy).

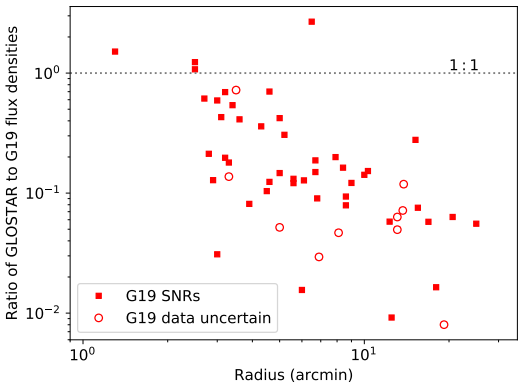

Fig. 4. Comparing the flux densities of G19 SNRs measured in the GLOSTAR-VLA 5.8 GHz data and the flux densities reported in the G19 catalog scaled from 1 GHz to 5.8 GHz. Those with uncertain flux densities or spectral indices in the G19 catalog are marked with circles.

the scale and structure of the emission, although spectral index also plays a role because of the wide bandwidth of the survey. While it is true that a single power-law model may not suffice for extrapolating over a wide range of frequencies, one can still get a rough estimation of the undetected flux density by measuring the flux densities of known extended objects. Green (2019) report a flux density and spectral index for most objects in their catalog (albeit without uncertainties in the measurements). In Fig. 4, we plot the ratio of the GLOSTAR-VLA flux density to the G19 flux density, scaled to 5.8 GHz using their individual spectral indices, against the radius of each object in the G19 catalog. The median ratio is ~0.15. As expected, most objects fall below the 1:1 line, and the amount of flux density not recovered increases with the size of the object. There are four G19 SNRs with ratios >1, with the largest ratio being ~2.7. This is probably because of uncertainties in the G19 flux density, and the fact that SNRs need not follow a single power-law model.

4.2.2. H II regions mistaken for SNRs

Four G19 SNRs, G8.3−0.0, G10.5−0.0, G11.1−1.0, and G14.3+0.1, have coincident MIR emission (Fig. 5) and are present in the A14 H II region catalog. They were also noted as H II regions in earlier studies (Lockman 1989; Lockman et al. 1996; Gao et al. 2019). We detect no significant polarization from these objects, agreeing with their identifications as H II regions.

4.2.3. G19 SNRs with ambiguous radio emission

G5.5+0.3. was identified by Brogan et al. (2006) as a class II SNR candidate (class I being very likely to be a SNR, and class III being least likely). Liszt (2009) report strong CO emission from the periphery of this SNR at $l = 5.64$, $b = 0.23$; this is probably associated with the presence of A14 H II regions G005.633+00.238 and G005.637+00.232. Stupar & Parker (2011) studied G5.5+0.3 at optical wavelengths, but could not confidently associate optical and radio emission. Green (2019) reports a spectral index of −0.7, a 1 GHz flux density of 5.5 Jy, and a size $15' \times 12'$. These values translate to an expected average surface brightness of over ~1.1 mJy beam^{-1} in the GLOSTAR-VLA data, which is well above the local noise (~0.1 mJy beam^{-1}). Emission from this region is indeed detected in the GLOSTAR-VLA data (Fig. 6), but it is part of a much larger structure (marked with a dashed cyan polygon in Fig. 6) that is ~0.6° in angular extent. We also observe no significant polarization. Considering the fact that we recover only a small fraction of the flux density (see Sects. 2.1 and 4.2.1), it

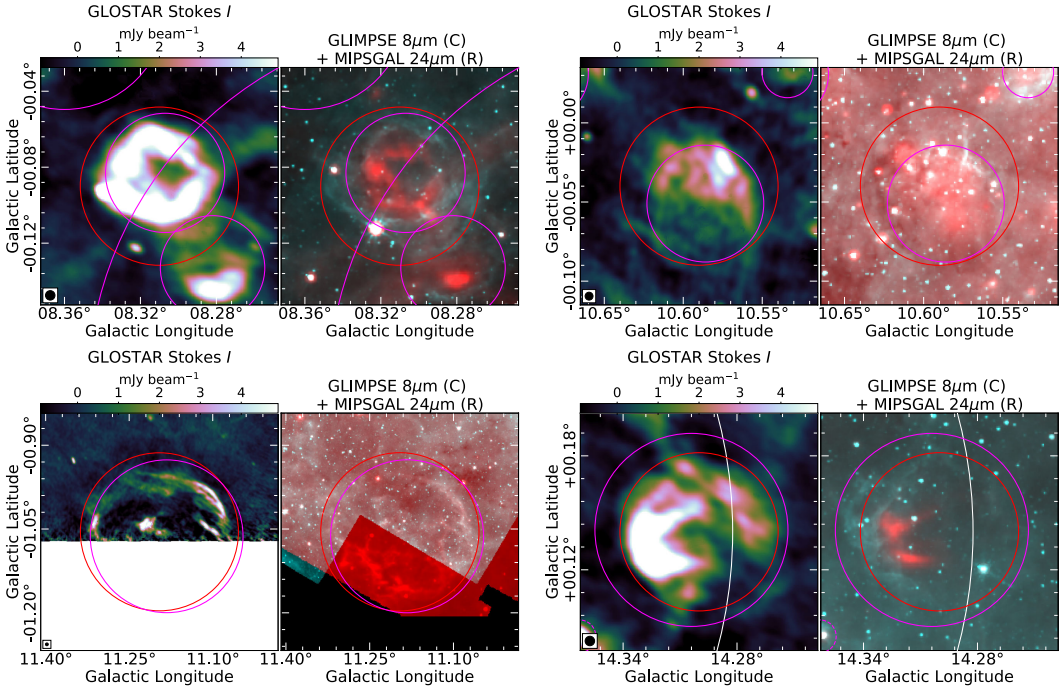

Fig. 5. Objects in both G19 SNR and A14 H II region catalogs: G8.3−0.0 (*top left*), G10.5−0.0 (*top right*), G11.1−1.0 (*bottom left*, partially covered) and G14.3+0.1 (*bottom right*). The left panels are the GLOSTAR-VLA images and the right panels are MIR data: MIPSGAL 24 µm (red) and GLIMPSE 8 µm (cyan). The marking scheme is explained in Fig. 1.

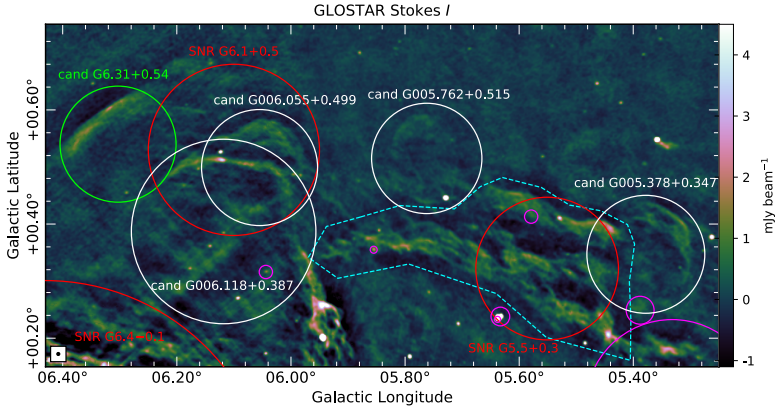

Fig. 6. Field of G19 SNRs G5.5+0.3 and G6.1+0.5. The region of G5.5+0.3 defined by Brogan et al. (2006) seems to be a part of a larger structure with no easily recognizable shape (marked with a dashed cyan polygon).

is likely that the nonthermal emission from the SNR is actually undetected.

G6.1+0.5. This appears to be a superposition of two objects in the GLOSTAR-VLA data (Fig. 6). One object centered at $l = 6.118°, b = 0.387$ has a bright arc-shaped emission on its northern edge, whereas the rest of its shell is faint. This arc-shaped emission passes through another object, centered at $l = 6.055, b = 0.499$, which has a clear shell morphology. These newly resolved shells from G6.1+0.5 are included in the list of GLOSTAR SNR candidates (see Table 3).

G14.1−0.1. The emission from this object as seen in the GLOSTAR-VLA data (Fig. 7) is dominated by the bright A14 H II region G014.207−00.110 in the northeast, and these objects lie inside the large A14 H II region G014.207−00.193. Given the flux density of 0.5 Jy, spectral index of −0.6, and a size of $6' \times 5'$ reported by Green (2019), the nonthermal emission

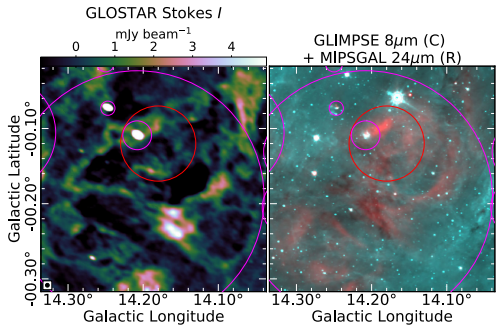

Fig. 7. Environment of G19 SNR G14.1−0.1 (encircled in red). *The left panel* shows the GLOSTAR-VLA data and the *right panel* shows MIPSGAL 24 μm data in cyan and GLIMPSE 8 μm in red. The supposed shell of G14.1−0.1 is not clearly detected in the GLOSTAR-VLA data.

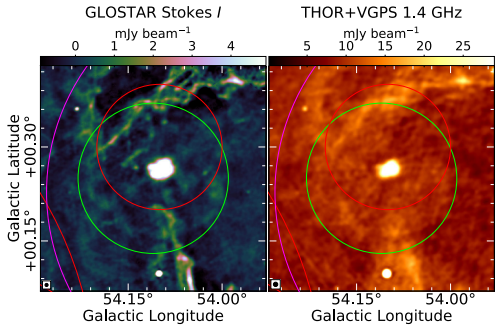

Fig. 8. Supposed shell of G54.1+0.3 encircled in red, and THOR SNR candidate G54.11+0.25 encircled in green.

from G14.1−0.1 should have an average surface brightness of ∼0.75 mJy beam^{-1} in the GLOSTAR-VLA data. However, we cannot positively identify an object distinct from the surrounding emission. In addition, the northern part of G14.1−0.1 is detected in MIPSGAL. These facts indicate that the emission we observe in the GLOSTAR-VLA data may just be from the large H II region G014.207−00.193, and not the SNR G14.1−0.1. Similar to G5.5+0.3, the nonthermal emission from this SNR is also probably undetected.

G54.1+0.3. The pulsar wind nebula (PWN) G54.1+0.3 is identified as a bright source in the GLOSTAR-VLA data, with a faint shell surrounding this emission (Fig. 8). Lang et al. (2010) and Anderson et al. (2017) also identify a shell with similar morphology, but it is not yet known if it is associated with the PWN. Anderson et al. (2017) included this shell in the list of THOR SNR candidates, named G54.11+0.25. Distance measurements to the PWN have yielded inconsistent results (Ranasinghe & Leahy 2018; Kim et al. 2013; Lee et al. 2012), and a multiwavelength study by Driessen et al. (2018) suggests that the shell is unlikely to be a SNR, indicating that further observational studies are required to fully disentangle the emission from this region.

4.3. SNR candidates

We identify 80 new candidate SNRs using the methodology described in Sect. 3.1. We visually identify counterparts of 50 of these objects in either of the 20 cm (1400 MHz) THOR+VGPS, the 20/90 cm (1400/325 MHz) MAGPIS, or the 150 cm (200 MHz) GLEAM data. As SNRs are brighter at lower frequencies, the detection of the SNR candidates in these lower frequency surveys data can be used as an assessment of our confidence level in these candidates. The positions of these objects, their sizes, and their flux densities are listed in Table 3. The images of all these candidates are presented in Appendix A.

In addition, we also identify 77 SNR candidates in the GLOSTAR-VLA data that were discovered in earlier studies (see Sect. 2.3.3). The details of these candidates, along with references to the studies that identified them, are presented in Table 4; if they are found to have MIR emission in the MIPSGAL 24 μm and GLIMPSE 8 μm images, they are marked as thermal in the remarks column.

4.3.1. Comparing the properties of SNR candidates with G19 SNRs and H II regions

In Fig. 9, we present the cumulative distribution functions (CDFs) of 5.8 GHz surface brightness (defined as the ratio of flux density to the area subtended), GLOSTAR-VLA flux density, and radius of the three samples of G19 SNRs, the previously identified SNR candidates detected in the GLOSTAR-VLA data, and the newly discovered GLOSTAR-VLA SNR candidates. The CDFs show that the new SNR candidates discovered in the GLOSTAR-VLA data are in general smaller and fainter than the other two samples; this is expected because of the survey's better surface brightness sensitivity and better resolution than many previous large-scale studies. The sample of G19 SNRs consists of objects that were easily detected and well studied, and hence they are brighter and larger than the other two samples. We note that the observed differences across the three samples in the 5.8 GHz surface brightness and flux density are not artefacts of the problem of flux density resolved out by the interferometer. All the measurements presented in Fig. 9 are from the GLOSTAR-VLA data, and the "missing flux density" problem affects all the measurements. As G19 SNRs are in general larger than the two samples of SNR candidates, more flux density is resolved out from G19 SNRs than the other two. Future addition of single-dish data (currently being collected with the Effelsberg 100 m telescope) is only expected to widen the differences in flux density and surface brightness of these samples.

The histograms of Galactic longitudes and latitudes of A14 H II regions, G19 SNRs, and SNR candidates (both newly discovered and previously identified ones together) detected in the GLOSTAR-VLA survey are shown in Fig. 10. H II regions and SNRs trace recent massive star formation activity, and are generally expected to have similar distributions, although local discrepancies are common. Anderson et al. (2017) note that there could be physical reasons for the apparent differences, such as the progenitors of supernovae being both O- and B-stars, and H II regions generally tracing only O-stars. The survey by Brogan et al. (2006), which covered the longitude range $22° > l > 4.5°$, nearly doubled the number of confirmed SNRs in their survey region. The number of SNR candidates in this region is also relatively small, and so the observed differences in Galactic longitude among the three samples (top panel, Fig. 10) seem to be a result of previous surveys focusing on selected regions. We also observe a difference in the Galactic latitudes of SNR candidates compared with the other two samples. Both G19 SNRs and A14 H II regions peak at b∼0° and populate the $b < 0°$ latitudes slightly more than $b > 0°$, but the distribution of SNR candidates is quite asymmetric and skewed toward $b > 0°$ with its peak at

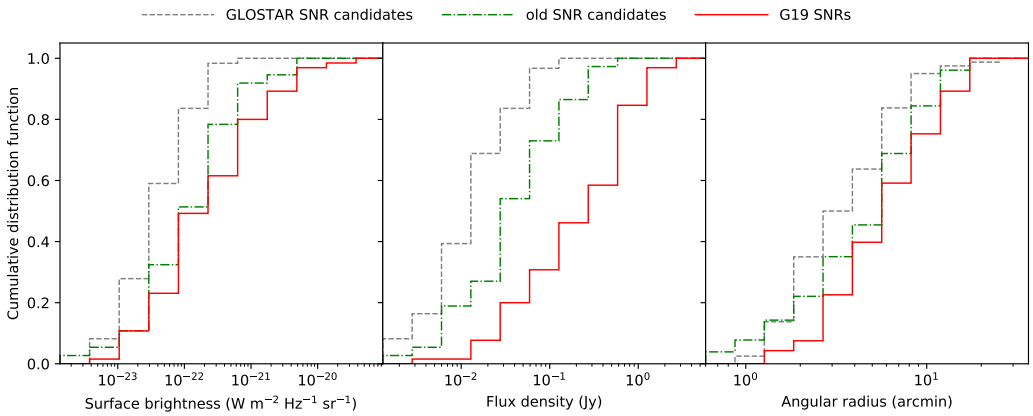

Fig. 9. Cumulative distribution functions of average 5.8 GHz surface brightness (*left*), flux density (*middle*), and angular radius (*right*) of G19 SNRs (red), the SNR candidates discovered in earlier studies (green), and the new SNR candidates identified in the GLOSTAR-VLA survey (gray). The average surface brightness is obtained by dividing the flux density by the angular area subtended by the object. All the properties presented here are as measured in the GLOSTAR-VLA data.

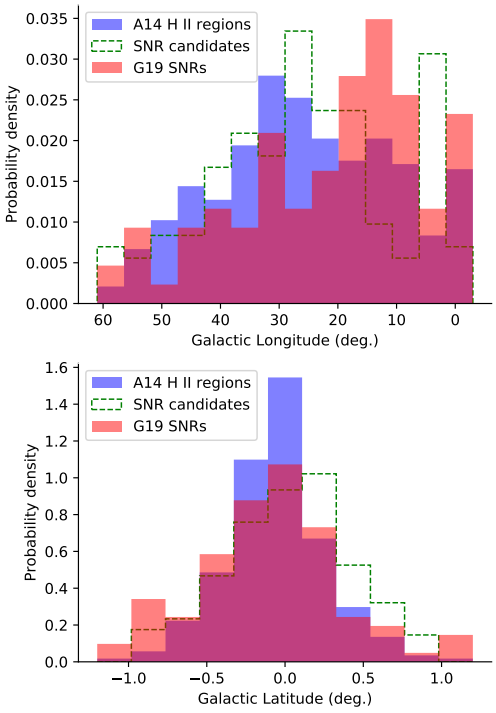

Fig. 10. Probability distribution functions of the Galactic longitudes (*top*) and latitudes (*bottom*) for the three samples of G19 SNRs, A14 H II regions, and SNR candidates detected in the GLOSTAR-VLA data (both previously discovered candidates and new GLOSTAR candidates together).

b~0.2°. Anderson et al. (2017) also report a similar shift toward positive latitudes for the THOR SNR candidates, although less apparent. The reason for this unexpected shift seems unclear. The current sample of G19 SNRs and SNR candidates may still not be representative of the overall Galactic SNR population.

4.3.2. The number of SNRs in the Galaxy

Helfand et al. (1989) estimated that the Galaxy should contain ≳590 SNRs by studying the distribution of approximately 155 SNRs known at that time. They arrived at this number by assuming that the surface density of Galactic SNRs in the longitude range 270° > l > 90° provides a stringent lower limit to the actual surface density of SNRs across the Milky Way, and they used a linear gradient of SNR number density. These latter authors also provide the total expected number of SNRs in different regions of the Galaxy which they named from A–M. Li et al. (1991) further analyzed the distribution of SNRs in a similar statistical manner, but they assumed a "selection-free" zone of 3 kpc around the Sun and used exponential disk and spiral arm scales to model the SNR number surface density. These authors estimate that there must be ≳1000 SNRs and also predict the number of SNRs in various regions of the Milky Way defined by Helfand et al. (1989). The estimates given by Li et al. (1991) outnumber the estimates of Helfand et al. (1989) in most regions (see Table 4 of Li et al. 1991). The total number of SNRs given by Li et al. (1991), about 1000, is in agreement with other studies (Tammann et al. 1994; Mertsch & Sarkar 2013). A simple calculation involving the lifetimes of SNRs (~60 000 years; Frail et al. 1994) and a supernova rate of two per century (Cappellaro et al. 1993; Adams et al. 2013) also gives a number upwards of 1000 SNRs. With this context, below we discuss the distributions of SNRs observed in the GLOSTAR-VLA data.

In Table 1, we compare the results of our search with the expected numbers of SNRs given by Helfand et al. (1989) and Li et al. (1991), assuming that all the SNR candidates are positive identifications. Our results are a surprisingly good match with the predictions by Helfand et al. (1989), but fall well short of the numbers given by Li et al. (1991). We believe that the agreement between our results and the predictions of Helfand et al. (1989) is a coincidence. Our survey is unlikely to be sensitive enough to detect all the SNRs in the survey region. A simple way to test this would be to conduct deeper searches for SNRs in

Table 1. Comparing the distributions of Galactic longitudes of SNRs observed in the GLOSTAR-VLA survey with the predictions by Helfand et al. (1989) and Li et al. (1991).

	0°−30°	30°−45°	45°−60°
Li et al. (1991)	316−380	101	30−36
Helfand et al. (1989)	146−176	53	27−32
SNRs in GLOSTAR	155	58	26

Notes. The numbers presented against Li et al. (1991) are for their 1000 SNRs model, and those against "SNRs in GLOSTAR" include the three samples of G19 SNRs, and previously and newly discovered SNR candidates in GLOSTAR. The expected number of SNRs in the longitude range $0° < l < 30°$ is obtained by assuming that SNRs in $0° < l < 30°$ account for 50%−60% of the SNRs in the $|l| < 30°$ range (regions F+G+H+I as defined by Helfand et al. 1989; see their Fig. 8). Similarly for $45° < l < 60°$ (33–40% of SNRs in $45° < l < 90°$, i.e., regions B + C).

the longitude range $0° < l < 30°$. Comparing our results with the numbers estimated by Li et al. (1991), we find that over 150 SNRs remain to be detected in this region (see Table 1). Therefore, if deeper surveys reveal more SNRs, then the good agreement with the expected number given by Helfand et al. (1989) is purely a coincidence. However, if no new SNR candidates were to be discovered in future deeper surveys – which we believe is unlikely – then we may need to rethink the distributions of SNRs and also possibly the total number of SNRs in the Milky Way.

4.4. New SNR candidates with polarized emission

Three new SNR candidates have significant linearly polarized emission clearly coming from their Stokes I counterparts, namely G005.989+0.019, G034.524−0.761, and G039.539+0.366, with degrees of polarization 0.18 ± 0.03, 0.07 ± 0.02, and 0.06 ± 0.02, respectively. All three have a lone arc morphology that is reminiscent of a shell (see Fig. 11). These three candidates are also detected in lower frequency surveys (shown in the right panels of Fig. 11). The other newly discovered candidates with counterparts in lower frequency surveys are marked in Table 3. The low number of detections in polarization may imply that a large portion of our new candidates may in fact be H II regions that are too faint to be detected by the GLIMPSE and MIPSGAL surveys, although this is unlikely (Anderson et al. 2014). Spectral index measurements can ascertain the nature of these new candidates.

4.5. Previously identified SNR candidates with polarized emission

4.5.1. G26.75+0.73

Candidate SNR G26.75+0.73 was identified by Anderson et al. (2017) using data from the THOR survey. We observe a partial shell morphology in the GLOSTAR-VLA data similar to the THOR+VGPS data (Fig. 12). We find that it has a high degree of polarization, 0.70 ± 0.40, suggesting that this shell-shaped object is a SNR. We note that the degree of polarization observed in the GLOSTAR-VLA data is an over-estimation (see Sect. 3.2). In addition, we also find faint emission from this object in the 200 MHz GLEAM data[9] (Hurley-Walker et al. 2019c). We measure its flux density as 1.0 ± 0.5 Jy in the GLEAM data after subtracting the local background. Comparing this to its THOR+VGPS flux density of ∼0.5 Jy (Anderson et al. 2017), we measure a non-thermal spectral index of ~ -0.4, agreeing with its identification as a SNR.

4.5.2. G27.06+0.04

G27.06+0.04 is an arc-shaped SNR candidate detected in MAGPIS, THOR, and GLEAM surveys (Helfand et al. 2006; Anderson et al. 2017; Hurley-Walker et al. 2019b). We observe the same morphology in the GLOSTAR-VLA data (Fig. 13). For the arc, Hurley-Walker et al. (2019b) report a flux density of 4.9 ± 0.1 Jy at 200 MHz, while we measure its flux density to be 1.4 ± 0.3 Jy in the THOR+VGPS data (Beuther et al. 2016). This implies that this arc has a spectral index of -0.65 ± 0.31, consistent with the value of -0.53 ± 0.22 from the TGSS-NVSS spectral index map[10] (de Gasperin et al. 2018). In the GLOSTAR-VLA data, we measure a degree of polarization of 0.10 ± 0.01 for the arc. We observe different RMs for the northern (~ -100 rad m^{-2}) and southern ($\sim +150$ rad m^{-2}) parts of the arc. This is likely due to a change in the magnetic field direction, or local Faraday screens. Such large RMs and changes in RMs are not uncommon in SNRs (e.g., Milne & Dickel 1974a,b; Gaensler et al. 2000; Harvey-Smith et al. 2010). Further studies are necessary to fully analyze the emission from this region. Nonetheless, the polarization and spectral index measurements provide sufficient evidence of the nonthermal nature of this object.

4.5.3. G28.78−0.44

G28.78−0.44 was first identified in the MAGPIS survey (Helfand et al. 2006) and subsequently in the THOR and GLEAM surveys (Anderson et al. 2017; Hurley-Walker et al. 2019b) as a near-complete shell. A spectral index of -0.79 ± 0.12 was derived by Hurley-Walker et al. (2019b), which is consistent with the value of -0.75 ± 0.22 for a part of the shell measured from the TGSS-NVSS spectral index data (de Gasperin et al. 2018). In the GLOSTAR-VLA data, we find the object to have a partial shell morphology along with clear polarized emission ($p = 0.49 \pm 0.12$, Fig. 14). The polarized emission from this object is further evidence that this object is a SNR. We find that the electric field vectors are generally tangential to the shell, implying that the ambient magnetic field is either radial or nearly parallel to the line of sight. Radial magnetic fields are seen in young shell-type SNRs, likely because of Rayleigh-Taylor instability (Milne 1987; Jun & Norman 1996; Fürst & Reich 2004).

4.5.4. G29.38+0.10

G29.38+0.10 was observed in the MAGPIS and THOR surveys as a source with bright central compact emission inside a weakly emitting shell (Helfand et al. 2006; Anderson et al. 2017). Hurley-Walker et al. (2019b) measured a spectral index of 0.09 ± 0.14, noting it as a potential PWN. A similar spectral index is obtained from the TGSS-NVSS spectral index map (0.17 ± 0.06, de Gasperin et al. 2018). We observe the central emission at higher resolution in the GLOSTAR-VLA data; it shows a faint unresolved central object inside the bright

[9] http://gleam-vo.icrar.org/gleam_postage/q/form

[10] http://tgssadr.strw.leidenuniv.nl/doku.php?id=spidx#spectral_index_map

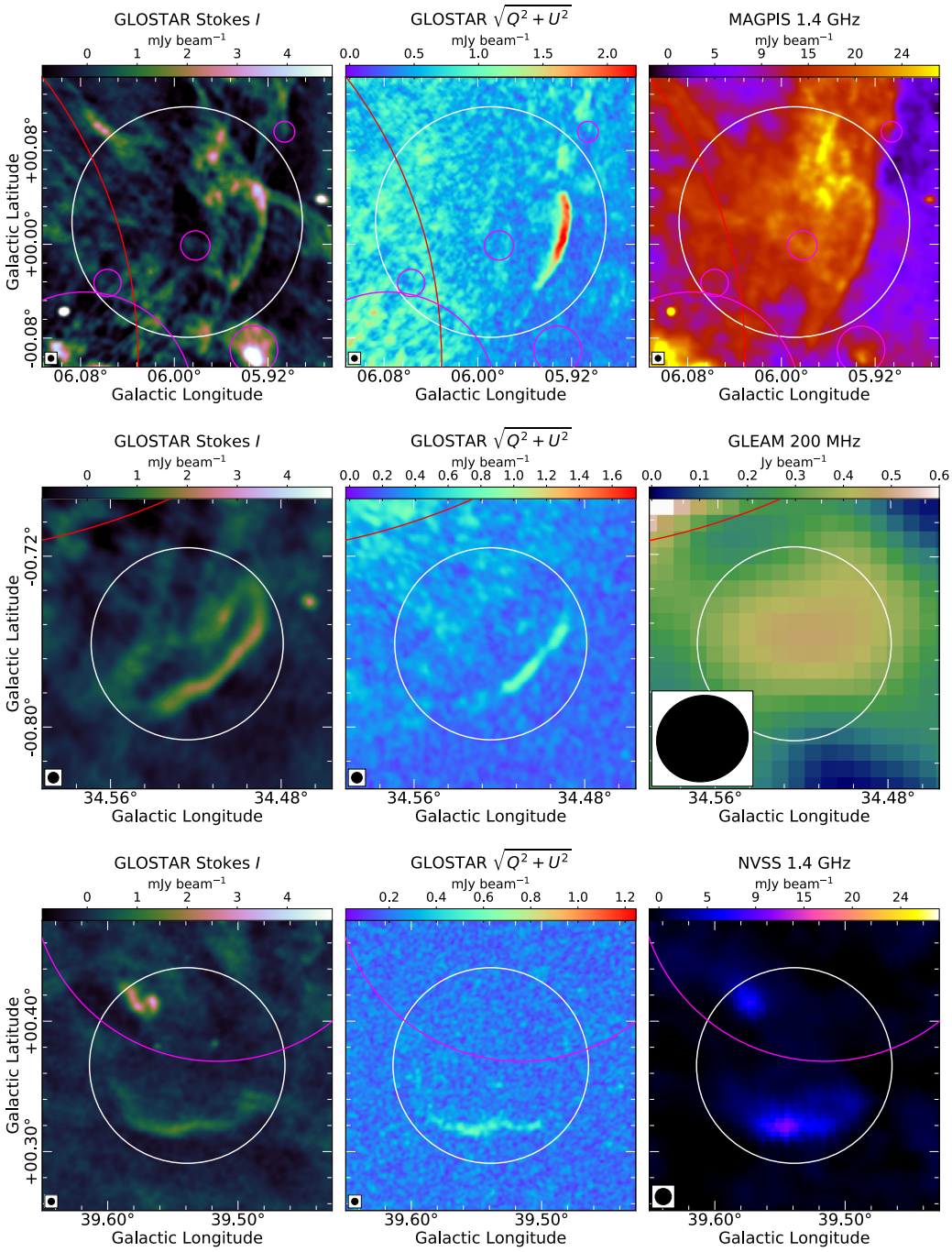

Fig. 11. New SNR candidates identified in the GLOSTAR-VLA data with significant polarization: G005.989+0.019 (*top panels*), G034.524−0.761 (*middle panels*), and G039.539+0.366 (*bottom panels*). Although we correct the linearly polarized flux density for Ricean bias (see Sect. 3.2), we present the polarization data in all the figures without bias correction so that the structures are clearly seen.

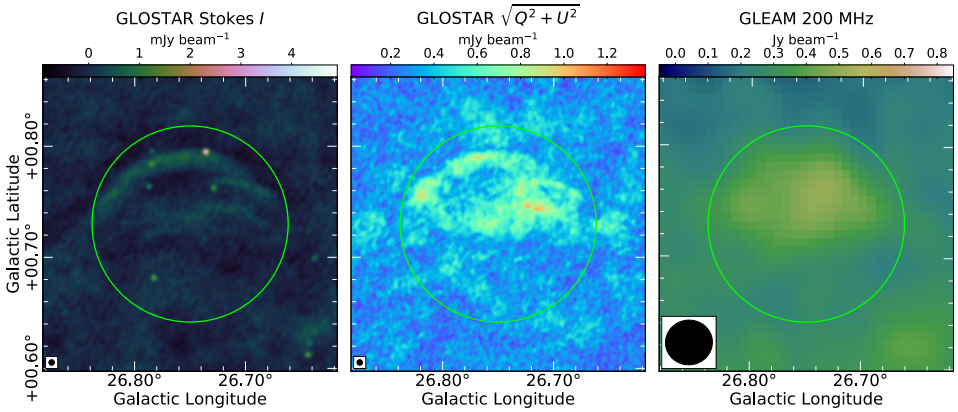

Fig. 12. G26.75+0.73, encircled in green, as seen in the GLOSTAR-VLA data (*left and middle panels*) and the GLEAM 200 MHz data (*right panel*).

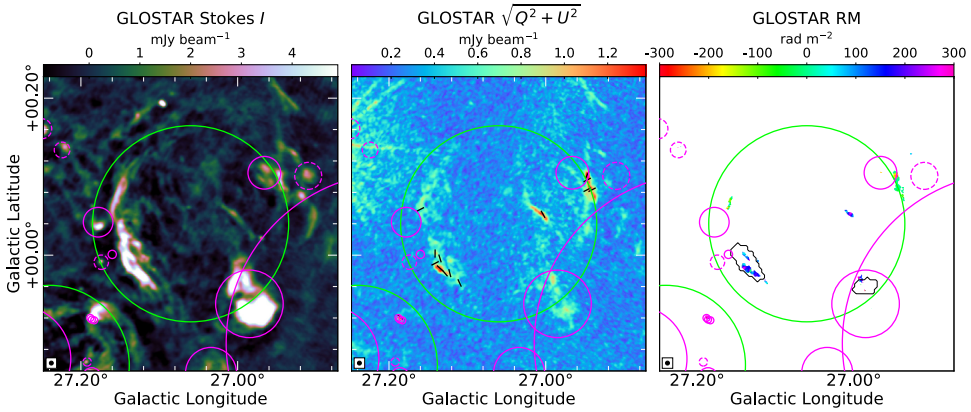

Fig. 13. G27.06+0.04. The RMs presented in the right-most panel typically have uncertainties of 30–40 rad m^{-2}. The black contours on the rotation measure map show the regions for which the TIFR GMRT Sky Survey-NRAO VLA Sky Survey (TGSS-NVSS) spectral index was measured. The eastern region (on the arc) and the western region (overlapping with two H II regions) have a similar spectral index of ∼−0.5. For this and all subsequent figures, the directions of the electric field vector position angles (after accounting for Faraday rotation) are plotted with black lines on the polarization map.

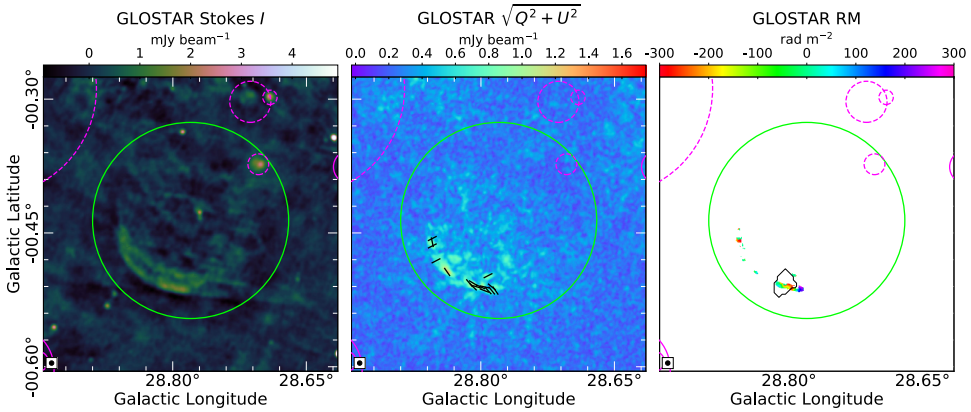

Fig. 14. G28.78−0.44. The black contour on the RM map shows the region for which the TGSS-NVSS spectral index ($\alpha = -0.75 \pm 0.22$) was measured. The RMs have uncertainties of 25−35 rad m^{-2}.

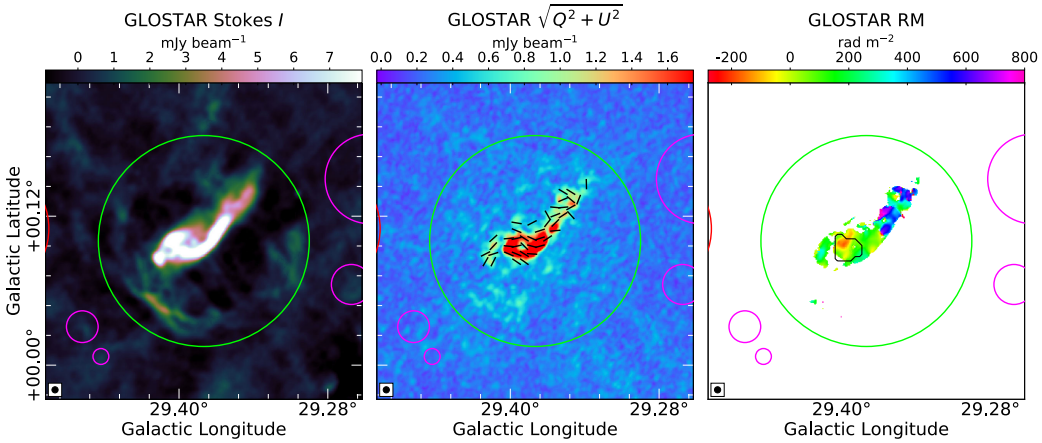

Fig. 15. G29.38+0.10. The black contour on the RM map shows the region for which the TGSS-NVSS spectral index ($\alpha = 0.17 \pm 0.06$) was measured. The uncertainties in the RMs are ∼10–20 rad m^{-2}.

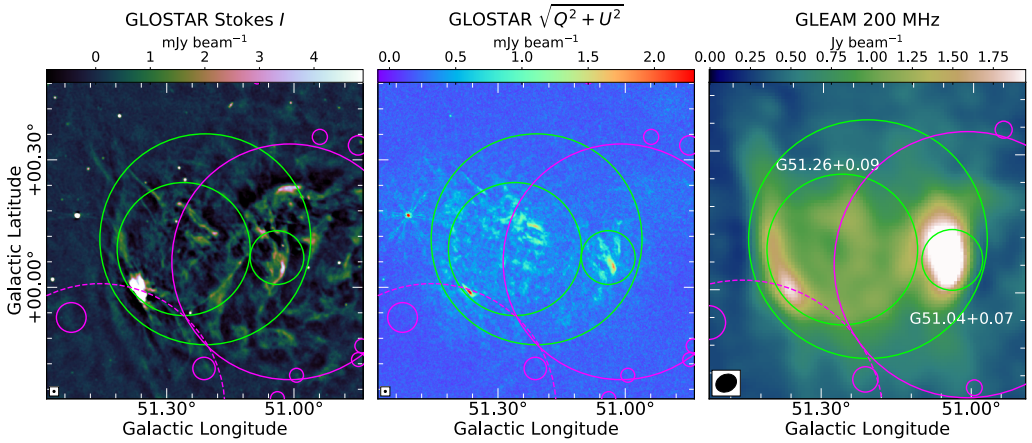

Fig. 16. Complex G51.21+0.11 (largest green circle, defined by Anderson et al. 2017) containing the SNRs G51.04+0.07 and G51.26+0.11 (smaller green circles, defined by Dokara et al. 2018).

elongated nebula, which itself is surrounded by a weak shell, the remnant of the SN that had the pulsar as its end product (Fig. 15). An ordered magnetic field can be inferred from the electric field vectors. The derived RMs range from ∼−200 to ∼+600 rad m^{-2}. Such a large spread is not typically seen in objects in the Milky Way, and may be due to Faraday thick structures or a superposition with sources unrelated to the PWN. The PWN and its shell have measured degrees of polarization of 0.17 ± 0.02 and 0.02 ± 0.01, respectively.

This region was analyzed across several spectral bands by Castelletti et al. (2017) and Petriella (2019), searching for evidence for an association of the radio detection with the TeV source HESS J1844-030 (H.E.S.S. Collaboration 2018). No evidence for pulsations was found in any band and the S-shaped feature is suggested to be a radio galaxy. It is argued that the radio galaxy is responsible for only a part of the observed emission and that this source most likely represents a chance superposition of the radio galaxy, and a PWN and its remnant shell. This may explain the large variation in our RM measurements near the tail. The polarization and spectral index measurements, combined with the analysis by Castelletti et al. (2017) and Petriella (2019), confirm the status of this candidate as a SNR.

4.5.5. G51.21+0.11 complex: G51.04+0.07 and G51.26+0.11

The candidate G51.21+0.11 was identified by Anderson et al. (2017) in the THOR survey. Further studies by Supan et al. (2018) and Dokara et al. (2018) have shown evidence of non-thermal emission arising from two distinct regions in this complex. Dokara et al. (2018) classify it as two separate SNRs, G51.04+0.07 and G51.26+0.11. Recently, Araya (2021) identified GeV emission from this region. They rule out nearby star-forming regions and Bremsstrahlung radiation as the origin of this GeV emission and support the hypothesis that this emission is from at least one SNR. In the GLOSTAR-VLA data, a morphology similar to the one in THOR+VGPS data is observed (Fig. 16). We measure a degree of polarization of

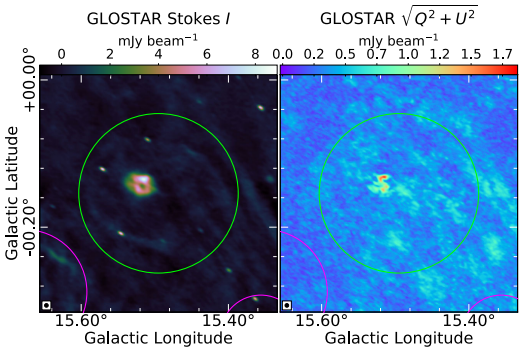

Fig. 17. Candidate SNR G15.51−0.15. The morphology and polarization from the central object imply the presence of a PWN at the center, but previous studies derive a spectral index of $\alpha \sim -0.5$, which is not expected from PWNe.

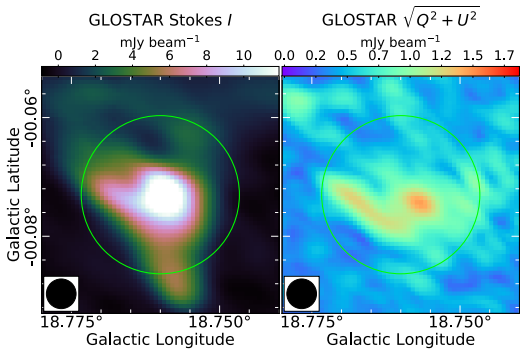

Fig. 18. SNR candidate G18.76−0.07. We hypothesize that this is a complex region with at least one extragalactic object.

0.07 ± 0.01 for G51.04+0.07 and 0.06 ± 0.02 for G51.26+0.11. In the 1.4 GHz THOR+VGPS data and the 200 MHz GLEAM data, we subtracted the local background and measured the flux densities of these objects. The 200 MHz and 1.4 GHz flux densities of G51.04+0.07 are 6.3 ± 2.1 Jy and 2.0 ± 0.3 Jy respectively, whereas G51.26+0.11 has 25.8 ± 3.6 Jy and 12.4 ± 0.6 Jy, respectively. These values imply spectral indices of ~ -0.6 for G51.04+0.07 and ~ -0.4 for G51.26+0.11. The above polarization and spectral index measurements further strengthen the case of these two objects as SNRs.

4.6. Other observed SNR candidates

4.6.1. G15.51−0.15

Brogan et al. (2006) identified G15.51−0.15 as a potential shell-type remnant that is less likely to be a SNR[11]. Hurley-Walker et al. (2019b) studied this object in GLEAM and the archival NRAO VLA Sky Survey data (NVSS; Condon et al. 1998). They derive a spectral index of ~ -0.6 for both the central object and the surrounding emission and speculate a common origin for both.

In the GLOSTAR-VLA data (Fig. 17), we clearly resolve this candidate into a shell that surrounds off-center compact emission. This morphology is indicative of a PWN. However, PWNe generally have a spectral index of $\alpha > -0.3$, although known exceptions exist (see Kothes et al. 2008). We note that the spectral index calculations for the shell by Hurley-Walker et al. (2019b) are unlikely to be influenced significantly by the three point sources on the shell. In the GLOSTAR-VLA data, these point sources have flux densities of 4–8 mJy and spectral indices close to zero, implying that they would have similarly small flux densities in the GLEAM band as well. Comparing with the flux density of ∼2.8 Jy derived by Hurley-Walker et al. (2019b), it can be seen that the contribution of these three point sources to the flux density at 200 MHz, and hence to their 200–1400 MHz spectral index calculation, would be negligible. It is possible that the shell and the central object are two separate SNRs, or it may be a composite-type remnant. Distance measurements are required to study whether the shell and the central object are related.

In order to measure the polarization of the shell, we excluded the three compact objects on the shell that are likely unrelated sources. The remaining part of the shell is faint and we could only derive an upper limit on the degree of linear polarization, $p < 0.08$. We measure a low degree of polarization of 0.03 ± 0.01 from the central object.

4.6.2. G18.76−0.07

With a diameter of 96″, G18.76−0.07 is one of the SNR candidates of the smallest angular size. It was first discovered in the MAGPIS survey (Helfand et al. 2006) and then in the THOR survey (Anderson et al. 2017). We measure in the GLOSTAR-VLA data a degree of polarization of 0.08 ± 0.01. The polarization map (Fig. 18) shows a point source and an elongated source in this region. A large negative spectral index of ~ -1.8 was measured from the GLEAM (∼200 MHz) and the NVSS data (1400 MHz) by Hurley-Walker et al. (2019b), and the TGSS-NVSS spectral index map (150–1400 MHz; de Gasperin et al. 2018) also shows a similar value (~ -1.2). Such values for SNRs have been reported only at higher frequencies after a "spectral break" (see Kothes et al. 2020, for instance). As such a spectral index below L-band frequencies is generally seen only in extragalactic objects, and because of the morphology of the linearly polarized emission, we infer that at least one extragalactic object is located within the angular extent of this candidate.

4.6.3. G22.00+0.00/G022.045−0.028

Ueno et al. (2006) discovered G22.00+0.00 at X-ray energies, noting that synchrotron X-ray emitting SNRs have low radio surface brightness. Yamauchi et al. (2016) hint that this candidate may be a PWN. We do not find any PWN-like object, but we do identify a shell-like object in the GLOSTAR-VLA and the THOR+VGPS data (Fig. 19), overlapping with the diffuse X-ray emission detected by Ueno et al. (2006) and Yamauchi et al. (2016) at $l = 22.00$, $b = 0.00$. We name this a GLOSTAR SNR candidate G022.045−0.028. The spatial overlap indicates that this may be the shell corresponding to the PWN suggested by Yamauchi et al. (2016). We observe polarization in the GLOSTAR-VLA data from the eastern part of the shell, but

[11] Brogan et al. (2006) classified the candidate G15.51−0.15 as a class III-type shell in their Table 1 and have not discussed this candidate further in the text. However, the image of this candidate they showed in their Plate 1 has a bright central object and only a weak partial shell.

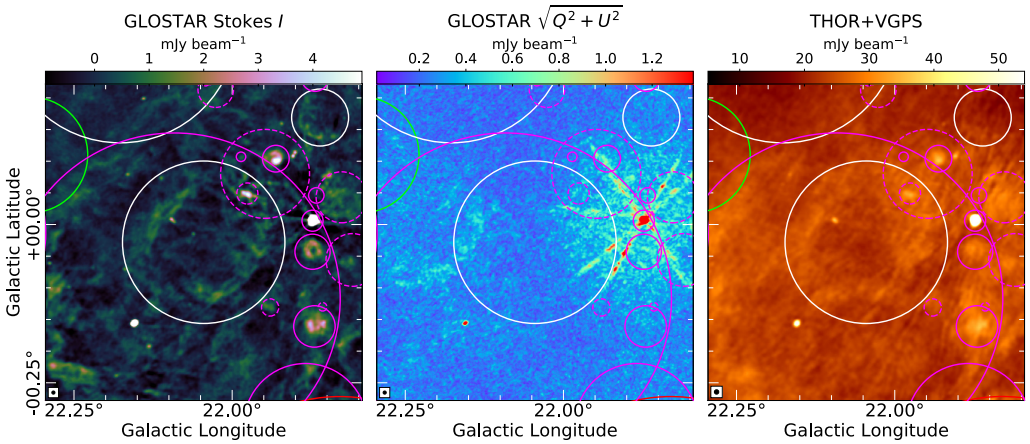

Fig. 19. GLOSTAR SNR candidate G022.045−0.028: Shell-shaped object near the X-ray SNR candidate G22.00+0.00. There is no clear association of the radio and the X-ray morphologies (see Fig. 1 of Ueno et al. 2006).

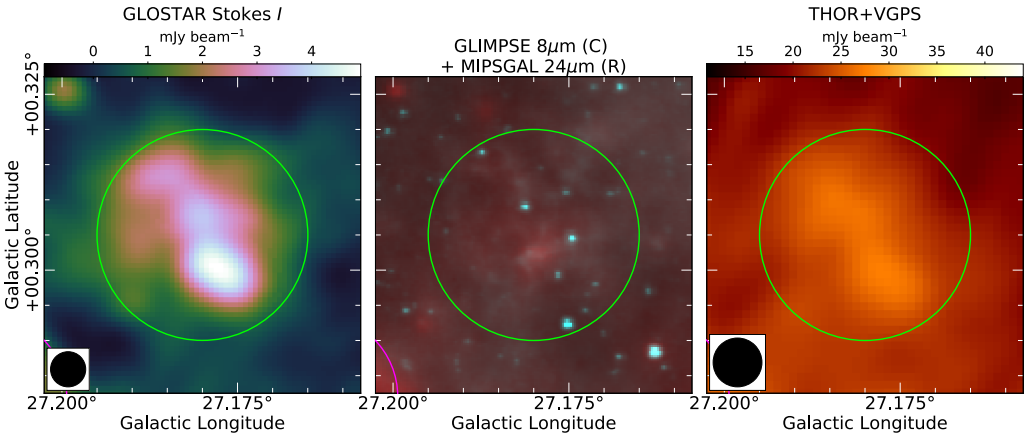

Fig. 20. THOR SNR candidate G27.18+0.30, as seen in GLOSTAR Stokes *I* (*left*), MIR (*middle*) and THOR+VGPS (*right*).

it appears to be from unrelated shell-shaped emission extending further east without a Stokes *I* counterpart in either of the THOR+VGPS and GLOSTAR-VLA data (Fig. 19). It is as yet unclear whether the radio shell is associated with the X-ray detection.

4.6.4. G27.18+0.30

The THOR SNR candidate G27.18+0.30 is clearly seen in the GLOSTAR-VLA data (Fig. 20). It seems to have faint counterparts in MIPSGAL 24 µm and GLIMPSE 8 µm images, but this may be just the diffuse MIR background unrelated to the radio emission. Anderson et al. (2017) report a flux density of 0.05 ± 0.03 Jy in the THOR+VGPS data, similar to the GLOSTAR-VLA data flux density of 0.048 ± 0.001 Jy. The object has a size of ∼1.5′, and so we take the GLOSTAR-VLA flux density as a lower limit and estimate the lower limit of the spectral index of this candidate:

$$\alpha_{\rm low} = \frac{\ln S_{\rm GLOSTAR-VLA} - \ln S_{\rm THOR+VGPS}}{\ln 5.8\,{\rm GHz} - \ln 1.4\,{\rm GHz}} \implies -0.36 < \alpha_{\rm low} < 0.62. \quad (5)$$

The lower limit of the spectral index implies that G27.18+0.30 may be a PWN, although the morphology is atypical.

4.6.5. G53.07+0.49

Anderson et al. (2017) identified this object as a SNR candidate in the THOR survey. In the GLOSTAR-VLA data, we find a slightly elongated structure (Fig. 21). The polarization data show that the electric field vectors near the center roughly line up along the long axis of this candidate. It has a degree of polarization of 0.12 ± 0.02. We note that this small angular

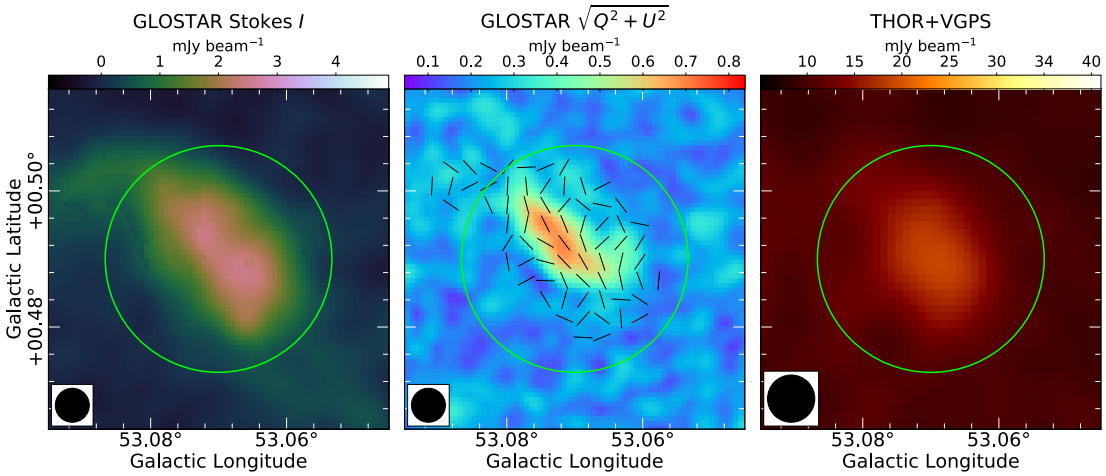

Fig. 21. THOR SNR candidate G53.07+0.49 as seen in the GLOSTAR-VLA data (Stokes *I*, *left*, and linear polarization, *middle*), and the THOR+VGPS data on the *right*.

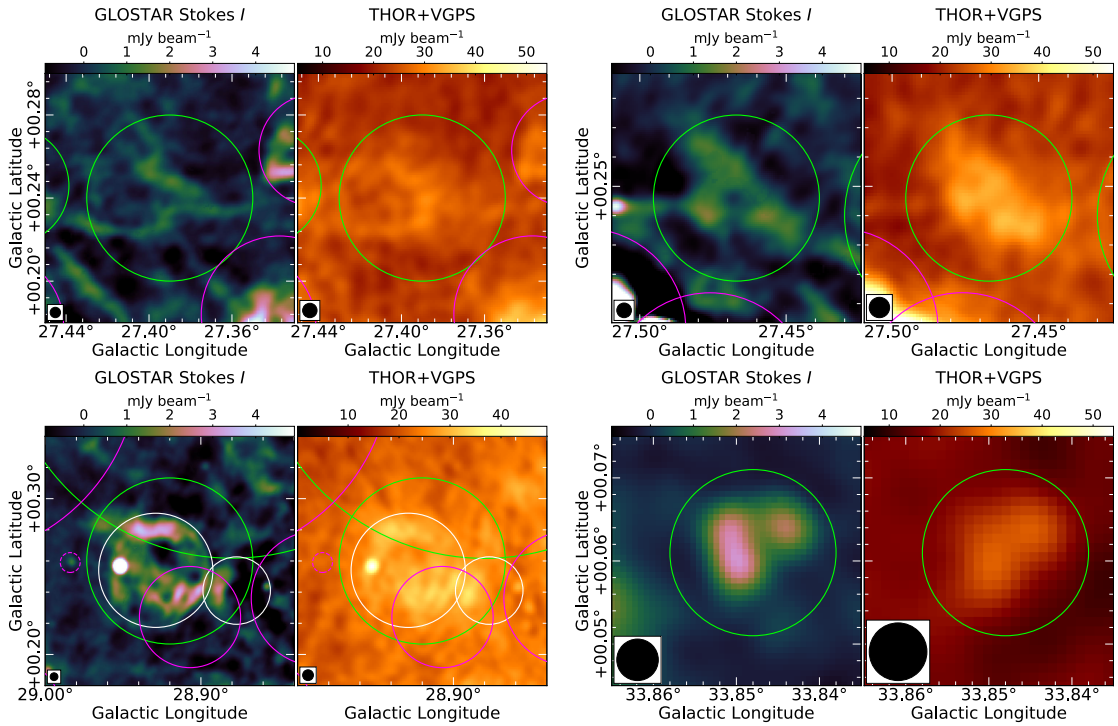

Fig. 22. THOR SNR candidates resolved in the GLOSTAR-VLA data: G27.39+0.24 (*top left*), G27.47+0.25 (*top right*) G28.92+0.26 (*bottom left*), and G33.85+0.06 (*bottom right*). The left panels are the GLOSTAR-VLA data, and the right panels are the THOR+VGPS data. G27.39+0.24 and G27.47+0.25 are filaments mistaken for SNR emission, whereas G28.92+0.26 and G33.85+0.06 contain multiple distinct objects.

size candidate is quite asymmetric. If it were indeed a SNR, it must be quite young or far and/or be expanding into a region of the ISM with a large density gradient. While we find that the emission in the GLOSTAR-VLA data arises from the same position reported by Anderson et al. (2017), Driessen et al. (2018) report that the peaks of flux density in low-frequency

data obtained with the Westerbork Synthesis Radio Telescope (WSRT) and the Low Frequency Array (LOFAR) have a large offset (2′ to 3′) from the VLA data, but this could be the result of confusion with nearby sources due to the elongated beam at lower frequencies (see Fig. 3 of Driessen et al. 2018). Further observational campaigns at multiple frequencies sensitive to various angular scales are needed to shed light on the nature of this candidate.

4.6.6. Resolved SNR candidates

The THOR candidates G27.39+0.24, G27.47+0.25, G28.92+0.26, and G33.85+0.06 are better resolved in the GLOSTAR-VLA data (Fig. 22). The filamentary structures of G27.39+0.24 and G27.47+0.25 that we observe in the GLOSTAR-VLA data suggest that these may be nearby filaments that were unresolved by THOR+VGPS data, rather than SNRs. There seem to be two objects – possibly unrelated – in the extent of G33.85+0.06. Their sizes are comparable to the beam size; they are more likely to be radio galaxies than SNRs.

In the region of the candidate G28.92+0.26, we observe a larger shell-shaped object centered at $l = 28.93$, $b = 0.26$, and to its west, a smaller object that resembles a partial shell (marked with two white circles in Fig. 22). The bright compact object near $l = 28.95$, $b = 0.26$ has a thermal spectral index in the GLOSTAR-VLA data ($\alpha \sim 0$) and was detected in MIPSGAL, implying thermal emission. The other two shell-shaped objects are included in the list of GLOSTAR SNR candidates (G028.877+0.241 and G028.929+0.254).

5. Conclusions

In the GLOSTAR-VLA data, we discover 80 new SNR candidates using the radio-MIR anti-correlation property of SNRs. In addition, 77 previously identified candidates have also been detected. We show that the degree of polarization measured using the GLOSTAR-VLA data can reliably distinguish thermal and nonthermal emission in many cases, in spite of the diffuse synchrotron emission that permeates the ISM. Following the positive polarization measurements from the GLOSTAR-VLA data and favorable spectral index measurements using data from lower frequency surveys, we are able to confirm six previously identified candidates as SNRs (G26.75+0.73, G27.06+0.04, G28.78−0.44, G29.38+0.10, G51.04+0.07 and G51.26+0.11). We were also able to measure significant polarization from three newly discovered GLOSTAR SNR candidates, G005.989+0.019, G034.524−0.761, and G039.539+0.366. Comparing our results with the predictions by Li et al. (1991), we find that over 50% of SNRs in our survey region are yet to be discovered (Sect. 4.3.2).

The G19 SNR catalog contains 94 objects in the survey region of GLOSTAR, and we detect all the objects previously identified in radio continuum data, except G0.0+0.0 and G0.3+0.0, which lie in a very confused region. We find that four of these objects (G8.3−0.0, G10.5−0.0, G11.1−1.0 and G14.3+0.1) are actually H II regions mistaken for SNRs by cross-matching with the A14 catalog of Galactic H II regions.

The GLOSTAR-VLA data highlight the importance of resolution and sensitivity in large-scale surveys: we were able to detect almost all radio SNRs in the survey due to the remarkable sensitivity, and the higher resolution made it possible to reclassify several objects. The SNR candidates G27.39+0.24 and G27.47+0.25 are filaments, and multiple objects were identified in the candidates G18.76−0.07, G28.92+0.26, G33.85+0.06, and in the G19 SNR G6.1+0.5.

The future addition of single dish data – which are presently collected with the Effelsberg 100 meter radio telescope – to the GLOSTAR-VLA images will make reliable spectral index measurements possible for extended objects. This should prove useful in confirming the SNR candidates. If all the detected candidates were confirmed as SNRs, it would nearly triple the number of SNRs in the first quadrant of the Galaxy, bringing us closer to the predicted number of SNRs in the Milky Way (∼1000; Li et al. 1991). Further deeper large-scale surveys covering the entire Galactic plane should be able to rectify the apparent deficiency of SNRs in the Galaxy.

Acknowledgements. We thank the referee David Helfand for his valuable comments on the draft which helped improve the discussion and presentation of our work. We thank Miguel Araya for pointing out a naming inconsistency. HB acknowledges support from the European Research Council under the Horizon 2020 Framework Program via the ERC Consolidator Grant CSF-648505. HB also acknowledges support from the Deutsche Forschungsgemeinschaft in the Collaborative Research Center (SFB 881) "The Milky Way System" (subproject B1). NR acknowledges Max-Planck-Gesellschaft for funding support through the Max Planck India Partner Group grant. This research has made use of NASA's Astrophysics Data System and the SIMBAD database. We have used the softwares Astropy (Astropy Collaboration 2013), APLpy (Robitaille & Bressert 2012), DS9 (Joye & Mandel 2003) and Aladin (Bonnarel et al. 2000) at various stages of this research.

References

Adams, S. M., Kochanek, C. S., Beacom, J. F., Vagins, M. R., & Stanek, K. Z. 2013, ApJ, 778, 164
Anderson, L. D., Bania, T. M., Balser, D. S., et al. 2014, ApJS, 212, 1
Anderson, L. D., Wang, Y., Bihr, S., et al. 2017, A&A, 605, A58
Araya, M. 2021, A&A, submitted, [arXiv:2102.08851]
Astropy Collaboration (Robitaille, T. P., et al.) 2013, A&A, 558, A33
Bertin, E., & Arnouts, S. 1996, A&AS, 117, 393
Beuther, H., Bihr, S., Rugel, M., et al. 2016, A&A, 595, A32
Bonnarel, F., Fernique, P., Bienaymé, O., et al. 2000, A&AS, 143, 33
Brentjens, M. A., & de Bruyn, A. G. 2005, A&A, 441, 1217
Brogan, C. L., Gelfand, J. D., Gaensler, B. M., Kassim, N. E., & Lazio, T. J. W. 2006, ApJ, 639, L25
Brose, R., Pohl, M., Sushch, I., Petruk, O., & Kuzyo, T. 2020, A&A, 634, A59
Brunthaler, A., Menten, K. M., Dzib, S. A., et al. 2021, A&A, 651, A85
Cappellaro, E., Turatto, M., Benetti, S., et al. 1993, A&A, 273, 383
Carey, S. J., Noriega-Crespo, A., Mizuno, D. R., et al. 2009, PASP, 121, 76
Castelletti, G., Supan, L., Petriella, A., Giacani, E., & Joshi, B. C. 2017, A&A, 602, A31
Churchwell, E., Babler, B. L., Meade, M. R., et al. 2009, PASP, 121, 213
Clark, D. H., & Caswell, J. L. 1976, MNRAS, 174, 267
Condon, J. J., Cotton, W. D., Greisen, E. W., et al. 1998, AJ, 115, 1693
Cotton, W. D. 2008, PASP, 120, 439
Cox, P., Kruegel, E., & Mezger, P. G. 1986, A&A, 155, 380
de Gasperin, F., Intema, H. T., & Frail, D. A. 2018, MNRAS, 474, 5008
Dokara, R., Roy, N., Beuther, H., et al. 2018, ApJ, 866, 61
Driessen, L. N., Domček, V., Vink, J., et al. 2018, ApJ, 860, 133
Dubner, G., & Giacani, E. 2015, A&ARv, 23, 3
Frail, D. A., Goss, W. M., & Whiteoak, J. B. Z. 1994, ApJ, 437, 781
Fürst, E., & Reich, W. 2004, in The Magnetized Interstellar Medium, eds. B. Uyaniker, W. Reich, & R. Wielebinski, 141
Fürst, E., Reich, W., & Sofue, Y. 1987, A&AS, 71, 63
Gaensler, B. M., & Slane, P. O. 2006, ARA&A, 44, 17
Gaensler, B. M., Dickel, J. R., & Green, A. J. 2000, ApJ, 542, 380
Gaensler, B. M., Dickey, J. M., McClure-Griffiths, N. M., et al. 2001, ApJ, 549, 959
Gao, X. Y., Reich, P., Hou, L. G., Reich, W., & Han, J. L. 2019, A&A, 623, A105
Green, D. A. 2019, J. Astrophys. Astron., 40, 36
Green, A. J., Reeves, S. N., & Murphy, T. 2014, PASA, 31, e042
H. E. S. S. Collaboration (Abdalla, H., et al.) 2018, A&A, 612, A2
Hales, C. A., Murphy, T., Curran, J. R., et al. 2012, MNRAS, 425, 979
Harvey-Smith, L., Gaensler, B. M., Kothes, R., et al. 2010, ApJ, 712, 1157

Helfand, D. J., Velusamy, T., Becker, R. H., & Lockman, F. J. 1989, ApJ, 341, 151
Helfand, D. J., Becker, R. H., White, R. L., Fallon, A., & Tuttle, S. 2006, AJ, 131, 2525
Hurley-Walker, N., Filipović, M. D., Gaensler, B. M., et al. 2019a, PASA, 36, e045
Hurley-Walker, N., Gaensler, B. M., Leahy, D. A., et al. 2019b, PASA, 36, e048
Hurley-Walker, N., Hancock, P. J., Franzen, T. M. O., et al. 2019c, PASA, 36, e047
Iffrig, O., & Hennebelle, P. 2017, A&A, 604, A70
Intema, H. T., Jagannathan, P., Mooley, K. P., & Frail, D. A. 2017, A&A, 598, A78
Joye, W. A., & Mandel, E. 2003, Astronomical Society of the Pacific Conference Series, 295, New Features of SAOImage DS9, eds. H. E. Payne, R. I. Jedrzejewski, & R. N. Hook, 489
Jun, B.-I., & Norman, M. L. 1996, ApJ, 472, 245
Kim, H.-J., Koo, B.-C., & Moon, D.-S. 2013, ApJ, 774, 5
Kothes, R., Landecker, T. L., Reich, W., Safi-Harb, S., & Arzoumanian, Z. 2008, ApJ, 687, 516
Kothes, R., Reich, P., Foster, T. J., & Reich, W. 2017, A&A, 597, A116
Kothes, R., Reich, W., Safi-Harb, S., et al. 2020, MNRAS, 496, 723
Lang, C. C., Wang, Q. D., Lu, F., & Clubb, K. I. 2010, ApJ, 709, 1125
Lee, J.-W., Koo, B.-C., & Lee, J.-E. 2012, J. Korean Astron. Soc., 45, 117
Li, Z., Wheeler, J. C., Bash, F. N., & Jefferys, W. H. 1991, ApJ, 378, 93
Liszt, H. S. 2009, A&A, 508, 1331
Lockman, F. J. 1989, ApJS, 71, 469
Lockman, F. J., Pisano, D. J., & Howard, G. J. 1996, ApJ, 472, 173
Medina, S. N. X., Urquhart, J. S., Dzib, S. A., et al. 2019, A&A, 627, A175
Mertsch, P., & Sarkar, S. 2013, J. Cosmology Astropart. Phys., 2013, 041
Milne, D. K. 1987, Austr. J. Phys., 40, 771
Milne, D. K., & Dickel, J. R. 1974a, Austr. J. Phys., 27, 549
Milne, D. K., & Dickel, J. R. 1974b, in Galactic Radio Astronomy, eds. F. J. Kerr, & S. C. Simonson, 60, 335
Petriella, A. 2019, A&A, 626, A65
Pinheiro Gonçalves, D., Noriega-Crespo, A., Paladini, R., Martin, P. G., & Carey, S. J. 2011, AJ, 142, 47
Ranasinghe, S., & Leahy, D. A. 2018, AJ, 155, 204
Robitaille, T., & Bressert, E. 2012, APLpy: Astronomical Plotting Library in Python
Simmons, J. F. L., & Stewart, B. G. 1985, A&A, 142, 100
Stupar, M., & Parker, Q. A. 2011, MNRAS, 414, 2282
Sun, X. H., Han, J. L., Reich, W., et al. 2007, A&A, 463, 993
Sun, X. H., Reich, P., Reich, W., et al. 2011, A&A, 536, A83
Supan, L., Castelletti, G., Peters, W. M., & Kassim, N. E. 2018, A&A, 616, A98
Tammann, G. A., Loeffler, W., & Schroeder, A. 1994, ApJS, 92, 487
Ueno, M., Yamauchi, S., Bamba, A., et al. 2006, in IAU Symposium, 230, Populations of High Energy Sources in Galaxies, eds. E. J. A. Meurs, & G. Fabbiano, 333
Wardle, J. F. C., & Kronberg, P. P. 1974, ApJ, 194, 249
Whiteoak, J. B. Z., & Green, A. J. 1996, A&AS, 118, 329
Wilson, T. L., Rohlfs, K., & Hüttemeister, S. 2013, Tools of Radio Astronomy
Yamauchi, S., Sumita, M., & Bamba, A. 2016, PASJ, 68, S6

Appendix A: GLOSTAR-VLA and GLIMPSE images of newly identified SNR candidates

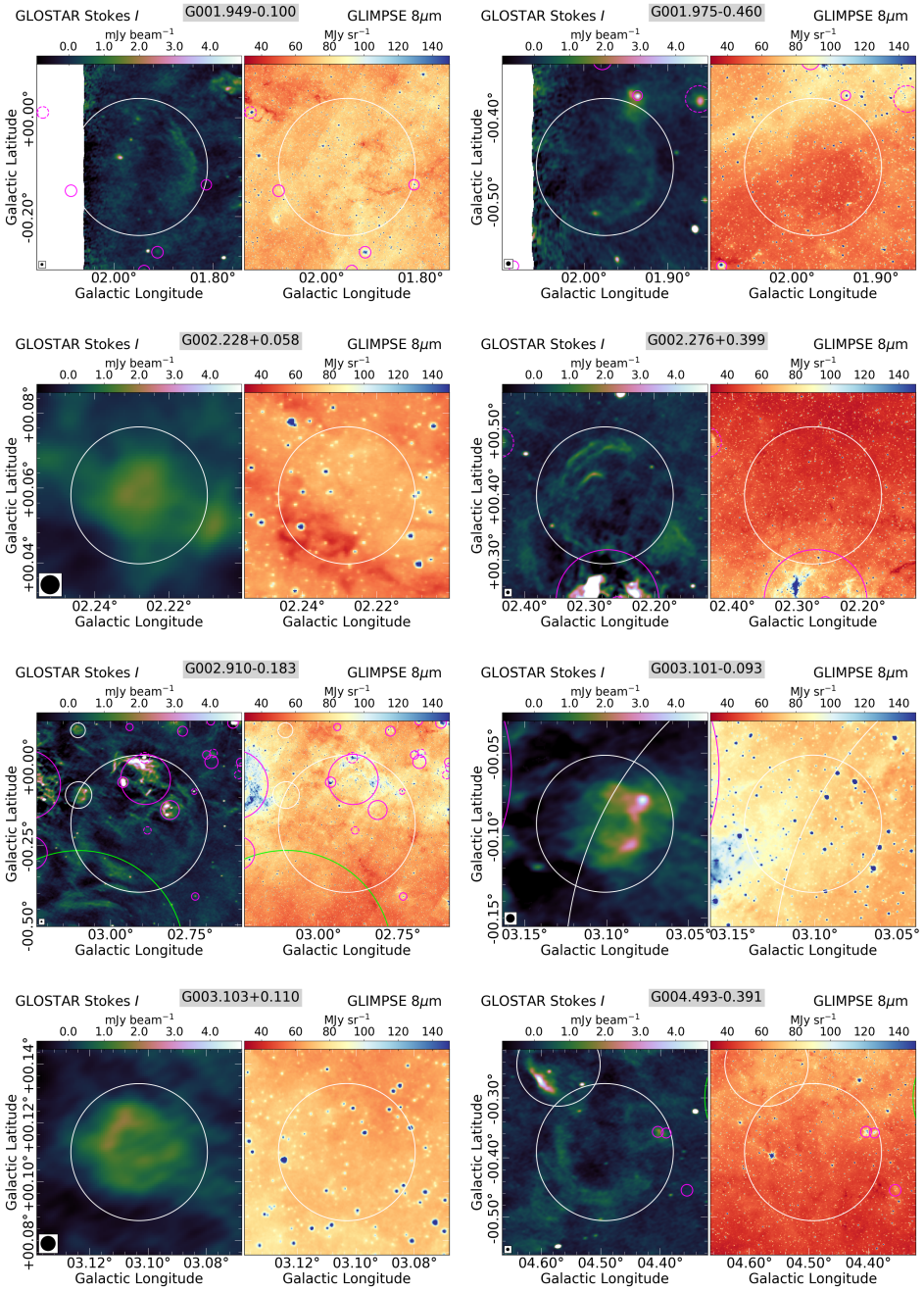

Fig. A.1. The images of newly identified SNR candidates from the GLOSTAR-VLA data are shown here. The marking scheme is the same as in the text: red circles mark G19 SNRs, solid and dashed magenta circles mark confirmed and candidate H II regions from A14 catalog, green circles mark previously identified SNR candidates, and white circles mark new GLOSTAR SNR candidates. The beam of GLOSTAR-VLA data is shown in the bottom left corner in black. Continued on the following pages.

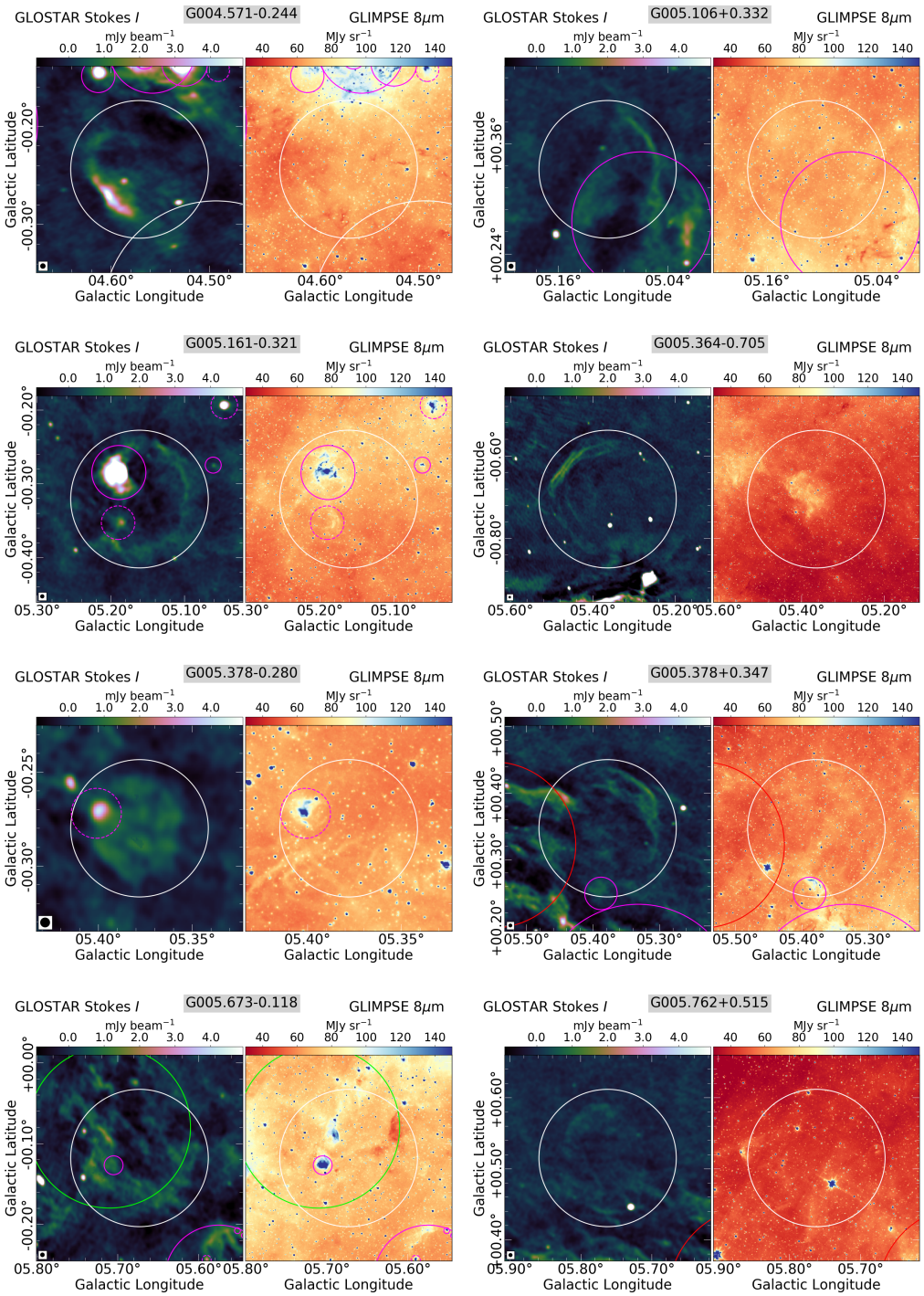

Fig. A.1. continued.

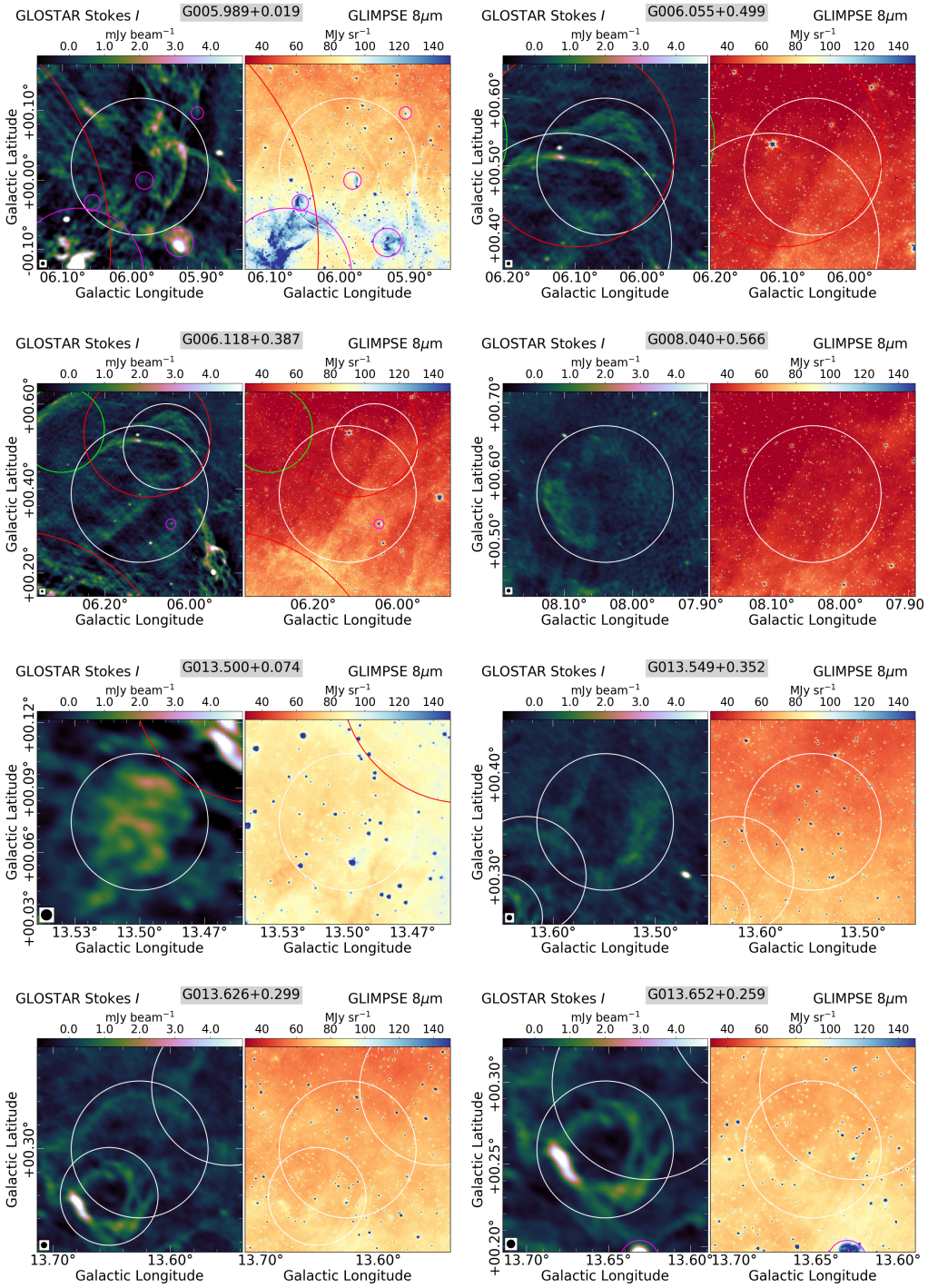

Fig. A.1. continued.

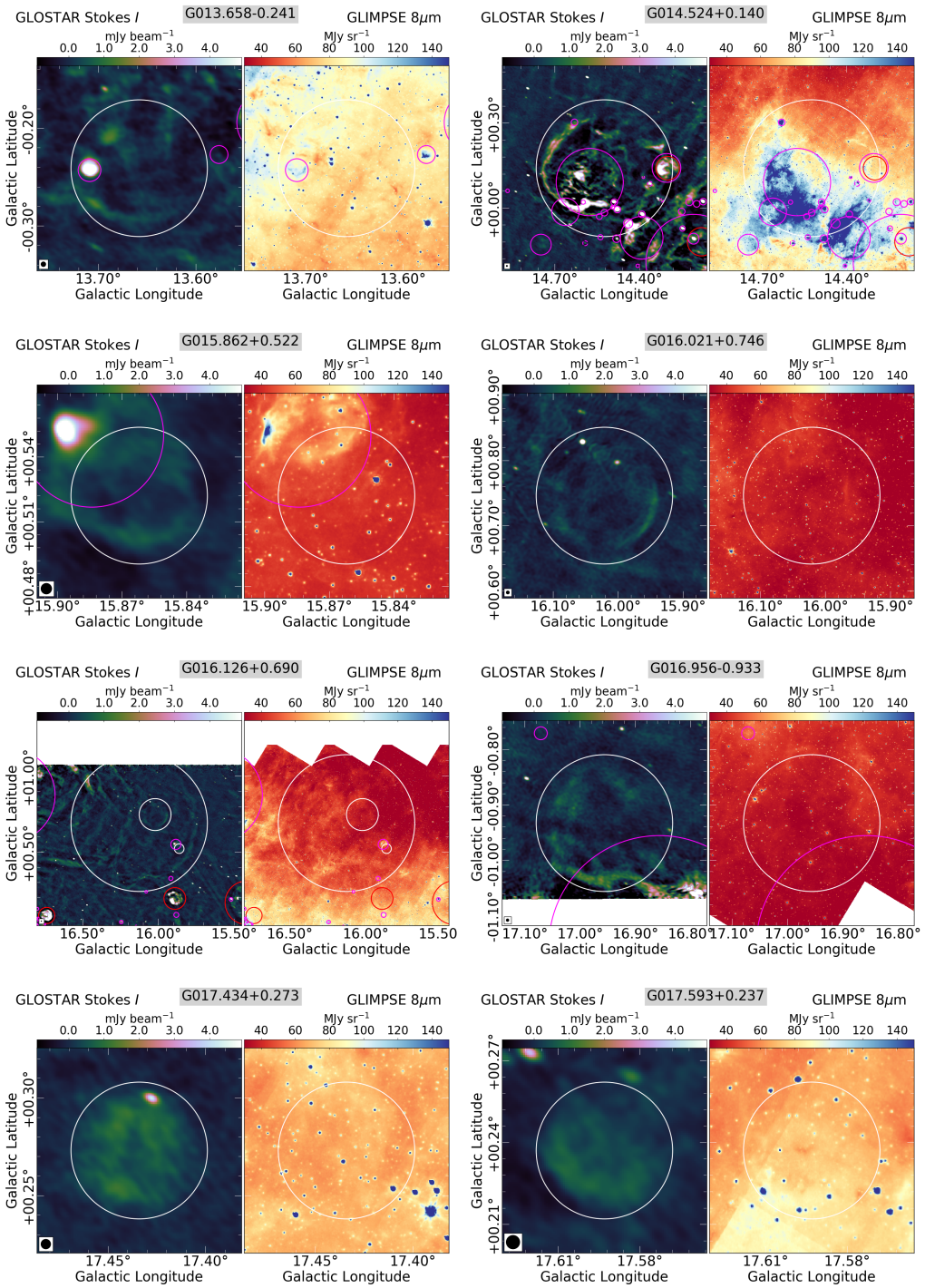

Fig. A.1. continued.

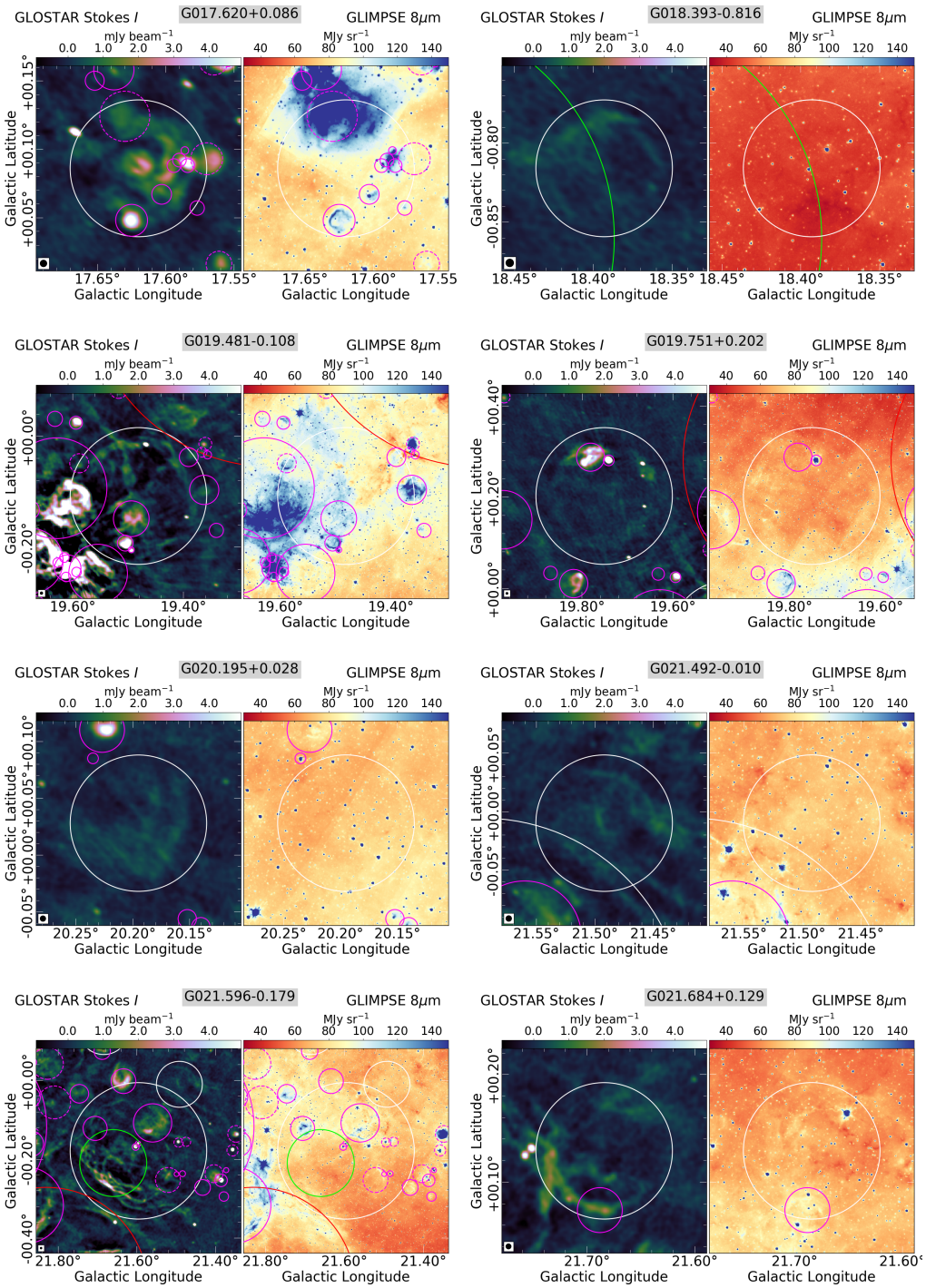

Fig. A.1. continued.

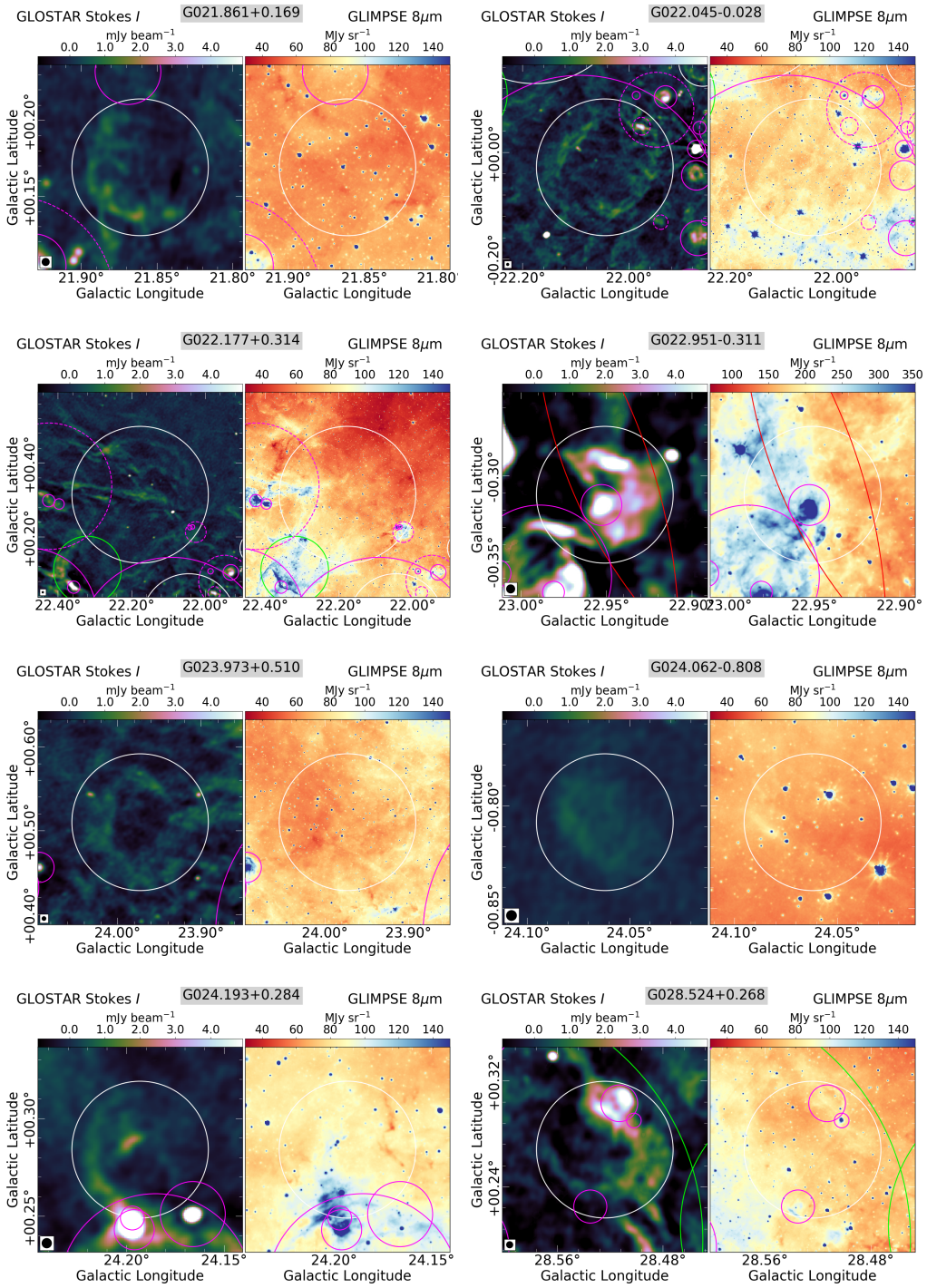

Fig. A.1. continued.

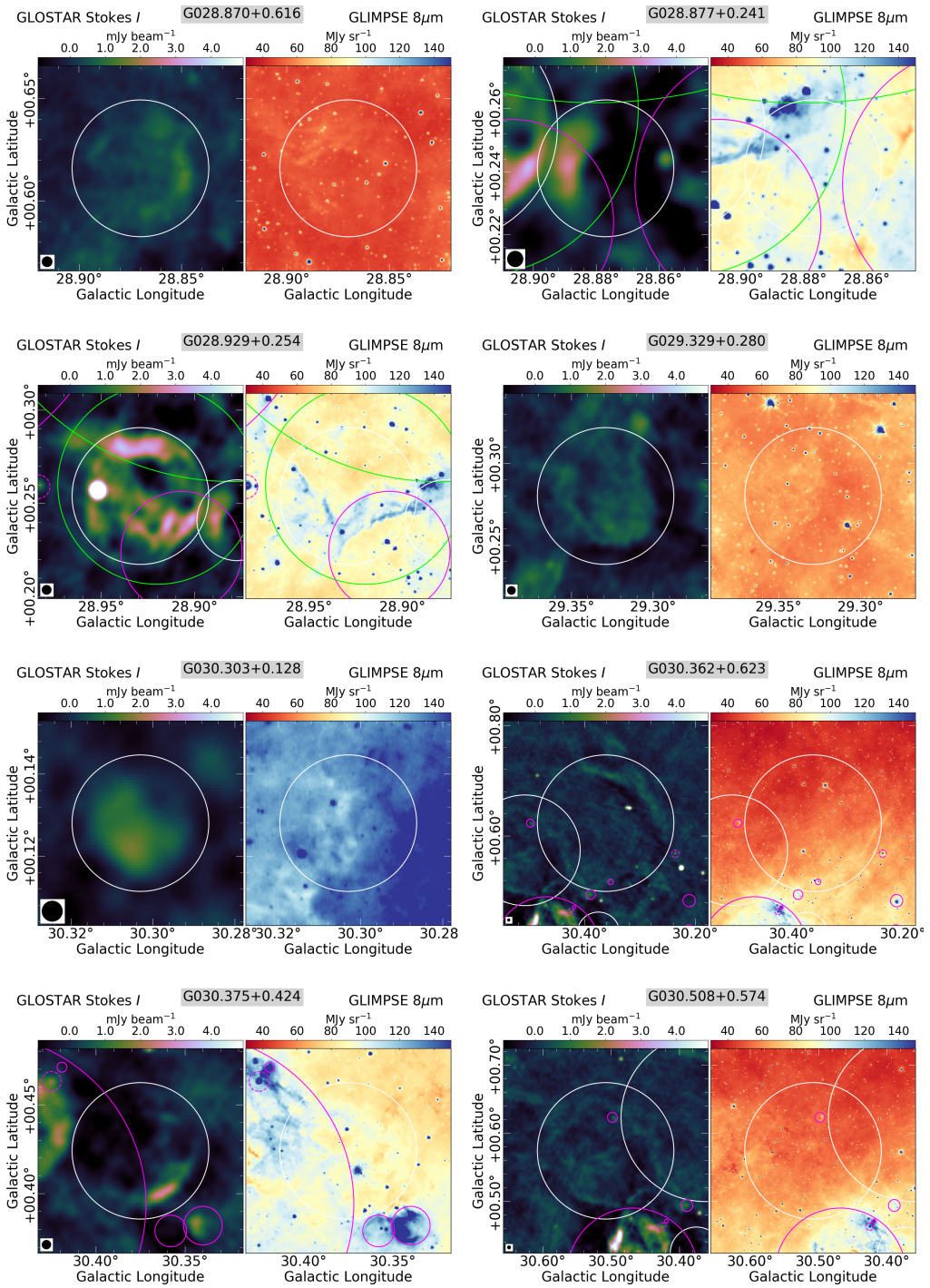

Fig. A.1. continued.

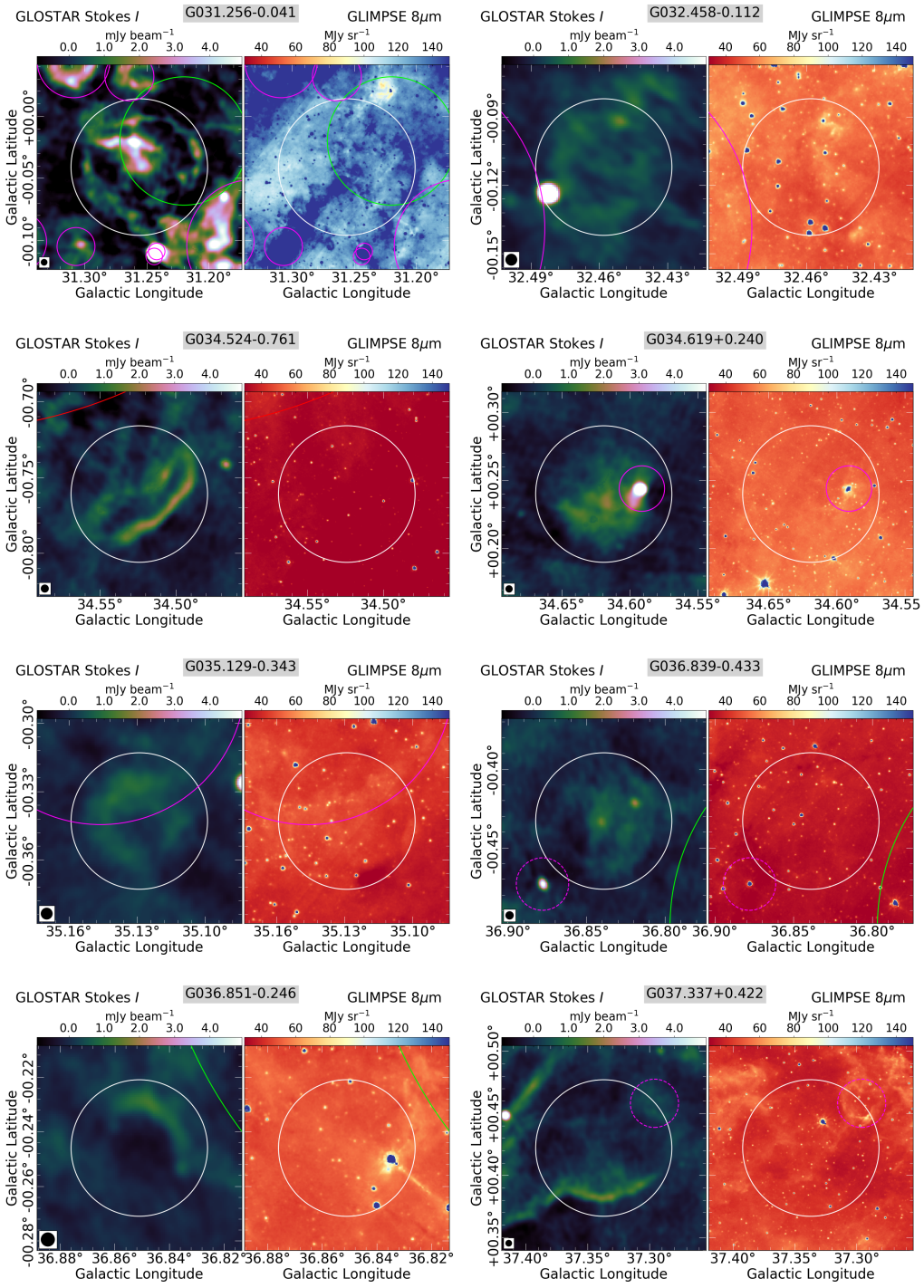

Fig. A.1. continued.

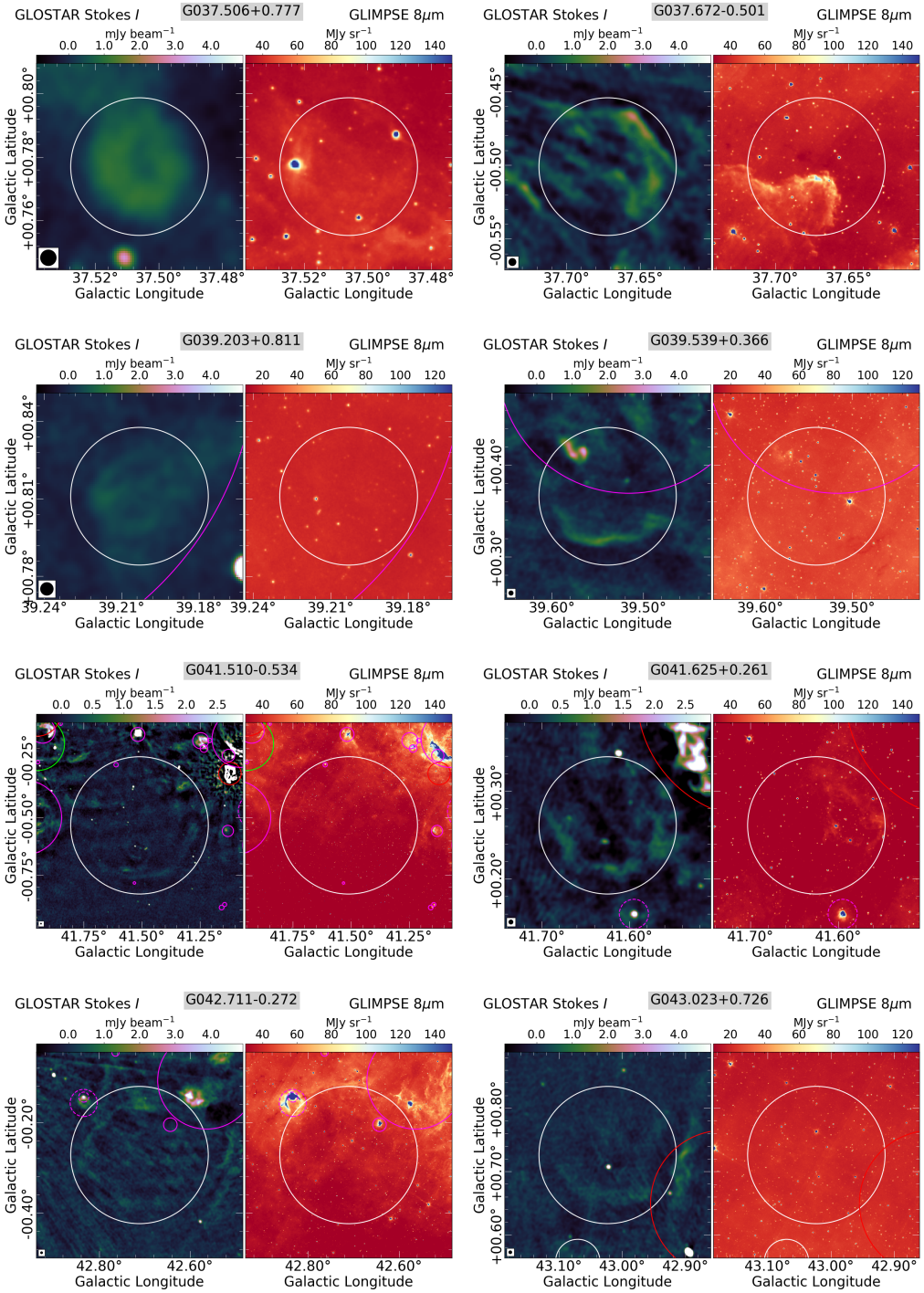

Fig. A.1. continued.

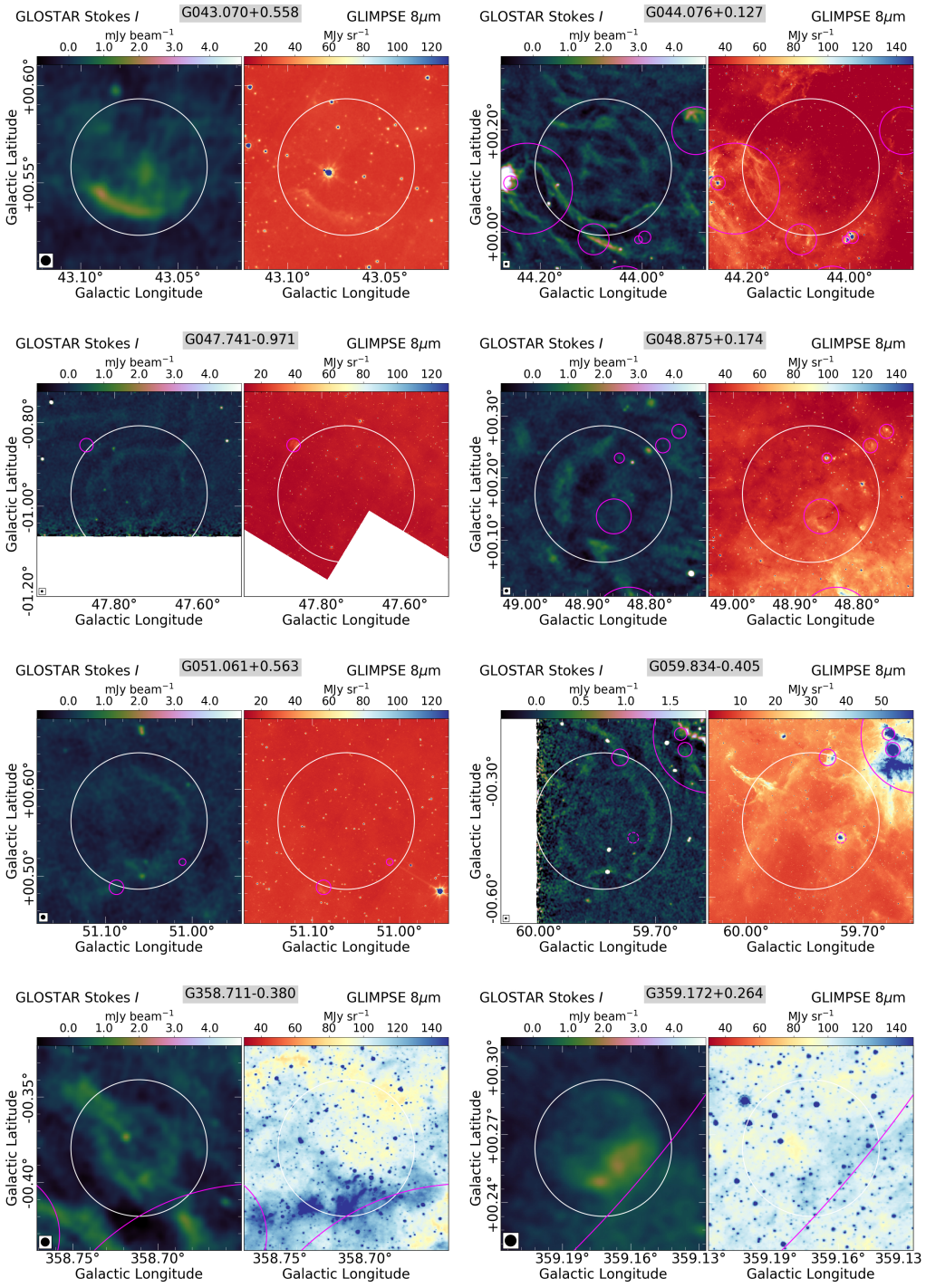

Fig. A.1. continued.

Appendix D

Paper II: SNRs in GLOSTAR combination images

The pdf of Dokara et al. (2023), which is summarized in Chapter 5, is reproduced below. The paper was accepted in November 2022, and it is in press as of this writing. It is expected to be published soon.

Astronomy & Astrophysics manuscript no. output
January 28, 2023

A global view on star formation: The GLOSTAR Galactic plane survey

VII. Supernova remnants in the Galactic longitude range $28° < l < 36°$

R. Dokara[1,⋆], Y. Gong[1], W. Reich[1], M. R. Rugel[1,2,3,⋆⋆], A. Brunthaler[1], K. M. Menten[1], W. D. Cotton[4,5], S. A. Dzib[6,1], S. Khan[1,⋆], S. -N. X. Medina[1,7], H. Nguyen[1,⋆], G. N. Ortiz-León[8,1], J. S. Urquhart[9], F. Wyrowski[1], A. Y. Yang[1], L. D. Anderson[10], H. Beuther[11], T. Csengeri[12], P. Müller[1], J. Ott[3], J. D. Pandian[13], and N. Roy[14]

[1] Max Planck Institute for Radioastronomy (MPIfR), Auf dem Hügel 69, 53121 Bonn, Germany
e-mail: rdokara@mpifr-bonn.mpg.de
[2] Center for Astrophysics, Harvard & Smithsonian, 60 Garden St., Cambridge, MA 02138, USA
[3] National Radio Astronomy Observatory, 1003 Lopezville Rd, Socorro, NM 87801, USA
[4] National Radio Astronomy Observatory, 520 Edgemont Road, Charlottesville, VA, 22903, USA
[5] South African Radio Astronomy Observatory, 2 Fir St, Black River Park, Observatory, 7925, South Africa
[6] IRAM, 300 rue de la piscine, 38406 Saint Martin d'Hères, France
[7] German Aerospace Center, Scientific Information, 51147 Cologne, Germany
[8] Instituto de Astronomía, Universidad Nacional Autónoma de México (UNAM), Apdo Postal 70-264, Ciudad de México, México
[9] Centre for Astrophysics and Planetary Science, University of Kent, Ingram Building, Canterbury, Kent CT2 7NH, UK
[10] Department of Physics and Astronomy, West Virginia University, Morgantown, WV, 26506, USA
[11] Max Planck Institute for Astronomy, Königstuhl 17, D-69117 Heidelberg, Germany
[12] Laboratoire d'astrophysique de Bordeaux, Univ. Bordeaux, CNRS, B18N, allée Geoffroy Saint-Hilaire, 33615 Pessac, France
[13] Department of Earth & Space Sciences, Indian Institute of Space Science and Technology, Trivandrum 695547, India
[14] Department of Physics, Indian Institute of Science, Bengaluru 560012, India

Received 31 October 2022 / accepted 25 November 2022

ABSTRACT

Context. While over 1000 supernova remnants (SNRs) are estimated to exist in the Milky Way, fewer than 400 have been found to date. In the context of this apparent deficiency, more than 150 SNR candidates were recently identified in the D-configuration Very Large Array (VLA-D) continuum images of the 4–8 GHz Global View on Star Formation (GLOSTAR) survey, in the Galactic longitude range $-2° < l < 60°$.

Aims. We attempt to find evidence of nonthermal synchrotron emission from 35 SNR candidates in the Galactic longitude range $28° < l < 36°$, and to study the radio continuum emission from the previously confirmed SNRs in this region.

Methods. Using the short-spacing-corrected GLOSTAR VLA-D+Effelsberg images, we measured the ∼6 GHz total and linearly polarized flux densities of the SNR candidates and the confirmed SNRs. We also attempted to determine the spectral indices by measuring flux densities from complementary Galactic plane surveys and from the temperature-temperature plots of the GLOSTAR-Effelsberg images.

Results. We provide evidence of nonthermal emission from four candidates that have spectral indices and polarization consistent with a SNR origin, and, considering their morphology, we are confident that three of these (G28.36+0.21, G28.78-0.44, and G29.38+0.10) are indeed SNRs. However, about 25% of the candidates (8 out of 35) have spectral index measurements that indicate thermal emission, and the rest of them are so faint that is not possible to place a good constraint on the spectral index.

Conclusions. Additional observations at longer wavelengths and higher sensitivities will shed more light on the nature of these candidates. A simple Monte Carlo simulation reiterates the view that future studies must persist with the current strategy of searching for SNRs with small angular sizes to solve the problem of the Milky Way's missing SNRs.

Key words. ISM: supernova remnants – Radio continuum: ISM – polarization – surveys

1. Introduction

The structure formed from the expelled material and the shock wave of a supernova (SN) explosion interacting with the surrounding interstellar medium (ISM) is known as a supernova remnant (SNR). The interactions of expanding SNRs and the ISM are important feedback mechanisms that may trigger star formation or, on the contrary, disperse gas and thus suppress the star formation rate in a galaxy. Gas can be blown out of the Galactic plane, and turbulent pressure is produced and maintained on both small (molecular-cloud) and large (galaxy-wide) scales (e.g., Efstathiou 2000; Ostriker & Shetty 2011; Dubner & Giacani 2015; Bacchini et al. 2020). To fully understand and quantify the impact SNRs have on the dynamics of star formation in the Milky Way from an observational point of view, having a complete catalog of Galactic SNRs is highly desirable.

⋆ Member of the International Max Planck Research School (IMPRS) for Astronomy and Astrophysics at the Universities of Bonn and Cologne
⋆⋆ Jansky Fellow of the National Radio Astronomy Observatory

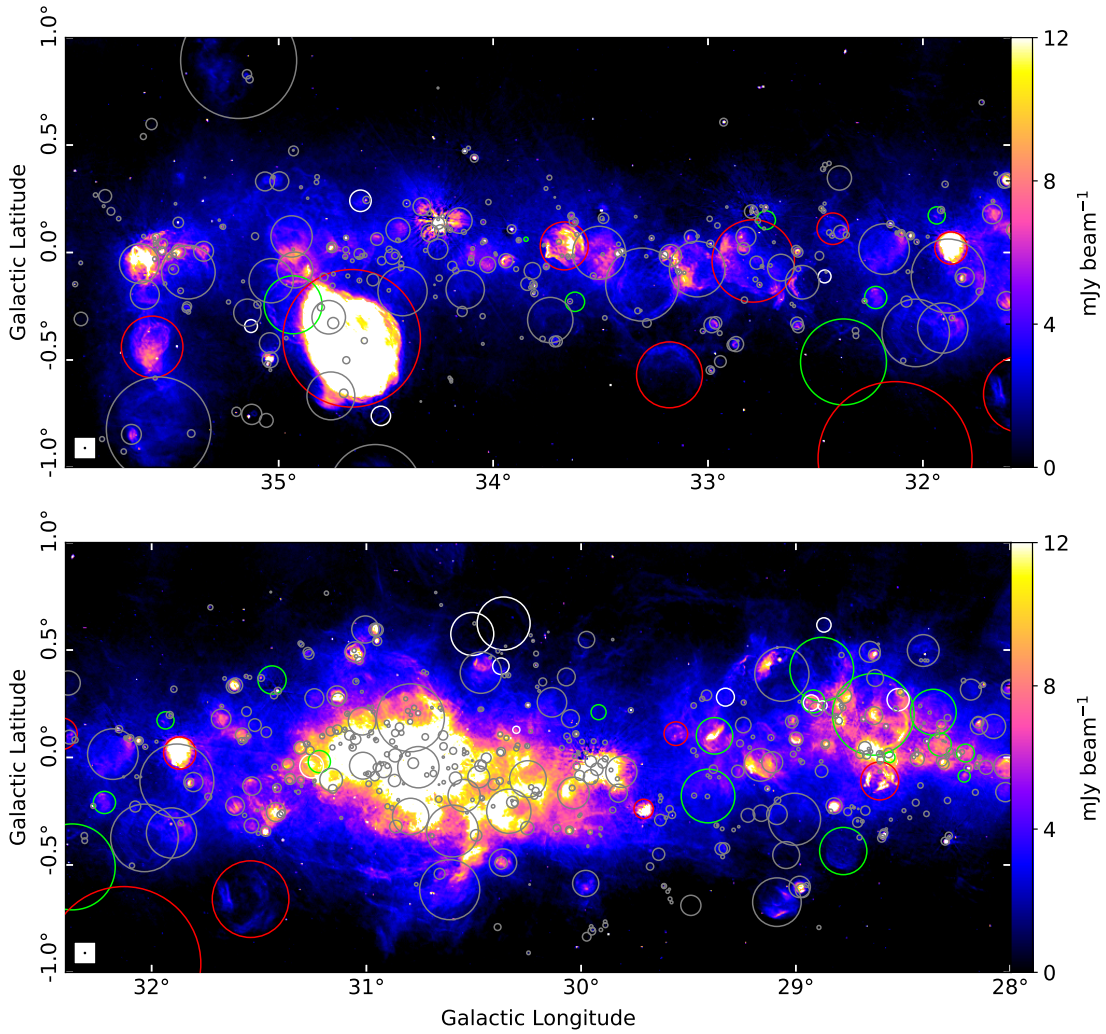

Fig. 1: GLOSTAR combination (VLA-D+Effelsberg; Brunthaler et al. 2021) image of the region of interest of this study, without the restoration using Urumqi maps (see text for details). The red, green, and white circles mark the known SNRs (Ferrand & Safi-Harb 2012; Green 2019), the THOR SNR candidates (from Anderson et al. 2017), and the GLOSTAR SNR candidates (from Dokara et al. 2021), respectively. The much more numerous H II regions, from the WISE catalog (Anderson et al. 2014) and the GLOSTAR VLA D-configuration catalog (Medina et al. 2019), are marked using gray circles.

The most recent Galactic SNR catalogs (Ferrand & Safi-Harb 2012; Green 2019) contain fewer than 400 objects. This number is, however, significantly smaller than the expected ~1000 discussed by Li et al. (1991), who arrived at this estimate by using statistical arguments primarily based on our knowledge of the distances to SNRs in the Milky Way. Ranasinghe & Leahy (2022), using a similar statistical analysis but with improved distances to the currently known SNRs, estimate that the number quoted by Li et al. (1991) must be a lower limit, and that there could be over 3000 SNRs in the Galaxy. It is believed that this apparent discrepancy is only due to SNRs that are fainter and smaller than the currently known sample of SNRs not being detected, rather than insufficient knowledge of the local Universe (Brogan et al. 2006; Anderson et al. 2017: hereafter A17).

In an attempt to improve this situation, recent radio Galactic plane surveys have been carried out with good sensitivity to both compact and extended emission, leading to the identification of well over one hundred SNR candidates (A17; Hurley-Walker et al. 2019; Dokara et al. 2021: D21 from here on). These studies used the radio and mid-infrared (MIR) anticorrelation property of SNRs (Fürst et al. 1987b; Haslam & Osborne 1987). While H II regions emit brightly at both radio and MIR wavelengths,

SNRs are typically bright radio emitters but weak MIR emitters. Fürst et al. (1987b) found that the ratio (R) of 60 μm MIR to 11 cm radio flux density is much higher for H II regions than SNRs ($R_{\rm HII}$~1000 and $R_{\rm SNR}$~15). Multiple other studies subsequently confirmed this anticorrelation property (Broadbent et al. 1989; Whiteoak & Green 1996; Pinheiro Gonçalves et al. 2011).

Most of these SNR candidates are yet to be confirmed as genuine SNRs with clear nonthermal radio emission. In addition, some objects in the Galactic SNR catalogs either do not have good radio measurements (such as G32.1-0.9 and G32.4+0.1), or, worse, the evidence that they emit nonthermal synchrotron radiation is rather weak (e.g., G31.5-0.6; Mavromatakis et al. 2001). It is not uncommon for H II regions, which emit thermally, to be confused as SNRs due to their similar radio morphology (e.g., A17 and D21). The presence of nonthermal synchrotron radio emission is thus vital for determining whether an object is truly a SNR. Synchrotron radiation is linearly polarized and typically has a negative spectral index at frequencies where synchrotron losses do not occur (typically over 1 GHz; Wilson et al. 2013), where the spectral index, α, is determined via a power law fit to the flux density spectrum as $S_\nu \propto \nu^\alpha$, with S_ν being the flux density and ν the frequency. In this work we focus on confirming the status of the SNR candidates and the sample of objects that were cataloged as SNRs (hereafter called "known SNRs") in the Galactic longitude range $28^\circ < l < 36^\circ$ and $|b| < 1^\circ$ (hereafter called "the pilot region") by measuring linearly polarized flux densities (LPFDs) and spectral indices.

The rest of the paper is organized as follows: Sect. 2 contains the descriptions of the data and the methods used for this study. The results for known and candidate SNRs are presented in Sects. 3 and 4, respectively. Their implications are discussed in Sect. 5, and we provide a summary of this work in Sect. 6.

2. Data and methods

2.1. The GLOSTAR survey

The Global View on Star Formation (GLOSTAR) survey[1] is a 4–8 GHz sensitive, unbiased, large-scale continuum and spectral line survey of the first quadrant of the Milky Way, covering the region bounded by the Galactic longitudes $-2^\circ < l < 60^\circ$ and Galactic latitudes $|b| < 1^\circ$, in addition to the Cygnus X star forming complex ($76^\circ < l < 83^\circ$ and $-1^\circ < b < 2^\circ$). The observations were done using the *Karl Jansky* Very Large Array (VLA) in B and D configurations, as well as the 100 meter Effelsberg telescope. Full details of the observations and the data reduction are presented in Medina et al. (2019) and Brunthaler et al. (2021). The catalogs of continuum sources in the GLOSTAR pilot region ($28^\circ < l < 36^\circ$ and $|b| < 1^\circ$) from the VLA images, which contain 1575 sources in the D-configuration images including several SNRs and 1457 in the B-configuration images, are discussed in Medina et al. (2019) and Dzib et al. (2022), respectively. An overview of the survey and initial results are described in Brunthaler et al. (2021). Further results are presented in D21 (SNRs), Ortiz-León et al. (2021, Cygnus X methanol masers), Nguyen et al. (2021, Galactic center continuum sources), and Nguyen et al. (2022, methanol maser catalog). Here, we give a brief overview of the data that we use for this study.

We focus on the GLOSTAR pilot region, which contains numerous extended and compact sources overlapping with a strong Galactic background (see Fig. 1 and also Medina et al. 2019). The W43 mini-starburst complex located at l~30° (where the bar of the Milky Way meets the Scutum–Centaurus Arm; e.g., Zhang et al. 2014) and the W44 SNR at l~35° are among the brightest objects observed in this region. In our previous work (D21), we detected over 150 SNR candidates in the D-configuration Very Large Array (VLA-D) images of the full survey, with the pilot region containing 35 of them. We use only the VLA-D and the Effelsberg continuum images in this work.

Since the VLA-D images do not completely recover emission on scales larger than a few arcminutes, they are not suitable to accurately measure the total flux densities and spectral indices of extended objects such as many SNRs. For this purpose, we use images from the single-dish 100 m Effelsberg telescope and their combination with the VLA-D images. The Effelsberg images of this survey do not contain information on the very large scales (> 1°) due to the baseline subtraction and limited coverage in Galactic latitude ($|b| < 1^\circ$). The large-scale information had been "restored" using the Urumqi 6 cm survey images (Sun et al. 2007, 2011b) to produce the GLOSTAR Effelsberg maps with the correct intensities (see Brunthaler et al. 2021, for details). However, all the objects we study are smaller than half a degree, and since we need to filter out the large-scale background in any case, we use the original maps directly (i.e., without restoration using the Urumqi maps) to avoid a source of uncertainty.

The calibration and imaging of the VLA and the Effelsberg data, along with their feathering for the total power Stokes I images, are described by Brunthaler et al. (2021). Feathering is a method for combining two images with emission from different angular scales, where the two images are co-added in the Fourier domain (uv space) weighted by their spatial frequency response (e.g., Vogel et al. 1984; Cotton 2017). In this work, we exclusively use the combination of VLA-D and Effelsberg data, and hereafter these images are called "the combination images." Since the frequency coverage is not exactly the same on both the VLA and the Effelsberg telescopes, producing the combination images is not straightforward. The final VLA continuum data from the GLOSTAR survey are binned into nine subbands centered on frequencies from ~4.2 GHz to ~7.5 GHz, whereas the Effelsberg continuum maps have two subbands centered at frequencies $f_{\rm E,lo}$~4.9 GHz and $f_{\rm E,hi}$~6.8 GHz (see Brunthaler et al. 2021, for more details). The procedure that we followed to combine the VLA-D and the Effelsberg data for the different Stokes parameters is described below.

2.1.1. Image combination: Stokes I

We averaged the VLA images from the first five subbands at lower frequencies and the next three subbands at higher frequencies separately to form two VLA images, $I_{\rm V,f_{V,lo}}$ and $I_{\rm V,f_{V,hi}}$, respectively. We discard the ninth subband since it is mostly corrupted by radio frequency interference. The first five subbands have an average frequency $f_{\rm V,lo}$~4.7 GHz and the next three subbands have $f_{\rm V,hi}$~6.9 GHz, which are already close to the central frequencies of the Effelsberg continuum data, $f_{\rm E,lo}$~4.9 GHz and $f_{\rm E,hi}$~6.8 GHz, respectively, but they are not exactly equal. To bring the two VLA images ($I_{\rm V,f_{V,lo}}$ and $I_{\rm V,f_{V,hi}}$) to the frequencies of the Effelsberg images, we use a pixel-by-pixel VLA spectral index, $\alpha_{\rm pix}$, to scale the intensities of each pixel:

$$I^{\rm pix}_{\rm V,f_{E,lo}} = I^{\rm pix}_{\rm V,f_{V,lo}} \left(\frac{f_{\rm E,lo}}{f_{\rm V,lo}}\right)^{\alpha_{\rm pix}} \text{ and } I^{\rm pix}_{\rm V,f_{E,hi}} = I^{\rm pix}_{\rm V,f_{V,hi}} \left(\frac{f_{\rm E,hi}}{f_{\rm V,hi}}\right)^{\alpha_{\rm pix}}, \quad (1)$$

[1] https://glostar.mpifr-bonn.mpg.de/glostar/

where $I^{\rm pix}_{\rm V,f_{E,lo}}$ and $I^{\rm pix}_{\rm V,f_{E,hi}}$ are the VLA pixel values estimated at the Effelsberg central frequencies. For pixels with intensities above a signal-to-noise threshold of three, $\alpha_{\rm pix}$ is measured from the two Stokes I images $I_{\rm V,f_{V,lo}}$ and $I_{\rm V,f_{V,hi}}$. For pixels below the threshold, we take a spectral index of zero (i.e., we use the average intensity). After bringing the VLA images to the central frequencies of the Effelsberg images, we feather the VLA and the Effelsberg maps $I_{\rm V,f_{E,lo}} + I_{\rm E,f_{E,lo}}$ to produce the low frequency combination image, and $I_{\rm V,f_{E,hi}} + I_{\rm E,f_{E,hi}}$ to produce the high frequency combination image. Finally, the low and high frequency images are averaged to form the 5.85 GHz GLOSTAR combination image. These combination images will be made available on the GLOSTAR image server[2] before the publication of this work.

2.1.2. Image combination: Stokes Q and U

Similar to the Stokes I procedure, we created the low- and high-frequency VLA images by averaging the first five and next three subbands. We then directly feather each of these averaged images with their respective Effelsberg maps: $P_{\rm V,f_{V,lo}} + P_{\rm E,f_{E,lo}}$ and $P_{\rm V,f_{V,hi}} + P_{\rm E,f_{E,hi}}$, where P represents Stokes Q or U. We do this without any intensity scaling applied to bring them to the exact same frequency as we did for Stokes I. This is because Stokes Q and U have both positive and negative features, and a direct spectral index calculation is not possible. The Stokes Q and U images at each of the two frequencies are then combined to form the linearly polarized intensity maps $\sqrt{Q^2 + U^2}$. The low and high frequency maps are then averaged to form the 5.85 GHz GLOSTAR combination image of linearly polarized intensity.

We note that this method may introduce a bias in the measured polarized intensities and the polarization vectors due to the different central frequencies. However, we find that this bias is negligible since the frequencies are quite close ($f_{\rm V,lo} \approx f_{\rm E,lo}$ and $f_{\rm V,hi} \approx f_{\rm E,hi}$). Assuming a spectral index of -0.7 for synchrotron emission, the different central frequencies of the feathered VLA and Effelsberg images of linearly polarized emission introduce an error of approximately 4%, which is close to the calibration uncertainty. For the polarization vector to change by just five degrees from $f_{\rm V,lo}$ to $f_{\rm E,lo}$, the rotation measure must be greater than about 2500 rad m^{-2}, which is unlikely to be seen in any typical Galactic source. Nonetheless, to introduce this bias in the uncertainty measurement of flux densities and also the instrumental polarization ($\lesssim$2% in both VLA and Effelsberg data), we adopt a conservative 10% error that will be added in quadrature to the usual uncertainty we obtain from the measurement of flux density of an extended source. In addition, we observe that the LPFD measured in the combination images may be lower than the values measured in the VLA-D-only images. This can happen due to the depolarization that occurs when the polarization vectors in the small scale structure detected by the VLA are misaligned with the polarization vectors measured from the Effelsberg data. It is worth noting that, in this study, the exact degree of polarization is not exceptionally important except to the degree it establishes whether the source is or is not polarized, since we only use it as a tool to identify nonthermal emission.

2.2. Supernova remnant catalogs

In D21we presented the list of the SNR candidates that are detected in the VLA-D images of the GLOSTAR survey. It contains 77 objects that were noted as potential SNRs by earlier studies (their table 3), and 80 new identifications as well (their table 4). These candidates were identified using the MIR-radio anticorrelation property of SNRs as discussed earlier.

In the GLOSTAR pilot region, there are 21 candidates discovered in the 1–2 GHz HI/OH/Recombination line survey (THOR; A17) and 14 from the GLOSTAR survey (D21). These 35 candidates, in addition to the 12 confirmed SNRs in the Galactic SNR catalogs by Ferrand & Safi-Harb (2012) and Green (2019), are the targets of this study.

2.3. Ancillary data

In addition to the GLOSTAR survey continuum images previously described, we also used other complementary radio surveys that are able to recover emissions at the scale of several arcminutes: the 1–2 GHz HI/OH/Recombination line survey (Beuther et al. 2016; Wang et al. 2020) combined with the VLA Galactic Plane Survey (VGPS; Stil et al. 2006), which is called the THOR+VGPS[3], the 80–230 MHz GaLactic and Extragalactic All-sky Murchison Widefield Array survey (GLEAM; Hurley-Walker et al. 2019)[4], the Effelsberg 11 cm (∼2.7 GHz) survey of the Galactic plane by Reich et al. (1984)[5], and the 3 cm (10 GHz) survey of the Galactic plane with the Nobeyama telescope by Handa et al. (1987)[6].

2.4. Flux density and spectral index measurements

We used the GLOSTAR combination images to measure the flux densities at 5.85 GHz, in addition to the other surveys mentioned earlier (Sect. 2.3). We note that we do not measure the flux densities from the two subbands to derive an "in-band" GLOSTAR spectral index, since each of those images depends upon—though only partly—the pixel-by-pixel spectral index from the VLA data, which suffer from the problem of the undetected large-scale flux density (see Sect. 2.1.1).

The presence of background emission may bias the value of the measured spectral index. This is particularly true for extended objects in the Galactic plane since the nonthermal Galactic background is strong and ubiquitous at low radio frequencies. In addition, the intensity of this background is dependent on frequency and position (e.g., Paladini et al. 2005). The method of "unsharp masking" (Sofue & Reich 1979) is generally used to filter out the large-scale Galactic emission, but it is not appropriate for smaller scale background emission across an object with the size of a few arcminutes. In this work, we fit a "twisted plane" that removes the background contribution up to a first order variation. Points are chosen around an object such that they represent the background emission in that area, and a two-dimensional least-squares linear fit is performed to the pixel intensities to measure the background variation. The uncertainty from this background subtraction operation is determined by choosing multiple sets of vertices. We subtract the local background in both the total intensity and the polarized intensity images, and we mask pixels typically below a 3σ level, where the noise is determined locally by a sigma-clipping algorithm.

While several objects we discuss in this paper already have their low frequency flux densities derived in multiple previous

[2] https://glostar.mpifr-bonn.mpg.de/glostar/image_server

[3] https://www2.mpia-hd.mpg.de/thor/Data_%26_Publications.html

[4] http://gleam-vo.icrar.org/gleam_postage/q/form

[5] https://www3.mpifr-bonn.mpg.de/survey.html

[6] http://milkyway.sci.kagoshima-u.ac.jp/~handa/

studies, for the sake of consistency with regards to spectral index, we make our own measurements of the flux densities of these objects using the images directly from their survey data, performing background subtraction in the same manner as we do for the GLOSTAR images. We also mask the point sources that are clearly unrelated (e.g., Tian & Leahy 2005) to keep the measurement as accurate as possible. In addition, since radio interferometric artifacts such as radial "spokes" are common near bright sources, we do not measure any flux densities if we are unable to disentangle such effects from the emission of an object. Due to such artifacts, polarization measurements are not possible for about a third of the objects studied in this work.

The spectral index of an object is usually measured by fitting a straight line to the relation between flux densities and frequencies in logarithmic space:

$$\alpha_{\rm FD} = \frac{\log(S_\nu)}{\log(\nu)}. \quad (2)$$

However, the values determined in this manner are sensitive to the presence of background emission. Turtle et al. (1962) introduced the concept of temperature-temperature (TT) plots, in which a spectral index is extracted from the slope of a straight line fit to the pixel intensities at one frequency against the pixel intensities at another frequency. In essence, we integrate over the whole area to measure the flux density spectral index ($\alpha_{\rm FD}$), whereas the TT-plot spectral index ($\alpha_{\rm TT}$) is calculated by measuring the variation of each pixel at different frequencies.

The intensities on TT plots can be represented by brightness temperatures in kelvins, or pixel intensities in Jy beam^{-1}. In this work, we exclusively use pixel intensities, and the spectral index is calculated using

$$\alpha_{\rm TT} = \frac{\log(m_{\rm S})}{\log(\nu_1/\nu_2)}, \quad (3)$$

where $m_{\rm S}$ is the slope of the line that is fit to pixel intensities. This is a more reliable measurement of the spectral index of an extended object because the flux density bias introduced by a constant large-scale background emission moves all the points equally, and hence does not affect the slope of the fit. Since the combination images are produced using the spectral index derived from the VLA-D images, they are not suitable to measure the TT-plot spectral index ($\alpha_{\rm TT}$). We only use the GLOSTAR-Effelsberg images for this purpose. We also measure the flux density spectral index ($\alpha_{\rm FD}$); this serves as a useful consistency check since we subtract the background regardless, as described above.

We note that, at low radio frequencies such as the regime of the GLEAM survey ($\lesssim$200 MHz), absorption effects become important, either via synchrotron self-absorption or free-free absorption (e.g., Wilson et al. 2013; Arias et al. 2019). This lowers the emitted flux at low frequencies and increases the power-law spectral index compared to values determined at higher frequencies. Such a "spectral break" effect had been noted in several SNRs before (e.g., Sun et al. 2011a). Spectral breaks are also observed in pulsar wind nebulae (PWNe) due to the central pulsar's time-dependent energy injection (Reynolds & Chevalier 1984; Woltjer et al. 1997). When we calculate the flux density spectral index in this work, if we clearly see a break, we split the spectrum into two and calculate two spectral indices; if the break is not obvious, we calculate only a single spectral index.

The nonthermal emission from the Galactic disk is polarized, and it may have structure on small scales that is not filtered out by an interferometer. While this is more significant at longer wavelengths, it might affect the GLOSTAR images too (see D21). We verify that in the objects we study in this work, there exist no features with no Stokes I counterparts when measuring the LPFD. In addition, a Ricean polarization bias might introduce a positive offset. This occurs because the LPFD is the square root of the sum of squares ($\sqrt{Q^2 + U^2}$), and any positive or negative noise in Q and U will always add up and result in a nonzero LPFD. We find that this effect is an order of magnitude smaller than the flux densities we report, and in fact there is no need to correct for this bias due to the background subtraction procedure and the 3σ-level mask we use (see Wardle & Kronberg 1974). Nonetheless, the twisted-plane background subtraction procedure is applied to the linearly polarized intensity images as well, which accounts for the Galactic plane polarized background and also any possible Ricean polarization bias.

3. Known SNRs

The Galactic SNR catalogs of Green (2019) and Ferrand & Safi-Harb (2012) list 12 confirmed SNRs in the region we study. In Table 1, we present the GLOSTAR 5.8 GHz integrated flux densities of these SNRs along with their spectral indices. If possible, overlapping H II regions and clearly unrelated point sources are masked while measuring the flux densities, taking special care in crowded regions. If it is unclear whether a particular region of emission belongs to the SNR, we do not remove that region. We find that the flux densities and spectral indices are generally consistent with previous studies. We present the GLOSTAR combination images of some interesting known SNRs and discuss them below. The total intensity images and the linearly polarized intensity images of all the known SNRs studied in this work are shown in Appendix A.

3.1. G29.6+0.1

While we had already detected linear polarization in the SNR G29.6+0.1 using the VLA-D images (in D21), the emission in the combination images seems to be depolarized due to the addition of large-scale information from the GLOSTAR-Effelsberg data. We do not measure any polarized emission over a 1σ upper limit of ~0.1 Jy. The flux densities we measure (see Table 1) appear to be lower than what is expected from the lower limits reported by Gaensler et al. (1999): ~0.41 Jy and ~0.26 Jy at 5 GHz and 8 GHz, respectively. The reason for this inconsistency is unclear. Nonetheless, the broadband spectral index we derive from our measurements (~−0.5) is in line with the TT-plot spectral indices derived by Gaensler et al. (1999). We show the GLOSTAR combination image of the SNR G29.6+0.1 in Fig. 2. The spectrum of this SNR shows that it might be falling more rapidly from 1.4–5.8 GHz than from 0.2–1.4 GHz, suggesting the presence of a spectral break around 1 GHz. But given the uncertainties, we reserve judgment on the changing spectral index.

3.2. G31.5-0.6

We show the GLOSTAR combination Stokes I image of the known SNR G31.5-0.6 along with its flux density spectrum in Fig. 2. We find no significant linear polarization in agreement with the observations of Fürst et al. (1987a), who suggest that this is a SNR–H II region complex. The Stokes I flux densities we measure are consistent with those given by Fürst et al. (1987a) within uncertainties, and we also find a morphology similar to their image. However, the spectral index we derive

Table 1: Flux densities and spectral indices of the known SNRs in the pilot region.

Name	$S_{0.2\mathrm{GHz}}$ (Jy)	$S_{1.4\mathrm{GHz}}$ (Jy)	$S_{2.7\mathrm{GHz}}$ (Jy)	$S_{5.8\mathrm{GHz}}$ (Jy)	$p_{5.8\mathrm{GHz}}$ (%)	$S_{10.5\mathrm{GHz}}$ (Jy)	α_{FD}
G28.6−0.1	15.2 ± 1.6	4.4 ± 0.4	3.4 ± 0.4	1.7 ± 0.2	2.6 ± 0.6	1.4 ± 0.2	−0.61 ± 0.04
G29.6+0.1	0.84 ± 0.11	0.48 ± 0.06	0.25 ± 0.03	0.14 ± 0.02	< 71	–	−0.50 ± 0.12
G29.7−0.3	25.4 ± 2.6	7.0 ± 0.7	3.9 ± 0.4	3.1 ± 0.3	2.3 ± 0.8	1.5 ± 0.2	−0.69 ± 0.05
G31.5−0.6	1.9 ± 0.6	1.6 ± 0.5	1.7 ± 0.2	1.6 ± 0.2	< 81	1.5 ± 0.2	−0.04 ± 0.09
G31.9+0.0	34.3 ± 3.4	16.3 ± 1.6	12.8 ± 1.3	8.8 ± 0.9	0.8 ± 0.2	6.2 ± 0.7	−0.42 ± 0.03
G32.1−0.9	12.5 ± 2.4	3.5 ± 0.5	2.1 ± 0.5	–	–	–	−0.68 ± 0.11
G32.4+0.1	1.1 ± 0.2	0.75 ± 0.13	–	0.53 ± 0.07	< 58	–	−0.21 ± 0.07
G32.8−0.1	16.3 ± 1.7	10.9 ± 1.1	7.3 ± 0.8	6.5 ± 0.9	2.5 ± 1.3	5.9 ± 0.7	−0.27 ± 0.04
G33.2−0.6	5.0 ± 0.5	2.9 ± 0.3	2.3 ± 0.3	1.9 ± 0.3	0.11 ± 0.07	–	−0.29 ± 0.05
G33.6+0.1	26.6 ± 2.7	10.9 ± 1.1	6.9 ± 0.8	5.5 ± 0.7	8.1 ± 1.9	3.5 ± 0.5	−0.50 ± 0.04
G34.7−0.4	320 ± 32	193 ± 19	145 ± 15	112 ± 11	6.8 ± 1.4	57 ± 6	−0.40 ± 0.07
G35.6−0.4	8.6 ± 0.9	8.8 ± 0.9	7.5 ± 0.8	6.0 ± 0.6	7.1 ± 2.0	4.7 ± 0.5	$+0.02 \pm 0.08^{\dagger}$
							$-0.31 \pm 0.07^{\dagger}$

Notes. $S_{0.2\mathrm{GHz}}$, $S_{1.4\mathrm{GHz}}$, $S_{2.7\mathrm{GHz}}$, $S_{5.8\mathrm{GHz}}$, and $S_{10.5\mathrm{GHz}}$ are the continuum flux densities we measured from the 200 MHz GLEAM, the 1.4 GHz THOR+VGPS, 11 cm Effelsberg, the 5.8 GHz GLOSTAR combination, and the 3 cm Nobeyama survey images. $p_{5.8\mathrm{GHz}}$ is the percentage linear polarization measured in the GLOSTAR combination images. If no emission is found, then the 1σ upper limits are quoted. α_{FD} is the broadband spectral index derived from the measured flux densities.
† Since a break in the spectrum is clearly visible, we report both the spectral indices.

from 200 MHz to 10 GHz is essentially zero, which is consistent with our TT-plot result (Fig. 2), but in slight tension with the value of ~ -0.2 given by Fürst et al. (1987a). Even after separating from the region the thermal emission that they reported, we find no evidence for synchrotron emission. In the 24 μm images of MIPSGAL (Multiband Infrared Photometer for Spitzer Galactic plane survey; Carey et al. 2009), we find weak emission following the radio morphology, hinting that the emission may be thermal. Based on sulfur and Hα optical lines, Mavromatakis et al. (2001) also suggest that this may be an H II region instead of a SNR. High resolution deeper observations at lower frequencies will shed more light on the nature of the emission from this object, but the evidence so far suggests that G31.5-0.6 is not a SNR.

3.3. G32.1-0.9

Folgheraiter et al. (1997) discovered the SNR G32.1-0.9 in the X-ray regime, and they found a possible faint radio counterpart in the 11 cm Effelsberg images. A17 reported a possible detection in the THOR+VGPS data too, but no radio spectral index was ever determined. While we cannot confidently identify any counterpart in the GLOSTAR data, the 200 MHz GLEAM image shows a shell that corresponds to the 11 cm Effelsberg and THOR+VGPS detections (Fig. 3). Using these three images, we derive a radio spectral index for this unusually faint SNR for the first time, $\alpha_{\mathrm{FD}} = -0.68 \pm 0.12$. Its average 1 GHz surface brightness is approximately 3×10^{-22} W m^{-2} Hz^{-1} sr^{-1}, which makes it one of the faintest radio SNRs currently known: it is only three times brighter than the faintest SNR known in the Milky Way (G181.1+9.5; Kothes et al. 2017).

3.4. G32.4+0.1

G32.4+0.1 was discovered in the X-ray regime by Yamaguchi et al. (2004), who also noted a possible counterpart in the images of the 1.4 GHz NRAO VLA Sky Survey (NVSS; Condon et al. 1998). The radio emission from this SNR is faint but clearly visible in the GLEAM, the THOR+VGPS and the GLOSTAR combination images, allowing us to measure, for the first time for this SNR, a spectral index of -0.21 ± 0.07 (from the flux densities) and -0.39 ± 0.10 (from a TT plot). The GLOSTAR combination image and the plots for spectral index determination are shown in Fig. 2. As noted in Sect.2.4, the low frequency emission detected in GLEAM may be self-absorbed, which brings the spectral index close to zero; hence we favor the TT-plot spectral index (~ -0.4) for higher frequencies where the effects of synchrotron self-absorption are not important. Linear polarization is undetected, with an upper limit on the linearly polarized flux density of ∼0.3 Jy.

3.5. G32.8-0.1

Green (2019) lists the SNR G32.8-0.1 with an uncertain spectral index of −0.2 based on the work of Caswell et al. (1975), who report a flux density of 12.8 Jy at 408 MHz. Unfortunately, no uncertainties were quoted, but they reported that their error might be large. Later, Kassim (1992) observed this SNR with the VLA at a similar frequency of 330 MHz, and their results are in dispute with the result from Caswell et al. (1975). They measured a significantly higher flux density of ∼32 Jy and consequently a more negative spectral index of ~ -0.5, but no uncertainties were quoted once again. This SNR is clearly visible in the GLOSTAR survey, in addition to the GLEAM and the THOR surveys (Fig. 2), which helps us resolve the tension. Our measurements of flux density (16.3 ± 1.7 Jy at 200 MHz) and spectral index ($\alpha_{\mathrm{TT}} = -0.27 \pm 0.04$) are consistent with the values given by Caswell et al. (1975), which is confirmed by our TT-plot spectral index ($\alpha_{\mathrm{TT}} = -0.32 \pm 0.05$).

3.6. G35.6-0.4

The nature of emission from G35.6-0.4 had been a subject of discussion for a long time. It was included in the early SNR catalogs (e.g., Downes 1971; Milne 1979), but the detection of a radio recombination line by Lockman (1989) among other studies, had cast doubts that the emission is nonthermal (see Green 2009, for an overview). Finally, using higher quality radio con-

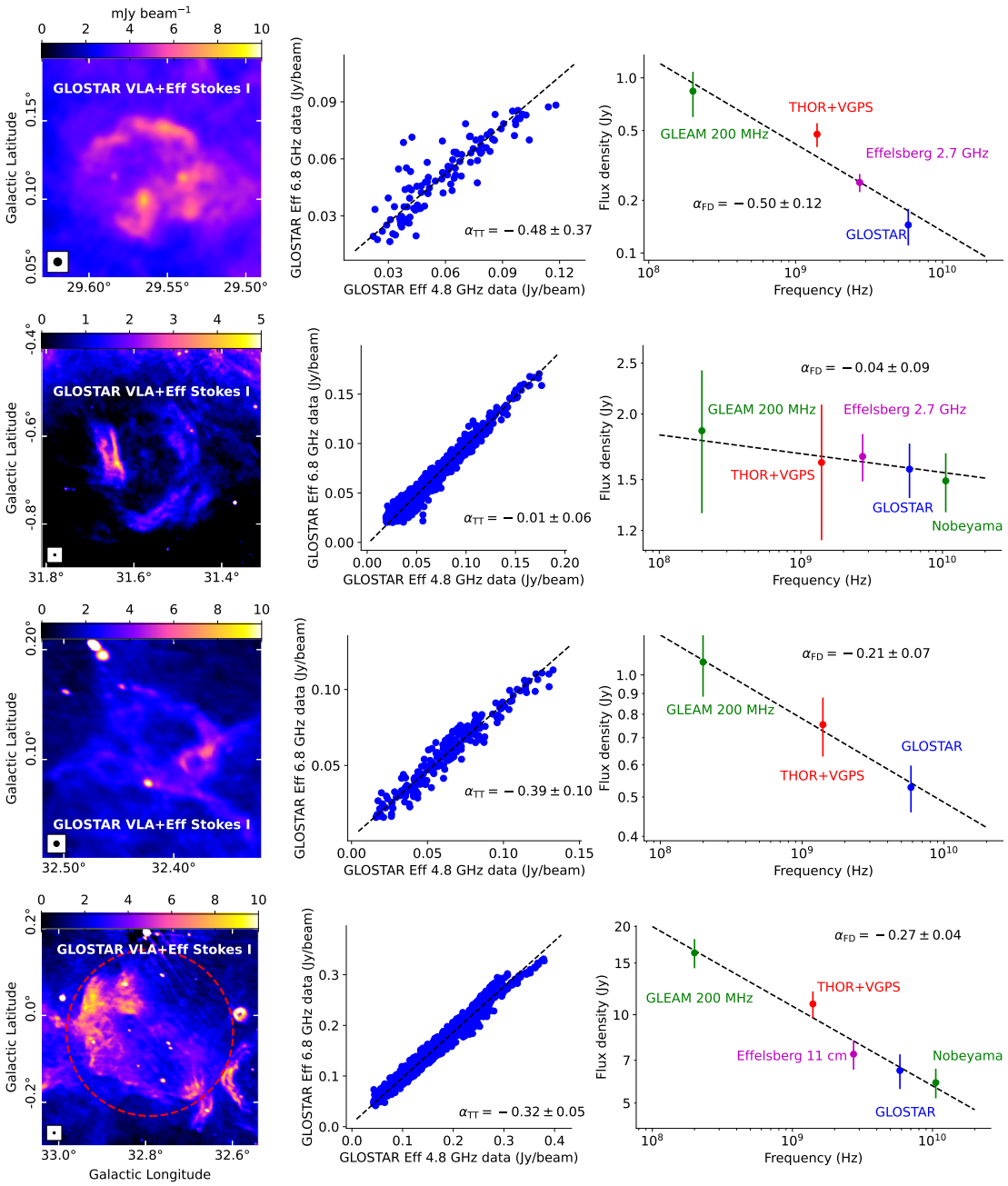

Fig. 2: From top to bottom: G29.6+0.1, G31.5-0.6, G32.4+0.1, and G32.8-0.1. Left panels show the GLOSTAR combination images. The TT plot from the GLOSTAR-Effelsberg images and the flux density spectrum using the GLOSTAR combination images and ancillary data are presented in the middle and right panels, respectively.

tinuum data, Green (2009) "re-identified" this as a SNR with a spectral index of ~ -0.5. This object is clearly visible in the GLOSTAR survey, where we also unambiguously detect linearly polarized emission (Fig. 4). Its spectrum appears to be broken;

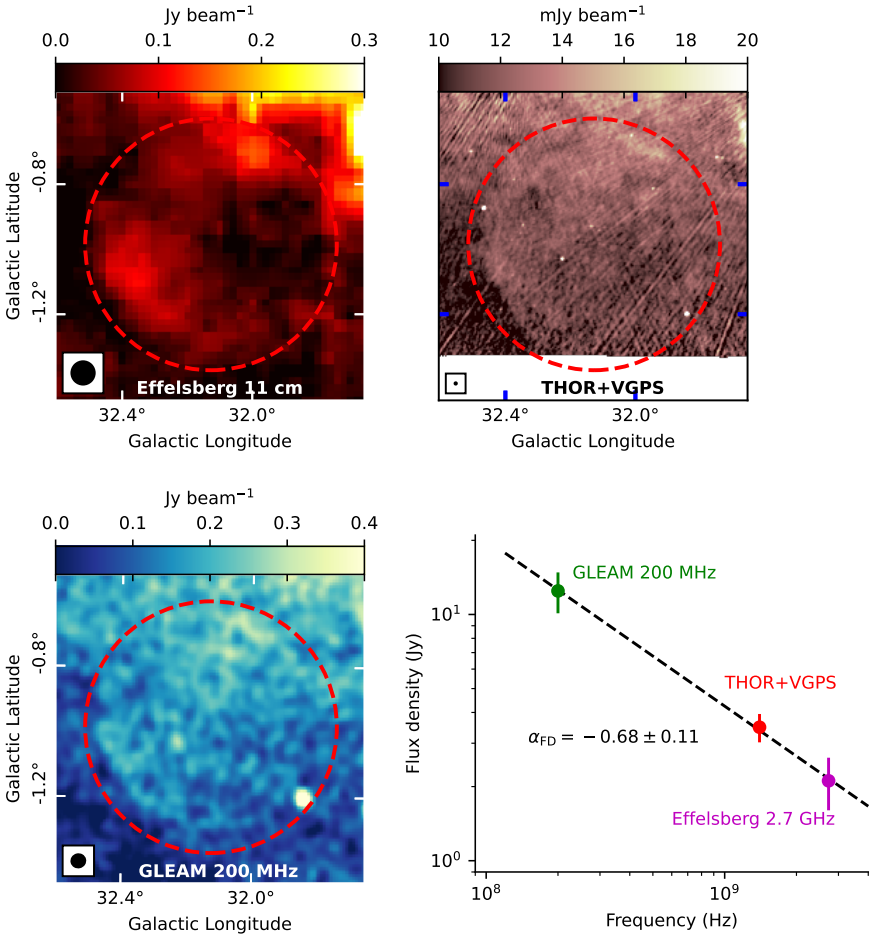

Fig. 3: SNR G32.1-0.9 as seen in the Effelsberg 11 cm (top left), THOR+VGPS (top right), and GLEAM 200 MHz images (bottom left). Its flux density spectrum is shown in the bottom-right panel.

from 200 MHz to 1.4 GHz the flux density has no significant change (α~0), and from 1.4 GHz to 10 GHz it falls with a spectral index of $\alpha = -0.31 \pm 0.07$. This is confirmed with the GLOSTAR Effelsberg TT-plot spectral index as well (Fig. 4). This result ($\alpha \sim -0.3$) is also quite consistent with the spectral index derived by Rennie et al. (2022): $\alpha = -0.34 \pm 0.08$ from 2.7–30 GHz. Green (2009) derives a slightly steeper spectral index of -0.47 ± 0.07. This is probably because of the different choice of polygons used for measuring the flux density and also the subtraction of background emission in this complex region, but we note that the values are consistent within 2σ.

Given the presence of radio recombination lines that indicate thermal emission and a spectral index ~ -0.3, this region appears to be a complex of thermal and nonthermal emissions. Paredes et al. (2014) suggest that there may be two circularly shaped extended objects present in this complex (marked by two red dotted circles in Fig. 4), and with one of them with thermal and the other one with nonthermal emission. We find that MIR emission is detected from the southern part in the GLIMPSE (Galactic Legacy Infrared Mid-Plane Survey Extraordinaire) and MIPSGAL images (Churchwell et al. 2009; Carey et al. 2009), providing further evidence of thermal emission from this region. The linearly polarized emission detected in the GLOSTAR combination data (see Fig. 4) also hints at the presence of two shells, one centered at G35.60-0.40 and the other at G35.55-0.55, similar to those reported by Paredes et al. (2014). However, since we find polarization from both these regions, it is likely that emissions from these regions have both thermal and nonthermal components.

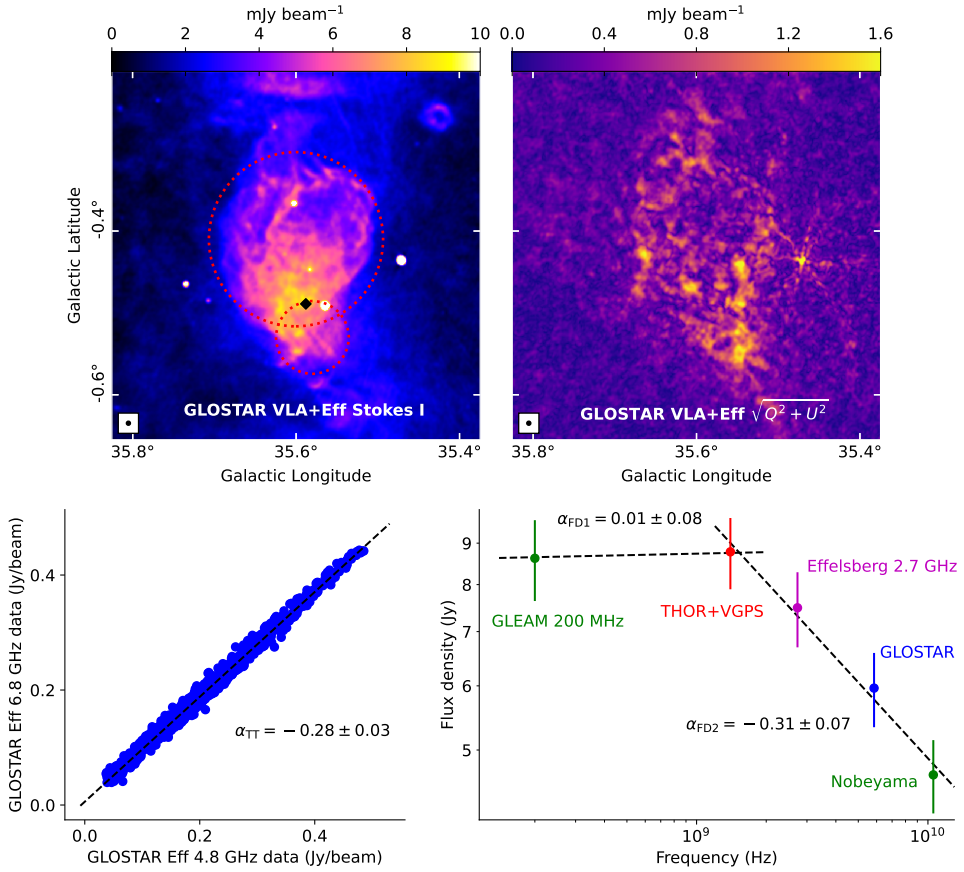

Fig. 4: SNR G35.6-0.4. The top-left and top-right panels show the GLOSTAR combination images of total and linearly polarized intensity. The dotted red circles represent the two shell-like structures identified at 610 MHz by Paredes et al. (2014), while the black diamond marks the position of the recombination line discovered by Lockman (1989). The TT plot from GLOSTAR-Effelsberg images and the flux density spectrum are presented in the bottom-left and the bottom-right panels, respectively.

4. Candidate SNRs

In the pilot region we had discovered 14 new candidate SNRs from the GLOSTAR survey in our previous work (D21), in addition to the 21 candidates discovered by A17 using THOR+VGPS images. The continuum flux densities of these candidates are presented in Table 2 (from THOR+VGPS) and Table 3 (from GLOSTAR). We derived flux density spectral indices whenever possible, and these are plotted in Fig. 5. We discuss five objects for which there is good evidence of nonthermal emission in detail in the following sections. We also find that 14 other candidates possibly have a negative spectral index. But since they are quite faint and the morphology of these candidates is not clear (see Figs. B.1 and B.2), we do not discuss them further.

4.1. G28.36+0.21

First identified by A17 as a SNR candidate using the THOR+VGPS images, G28.36+0.21 has a limb-brightened structure that is typical of SNRs. Hurley-Walker et al. (2019) noted this object as a high confidence level candidate, deriving a spectral index of ~ -0.7 from 70 – 230 MHz. We detect this object in the Stokes *I* images of our GLOSTAR survey (Fig. 6), with the same morphology as observed in the THOR+VGPS images. Its fractional polarization is about 2%, which is not unusual in SNRs (e.g., Sun et al. 2011a). The linearly polarized intensity map from GLOSTAR shows a faint structure, close to the noise level in this region, that resembles the total intensity of the shell of this object. From the Effelsberg images of our survey, we made a TT plot and obtained a spectral index of -0.33 ± 0.14. By measuring the background-subtracted flux densities in the images of GLOSTAR combination, THOR+VGPS and GLEAM, we obtain a spectral index of -0.28 ± 0.11. These measurements and the morphology we observe in the total and linearly polarized intensity images provide ample evidence of nonthermal emission from this object, and hence we conclude that G28.36+0.21 is indeed a SNR.

Table 2: Flux densities and spectral indices of the THOR SNR candidates in the pilot region.

Name	$S_{0.2\mathrm{GHz}}$ (Jy)	$S_{1.4\mathrm{GHz}}$ (Jy)	$S_{5.8\mathrm{GHz}}$ (Jy)	$p_{5.8\mathrm{GHz}}$ (%)	α_{FD}	Remarks
G28.21+0.02	–	0.27 ± 0.03	0.18 ± 0.02	–	−0.30 ± 0.11	SNR?
G28.22−0.09	< 1.5	0.04 ± 0.01	0.05 ± 0.01	< 10	+0.23 ± 0.38	
G28.33+0.06	–	0.56 ± 0.11	0.42 ± 0.06	–	−0.18 ± 0.18	
G28.36+0.21	3.6 ± 0.5	2.2 ± 0.4	1.4 ± 0.4	16 ± 18	−0.28 ± 0.11	SNR: §4.1
G28.56+0.00	0.64 ± 0.15	0.89 ± 0.10	0.77 ± 0.09	5.2 ± 7.1	+0.07 ± 0.08	
G28.64+0.20	–	2.4 ± 0.3	2.2 ± 0.2	< 18	−0.14 ± 0.09	(1,2)
G28.78−0.44	2.2 ± 0.2	1.1 ± 0.1	0.55 ± 0.07	4.4 ± 1.9	−0.42 ± 0.04	SNR: §4.2, (1)
G28.88+0.41	1.8 ± 0.5	2.2 ± 0.6	2.1 ± 0.8	3.3 ± 6.0	+0.02 ± 0.17	
G28.92+0.26	–	–	–	–	–	(3)
G29.38+0.10	2.6 ± 0.3	2.5 ± 0.2	1.6 ± 0.2	5.5 ± 1.0	$-0.04 \pm 0.07^{\dagger}$ $-0.35 \pm 0.07^{\dagger}$	SNR: §4.3, (1)
G29.41−0.18	–	1.27 ± 0.37	0.94 ± 0.24	–	−0.21 ± 0.29	
G29.92+0.21	< 1.4	0.28 ± 0.05	< 0.12	< 1.7	∼ −0.5 to − 0.8	SNR?
G31.22−0.02	–	–	–	–	–	(4)
G31.44+0.36	–	–	–	–	–	(5)
G31.93+0.16	0.24 ± 0.02	0.10 ± 0.04	0.05 ± 0.01	< 80	−0.45 ± 0.07	SNR?
G32.22−0.21	0.36 ± 0.04	0.54 ± 0.09	0.48 ± 0.05	–	+0.10 ± 0.08	
G32.37−0.51	< 14	< 33	< 4.4	< 16	–	
G32.73+0.15	0.41 ± 0.08	0.13 ± 0.07	–	–	−0.68 ± 0.42	SNR?
G33.62−0.23	0.19 ± 0.05	0.15 ± 0.05	< 0.22	< 27	−0.15 ± 0.46	
G33.85+0.06						point sources
G34.93−0.24	0.73 ± 0.17	0.64 ± 0.26	0.82 ± 0.35	–	−0.00 ± 0.19	

Notes. $S_{0.2\mathrm{GHz}}$, $S_{1.4\mathrm{GHz}}$, $S_{5.8\mathrm{GHz}}$, and $p_{5.8\mathrm{GHz}}$ are as defined in Table 1.
(†) Since a break in the spectrum is clearly visible, we report both the spectral indices.
(1) The spectral index of G28.64+0.20, G28.78−0.44 and G29.38+0.10 was derived using flux densities from the Effelsberg 11 cm and the Nobeyama 3 cm surveys as well.
(2) The flux densities of G28.64+0.20 are measured only for the arc-shaped structure to the west.
(3) G28.92+0.26 is resolved to the GLOSTAR candidates G028.929+0.254 and G028.877+0.241.
(4) We study G31.22−0.02 as the GLOSTAR candidate G031.256−0.041.
(5) No measurement possible in any survey, either due to artifact contamination or insufficient sensitivity.

Table 3: Flux densities and spectral indices of the GLOSTAR SNR candidates in the pilot region.

Name	$S_{0.2\mathrm{GHz}}$ (Jy)	$S_{1.4\mathrm{GHz}}$ (Jy)	$S_{5.8\mathrm{GHz}}$ (Jy)	$p_{5.8\mathrm{GHz}}$ (%)	α_{FD}	Remarks
G028.524+0.268	0.50 ± 0.08	0.54 ± 0.06	0.54 ± 0.07	< 18	+0.03 ± 0.06	
G028.870+0.616	0.10 ± 0.01	0.019 ± 0.017	0.026 ± 0.011	< 100	−0.43 ± 0.31	
G028.877+0.241	–	0.023 ± 0.016	0.015 ± 0.011	< 47	−0.33 ± 0.87	
G028.929+0.254	0.74 ± 0.17	0.28 ± 0.03	0.27 ± 0.03	< 17	−0.31 ± 0.14	
G029.329+0.280	< 0.64	< 0.26	0.08 ± 0.02	< 49	> −0.63	
G030.303+0.128	–	< 0.04	0.021 ± 0.003	< 33	> −0.38	
G030.362+0.623	< 0.8	< 1.2	0.11 ± 0.02	< 100	> −0.59	
G030.375+0.424	–	0.04 ± 0.01	0.02 ± 0.01	< 17	−0.58 ± 0.54	
G030.508+0.574	–	–	0.07 ± 0.03	< 100	–	
G031.256−0.041	∼ 0.4	0.33 ± 0.07	0.37 ± 0.05	–	+0.04 ± 0.10	PWN?: §4.4
G032.458−0.112	–	0.03 ± 0.01	0.03 ± 0.01	< 63	+0.11 ± 0.52	
G034.524−0.761	0.83 ± 0.14	0.18 ± 0.03	0.04 ± 0.01	13 ± 10	−0.93 ± 0.15	SNR?: §4.5
G034.619+0.240	0.30 ± 0.10	0.20 ± 0.03	0.20 ± 0.02	< 31	−0.09 ± 0.16	
G035.129−0.343	< 0.11	0.04 ± 0.01	0.033 ± 0.005	< 82	−0.17 ± 0.16	

Notes. $S_{0.2\mathrm{GHz}}$, $S_{1.4\mathrm{GHz}}$, $S_{5.8\mathrm{GHz}}$, and $p_{5.8\mathrm{GHz}}$ are as defined in Table 1.

4.2. G28.78-0.44

The candidate SNR G28.78-0.44 (Fig. 7) had previously been identified in the MAGPIS (Multi-Array Galactic Plane Imaging Survey) and the THOR+VGPS surveys (Helfand et al. 2006; A17). Hurley-Walker et al. (2019) derive a spectral index of ∼ − 0.7 in their GLEAM survey (70–230 MHz), consistent with the spectral index from the TIFR-GMRT Sky Survey and the NRAO VLA Sky Survey (de Gasperin et al. 2018; Dokara et al. 2018). While the polarization from this object was already clearly visible in the VLA images of the GLOSTAR survey (D21), the addition of the Effelsberg data allows us to measure its flux densities at 5.8 GHz. The fractional polarization we measure in the combination images is about 4%. We also detect

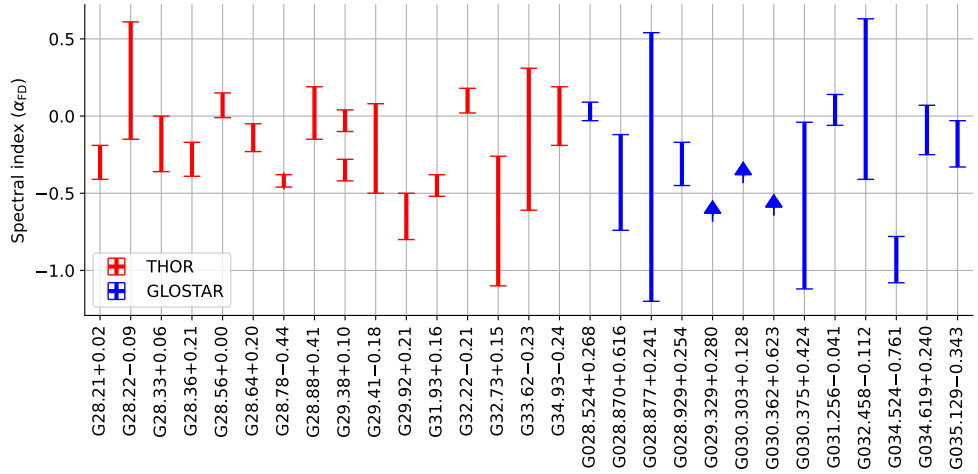

Fig. 5: Flux density spectral indices (α_{FD}) of the candidate SNRs studied in this work. Candidates with lower limits are represented by upward arrows. Since G29.38+0.10 has a spectral break, both spectral indices are shown.

this object in the Effelsberg 11 cm survey (Reich et al. 1984) and the Nobeyama 10 GHz survey (Handa et al. 1987). These give us a broadband flux density spectral index of -0.42 ± 0.04, which is consistent with the TT-plot spectral index from the Effelsberg images of the GLOSTAR survey alone (-0.52 ± 0.12; see Fig. 7). Thus, we find strong evidence that this filled-shell object is a SNR.

4.3. G29.38+0.10

This source appears to have a complex structure with a bright PWN and a faint SNR shell in the GLOSTAR combination image (Fig. 8). The central structure of this complex is bright and highly polarized in the combination images, with the degree of linear polarization reaching as high as 30% in some pixels. For the whole complex, this value is 5.5 ± 0.8%. We had detected strong linear polarization from this object in our previous work as well (D21), which was based only on the VLA-D images. Its low frequency spectral index measured using the GLEAM images by Hurley-Walker et al. (2019) for the whole complex, and for the central source by Dokara et al. (2018) using the TGSS-NVSS spectral index map (de Gasperin et al. 2018) is approximately zero, which is typical of PWNe. We calculate a similar spectral index using the THOR+VGPS and GLEAM images as well. However, between the THOR+VGPS and the GLOSTAR combination images, the flux density falls with a spectral index of $\alpha_{FD} \sim -0.34$. Constructing a TT plot using images from the two bands of the GLOSTAR Effelsberg data, we measure a value $\alpha_{TT} \sim -0.46$. This implies that there is a break in the spectrum of this source near 2 GHz, or a gradual turnover. Such a varying spectral index at these frequencies is once again typical of PWNe (see Pacini & Salvati 1973; Reynolds & Chevalier 1984; Sun et al. 2011a). These facts provide further evidence that G29.38+0.10 is a PWN+SNR shell complex.

4.4. G031.256-0.041

A17 cataloged G31.22-0.02 as a shell-shaped SNR candidate based on the THOR+VGPS images. It lies in a crowded field with a strong background, due to which the determination of the TT-plot spectral index from the Effelsberg images (α_{TT}) was not possible. This region is better resolved in the GLOSTAR combination images, in which we identify the brightest part of the supposed shell of G31.22-0.02 (at $l \sim 31.26°$, $b \sim -0.02°$) to be inside another shell (Fig. 9). We believe that this is a PWN+shell complex, and named it as a GLOSTAR SNR candidate G031.256-0.041 in our previous work (D21). The flux densities we measured in the THOR+VGPS and the GLOSTAR combination images are similar within uncertainties ($S \sim 0.35$ Jy), giving a spectral index close to zero between 1.4 GHz and 5.8 GHz. In the 200 MHz GLEAM images, what we believe is the center of the PWN (at $l \sim 31.26°$, $b \sim -0.02°$) is barely resolved, with a peak brightness of nearly 0.8 Jy beam^{-1}. The background level in this region is about 0.4 Jy, implying that the flux density of the peak is ~0.4 Jy, similar to the flux densities from the GLOSTAR combination and the THOR+VGPS images. Unfortunately, the linearly polarized intensity images from GLOSTAR in this region are contaminated with sidelobe artifacts of nearby bright sources, prohibiting us from measuring its degree of polarization. The morphology and the estimated spectral index are, however, consistent with our PWN+SNR shell interpretation.

4.5. G034.524-0.761

We discovered the SNR candidate G034.524-0.761 in our previous GLOSTAR work, where we had identified clear linear polarization from the VLA data (see Fig. 11 of D21). With the addition of the Effelsberg data to the VLA images, we now obtain a degree of polarization ~10% from this candidate. In addition, we obtain a TT-plot spectral index of ~ -0.6 using the Effelsberg images, although with a large uncertainty of ~0.5. We measured flux densities in the 200 MHz GLEAM and the 1.4 GHz THOR+VGPS images, which give us a spectral index of ~ -0.9.

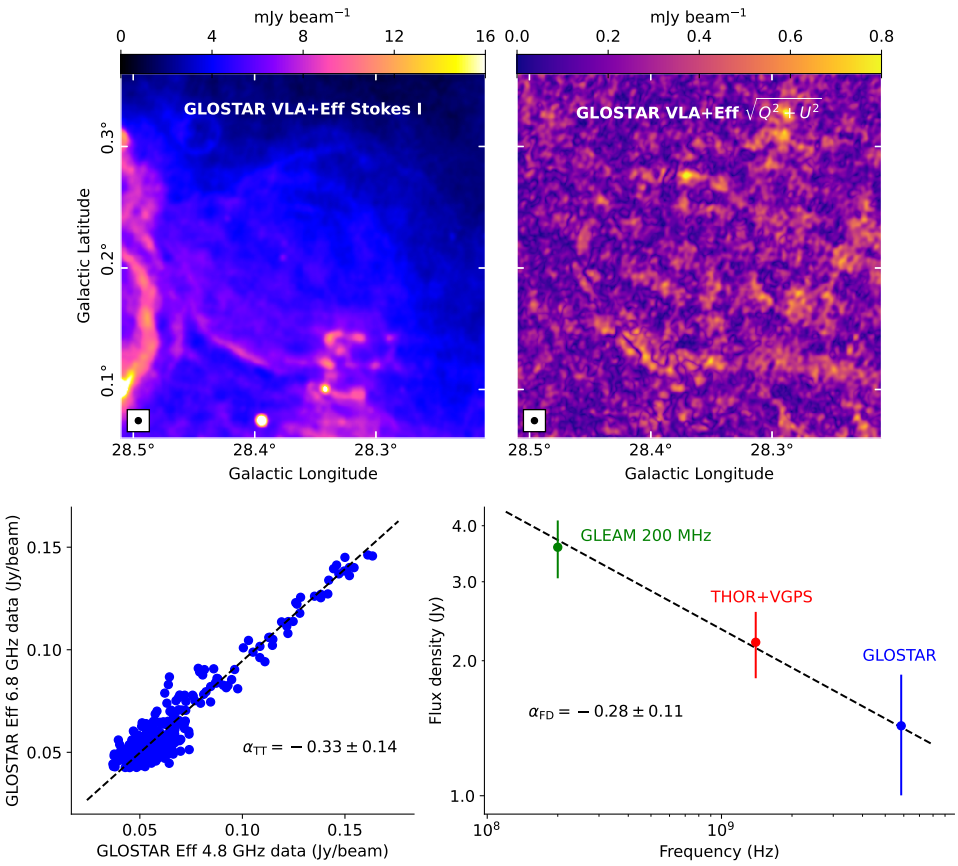

Fig. 6: Same as Fig. 4 but for SNR G28.36+0.21.

While all these facts point to a nonthermal origin of the emission from this region, the morphology of this candidate (Fig. 10) indicates that this might be a filament. For this reason, we cannot conclude that this object is a SNR.

5. Discussion

It is evident from Fig. 5 that the spectral indices of several SNR candidates are not well constrained yet. Most of them have a small angular size and a low surface brightness, and they lie in crowded regions with a strong background; these conditions result in large uncertainties in the measurement of their spectral indices. Moreover, the polarization signals from several SNRs may remain undetected because of limited sensitivity (the LPFD is typically only a few percent of the total flux density; e.g., Sun et al. 2011a). Deeper observations of these candidates across the radio band are necessary to constrain their spectral indices and linear polarization better. However, the current results do not look very promising since the rate of confirmation appears to be quite low, and we are forced to ponder over the strategy to identify new SNRs.

Since most of the bright SNRs are likely to have been discovered already, it might progressively get more difficult to find the remaining fainter ones. H II regions are more numerous in the Galaxy, and there is a chance that the fainter H II regions contaminate the sample of the faint SNRs. However, the SNR candidates identified by A17 and D21 do not have any significant coincident MIR emissions detected in the *Spitzer* MIR surveys, which can detect H II regions anywhere in the Galaxy (Anderson et al. 2014). Hence, we believe that, if the SNR candidates do not turn out to be SNRs, the confusion must be due to radio emitters other than H II regions, although it is unclear what kind of objects they might be. A17 and D21 suggest that the remaining undetected SNRs must be faint and also have a small angular size. We turn our attention toward these properties of the sample of the SNR candidates.

5.1. Angular radius

One question that needs to be answered before starting the search for the remaining SNRs is whether most of them are indeed small, since that would determine what resolution is necessary to detect the "missing" SNRs. To estimate their apparent angular extents, we ran a simple Monte Carlo simulation of evolution of SNRs in the Milky Way. Supernova remnants are evolved in a locally uniform ISM using the expressions from Draine (2011),

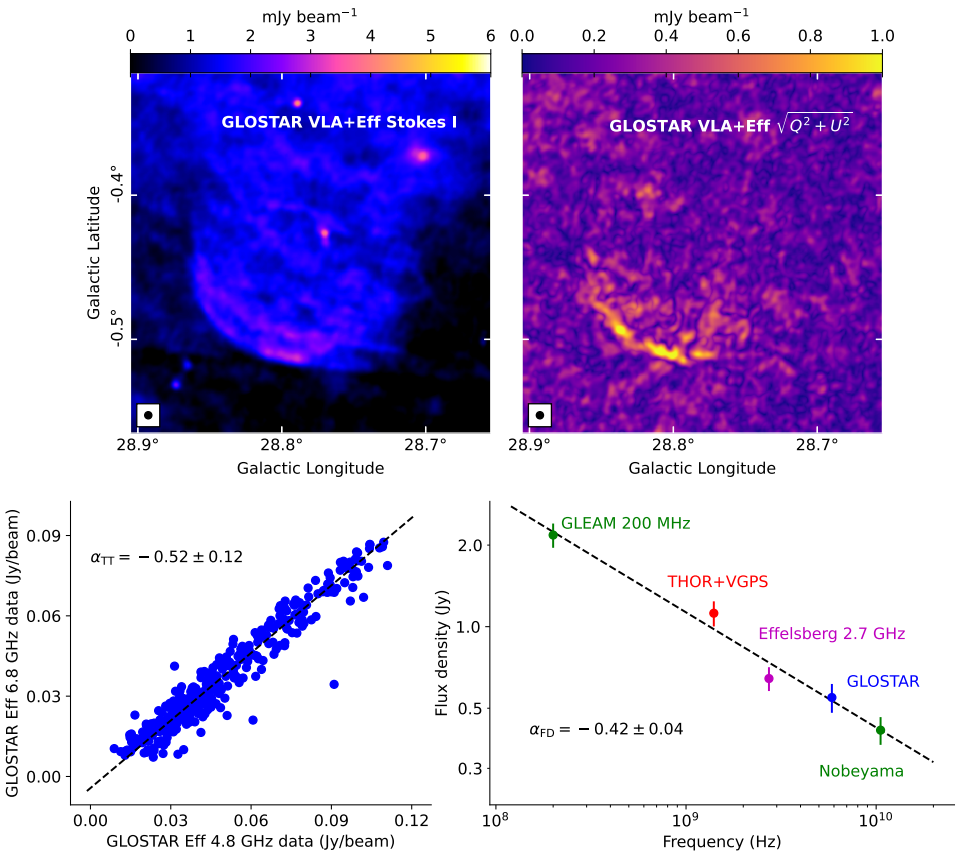

Fig. 7: Same as Fig. 4 but for SNR G28.78-0.44.

which are based on the four classical stages proposed by Woltjer (1972): (1) The earliest part of the evolution is known as the free-expansion or the ejecta-dominated phase. We assume that the mass of the swept up ISM (m_{sw}) is negligible compared to the mass of the SN ejecta (m_{ej}) in this stage. (2) The Sedov-Taylor phase begins when the shocked and swept up mass is comparable to the ejecta mass $m_{sw} \sim m_{ej}$, during which the explosion can be approximated as a point source injecting only energy. (3) The snowplow phase begins when the radiative cooling losses become important and the matter behind the SNR shock cools rapidly to form a cold and dense shell. In the hot and tenuous medium that is interior to the shock, however, the energy losses do not yet play a role, and the pressure from this hot central volume drives the momentum of the dense outer shell. (4) The final phase is "dispersion" as the SNR merges into the surrounding ISM and fades away when the shock speed drops to the ambient velocity dispersion levels.

We derived the radius of each SNR based on the time since explosion and the position in the Galaxy. The main parameters and inputs of the simulation are as follows: (1) the Galactic SN rate is taken to be one per 40 years, with the core-collapse and thermo-nuclear types being 85% and 15%, respectively (Tammann et al. 1994; Reed 2005); (2) the three-dimensional gas density model of the Milky Way from Misiriotis et al. (2006) is used; (3) SN events are obtained from a random Monte Carlo model of the two-dimensional distribution in a disk with a central hole and a two-arm spiral following Li et al. (1991), where the central hole is to account for the dearth of massive star formation, and by extension SNRs, near the Galactic center (see Nguyen et al. 2021; Ranasinghe & Leahy 2022, for example); (4) core-collapse SN events, which trace massive star formation, are chosen to have a scale height of 80 pc, the same as the scale height of the molecular gas (from Misiriotis et al. 2006); (5) type Ia SNe, which arise due to mass accretion onto old degenerate stars, are assumed to follow the thick disk scale height of 0.7 kpc from Kordopatis et al. (2011); (6) the maximum lifetime of SNRs is fixed at 80 000 years (Frail et al. 1994); (7) for a Type Ia SN, the kinetic energy of the ejecta is fixed at 10^{51} erg and the ejecta mass is taken from a random normal distribution that ranges from $0.8M_{\odot}$–$1.8M_{\odot}$ (following Scalzo et al. 2014); (8) for the more numerous core-collapse SN events, the ejecta mass ($8M_{\odot}$–$11M_{\odot}$) and the kinetic energy (0.2–1.3 times 10^{51} erg) are randomly drawn from distributions adapted from the results of Martinez et al. (2022).

There are, however, some caveats to consider. The first is that, realistically, the properties of the ISM are not smoothly

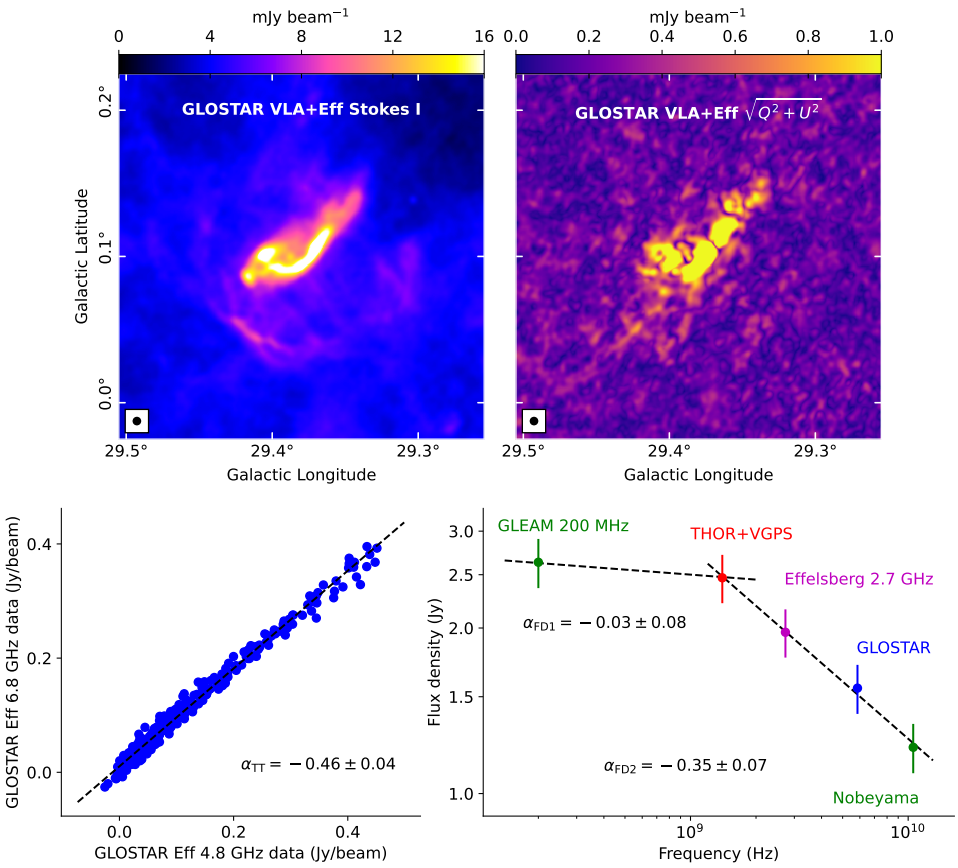

Fig. 8: Same as Fig. 4 but for SNR G29.38+0.10.

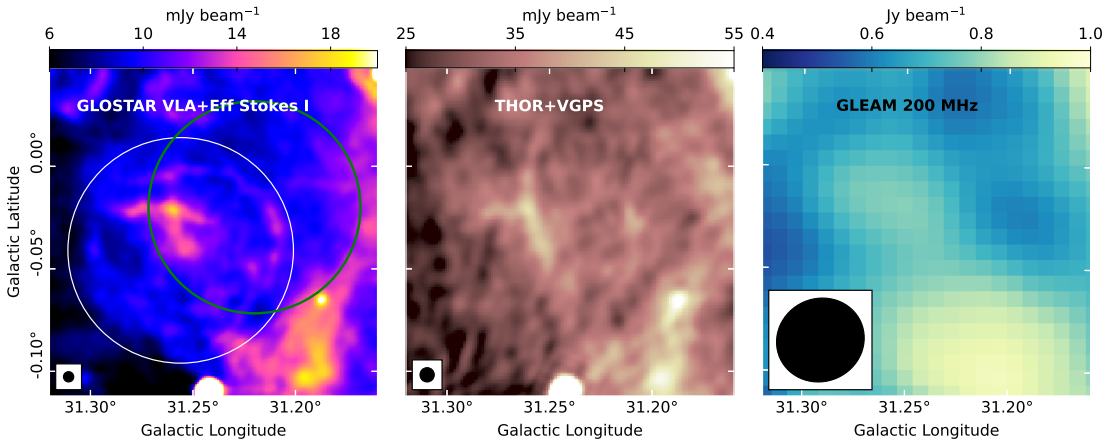

Fig. 9: GLOSTAR SNR candidate G031.256-0.041 as seen in the GLOSTAR combination, THOR+VGPS, and 200 MHz GLEAM images. The white circle marks the extent of the GLOSTAR candidate G031.256-0.041, and the green circle marks the THOR SNR candidate G31.22-0.02.

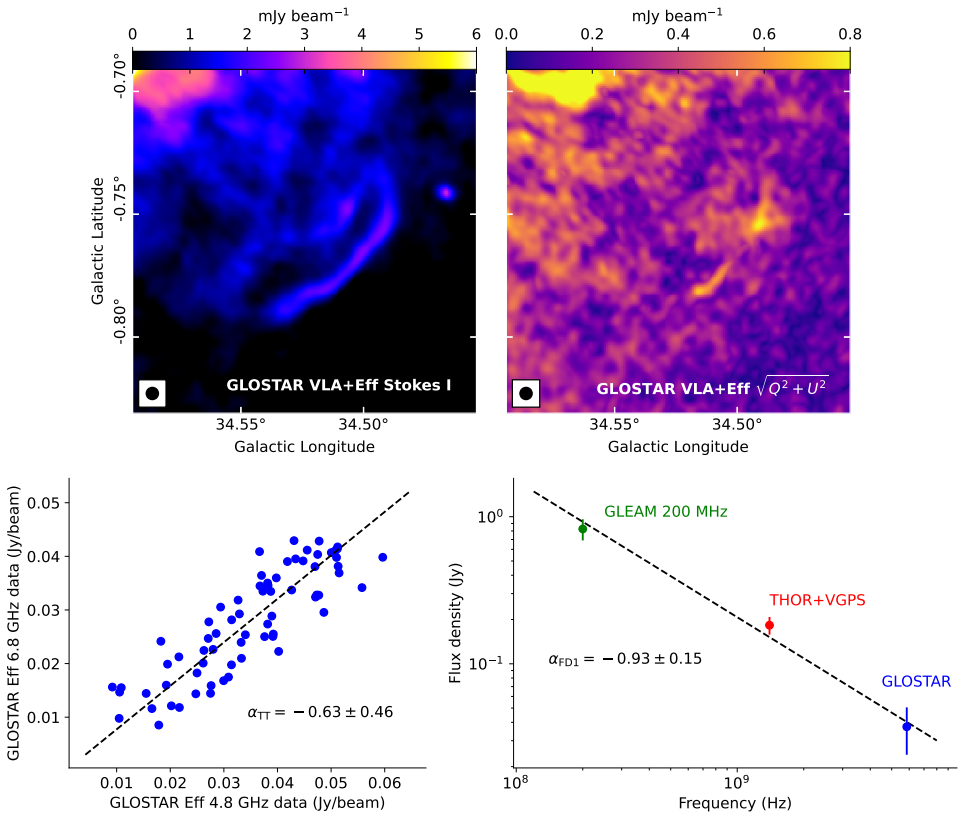

Fig. 10: Same as Fig. 4 but for GLOSTAR SNR candidate G034.524-0.761.

varying functions of position as the model given by Misiriotis et al. (2006). The ISM number density can drastically change depending on the environment, especially in the case of previous mass-loss events such as stellar winds. These affect the evolution of SNRs in a crucial and nontrivial manner (e.g., Yasuda et al. 2021).

Second, the distribution of SN events follows the model of Li et al. (1991), which is quite simplistic. But similar to their findings, we also observe that the results are insensitive to parameters of the disk and the spiral arms. The inverse dependence of angular radius with distance makes our result even more robust than that of Li et al. (1991).

Third, the distributions of ejecta mass we used (from Scalzo et al. 2014; Martinez et al. 2022) may not hold for the Milky Way accurately, since those results are from the nearby local Universe with SNe from several galaxies. However, we find that even if the ejecta mass for core-collapse SNe was only $1 M_\odot$ instead of $8 M_\odot$–$11 M_\odot$, the results are mostly the same.

Fourth, there is evidence that the explosion energies of SNe can have a range wider than that we have taken, for both Type Ia and core-collapse, from $\sim 10^{49}$ to $\sim 10^{52}$ erg (e.g., Benetti et al. 2005; Fisher & Jumper 2015; Pejcha & Thompson 2015; Murphy et al. 2019; Leahy et al. 2020). Even with a wider range, we find that the resultant radius distribution does not significantly change.

Finally, we did not take the effects of clustering into account. This is the main drawback of this simulation. A significant fraction of massive star formation—and the number of SN events by extension—happens in clusters (e.g., Krumholz 2014). Ferrière (2001) estimates that ~60% of O stars probably remain in their natal group, while the rest of them end up in the "field." If multiple SNe occur in succession in such clusters, this might result in the formation of a super-bubble (e.g., Ehlerová & Palouš 2013).

We ran the simulation for two million years, which is several generations of SNRs. A snapshot at a time of 1.8 million years is presented in Fig. 11, and a movie of the whole two million years is available online. Given that the lifetime of a SNR and the SN rate are fixed at 80,000 years and one for every 40 years, respectively, about 2000 SNRs exist at the end of the simulation. It is clear that most of the SNRs are quite small with angular radii of only a few arcminutes, similar to the THOR and GLOSTAR SNR candidates. Even if the lifetime of a typical SNR is longer than 80,000 years as we had used, the resultant distribution does not shift to higher angular scales significantly. This is due to the fact that the expansion is considerably slower in the later stages of SNR evolution. While this simulation only serves as a first approximation since we do not consider several effects such as those mentioned above, it is nevertheless useful to give us an idea of what to expect. And the result reiterates the views of

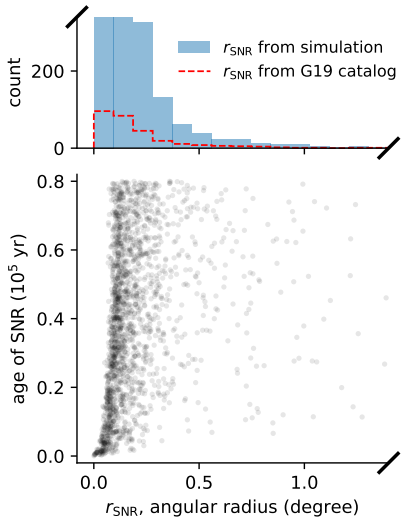

Fig. 11: Snapshot of the age and the angular radius distribution of SNRs (as seen from the Sun) from the simulation, at a time of 1.8 million years, is shown in the bottom panel. The angular radius distribution is shown on the top panel in blue, along with the distribution of the SNRs in the catalog of Green (2019) in dashed red lines. The axes are clipped to show the distributions better.

A17 and D21 that SNR searches must focus on small angular sized objects to make the most gains.

5.2. Radio surface brightness

In the simulation described above, we also measured the area of overlap of SNRs. We find it to be typically less than 10% of the total sky area covered by SNRs, suggesting that the confusion due to SNRs overlapping themselves may not be important. However, the SNRs originating from core-collapse events are located near massive star forming complexes, which also contain other extended structures emitting at radio wavelengths. H II regions are the most likely sources of positional overlapping confusion: they are probably over 8000 in number (Anderson et al. 2014), and the range of the values their radio surface brightness is similar to that of SNRs.

Currently, the faintest SNR known has a brightness temperature of about 0.33 K at 1 GHz (Kothes et al. 2017), and, by extrapolating to 1 GHz assuming a nonthermal spectral index, we find that the SNR candidates from A17 and D21 are at a similar or lower surface brightness. On the other hand, the background emission from the diffuse gas in the Milky Way is at a level of a few kelvins in the inner Galactic plane at 1 GHz (e.g., Reich et al. 1990), and it is even higher in regions such as the mini-starburst W43 where one expects many SNRs due to recent massive star formation activity. This implies that the diffuse background emission is a critical source of confusion, and finding new SNRs will probably be more difficult from now on. Interferometric surveys at lower frequencies, such as MeerKAT, appear promising in the search for new SNRs (e.g., Heywood et al. 2022), but the nonthermal Galactic background emission is also stronger at lower frequencies and may contribute to the confusion.

6. Summary and conclusions

We have derived spectral indices of previously confirmed SNRs in the Galactic longitude range $28° < l < 36°$ using the VLA-D+Effelsberg combination images of the 4–8 GHz GLOSTAR survey in addition to other complementary and archival survey data. This includes the first radio spectral index determinations for SNRs G32.1-0.9 and G32.4+0.1, along with the first reported spectral break for SNR G35.6-0.4. We have shown that G31.5-0.6 may not be a SNR, and we have provided further evidence of nonthermal emission from the SNR candidates G28.36+0.21, G28.78-0.44, G29.38+0.10, and G034.524-0.761. We find that G28.36+0.21 and G28.78-0.44 are typical SNR shells, and G29.38+0.10 is a PWN+shell complex. Based on a simple Monte Carlo simulation of SN events in the Milky Way, we find that most of the SNRs yet to be discovered must have angular sizes smaller than half a degree. Hence, despite the low rate of confirmation, we believe that future studies must focus on small-angular-sized objects such as the THOR and GLOSTAR SNR candidates. The forthcoming Effelsberg images from the GLOSTAR survey for the rest of the coverage will be analyzed in the coming months, which will undoubtedly help us study more SNRs and candidates in the near future.

Acknowledgements. Partly based on observations with the 100-m telescope of the MPIfR (Max-Planck-Institut für Radioastronomie) at Effelsberg. HB acknowledges support from the European Re-search Council under the Horizon 2020 Framework Programme via the ERC Consolidator Grant CSF-648505. HB also acknowledges support from the Deutsche Forschungsgemeinschaft in the Collaborative Research Center (SFB 881) "The Milky Way System" (subproject B1). NR acknowledges support from MPG through Max-Planck India partner group grant. This research has made use of NASA's Astrophysics Data System and the SIMBAD database. We have used the softwares Astropy (Astropy Collaboration et al. 2013), APLpy (Robitaille & Bressert 2012), and DS9 (Joye & Mandel 2003) at various stages of this research.

References

Anderson, L. D., Bania, T. M., Balser, D. S., et al. 2014, ApJS, 212, 1
Anderson, L. D., Wang, Y., Bihr, S., et al. 2017, A&A, 605, A58
Arias, M., Vink, J., Zhou, P., et al. 2019, AJ, 158, 253
Astropy Collaboration, Robitaille, T. P., Tollerud, E. J., et al. 2013, A&A, 558, A33
Bacchini, C., Fraternali, F., Iorio, G., et al. 2020, A&A, 641, A70
Benetti, S., Cappellaro, E., Mazzali, P. A., et al. 2005, ApJ, 623, 1011
Beuther, H., Bihr, S., Rugel, M., et al. 2016, A&A, 595, A32
Broadbent, A., Haslam, C. G. T., & Osborne, J. I. 1989, MNRAS, 237, 381
Brogan, C. L., Gelfand, J. D., Gaensler, B. M., Kassim, N. E., & Lazio, T. J. W. 2006, ApJ, 639, L25
Brunthaler, A., Menten, K. M., Dzib, S. A., et al. 2021, A&A, 651, A85
Carey, S. J., Noriega-Crespo, A., Mizuno, D. R., et al. 2009, PASP, 121, 76
Caswell, J. L., Clark, D. H., & Crawford, D. F. 1975, Australian Journal of Physics Astrophysical Supplement, 37, 39
Churchwell, E., Babler, B. L., Meade, M. R., et al. 2009, PASP, 121, 213
Condon, J. J., Cotton, W. D., Greisen, E. W., et al. 1998, AJ, 115, 1693
Cotton, W. D. 2017, PASP, 129, 094501
de Gasperin, F., Intema, H. T., & Frail, D. A. 2018, MNRAS, 474, 5008
Dokara, R., Brunthaler, A., Menten, K. M., et al. 2021, A&A, 651, A86
Dokara, R., Roy, N., Beuther, H., et al. 2018, ApJ, 866, 61
Downes, D. 1971, AJ, 76, 305
Draine, B. T. 2011, Physics of the Interstellar and Intergalactic Medium
Dubner, G. & Giacani, E. 2015, A&A Rev., 23, 3
Dzib, S. A., Yang, A. Y., Urquhart, J. S., et al. 2022, arXiv e-prints, arXiv:2210.00560
Efstathiou, G. 2000, MNRAS, 317, 697
Ehlerová, S. & Palouš, J. 2013, A&A, 550, A23
Ferrand, G. & Safi-Harb, S. 2012, Advances in Space Research, 49, 1313
Ferrière, K. M. 2001, Reviews of Modern Physics, 73, 1031

Fisher, R. & Jumper, K. 2015, ApJ, 805, 150
Folgheraiter, E. L., Warwick, R. S., Watson, M. G., & Koyama, K. 1997, MNRAS, 292, 365
Frail, D. A., Goss, W. M., & Whiteoak, J. B. Z. 1994, ApJ, 437, 781
Fürst, E., Reich, W., Reich, P., Handa, T., & Sofue, Y. 1987a, A&AS, 69, 403
Fürst, E., Reich, W., & Sofue, Y. 1987b, A&AS, 71, 63
Gaensler, B. M., Gotthelf, E. V., & Vasisht, G. 1999, ApJ, 526, L37
Green, D. A. 2009, MNRAS, 399, 177
Green, D. A. 2019, Journal of Astrophysics and Astronomy, 40, 36
Handa, T., Sofue, Y., Nakai, N., Hirabayashi, H., & Inoue, M. 1987, PASJ, 39, 709
Haslam, C. G. T. & Osborne, J. L. 1987, Nature, 327, 211
Helfand, D. J., Becker, R. H., White, R. L., Fallon, A., & Tuttle, S. 2006, AJ, 131, 2525
Heywood, I., Rammala, I., Camilo, F., et al. 2022, ApJ, 925, 165
Hurley-Walker, N., Hancock, P. J., Franzen, T. M. O., et al. 2019, PASA, 36, e047
Joye, W. A. & Mandel, E. 2003, Astronomical Society of the Pacific Conference Series, Vol. 295, New Features of SAOImage DS9, ed. H. E. Payne, R. I. Jedrzejewski, & R. N. Hook, 489
Kassim, N. E. 1992, AJ, 103, 943
Kordopatis, G., Recio-Blanco, A., de Laverny, P., et al. 2011, A&A, 535, A107
Kothes, R., Reich, P., Foster, T. J., & Reich, W. 2017, A&A, 597, A116
Krumholz, M. R. 2014, Phys. Rep., 539, 49
Leahy, D. A., Ranasinghe, S., & Gelowitz, M. 2020, ApJS, 248, 16
Li, Z., Wheeler, J. C., Bash, F. N., & Jefferys, W. H. 1991, ApJ, 378, 93
Lockman, F. J. 1989, ApJS, 71, 469
Martinez, L., Bersten, M. C., Anderson, J. P., et al. 2022, A&A, 660, A41
Mavromatakis, F., Papamastorakis, J., Ventura, J., et al. 2001, A&A, 370, 265
Medina, S. N. X., Urquhart, J. S., Dzib, S. A., et al. 2019, A&A, 627, A175
Milne, D. K. 1979, Australian Journal of Physics, 32, 83
Misiriotis, A., Xilouris, E. M., Papamastorakis, J., Boumis, P., & Goudis, C. D. 2006, A&A, 459, 113
Murphy, J. W., Mabanta, Q., & Dolence, J. C. 2019, MNRAS, 489, 641
Nguyen, H., Rugel, M. R., Menten, K. M., et al. 2021, A&A, 651, A88
Nguyen, H., Rugel, M. R., Murugeshan, C., et al. 2022, A&A, 666, A59
Ortiz-León, G. N., Menten, K. M., Brunthaler, A., et al. 2021, A&A, 651, A87
Ostriker, E. C. & Shetty, R. 2011, ApJ, 731, 41
Pacini, F. & Salvati, M. 1973, ApJ, 186, 249
Paladini, R., De Zotti, G., Davies, R. D., & Giard, M. 2005, MNRAS, 360, 1545
Paredes, J. M., Ishwara-Chandra, C. H., Bosch-Ramon, V., et al. 2014, A&A, 561, A56
Pejcha, O. & Thompson, T. A. 2015, ApJ, 801, 90
Pinheiro Gonçalves, D., Noriega-Crespo, A., Paladini, R., Martin, P. G., & Carey, S. J. 2011, AJ, 142, 47
Ranasinghe, S. & Leahy, D. 2022, arXiv e-prints, arXiv:2209.04570
Reed, B. C. 2005, AJ, 130, 1652
Reich, W., Fürst, E., Haslam, C. G. T., Steffen, P., & Reif, K. 1984, A&AS, 58, 197
Reich, W., Reich, P., & Fuerst, E. 1990, A&AS, 83, 539
Rennie, T. J., Harper, S. E., Dickinson, C., et al. 2022, ApJ, 933, 187
Reynolds, S. P. & Chevalier, R. A. 1984, ApJ, 278, 630
Robitaille, T. & Bressert, E. 2012, APLpy: Astronomical Plotting Library in Python, Astrophysics Source Code Library, record ascl:1208.017
Scalzo, R. A., Ruiter, A. J., & Sim, S. A. 2014, MNRAS, 445, 2535
Sofue, Y. & Reich, W. 1979, A&AS, 38, 251
Stil, J. M., Taylor, A. R., Dickey, J. M., et al. 2006, AJ, 132, 1158
Sun, X. H., Han, J. L., Reich, W., et al. 2007, A&A, 463, 993
Sun, X. H., Reich, P., Reich, W., et al. 2011a, A&A, 536, A83
Sun, X. H., Reich, W., Han, J. L., et al. 2011b, A&A, 527, A74
Tammann, G. A., Loeffler, W., & Schroeder, A. 1994, ApJS, 92, 487
Tian, W. W. & Leahy, D. 2005, A&A, 436, 187
Turtle, A. J., Pugh, J. F., Kenderdine, S., & Pauliny-Toth, I. I. K. 1962, MNRAS, 124, 297
Vogel, S. N., Wright, M. C. H., Plambeck, R. L., & Welch, W. J. 1984, ApJ, 283, 655
Wang, Y., Beuther, H., Rugel, M. R., et al. 2020, A&A, 634, A83
Wardle, J. F. C. & Kronberg, P. P. 1974, ApJ, 194, 249
Whiteoak, J. B. Z. & Green, A. J. 1996, A&AS, 118, 329
Wilson, T. L., Rohlfs, K., & Hüttemeister, S. 2013, Tools of Radio Astronomy
Woltjer, L. 1972, ARA&A, 10, 129
Woltjer, L., Salvati, M., Pacini, F., & Bandiera, R. 1997, A&A, 325, 295
Yamaguchi, H., Ueno, M., Koyama, K., Bamba, A., & Yamauchi, S. 2004, PASJ, 56, 1059
Yasuda, H., Lee, S.-H., & Maeda, K. 2021, ApJ, 919, L16
Zhang, B., Moscadelli, L., Sato, M., et al. 2014, ApJ, 781, 89

Appendix A: Images of the known SNRs studied in this work

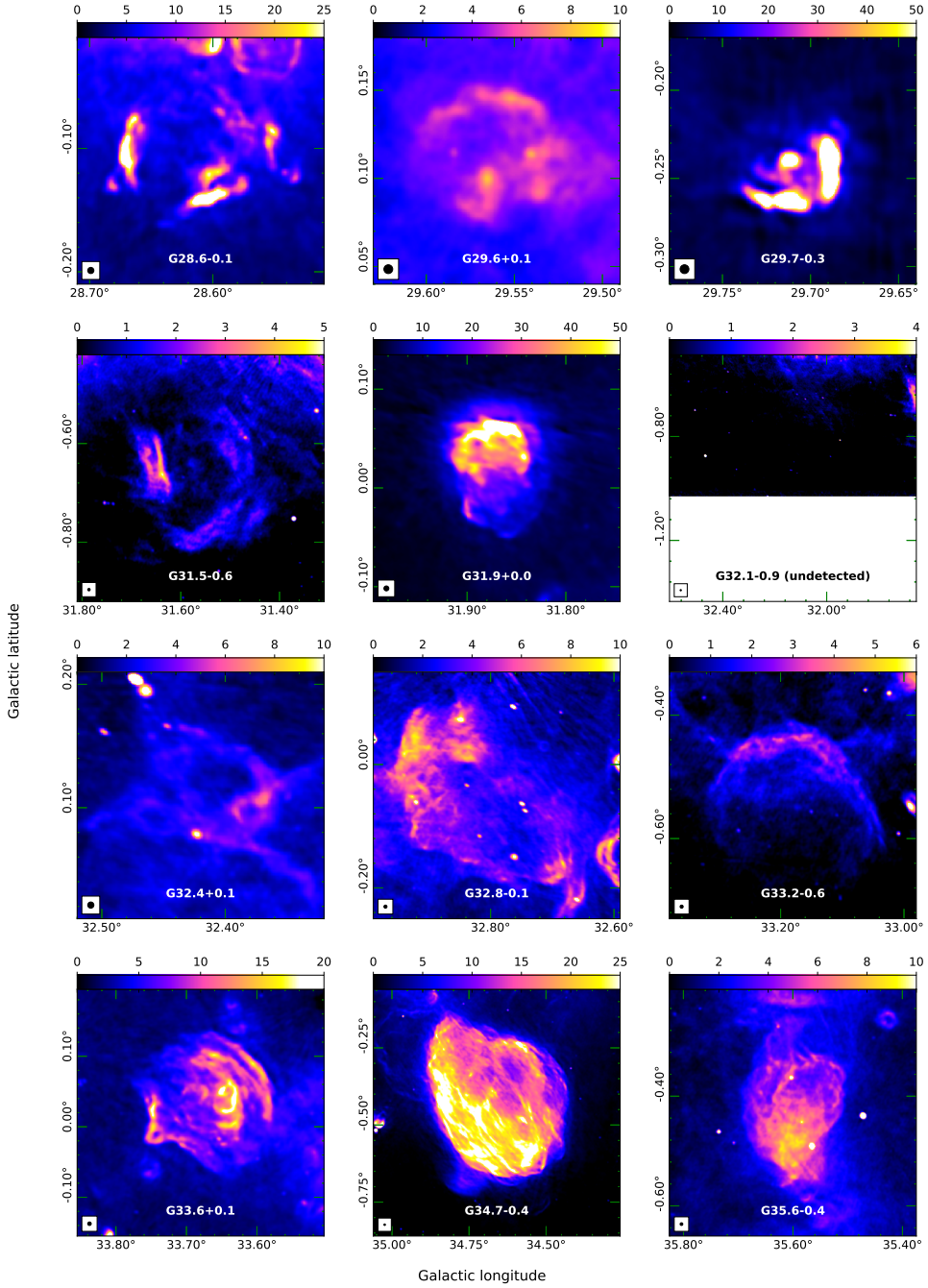

Fig. A.1: Total intensity maps of the GLOSTAR combination data of known SNRs in the pilot region in mJy beam^{-1}.

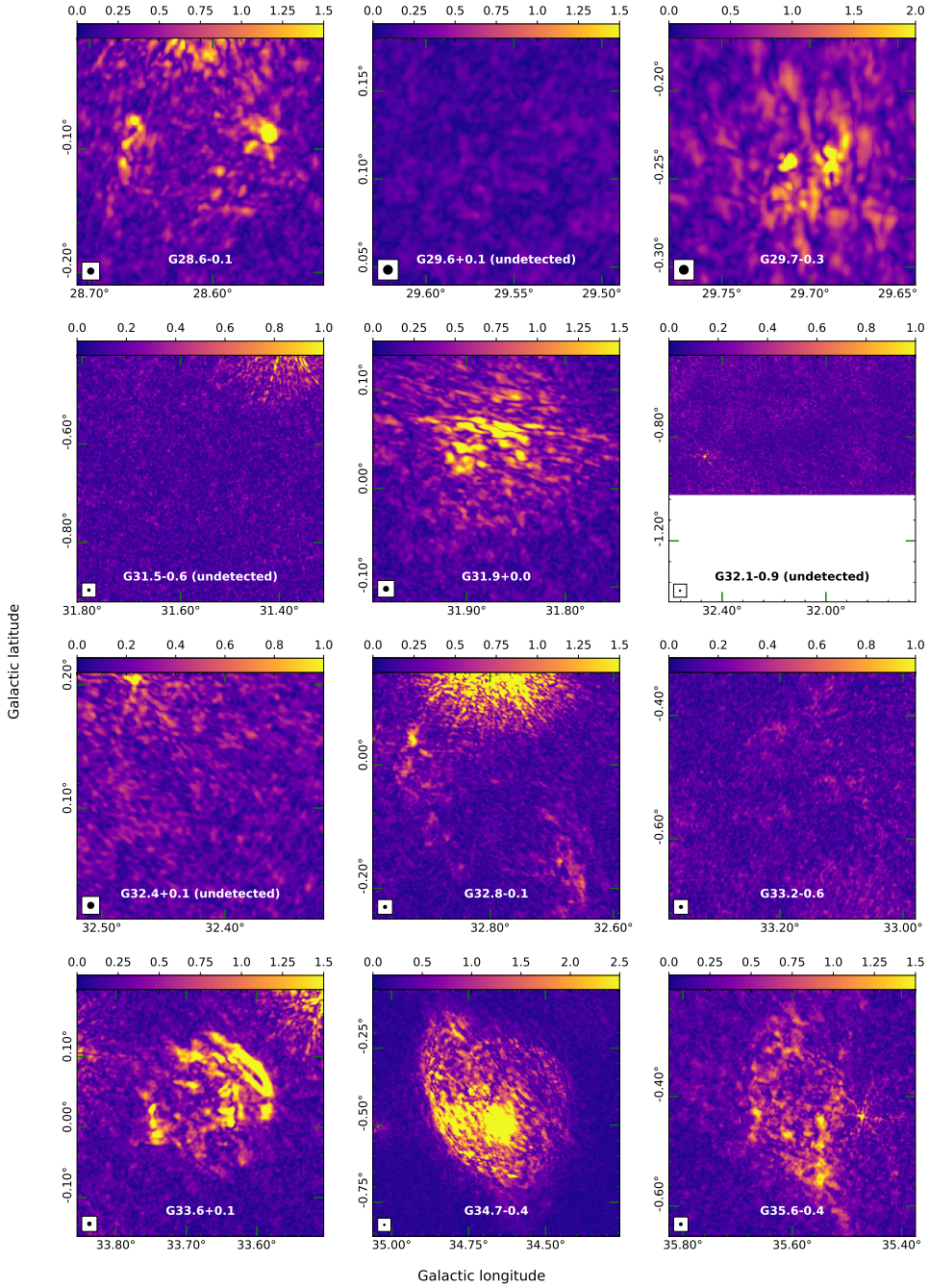

Fig. A.2: Linearly polarized intensity maps of the GLOSTAR combination data of known SNRs in the pilot region in mJy beam^{-1}.

Appendix B: Images of the SNR candidates with an unclear morphology

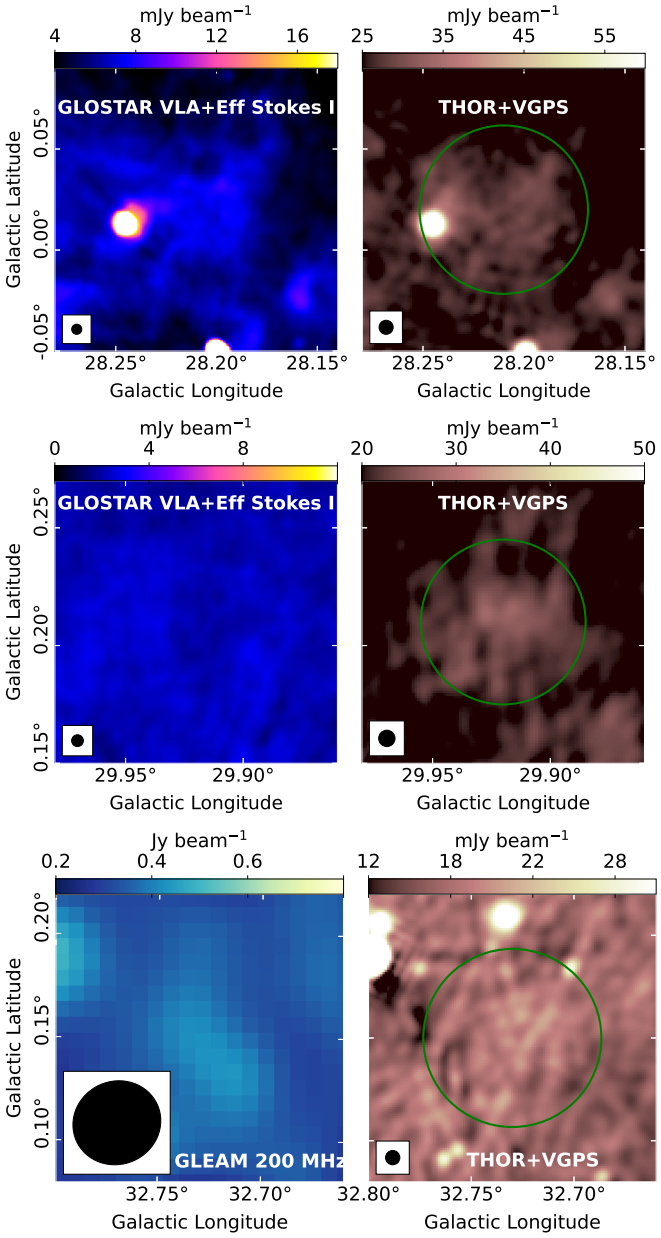

Fig. B.1: Images of three SNR candidates from THOR: G28.21+0.02 (top panels), G29.92+0.21 (middle panels), and G32.73+0.15 (bottom panels). The diffuse emission from G28.21+0.02 overlaps with the bright H II region at l~28.25°, b~0.01°. G29.92+0.21 and G32.73+0.15 are not detected in the GLOSTAR combination images.

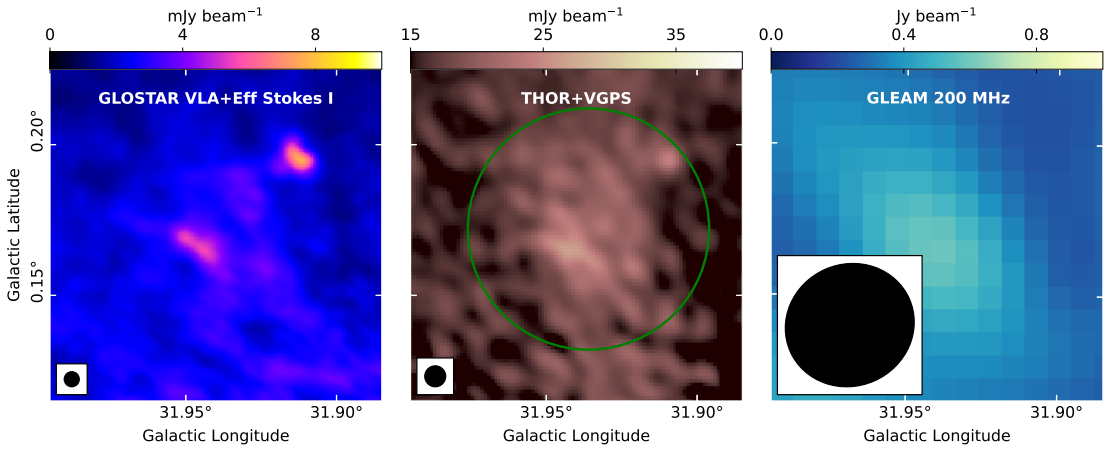

Fig. B.2: G31.93+0.16, a SNR candidate from THOR, as seen in the GLOSTAR combination (left), the THOR+VGPS (middle), and the 200 MHz GLEAM data (right).

List of Figures

Thesis front cover picture: GLOSTAR VLA-D + Effelsberg combined image: pilot region
Thesis back cover picture: GLOSTAR VLA-D + Effelsberg combined image: Galactic center

List of Tables

Acknowledgements

Some researchers have argued that, as a function of time, a person's happiness correlates the most with the quality of their relationships—even more than academic, economic, or social standing. Correlation doesn't necessarily mean causation, but here, correlation does imply causation: my happiness stems from the people in my life. These past few years that I spent working on my thesis were filled with joy and excitement; this was despite the tough condition of moving so far away from my comfort zone, and the even tougher conditions imposed by the virus of unknown origin. My gratitude extends to several people, without who this thesis wouldn't have been possible. They are listed below, non-exhaustively, in no particular order.

First of all, I am sincerely thankful to my advisors Karl and Andreas for taking me on in the GLOSTAR group. They gave me the freedom to work on the things I like, in the way I prefer, and they guided me with patience, assurance, and encouragement that stretched beyond work. I'm really glad for doing my PhD here. I must also thank my master's thesis advisor, Nirupam, and my uncle, Prasad mamayya, both of who had led me into this exciting field in the first place. I will forever be grateful for the constructive feedback and the advice I had received from these people over the past few years. I would also like to thank Prof. Dr. Pavel Kroupa, Prof. Dr. Simon Stellmer, and Prof. Dr. Leonie Esters for agreeing to be a part of my thesis committee.

The GLOSTAR collaboration. Aiyuan, Andreas, Friedrich, Gisela, James, Karl, Michael, Sergio, Yan, etc. all had a great impact on my work. Whether it was carefully dissecting the methods I used, patiently making my first drafts better, or helping with observations and proposals, you always had invaluable comments and suggestions. It was a pleasure to work on the GLOSTAR images; for this, I must thank Andreas, Bill, Sergio, and Yan. The combined VLA-D+Effelsberg images are simply quite beautiful.

A few other scientists that helped me over various issues are Dirk, Henrik, and Loren; I thank you too. Special thanks to Wolfgang and Patricia for thoroughly reading a part of my thesis, for playing a key role in sustaining my love for supernova remnants, and for the assistance in getting my work published.

Barbara, Boriana, Eva, Le, and Simone, for helping me navigate all the required paperwork, from before I entered Germany and throughout all these years.

Sebastian, Stefanie, and Thomas for the tutoring experience. The course on dark matter and dark energy in particular gave me a sense of joy in an otherwise drab winter.

`Hehskshfjajdhfs` (Hans, Jens, Maude, Prajwal, Sarwar, Venkat, etc.) for patiently making me better at hitting birdies and helping me keep myself (relatively) fit. I don't think I can ever be as good as you guys, but now I can say that I am not a complete badminton newbie like I was when I first came to Bonn.

`The Weekend Squad` (Estera, Irene, Merlin, Paloma, Parichay, Sabrina, Sonia) for all the lovely visits and the board-game nights, and also Parichay for everything. I realize that the squad game has weakened now (pun totally intended), but I will always cherish all the times

we had spent together, especially when we didn't follow some rules during the difficult second lockdown. You were the reason that I stayed sane and normal (well, more or less) despite being stuck inside for so long.

Mani, Pavan, Ravi Raj, and Ravi Teja, for always being only a text or a call away, even though we are rarely ever in the same country these past few years. A decade is a long time—I am glad to have been friends with you for even longer than that, and I am sure we will continue to be so for much, much longer.

Arshia, Ben, Dat, and Hans, for being my 'life coaches' and great friends. You were responsible for a lot of the good times I had during the making of this thesis. I will never forget when you told me that the game isn't worth the candle sometimes and stopped me from giving an unsavory reply. I am blessed to have had you guys around and I just cannot thank you enough.

The 12 pm lunch regulars Eleonore, Hans, Iason, Ivalu, Laure, Manali, Nina, Kartik, etc., for the innumerable facts and discussions ranging from the (very important) physiology of ducks to the (very, very important) reality TV, and for motivating me to go to work "early".

Laure and Eleonore, for being the best office-mates I ever had, despite an unfulfilled promise of going skiing and the roasting I received for not knowing how Beyoncé looks. Also thanks to all my other office-mates for letting me have peaceful siestas!

The University of Bonn 'PhD cafe', especially Christina for arranging them, and Dario, Elif, Jan, Manjusha, Mara, and Saeda, for joining regularly and making them lively.

Bhavya and Maitraiyee, for helping me settle in Bonn when I was like a fish out of water.

Home away from home: the Alte Straße 43 community (Bettina, Johanna, Marcus, Parichay, Prasan, Sarwar, and, of course, Renate and Michael). You are amazing neighbours / roommates / owners in addition to being great cooks. My special thanks to you for the adventures we shared, and also for not calling the *Ordnungsamt* even when the music was too loud.

There are many other incredible people who helped me get through this important period of my life: Amit, Anahat, Ashwin, Deepali, Franzi, Imke, Jessica, Konda, Kranthi, Pragya, Sourish, Swetha, to name a few. I thank you all, too!

I've had many lively discussions and invigorating debates with you ranging from science to religion, philosophy to politics, interesting to mundane, and I enjoyed all the middling messy things in between as well, despite sometimes going on endlessly. I'm especially grateful to the experiences (and memes) that you shared on navigating life as a PhD student. You were all there to lend an ear to my rants, to watch movies, to solve Python/LaTeX bugs with me, and to show me my shortcomings in a rather friendly manner. I will also cherish the numerous other things we had done together during the course of this thesis: the visits to Christmas markets and museums, the cooking sessions, the cozy night hangouts playing competitive board-games such as Wizard or Azul or S. H. or a million others, the excursions, the dates, the parties, and many more. I will sorely miss not only the good times we got to share, but also the support you guys gave me at my lowest and the tolerance you showed at my worst. Apologies to all the unintentionally missed names in this hastily (and perhaps *cheesily*) written acknowledgement, but please know that I thank you all too! The making of this thesis was rather smooth, and these little things (not so little, really) besides work were what made this time pass so easily.

In addition, I would like to thank the open-source community, especially those that work on or with CASA, Python, Ubuntu, or Linux, and the contributors on several Stack Exchange websites. Beneath the outwardly appearance of arrogance (for the lack of a better word), there exists a very cooperative *Gemeinschaft* with a sense of shared belief in the philosophy of open science and open technology. A lot of work in the present world, including this thesis, would not have happened if not for these strangers helping each other out on the internet. Also thanks to Olivier Commowick and Ioannis (John) Antoniadis for the LaTeX template, which was the basis of the format and the style of this thesis.

The one constant in my life is the unconditional love from my family, who always stood by my side. I dedicate this thesis to them as a small gesture of gratitude.

Bibliography

Albert, J. G., van Weeren, R. J., Intema, H. T., & Röttgering, H. J. A. 2020, A&A, 635, A147 (Cited on page 39.)

Altenhoff, W. J., Downes, D., Goad, L., Maxwell, A., & Rinehart, R. 1970, A&AS, 1, 319 (Cited on page 13.)

Anderson, L. D., Bania, T. M., Balser, D. S., et al. 2014, ApJS, 212, 1 (Cited on pages 48, 61, 62, 68, 77 and 139.)

Anderson, L. D., Wang, Y., Bihr, S., et al. 2017, A&A, 605, A58 (Cited on pages 13, 14, 37, 49, 61, 62, 67, 68, 71, 73, 75 and 139.)

Baars, J. W. M., Genzel, R., Pauliny-Toth, I. I. K., & Witzel, A. 1977, A&A, 500, 135 (Cited on page 47.)

Ballet, J. 2006, Advances in Space Research, 37, 1902 (Cited on page 78.)

Berezhko, E. G. & Völk, H. J. 2007, ApJ, 661, L175 (Cited on page 12.)

Bertin, E. & Arnouts, S. 1996, A&AS, 117, 393 (Cited on page 44.)

Beuther, H., Bihr, S., Rugel, M., et al. 2016, A&A, 595, A32 (Cited on pages 9, 35, 37, 52, 68 and 137.)

Bhat, N. D. R., Chengalur, J. N., Cox, P. J., et al. 2013, ApJS, 206, 2 (Cited on pages 36 and 138.)

Bihr, S., Johnston, K. G., Beuther, H., et al. 2016, A&A, 588, A97 (Cited on page 46.)

Blasi, P. 2013, A&A Rev., 21, 70 (Cited on page 12.)

Brentjens, M. A. & de Bruyn, A. G. 2005, A&A, 441, 1217 (Cited on page 40.)

Briggs, D. S. 1995, in American Astronomical Society Meeting Abstracts, Vol. 187, American Astronomical Society Meeting Abstracts, 112.02 (Cited on page 43.)

Brogan, C. L., Gelfand, J. D., Gaensler, B. M., Kassim, N. E., & Lazio, T. J. W. 2006, ApJ, 639, L25 (Cited on pages 14, 61 and 75.)

Brunthaler, A., Menten, K. M., Dzib, S. A., et al. 2021, A&A, 651, A85 (Cited on pages 15, 35, 37, 49, 51, 52, 55, 61, 68, 76, 137 and 139.)

Carey, S. J., Noriega-Crespo, A., Mizuno, D. R., et al. 2009, PASP, 121, 76 (Cited on pages 51, 61 and 70.)

Chakraborty, A., Roy, N., Wang, Y., et al. 2020, MNRAS, 492, 2236 (Cited on pages 37 and 76.)

Chandrasekhar, S. 1931, ApJ, 74, 81 (Cited on page 5.)

Chevalier, R. A. 1977, ARA&A, 15, 175 (Cited on page 10.)

Churchwell, E., Babler, B. L., Meade, M. R., et al. 2009, PASP, 121, 213 (Cited on pages 51 and 61.)

Condon, J. J., Cotton, W. D., Greisen, E. W., et al. 1998, AJ, 115, 1693 (Cited on pages 46, 47 and 70.)

Condon, J. J. & Ransom, S. M. 2016, Essential Radio Astronomy (Princeton) (Cited on page 16.)

Cornwell, T. J. 2009, A&A, 500, 65 (Cited on page 32.)

Cornwell, T. J., Golap, K., & Bhatnagar, S. 2008, IEEE Journal of Selected Topics in Signal Processing, 2, 647 (Cited on page 42.)

Cotton, W. D. 2008, PASP, 120, 439 (Cited on page 56.)

Cox, P., Kruegel, E., & Mezger, P. G. 1986, A&A, 155, 380 (Cited on page 61.)

de Gasperin, F., Intema, H. T., & Frail, D. A. 2018, MNRAS, 474, 5008 (Cited on pages 46, 47 and 138.)

Desai, K. M., Chu, Y.-H., Gruendl, R. A., et al. 2010, AJ, 140, 584 (Cited on page 12.)

Dokara, R. 2018, Master's thesis, Department of Physics, Indian Institute of Science, Bengaluru (Cited on page 16.)

Dokara, R., Brunthaler, A., Menten, K. M., et al. 2021, A&A, 651, A86 (Cited on pages 1, 14, 22, 37, 40, 47, 49, 52, 61, 64, 67, 68, 71, 76, 77, 85 and 139.)

Dokara, R., Gong, Y., Reich, W., et al. 2023, A&A, 671, A145 (Cited on pages 1, 51, 52, 58, 67, 76 and 115.)

Dokara, R., Roy, N., Beuther, H., et al. 2018, ApJ, 866, 61 (Cited on page 47.)

Downes, D. 1971, AJ, 76, 305 (Cited on page 13.)

Draine, B. T. 2011, Physics of the Interstellar and Intergalactic Medium (Princeton) (Cited on pages 10 and 73.)

Driessen, L. N., Domček, V., Vink, J., et al. 2018, ApJ, 860, 133 (Cited on page 75.)

Dubner, G. & Giacani, E. 2015, A&A Rev., 23, 3 (Cited on pages 48 and 78.)

Dzib, S. A., Yang, A. Y., Urquhart, J. S., et al. 2023, A&A, 670, A9 (Cited on pages 52 and 76.)

El-Badry, K., Ostriker, E. C., Kim, C.-G., Quataert, E., & Weisz, D. R. 2019, MNRAS, 490, 1961 (Cited on page 12.)

Farnes, J. S. 2012, PhD thesis, University of Cambridge (Cited on page 40.)

Farnes, J. S., Green, D. A., & Kantharia, N. G. 2014, MNRAS, 437, 3236 (Cited on page 40.)

Ferrand, G. & Safi-Harb, S. 2012, Advances in Space Research, 49, 1313 (Cited on pages 14, 37, 68, 77 and 139.)

Ferrière, K. M. 2001, Reviews of Modern Physics, 73, 1031 (Cited on pages 4 and 141.)

Field, G. B., Goldsmith, D. W., & Habing, H. J. 1969, ApJ, 155, L149 (Cited on page 4.)

Frew, D. J. & Parker, Q. A. 2010, PASA, 27, 129 (Cited on page 5.)

Fürst, E., Reich, W., Reich, P., Handa, T., & Sofue, Y. 1987, A&AS, 69, 403 (Cited on pages 13, 69 and 70.)

Gao, X., Reich, W., Sun, X., et al. 2022, arXiv e-prints, arXiv:2211.11408 (Cited on page 75.)

Gao, X. Y., Reich, P., Hou, L. G., Reich, W., & Han, J. L. 2019, A&A, 623, A105 (Cited on page 62.)

Green, A. J., Reeves, S. N., & Murphy, T. 2014, PASA, 31, e042 (Cited on page 61.)

Green, D. A. 1984, MNRAS, 209, 449 (Cited on page 14.)

Green, D. A. 1991, PASP, 103, 209 (Cited on page 78.)

Green, D. A. 2019, Journal of Astrophysics and Astronomy, 40, 36 (Cited on pages 10, 13, 14, 15, 37, 48, 61, 62, 68, 73, 77, 139 and 140.)

Grobler, T. L., Nunhokee, C. D., Smirnov, O. M., van Zyl, A. J., & de Bruyn, A. G. 2014, MNRAS, 439, 4030 (Cited on page 46.)

Hamaker, J. P., Bregman, J. D., & Sault, R. J. 1996, A&AS, 117, 137 (Cited on page 38.)

Handa, T., Sofue, Y., Nakai, N., Hirabayashi, H., & Inoue, M. 1987, PASJ, 39, 709 (Cited on page 68.)

Hartmann, J. 1904, ApJ, 19, 268 (Cited on page 3.)

Haslam, C. G. T., Salter, C. J., Stoffel, H., & Wilson, W. E. 1982, A&AS, 47, 1 (Cited on pages 3 and 137.)

Heger, A., Fryer, C. L., Woosley, S. E., Langer, N., & Hartmann, D. H. 2003, ApJ, 591, 288 (Cited on pages 9 and 141.)

Helfand, D. J., Becker, R. H., White, R. L., Fallon, A., & Tuttle, S. 2006, AJ, 131, 2525 (Cited on pages 14 and 61.)

Helfand, D. J., Velusamy, T., Becker, R. H., & Lockman, F. J. 1989, ApJ, 341, 151 (Cited on page 14.)

Högbom, J. A. 1974, A&AS, 15, 417 (Cited on page 32.)

Hubble, E. P. 1928, Leaflet of the Astronomical Society of the Pacific, 1, 55 (Cited on page 13.)

Huggins, W. & Miller, W. A. 1864, Philosophical Transactions of the Royal Society of London Series I, 154, 437 (Cited on page 3.)

Hurley-Walker, N. 2017, arXiv e-prints, arXiv:1703.06635 (Cited on page 47.)

Hurley-Walker, N., Filipović, M. D., Gaensler, B. M., et al. 2019a, PASA, 36, e045 (Cited on pages 14 and 61.)

Hurley-Walker, N., Gaensler, B. M., Leahy, D. A., et al. 2019b, PASA, 36, e048 (Cited on page 75.)

Hurley-Walker, N., Hancock, P. J., Franzen, T. M. O., et al. 2019c, PASA, 36, e047 (Cited on pages 35 and 68.)

Intema, H. T., Jagannathan, P., Mooley, K. P., & Frail, D. A. 2017, A&A, 598, A78 (Cited on pages 35 and 47.)

Jaskot, A. E., Strickland, D. K., Oey, M. S., Chu, Y. H., & García-Segura, G. 2011, ApJ, 729, 28 (Cited on page 12.)

Jeans, J. H. 1902, Philosophical Transactions of the Royal Society of London Series A, 199, 1 (Cited on page 4.)

Jurić, M., Ivezić, Ž., Brooks, A., et al. 2008, ApJ, 673, 864 (Cited on page 13.)

Kepley, A. A., Tsutsumi, T., Brogan, C. L., et al. 2020, PASP, 132, 024505 (Cited on page 43.)

Koda, J., Sawada, T., Wright, M. C. H., et al. 2011, ApJS, 193, 19 (Cited on page 58.)

Laughlin, G., Bodenheimer, P., & Adams, F. C. 1997, ApJ, 482, 420 (Cited on page 5.)

Li, Z., Wheeler, J. C., Bash, F. N., & Jefferys, W. H. 1991, ApJ, 378, 93 (Cited on pages 14, 37 and 65.)

Lockman, F. J. 1989, ApJS, 71, 469 (Cited on page 62.)

Lockman, F. J., Pisano, D. J., & Howard, G. J. 1996, ApJ, 472, 173 (Cited on page 62.)

Long, K. S. 2017, in Handbook of Supernovae, ed. A. W. Alsabti & P. Murdin, 2005 (Cited on page 13.)

Mancuso, S. & Spangler, S. R. 2000, ApJ, 539, 480 (Cited on page 40.)

Marti-Vidal, I. 2017, arXiv e-prints, arXiv:1706.00936 (Cited on pages 31 and 138.)

Martinez, L., Bersten, M. C., Anderson, J. P., et al. 2022, A&A, 660, A41 (Cited on page 73.)

Mavromatakis, F., Papamastorakis, J., Ventura, J., et al. 2001, A&A, 370, 265 (Cited on pages 67 and 70.)

Mayall, N. U. 1962, Science, 137, 91 (Cited on page 13.)

Mayall, N. U. & Oort, J. H. 1942, PASP, 54, 95 (Cited on page 13.)

McKee, C. F. & Ostriker, J. P. 1977, ApJ, 218, 148 (Cited on page 4.)

McMullin, J. P., Waters, B., Schiebel, D., Young, W., & Golap, K. 2007, in Astronomical Society of the Pacific Conference Series, Vol. 376, Astronomical Data Analysis Software and Systems XVI, ed. R. A. Shaw, F. Hill, & D. J. Bell, 127 (Cited on pages 33 and 39.)

Medina, S. N. X., Urquhart, J. S., Dzib, S. A., et al. 2019, A&A, 627, A175 (Cited on pages 51, 52, 68, 76 and 139.)

Milne, D. K. 1970, Australian Journal of Physics, 23, 425 (Cited on page 13.)

Misiriotis, A., Xilouris, E. M., Papamastorakis, J., Boumis, P., & Goudis, C. D. 2006, A&A, 459, 113 (Cited on page 73.)

Mohan, N., Chellappan Pillai, S. R., Swarup, G., & Oberoi, D. 2019, MNRAS, 487, 4819 (Cited on page 40.)

Molinari, S., Swinyard, B., Bally, J., et al. 2010, A&A, 518, L100 (Cited on page 51.)

Müller, P., Krause, M., Beck, R., & Schmidt, P. 2017, A&A, 606, A41 (Cited on page 57.)

Murphy, T., Mauch, T., Green, A., et al. 2007, MNRAS, 382, 382 (Cited on page 35.)

Nguyen, H., Rugel, M. R., Menten, K. M., et al. 2021, A&A, 651, A88 (Cited on pages 52 and 76.)

Nguyen, H., Rugel, M. R., Murugeshan, C., et al. 2022, A&A, 666, A59 (Cited on pages 52 and 76.)

Ortiz-León, G. N., Menten, K. M., Brunthaler, A., et al. 2021, A&A, 651, A87 (Cited on pages 52 and 76.)

Ostriker, E. C. & Shetty, R. 2011, ApJ, 731, 41 (Cited on page 12.)

Paladini, R., De Zotti, G., Davies, R. D., & Giard, M. 2005, MNRAS, 360, 1545 (Cited on page 69.)

Patnaude, D. J. & Fesen, R. A. 2007, AJ, 133, 147 (Cited on page 78.)

Perley, R. & Greisen, E. 2019, EVLA Memos, 207 (Cited on page 40.)

Perley, R. A. & Butler, B. J. 2013, ApJS, 206, 16 (Cited on page 40.)

Perley, R. A. & Butler, B. J. 2017, ApJS, 230, 7 (Cited on pages 39, 47 and 81.)

Ranasinghe, S. & Leahy, D. 2022, arXiv e-prints, arXiv:2209.04570 (Cited on page 14.)

Ranasinghe, S. & Leahy, D. A. 2018, AJ, 155, 204 (Cited on page 78.)

Rashid, M., Roy, N., & et al. in prep., in prep. (Cited on page 44.)

Rau, U., Bhatnagar, S., Voronkov, M. A., & Cornwell, T. J. 2009, IEEE Proceedings, 97, 1472 (Cited on pages 43 and 44.)

Rau, U. & Cornwell, T. J. 2011, A&A, 532, A71 (Cited on pages 33 and 43.)

Rau, U., Naik, N., & Braun, T. 2019, AJ, 158, 3 (Cited on page 58.)

Reich, W., Fürst, E., Haslam, C. G. T., Steffen, P., & Reif, K. 1984, A&AS, 58, 197 (Cited on page 68.)

Reich, W., Fürst, E., Reich, P., & Reif, K. 1990, A&AS, 85, 633 (Cited on page 58.)

Reich, W., Gao, X., & Reich, P. 2021, A&A, 655, A10 (Cited on page 75.)

Remazeilles, M., Dickinson, C., Banday, A. J., Bigot-Sazy, M. A., & Ghosh, T. 2015, MNRAS, 451, 4311 (Cited on pages 3 and 137.)

Scaife, A. M. M. & Heald, G. H. 2012, MNRAS, 423, L30 (Cited on page 47.)

Scalzo, R. A., Ruiter, A. J., & Sim, S. A. 2014, MNRAS, 445, 2535 (Cited on page 73.)

Schuller, F., Menten, K. M., Contreras, Y., et al. 2009, A&A, 504, 415 (Cited on page 51.)

Schwab, F. R. & Cotton, W. D. 1983, AJ, 88, 688 (Cited on page 42.)

Sedov, L. I. 1946, Journal of Applied Mathematics and Mechanics, 10, 241 (Cited on page 11.)

Shanahan, R., Lemmer, S. J., Stil, J. M., et al. 2019, ApJ, 887, L7 (Cited on page 76.)

Slavin, J. D., Dwek, E., & Jones, A. P. 2015, ApJ, 803, 7 (Cited on page 12.)

Slavin, J. D., Dwek, E., Mac Low, M.-M., & Hill, A. S. 2020, ApJ, 902, 135 (Cited on page 12.)

Sofue, Y. & Reich, W. 1979, A&AS, 38, 251 (Cited on pages 57 and 69.)

Stil, J. M., Taylor, A. R., Dickey, J. M., et al. 2006, AJ, 132, 1158 (Cited on pages 9, 68 and 137.)

Sun, X. H., Han, J. L., Reich, W., et al. 2007, A&A, 463, 993 (Cited on pages 22 and 57.)

Sun, X. H., Reich, P., Reich, W., et al. 2011, A&A, 536, A83 (Cited on page 22.)

Tammann, G. A., Loeffler, W., & Schroeder, A. 1994, ApJS, 92, 487 (Cited on page 7.)

Tamura, Y., Mawatari, K., Hashimoto, T., et al. 2019, ApJ, 874, 27 (Cited on page 12.)

Taylor, G. 1950, Proceedings of the Royal Society of London Series A, 201, 159 (Cited on page 11.)

Turatto, M. 2003, in Supernovae and Gamma-Ray Bursters, ed. K. Weiler, Vol. 598 (Springer), 21–36 (Cited on page 9.)

Turtle, A. J., Pugh, J. F., Kenderdine, S., & Pauliny-Toth, I. I. K. 1962, MNRAS, 124, 297 (Cited on page 69.)

Whiteoak, J. B. Z. & Green, A. J. 1996, A&AS, 118, 329 (Cited on pages 14 and 61.)

Wilson, T. L., Rohlfs, K., & Hüttemeister, S. 2013, Tools of Radio Astronomy (Springer) (Cited on pages 16, 35 and 48.)

Woltjer, L. 1972, ARA&A, 10, 129 (Cited on pages 10 and 73.)

Wykes, S., Intema, H. T., Hardcastle, M. J., et al. 2014, MNRAS, 442, 2867 (Cited on page 39.)

Yamaguchi, H., Ueno, M., Koyama, K., Bamba, A., & Yamauchi, S. 2004, PASJ, 56, 1059 (Cited on page 70.)

Yasuda, H., Lee, S.-H., & Maeda, K. 2021, ApJ, 919, L16 (Cited on page 11.)

Zhang, B., Moscadelli, L., Sato, M., et al. 2014, ApJ, 781, 89 (Cited on page 67.)

Zucker, C., Goodman, A. A., Alves, J., et al. 2022, Nature, 601, 334 (Cited on page 12.)